WEAK DECAYS OF CHARMED PARTICLES

by

Marc Gilles Turcotte

Physics Department

McGill University, Montreal

May 1986

A thesis submitted to the Faculty of Graduate Studies and Research
in partial fulfillment of the requirements for the degree of
Doctor of Philosophy

ABSTRACT

The lifetimes of charmed particles produced in interactions of high energy neutrinos with nucleons have been measured using a combination of a very high resolution emulsion-based vertex detector and a spectrometer allowing full kinematical reconstruction of the decays. The results from combining two runs of the experiment are:

$$\tau_{F^{+ \text{ or } -}} = 2.6^{+1.6}_{-0.9} \times 10^{-13} sec \qquad 6 \quad decays$$

$$\tau_{\Lambda_c^+} = 2.0^{+0.7}_{-0.5} \times 10^{-13} sec \qquad 13 \quad decays$$

$$\tau_{D^{+ \text{ or } -}} = 11.1^{+4.4}_{-2.9} \times 10^{-13} sec \qquad 23 \pm 5 \quad decays$$

where the quoted errors are all statistical. The lifetime of the charged D-meson is extracted using two independent methods and the results are found to be the same.

The uses of the statistical methods employed for the purpose of extracting the lifetimes are discussed. The applicability and resolving power of the methods are established using Monte Carlo simulations.

The ratio of the charged D-meson to neutral D-meson lifetimes is extracted from the charged and neutral data of the experiment. The result is found to be:

$$\frac{\tau_{D^{+ \text{ or } -}}}{\tau_{D^0 \text{ or } \overline{D}^0}} = 2.6^{+1.0}_{-0.9}$$

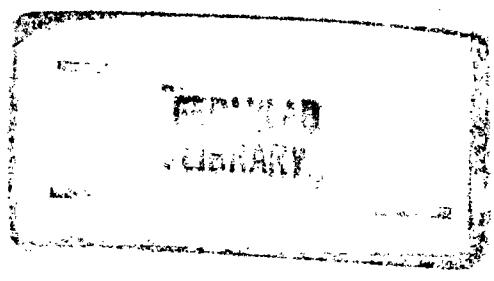

SOMMAIRE

Les durées de vie de particules charmées produites lors d'intéractions à hautes énergies de neutrinos avec des nucléons ont été mesurées à l'aide d'une combinaison d'un détecteur de vertex à très haute résolution composé d'émulsion et d'un spectromètre permettant une reconstruction cinématique complète des désintégrations. Les résultats obtenus après combinaison de deux prises de données sont les suivants:

$$\tau_{D^+ \text{ ou } -} = 2.6^{+1.6}_{-0.9} \times 10^{-13} sec \qquad 6 \quad \textit{désintégrations}$$

$$\tau_{\Lambda_c^+} = 2.0^{+0.7}_{-0.5} \times 10^{-13} sec \qquad 13 \quad \textit{désintégrations}$$

$$\tau_{D^+ \text{ ou } -} = 11.1^{+4.4}_{-2.9} \times 10^{-13} sec \qquad 23 \pm 5 \quad \textit{désintégrations}$$

où les erreurs indiquées sont entièrement statistiques. La durée de vie du méson chargé D est extraite à l'aide de deux méthodes indépendantes et le résultat trouvé est le même.

L'utilisation des méthodes statistiques employées aux fins d'extraction des durées de vie est discutée. L'applicabilité et le pouvoir de résolution des méthodes sont établis à l'aide de simulations Monte Carlo.

Le rapport des durées de vie des mésons neutres et chargés D est extrait des données neutres et chargées de cette expérience. Le résultat trouvé est le suivant:

$$\frac{\tau_{D^+ \text{ ou } -}}{\tau_{D^0 \text{ ou } \overline{D}^0}} = 2.6^{+1.0}_{-0.9}$$

ORIGINAL MATERIAL

The measurements of charmed particle lifetimes made by the E531 Collaboration are the best direct measurements performed to date. Such an achievement is primarily the result of a common effort sustained by constant competition towards excellence within the fine group of Experimentalists I was privileged to work with (Appendix 12.1) . The final results on lifetimes I present in Section 8 of this thesis are contributions to original knowledge.

My contributions to the experiment started with performing, as a member of a dedicated subgroup, the pre-2^{nd} Run tests of the Charged Particle Identifier. The success of these tests led directly to the implementation of the device.

I then took active part in the physical setting up of the experiment for its second run. I wrote sections of the on-line data-collecting and monitoring software and was involved in the introduction of new devices to the code.

As an active member of the Collaboration, I am responsible for having successfully collected a significant amount of the 2^{nd} Run data. This meant performing constant monitoring of the multitude of parameters of the experiment in order to make informed decisions pertaining to the conduct of the data collection. In the process of this, I had to detect malfunctions and sometimes fix the apparatus. I especially enjoyed assuming some of the responsibility associated with the data-collection aspect of E531.

After this, I performed the task of calibrating CPI. This was followed by my taking over the development of the off-line interactive track reconstruction programme. I wrote or modified large parts of the code used to successfully analyze the charm decays here at McGill University and contributed this to other members of the Collaboration.

I performed the kinematical analysis of the charged charmed events in parallel with the OSU analysis group. The results of this constitute the database on which this thesis rests.

I expanded the statistical methods of analysis previously used by the group to extract the lifetimes. I wrote a hybrid lifetime Monte Carlo simulation of the experiment. The results I obtained were highly instrumental in the understanding of the charged ambiguous sample.

ACKNOWLEDGEMENTS

I whish to extend my gratitude to **Suichi Kuramata** for his patient explanations of many emulsion topics, to **Jim Prentice** for his help in the analysis, to **Bill Reay** for his unequaled leadership in the Collaboration, to **Kurt Reibel** for his constant words of wisdom, to **Ron Sidwell** for being such an infinite source of information on all aspects of E531, to **Brian Stacey** for his kind guidance to the inner workings of the interactive fitting program, to **Noel Stanton** for his unique poised approach to many complex problems, to my **Advisor John Trischuk** for teaching me the meaning of a physical measurement and for his critical reading of the manuscript, to **Taek-Soon Yoon** for teaching me the ABC of scientific programming.

Many thanks to **Gordon Albrecht** for his contribution to the kinematical analysis, to **David Bailey** for his rôle in the set-up of the second run of the experiment and for his numerous attempts over many years at teaching me some of his profound understanding of a multitude of topics in Physics, History and Politics, to **Steve Errede** for providing an example to emulate, to **Soren Frederiksen** for his many patient responses to several queries, to **Alain Gauthier** for providing such an important and energetic contribution to the analysis, to **Mike Gutswiller** for introducing me to the early version of the analysis software, to **David Hanna** for his cooperation, to **JoAnne Hay** for booking all these flights and arrangements without a single glitch, to **Popat Patel** for his assistance, to **Ian Lovatt** for splitting close to six long months of night shifts on E531 with me, to **Roberto Mendel** for his patient and clear explanations of many fine points of the theory, to **Paul Mercure** for his constant help on all aspects of computing and his part in the second run data collection, to **Robert Nowac** for his meticulous building and testing of the CPI data collection electronics and for drawing all the figures in this thesis, to **Claude Plante** for his collaboration, to **Dale Pitman** for her work on some of the early versions of computer codes, to **Dave Ryan** for his sound advice, to the many (unfortunately not all of them known to me) **Scanners** of the E531 collaboration from Japan, Canada and Korea for their accurate work in the emulsions, to **Howard Trottier** for his clear explanations of some aspects of the theory, to **Mike Wong** for teaching me what I know about interactive programming on VAX-VMS, to **Mark Walton** for making many aspects of the theory much clearer to my mind and to all the other people from the third floor of the Physics Department.

I also thank **Stéphane Coutu** for his contribution to the analysis of the CPI data, **Steve Bracker** for his help with fixing the ECLIPSE, **Sean Lafleur** for writing software related to the hadron calorimeter, **Gordon McKeil** for the implementation of the lead-glass EPIC routines, **Anna Pesacki** for answering many software related questions, and **The FNAL Neutrino Crew Chiefs** for constant availability and responsiveness.

Finally, I wish to thank my **Parents** for their encouragement and my **Wife Marie Marois** , without whom life over the several years required for the analysis would not have been as enjoyable.

I extend full and sincere apologies to anyone who I might, inadvertently, have left out of this list.

TABLE OF CONTENTS

1.0) INTRODUCTION

The contemporary particle physicist's world is populated by a few fundamental particles called quarks and leptons together with a large number of composites of quarks called hadrons. The four known interactions between these particles are understood or believed to proceed via the exchange of virtual particles. The strong interactions proceed via exchange of gluons. The weak interactions proceed via exchange of the weak bosons. The electro-magnetic interactions proceed via exchange of the photon. Gravitation is thought to proceed via exchange of the graviton. The relative strengths of these interactions cover several orders of magnitude.

That there is some fundamental understanding at all on how the microscopic physical world of particles actually looks like is the result of the fine interplay of experimental and theoretical work that has been carried out since the early days of atom splitting. Probably one of the most important step in the advancement of the theoretical understanding of particle physics to date occured when the importance and relevance of gauge theories was realized and when their inner workings and the way they relate to Nature was uncovered. Not independently of this evolution, the experimental discovery of a new heavy quark flavour called Charm provided the key missing element which made the new approach to particle physics even more relevant. Of course, the experimental endeavour didn't stop there and continued on to reveal new features of the physical world. The recent experimental observation of the weak gauge bosons was entirely expected and provided a beautiful confirmation of the theoretical understanding adopted when charm was first seen.

Particles that carry a heavy quark like the charm quark as well as some other lighter quark(s) are interesting in their own right. Some properties of these particles are very interesting because they cannot yet be predicted with any certainty. The lifetime of charmed particles is such a quantity. The measurement of these lifetimes can provide indications as to what course the theoretical effort should follow. In that sense, such experimental work is of utmost importance.

This thesis is about a measurement and interpretation of the very short intervals of time the charged species of charmed particles live.

The E531 experiment which collected the data was located at the Fermi National Laboratory near Chicago Ill. . It was designed and built, the data collected and analyzed, by a small (by today's standards) group of physicists from four countries around the World: Canada, the United States, Japan and Korea. The paramount feature of the experiment and one of the reasons it was so successful, was its unique use of an emulsion-based very high-resolution vertex detector coupled to a specially designed electronic spectrometer.

The thesis is organized in the following way: Section 1 presents the current theoretical understanding of some relevant aspects of weak interactions and neutrino charm production as well as a review of the experimental evidence for charm. Section 2 deals with the current theoretical understanding of charm decay as well as a review of the current experimental situation concerning the flavour charm. Section 3 describes the equipment used to make the measurements while Section 4 describes its calibration and response properties. Section 5 presents the crucial and sometimes unique techniques used to make the measurements. Section 6 briefly describes the data taking and Section 7 explains how the charm candidates were analyzed. Section 8 presents the statistical analysis and the results. Finally, Section 9 sets the measurements against the World situation and offers some conclusions.

1.1) **The structure of matter: leptons and partons**

One of the most important lessons quantum physics has to give is that the physical description of phenomena is, in general, *not* independent on *how* it is being investigated. This is why it is not surprising to see that particles can only be defined in terms of how they interact or, using looser language, defined in terms of how they are being *looked* at.

1.1.1) **Leptons**

Some particles behave, with respect to the electro-magnetic and weak interactions almost as if they were copies of each other with different masses. These are the charged leptons: e^- , μ^- and τ^- and their corresponding anti-particles. The electron is stable but the muon decays into an electron in, on the average, $2.2 \times 10^{-6} sec$ while the tau turns into a muon or an electon in, on the average, $3.4 \times 10^{-13} sec$. Such processes, which are examples of the weak interactions at work, introduce, among the decay products, the very light and electrically neutral particles called neutrinos: ν_e , ν_μ and ν_τ together with their corresponding anti-particles. All these leptons have the same *intrinsic* quantity of angular momentum, or spin, which equals 1/2 of the fundamental quantum of angular momentum: $\hbar = 6.58 \times 10^{-25}\ GeV\ sec = 0.197\ GeV\ fm$. Spin shows up, for instance, in the form of the angular distribution of daughter products of a decaying particle or in the form of the angular distribution of scattered particles off a stable one. Leptons show no sign of interacting *strongly* with matter. That is, when interacting with material at high energy, they do so differently from the *hadrons* which experience the *strong* or loosely speaking, the nuclear force. Thus, leptons could perhaps be most simply characterised in terms of their *not* experiencing the strong interactions. Up to all probe energies presently available, the leptons have shown no sign of being composites of any smaller *building blocks*.

1.1.2) **Hadron partons: quarks and Gluons**

Hadrons in general and the nucleon in particular, are complicated particles. Not only do they dissipate energy at a far greater rate than leptons when they traverse dense material, thus suggesting that they interact in a fundamentally different way, but they show every sign of being composites of spin 1/2 components called partons. This we can tell from the angular distribution of scattered electrons in deep inelastic electron-nucleon scattering experiments. The data from these experiments are compatible with interpreting the nucleon as a three-quark state and this fact can be mathematically handled by group theory. Yet, the same data are incompatible with these quarks carrying all the momentum of nucleons; they only account for $\sim 1/2$ the nucleon's momentum. Experiments of other types provide more clues.

When an electron and a positron annihilate at high energy into a virtual photon, a quark-antiquark pair can then materialize: $e^+ e^- \rightarrow q \bar{q}$. In the center-of-mass, these two quarks fly-off back-to-back (to conserve momentum) and subsequently materialize as two opposite but collinear jets (cones) of hadrons. It is observed that individual hadrons within jets have momentum transverse to the quark or anti-quark directions, due to the process by which the quarks dress-up as hadrons and thus never show up themselves as *free* particles.

Some electron-positron collisions result in a three jet topology: the quark-jet, the anti-quark jet and a third jet whose distribution in perpendicular momentum relative to one of the other jets is compatible with the emission of a spin 1 massless virtual particle, the gluon: $e^+ e^- \rightarrow q \bar{q} g$. This is evidence for gluons as

fundamental building blocks of hadrons.

Thus, the current experimental picture of matter consists of leptons which are apparently point-like fundamental particles together with a collection of not-so-fundamental composites of quarks and gluons: the hadrons. Both leptons and quarks inside hadrons show signs that they are vulnerable to electromagnetic and weak interactions but only quarks can undergo strong interactions mediated by gluons. The quark-antiquark threshold production energies provide the list of known quarks: the up, down, strange, charm and beauty. An additional quark, called the top quark, is expected to show-up in high energy annihilation experiments on the basis of purely theoretical grounds. How interactions are mediated via the exchange of virtual quanta (gamma, gluon, weak-quanta) can be understood intuitively via Heisenberg's uncertainty principle. What quantum mechanics does not provide right off though, is the identity (quantum numbers of exchanged quanta) and range (masses of exchanged quanta) of such forces. Fortunately, gauge theories provide answers to such questions but, as could have been expected, bring new fundamental questions to mind.

This thesis deals with the measurement of a fundamental property of particles that carry the charm quark: their lifetime. To understand the meaning of the measurements and the purpose for which they are made, one must put them in the proper perspective provided by the current level of the theoretical understanding and inherent shortcomings of the known theory. The next few paragraphs are devoted to describing some of the required theoretical tools.

1.2) The Standard Model of electro-weak interactions

1.2.1) Explicit form

The steps of developing the $SU(2) \otimes U(1)$ Yang-Mills theory of the electro-weak interactions of both quarks † and leptons and pushing it through the spontaneous symmetry breaking process (thus introducing a scalar field known as the Higgs field) is the result of the work of S.L. Glashow [1] , Steven Weinberg [2] and Abdus Salam [3] for which they were awarded the 1979 Nobel Prize for Physics [4] . The renormalizability of the Weinberg-Salam Model was shown by G. 't Hooft in 1971 using renormalization group techniques [5] [6] .

In the Standard Model of electro-weak interactions, one finds: 1 *electric* charge from $U(1)$ and $2^2-1=3$ massive gauge fields from $SU(2)$ together with 6 lepton and 6 quark fields arranged in 6 weak-hypercharge *doublets* . The existence of the charm quark was predicted on theoretical grounds. §

† For a quick overview of those facts from gauge theory necessary to understand the basis of the Standard Model, see Appendix 12.2 . It may appear that all symmetries in nature need necessarily be broken in order to be useful. However, the Yang-Mills field-theory of spin 1/2 quarks inside hadrons assumes *un-broken* $SU(3)$ symmetry. It is known as quantum chromo-dynamics or QCD. In that theory, there are 3 charges called *colors* (as opposed to QED where there is only 1 charge because of the gauge group being $U(1)$) and $3^2-1=8$ gauge fields known as *gluons*. It turns out that, unlike QED's photon, QCD's gluons carry charge.

§ Before charm was discovered, there were already strong indications that it was required. Thus a certain "predictive" nature of the theory. This was because models of the time comprising only 3 quarks (u ,d and s) predicted fantastic rates for very rare strangeness-changing decays like $K_L^0 \rightarrow \mu^+\mu^-$, as much as for

The exact details of the process by which gauge fields acquire masses are presented, for example, in *Ref.* 8 where it is shown that, in the Higgs mechanism, it is not possible to diagonalize both the lepton and quark sectors simultaneously. Thus, leptons do not mix (in the limit of massless neutrinos †) but quarks do. This is usually referred to as the fact that the *weak* eigenstates are not the same as the *mass* eigenstates.

The Standard Model of electro-weak interactions [11] couples leptons & quarks through the massless electromagnetic gauge field of the photon γ and the massive gauge fields of the W^+ , W^- and Z^0 . The piece of the Lagrangian density responsible for this is:

$$\bar{\psi}\gamma^\mu \left[e\,Q\,A_\mu + \frac{e}{\sqrt{2}\sin\theta_w}\,(T^+ W_\mu^+ + T^- W_\mu^-) + \frac{e}{\sin\theta_w \cos\theta_w}\,(T_3 - \sin^2\theta_w\, Q)\, Z_\mu \right] \psi$$

where ψ is any of the 6 lepton or quark doublets:

$$\psi = \overbrace{\underbrace{\begin{pmatrix} u \\ d' \end{pmatrix}, \begin{pmatrix} c \\ s' \end{pmatrix}, \begin{pmatrix} t \\ b' \end{pmatrix}}_{Q_{up}=+2/3\,,\ Q_{down}=-1/3}, \underbrace{\begin{pmatrix} \nu_e \\ e^- \end{pmatrix}, \begin{pmatrix} \nu_\mu \\ \mu^- \end{pmatrix}, \begin{pmatrix} \nu_\tau \\ \tau^- \end{pmatrix}}_{Q_{up}=0\,,\ Q_{down}=-1}}^{6\ doublets} \begin{matrix} \leftarrow \textit{third component of weak isospin} = +1/2 \\ \leftarrow \textit{third component of weak isospin} = -1/2 \end{matrix}$$

and

$$T^+ = \frac{1}{2}(1-\gamma_5)\begin{pmatrix} 0 & 1 \\ 0 & 0 \end{pmatrix}$$

$$T^- = \frac{1}{2}(1-\gamma_5)\begin{pmatrix} 0 & 0 \\ 1 & 0 \end{pmatrix}$$

$$T_3 = \frac{1}{2}(1-\gamma_5)\frac{1}{2}\begin{pmatrix} 1 & 0 \\ 0 & -1 \end{pmatrix}$$

$Q =$ *electric charge*

$\theta_w =$ *weak mixing angle*

$A =$ *electromagnetic vetor potential (massless photon field)*

$W^\pm$ & $Z =$ *massive gauge fields*

The $W\,e\,\nu$ coupling is:

$$\frac{e}{\sqrt{2}\,sin\theta_w}\left[W_\mu^- \bar{e}\,\gamma^\mu \frac{1}{2}(1-\gamma_5)\,\nu + W_\mu^+ \bar{\nu}\,\gamma^\mu \frac{1}{2}(1-\gamma_5)\,e\right]$$

---

the leptonic decay of $K^+ \rightarrow \mu^+\nu_\mu$! Yet, such decays were known, at the time (mid to late 1960's), to be suppressed by a factor of 10^{-8}.[6] It was Glashow, Iliopoulos and Maiani (GIM) [7] who figured out a scheme to make these decays go at a much lower rate through the introduction of an additional quark flavour: charm.

† The mixing angle turns out to be proportional to the square of the mass difference [9] involved. Neutrinos which all have masses close to zero and thus close to each other could possibly turn into one another. E531 has set limits on the $\nu_\mu\ \nu_\tau$ oscillations and $\nu_\mu\ \tau$ coupling.[10]

and the $W\, q'_d\, q_u$ coupling is

$$\frac{e}{\sqrt{2}\,sin\theta_w}\left[W^-_\mu \overline{q}'_d\,\gamma^\mu \frac{1}{2}(1-\gamma_5)\,q_u \;+\; W^+_\mu \overline{q}_u\,\gamma^\mu \frac{1}{2}(1-\gamma_5)\,q'_d\right]$$

The electric charge, the third component of weak isospin and weak hypercharge are related through $Q = T_3 + \frac{1}{2}Y$. The ratio of the coupling constant of electromagnetism "e" to the coupling constant of charged-current weak interations "g" is parametrized by the Weinberg angle: $\sin\theta_w = e/g$. In lowest order, it turns out that

$$M_w^2 = \frac{\pi\alpha}{\sqrt{2}\,\sin^2_{\theta_w}\,G_F} \approx \left(\frac{37.3\;GeV/c^2}{\sin\theta_w}\right)^2$$

$$M_z^2 = \frac{M_w^2}{\cos^2\theta_w}$$

1.2.2) **Kobayashi-Maskawa quark mixing**

As was mentioned before, the quarks, as opposed to the leptons, do mix through the weak charged current. Since there are 3 up-type quarks and 3 down-type quarks, the matrix that performs this task is 3×3 . It must be unitary and have unit square-determinant so, in all, 4 parameters are required for its full specification [12] . If U denotes that matrix, then:

$$\begin{pmatrix} d' \\ s' \\ b' \end{pmatrix} = \begin{pmatrix} U_{ud} & U_{us} & U_{ub} \\ U_{cd} & U_{cs} & U_{cb} \\ U_{td} & U_{ts} & U_{tb} \end{pmatrix} \begin{pmatrix} d \\ s \\ b \end{pmatrix}$$

Kobayashi and Maskawa [13] parametrized this matrix using 3 angles (θ_1 , θ_2 and θ_3 ; $c_i \equiv \cos\theta_i$, $s_i \equiv \sin\theta_i$) and 1 phase δ in the following way:

$$U_{KM} = \begin{pmatrix} c_1 & -s_1\,c_3 & -s_1\,s_3 \\ s_1\,c_2 & c_1\,c_2\,c_3 \;-\; s_2\,s_3\,e^{i\delta} & c_1\,c_2\,s_3 \;+\; s_2\,c_3\,e^{i\delta} \\ s_1\,s_2 & c_1\,s_2\,c_3 \;+\; c_2\,s_3\,e^{i\delta} & c_1\,s_2\,s_3 \;-\; c_2\,c_3\,e^{i\delta} \end{pmatrix}$$

Of course, the actual values of the elements of the matrix have nothing to do with any particular parametrization. However, the parametrization is relevant because all elements are *not* independent of each other. The current experimental values (90% *C.L.*) of these elements is [14] :

$$U = \begin{pmatrix} U_{ud} = 0.9705\ to\ 0.9770 & U_{us} = 0.21\ to\ 0.24 & U_{ub} = 0.\ to\ 0.014 \\ U_{cd} = 0.21\ to\ 0.24 & U_{cs} = 0.971\ to\ 0.973 & U_{cb} = 0.036\ to\ 0.070 \\ U_{td} = 0.\ to\ 0.024 & U_{ts} = 0.036\ to\ 0.069 & U_{tb} = 0.997\ to\ 0.999 \end{pmatrix}$$

Every entry has a long experimental history behind it and the determination of the best overall set is presented in *Ref.* 15 .

If the third doublet of heavy quarks $\begin{pmatrix} t \\ b' \end{pmatrix}$ is ignored then one needs only a single parameter to describe the mixing: the Cabibbo [16] angle θ_c :

$$\begin{pmatrix} d' \\ s' \end{pmatrix} = \begin{pmatrix} V_{ud} & V_{us} \\ V_{cd} & V_{cs} \end{pmatrix} \begin{pmatrix} d \\ s \end{pmatrix}$$

in which

$$V = \begin{pmatrix} V_{ud} & V_{us} \\ V_{cd} & V_{cs} \end{pmatrix} = \begin{pmatrix} \cos\theta_c & \sin\theta_c \\ -\sin\theta_c & \cos\theta_c \end{pmatrix}$$

In the above, $\cos\theta_c = 0.9737 \pm 0.0025$ from $0^+ \rightarrow 0^+$ beta decays of ^{14}O and ^{26m}Al compared to μ-decay and $\sin\theta_c = 0.230 \pm 0.003$ from semi-leptonic (SL) decays of hyperons [17] . Thus, the remaining two doublets of quarks are:

$$\begin{pmatrix} u \\ d' \end{pmatrix} = \begin{pmatrix} u \\ d\cos\theta_c + s\sin\theta_c \end{pmatrix} \quad \begin{pmatrix} c \\ s' \end{pmatrix} = \begin{pmatrix} c \\ -d\sin\theta_c + s\cos\theta_c \end{pmatrix}$$

1.2.3) **Experimental support**

Hard experimental support for the Standard Model came from the discovery, in 1973 , of evidence for the weak neutral currents [18] .

$$\overline{\nu}_\mu\, e^- \rightarrow \overline{\nu}_\mu\, e^-$$

Then came the first recognized indirect evidence for the up-to-then missing charm quark (thus experimentally supporting the GIM hypothesis) from the observation, in November 1974 , of the 3.1 GeV/c^2 $J/\psi \equiv c\,\overline{c}$ meson production in pp collisions at BNL [19] and in $e^+\,e^-$ annihilations at SLAC [20] . The east-coast MIT-BNL collaboration observed a sharp peak in the $e^+\,e^-$ invariant mass spectrum from

$$p\,Be \rightarrow J + anything$$
$$J \rightarrow e^+\,e^-$$

This was attributed to a new particle, called J , produced through parton-antiparton annihilation (Drell-Yan process [21] ; partons are briefly discussed later) into virtual photon then materializing into an electron-positron pair. The west coast SLAC-LBL group observed the same particle, but named it ψ . It showed up as a sharp peak in the following cross-sections (at center-of-mass energy of 3.1 GeV):

$$\sigma_{e^+\,e^-\,\rightarrow\, anything}$$
$$\sigma_{e^+\,e^-\,\rightarrow\, e^+\,e^-}$$
$$\sigma_{e^+\,e^-\,\rightarrow\, \mu^+\,\mu^-}$$

Certainly, the picture of the weak-interactions remained incomplete until the experimental observation of the weak gauge bosons. Asssuming that $\sin^2\theta_W \approx 0.21$ [22] , the Standard Model yields $M_W \approx 81\ GeV/c^2$. Armed with a similar prediction, Carlo Rubbia convinced Geneva's CERN laboratory authorities to modify the Proton Synchrotron in order to allow $p\,\overline{p}$ collisions and also to build large electronic detectors. Storing the anti-proton beam required the development, headed by Simon Van der Meer, of a new *cooling* technique. Experiments [UA(1) and UA(2)] at the remodeled facility soon discovered the gauge bosons through the processes [23] [24] :

$$p\,\overline{p} \rightarrow W^\pm\, X \qquad W^\pm \rightarrow e^\pm\,\nu_e$$
$$p\,\overline{p} \rightarrow Z^0\, X \qquad Z^0 \rightarrow e^+\,e^-$$

at masses [25] [26] of

$$M_W^{UA(1)} = 80.9 \pm 1.5 \pm 2.4\ GeV/c^2$$
$$M_W^{UA(2)} = 83.1 \pm 1.9 \pm 1.3\ GeV/c^2$$
$$M_Z^{UA(1)} = 95.6 \pm 1.4 \pm 2.9\ GeV/c^2$$
$$M_Z^{UA(2)} = 92.7 \pm 1.7 \pm 1.4\ GeV/c^2$$

and thus determined

$$\sin^2\theta_w = 0.226 \pm 0.0015 \qquad UA(1)$$

$$\sin^2\theta_w = 0.216 \pm 0.010 \pm 0.007 \qquad UA(2)$$

In recognition of their leading rôles in this massive collective achievement, Rubbia and Van der Meer were awarded the 1984 Nobel Prize for Physics.

This section has displayed some of the most brilliant successes of the Standard Model. Experiments are continually probing and will continue to probe every detail of its predictions. Even before any experimental outcomes are known, theorists have already expressed dissatisfaction with many aspects of the theory. For instance, there is (within the confines of the Standard Model alone) no understanding of the pattern of quark and lepton masses and mixing angles nor is there any understanding of why quark-lepton generations repeat or how many there are. In that sense, there is a large amount of parametrization going on.

1.3) **Neutrino production of charmed particles**

1.3.1) **Charm quark production**

The subject of charm production by neutrinos and antineutrinos is extensively covered in *Ref.* 27 and *Ref.* 28 . Nevertheless, it is useful to briefly describe here some of the concepts associated with neutrino charm production so as to give as complete a picture as possible of the physics involved. The basic kinematics is shown on Figure # 1 . In what has become standard notation in the literature, k is the 4-momentum of the incident lepton (ν or $\overline{\nu}$) while k' is the 4-momentum of the outgoing lepton (for charged current: μ^- or μ^+ , for neutral current: ν or $\overline{\nu}$). The 4-momentum transfer to a quark inside the target nucleon is $q = k - k'$. The target nucleon has mass M and 4-momentum P . Important Lorentz-invariant quantities are:

$$\nu = \frac{q\cdot P}{M} \overset{lab}{=} E_{lab} - E'_{lab} \equiv \textit{lepton's energy loss in the lab.}$$

$$Q^2 = -q^2 = 2\left(EE' - \vec{k}\cdot\vec{k'}\right) - m_l^2 - m_{l'}^2 \quad m_l,\ m_{l'} \textit{ are the initial (final) lepton masses}$$

$$x = \frac{-q\cdot q}{q\cdot P} \overset{lab}{=} \frac{Q^2}{2M\nu}$$

$$y = \frac{q\cdot P}{k\cdot P} \overset{lab}{=} \frac{\nu}{E_{lab}} \equiv \textit{fraction of lepton's energy lost in the lab.}$$

$$W^2 = (P+q)^2 = M^2 + 2M\nu - Q^2 \equiv \textit{mass squared of the system recoiling against the lepton}$$

in which $0 \le x, y \le 1$.

The connection with the quark-parton model of hadrons is made through the quark distribution functions. In the so-called infinite momentum frame (no transverse momentum) ., $x_i = p_i/P$ is defined as the fractional momentum carried by the i^{th} parton. The probability that some quark of flavour q carries a momentum fraction between x and $x + dx$ is written $q(x)$. Thus,

$$\int_0^1 x\left[u(x) + d(x) + s(x) + c(x) + \ldots + \overline{u}(x) + \overline{d}(x) + \overline{s}(x) + \overline{c}(x) + \ldots + G(x)\right]\, dx = 1$$

where $G(x)$ is the probability that the gluons carry a fraction between x and $x+dx$ of the proton's momentum. Quarks account for $\sim 1/2$ of the nucleon's momentum while the rest is taken-up by gluons.

Neutrino-nucleon structure functions can be expressed in terms of the quark distribution functions which are, in the infinite momentum limit, functions of x only. However, a more comprehensive treatment includes effects due to the mass of the produced quark flavour. It turns out that, more generally, the structure functions depend on

$$\xi = x + m_f^2/2MEy$$

and Q^2 where m_f is the mass of the produced quark [29] . The variable ξ can still be interpreted as the fraction of the target nucleon's momentum carried by the struck quark in a special frame known as the Breit frame. † In the limit of large Q^2 , the structure functions only depend on ξ . It can be shown [30] that the differential cross-section for inclusive charged-current (c.c.) charm production

$$\nu_\mu N \rightarrow \mu^- c X$$
$$\overline{\nu}_\mu N \rightarrow \mu^+ \overline{c} X$$

is given by

$$\frac{d^2\sigma^{\nu \text{ or } \overline{\nu}}}{dxdy} = \frac{G_F^2 ME}{\pi} \left\{ (1-y) + \frac{x}{\xi}\left[\frac{y^2}{2} \pm \left(y - \frac{y^2}{2}\right)\right]\right\} F_2^{\nu \text{ or } \overline{\nu}}(\xi)\, \theta(1-\xi)\, \theta(W - W_{MIN})$$

$$W_{MIN} = M + m_H \quad \textit{where } m_H \equiv \textit{produced hadron's mass}$$

$$\theta(a) = 0 \textit{ when } a < 0$$
$$= 1 \textit{ when } a \geq 0$$

in which

$$F_2^{\nu}(\xi) \approx 2\xi \left[\sin^2\theta_c\, d(\xi) + \cos^2\theta_c\, s(\xi)\right]$$
$$F_2^{\overline{\nu}}(\xi) \approx 2\xi \left[\sin^2\theta_c\, \overline{d}(\xi) + \cos^2\theta_c\, \overline{s}(\xi)\right]$$

The limit in which the above formulae are derived neglects any charm-anticharm ocean content of the nucleon by dropping this quark's contribution to the structure functions leaving only an expression in terms of F_2 ‡ Thus, one neglects cases when a charm-anticharm pair is produced by a gluon off some valence quark of the nucleon. Charged-current would convert preferably the anti-charm to anti-strange ($\propto |U_{cs}|^2$), and less preferably to anti-down ($\propto |U_{cd}|^2$). The other member of the pair, the charm quark, would be left free to fly off. See Figure # 2a,b . The limit also involves neglecting charm production off beauty quarks because the beauty content of the nucleon is negligible as the mass of the b-quark is large. Thus, in the nucleon (proton $\equiv uud$ and neutron $\equiv udd$) charged current neutrino production of charm occurs off the valence down quarks and ocean strange quarks. There isn't as much ocean strange quark content as there is valence down quark

† The Breit frame is the so-called "brick-wall" frame. In this frame, the quark and gauge-boson are collinear and the 3-momentum of the quark is exactly reversed by the "collision". No energy is transferred from the gauge-boson to the struck quark.

‡ F_2 has been measured in lepton-nucleon interactions, for example by the CDHS collaboration [31] [32] . For a recent review, see *Ref.* 33 .

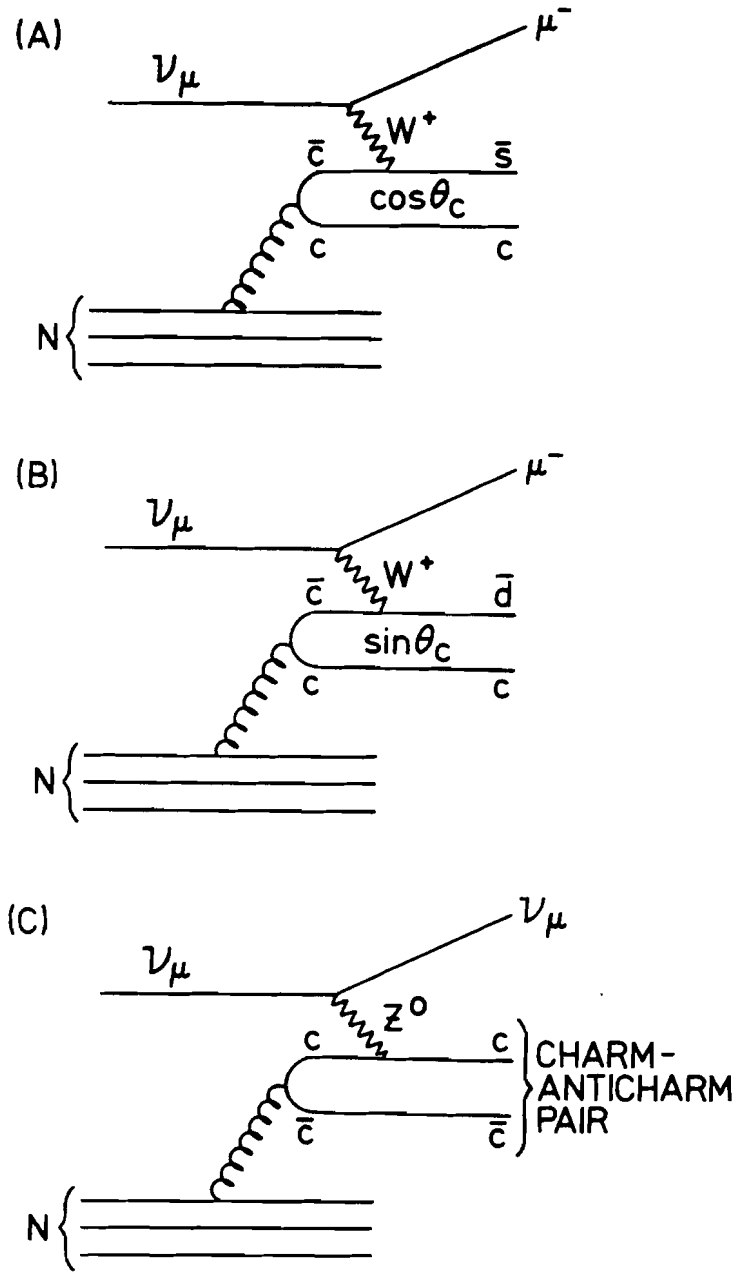

Figure # 2

Rare ν-production of charm mechanisms. In a), a gluon is radiated off a valence quark inside the target nucleon which turns into a charm/anti-charm pair. The weak charged current changes the anti-charm quark to an anti-strange quark while the charm quark flies off. In b), the anti-charm quark is changed to an anti-down quark while the charm quark flies off. In c), the ν scatters off the charm quark from a radiated pair through the weak neutral current leaving a charm/anti-charm pair flying off.

content but production off s-quarks is Cabibbo favored. Figure # 3 presents diagrams illustrating most probable processes.

Charm can also be produced via neutral currents. However, such processes are very rare as they involve popping a heavy $c\,\bar{c}$-pair from the ocean; see Figure # 2c .

1.3.2) **Charm quark fragmentation**

Up to now, only the part of heavy flavour lepto-production dealing with how the weak charged-current (W) picks a quark and turns it into another one has been dealt with. In doing so, the process $quark \rightarrow parton$ was characterized by the quark probability distribution functions $q_N^i(x)$ in which N denotes the target nucleon and i any of the quark flavour it contains. Given the differential cross-section for the weak charged-current to turn some quark i into some other quark j : $\frac{d^2\sigma}{dxdy}(i \rightarrow j)$, the total cross-section for the weak charged-current to turn quark i into any other quark is [30] :

$$\frac{d^2\sigma}{dxdy}(i \rightarrow anything) = \sum_j \frac{d^2\sigma}{dxdy}(i \rightarrow j)$$

Thus, the inclusive lepto-production coss-section is:

$$\frac{d^2\sigma}{dxdy} = \sum_i q_N^i(x) \frac{d^2\sigma}{dxdy}(i \rightarrow anything) = \sum_{ij} q_N^i(x) \frac{d^2\sigma}{dxdy}(i \rightarrow j)$$

The other process in which one deals with $parton \rightarrow quark$ or how the current-induced quark *picks up* other quarks to form hadrons is described by the so-called *fragmentation* functions $D_j^h(z)$ in which h stands for some outgoing hadron and j is the current-induced quark-flavour. The variable z has Lorentz-invariant definition

$$z_i = \frac{h_i \cdot P}{q \cdot P} \overset{lab}{=} \frac{E_i^{lab}}{\nu}$$

in which h_i is the i^{th} outgoing hadron's 4-momentum. In the laboratory frame, z_i is the fractional energy the i^{th} hadron carries away from the energy given off by the original incident lepton. The fragmentation functions are therefore the probability distributions that some outgoing hadron h carries a fractional energy between z and $z + dz$ of some current-induced quark j . So pretty much as for the quark distribution functions, one must have:

$$\sum_h \int_0^1 z D_q^h(z)\, dz = 1$$

The cross-section for lepto-production of hadron h with energy fraction z is thus written as:

$$\frac{d^3\sigma}{dxdydz} = \sum_{ij} q_h^i(x) \frac{d^2\sigma}{dxdy} D_j^h(z)$$

In the case of neutrino (anti-neutrino) production of charm (anti-charm), the sum over i is done for $i = d, s$ ($i = \bar{d}, \bar{s}$) while $j = c$ ($j = \bar{c}$). Thus:

$$\frac{d^3\sigma^{\nu}}{dxdydz}(\nu N \rightarrow \mu^- h_c X) = \sum_{i=d,s} q_h^i(x) \frac{d^2\sigma}{dxdy} D_c^h(z)$$

$$\frac{d^3\sigma^{\bar{\nu}}}{dxdydz}(\bar{\nu} N \rightarrow \mu^+ h_{\bar{c}} X) = \sum_{i=\bar{d},\bar{s}} q_h^i(x) \frac{d^2\sigma}{dxdy} D_{\bar{c}}^h(z)$$

where $D_c^h(z)$ ($D_{\bar{c}}^h(z)$) is the fragmentation function for the charm (anti-charm) quark to dress-up as charmed hadron h_c (anti-charmed hadron $h_{\bar{c}}$)... This distribution is presented in ***Ref.*** 34 and ***Ref.*** 35 .

1.4) **Expected and seen charmed hadrons**

1.4.1) **Quark Model predictions**

The quark model is a purely mathematical framework which allows some understanding of how the mesons and baryons are built from components. In that sense, the most relevant feature is that it predicts the quantum numbers of particles in terms of their valence quark content. Some details on how this comes about and on the difference between the symmetries in the quark model and symmetries of gauge theories are presented in Appendix 12.3 . The quark quantum numbers of the model are presented in Appendix 12.4 .

Figure # 4 presents quark-model predictions for the quantum numbers and quark content of a number of hadrons. The assumed flavour symmetry is $SU(4)_f$ and the peculiar patterns of the states are entirely dependent on this assumption. These predictions are useful, in the context of charm physics, because they provide, among other things, a list of expected charmed hadrons. Some degree of confidence in the predictions is secured by noting that ordinary (non-charmed) hadrons are all accounted for by the model.

1.4.2) **Experimental evidence for Charm: mesons and baryons**

In the following paragraphs, the experimental evidence for charm will be briefly discussed. The discovery experiments will be mentioned and some of the methods described. The different lifetime experiments are reviewed in some details.

As was noted before, charm made its first, yet indirect, entry into the experimental world when the $c\,\bar{c}$-state J/ψ at 3.1 GeV/c^2 was first observed [20] [19] . That its quantum numbers are that of the photon ($J^P = 1^-$) is a consequence of its being born out of the $e^+\,e^-$ annihilation process into a virtual photon. † If the J/ψ had been some high lying quark-excitation of some other meson made up of conventional quarks, it would have been observed to decay prominently and hadronically back to these *conventional* hadrons and its

† Evidence that the threshold for the production of a new quark flavour is reached shows up in several places. It turns out that, as one crosses a center-of-mass energy numerically equal to the mass of the ψ-resonance in the process $e^+\,e^- \rightarrow \mu^+\,\mu^-$, the total cross-section $\sigma_{e^+e^-\rightarrow\mu^+\mu^-}$ actually goes through an *interference* effect which is attributed to naive QED breakdown: vacuum polarization from the hadronic virtual states become important and $e^+\,e^- \rightarrow \psi^* \rightarrow \mu^+\,\mu^-$ *interferes* with $e^+\,e^- \rightarrow \gamma^* \rightarrow \mu^+\,\mu^-$ where the superscript "*" denotes a virtual particle. This is a technique actually used to verify that some *new* resonance has the same quantum numbers as the photon: the interference effects should be observed at the mass of the resonance and indeed were for the ϕ , $\psi(3.1\ GeV/c^2)$ and $\psi'(3.7\ GeV/c^2)$ [36] mesons. The presence of a new quark flavour also shows up in the following quantity:

$$R = \frac{\sigma\,(e^+\,e^- \rightarrow \textit{hadrons})}{\sigma\,(e^+\,e^- \rightarrow \mu^+\,\mu^-)}$$

as steps at the threshold energies corresponding to the new $q\,\bar{q}$ states being produced [32] . Actually, the R-coefficient not only counts the total number of quark flavours but also counts the number of quark *colours*.

width would have been typical of the strong interactions, that is, rather large. The inferred width ¶ of the J/ψ ($63 KeV$ [32]) is too small to be compatible with strong interactions and thus it decays electromagnetically (or radiatively) with a typical small width. The fact that J/ψ goes through electromagnetic decay instead of just $c\,\bar{c}$ annihilating into three gluons which would then materialize back into hadrons is an example of the OZI rule [38] which states that such *disconnected* quark diagrams are strongly suppressed. Of course, J/ψ could have decayed to a $D^+_{c\,\bar{d}}\,D^-_{\bar{c}\,d}$ pair or to $D^0_{c\,\bar{u}}\,\overline{D}^0_{\bar{c}\,u}$ pair without violating the OZI rule but only if those mesons did not have a higher mass than the parent J/ψ . As it is, it not only turns out that they do, but they were expected to, just on the basis of the observed decay mode and width of J/ψ . ‡ In fact, after the discovery of J/ψ , a whole new spectroscopy of its excited states (χ-states) was uncovered.

The lowest-lying charmed mesons, the pseudo-scalar $D^+_{c\,\bar{d}}$, $D^-_{\bar{c}\,d}$, $D^0_{c\,\bar{u}}$ and $\overline{D}^0_{\bar{c}\,u}$ were first recorded at SLAC's $e^+\,e^-$ SPEAR collider back in the late 1970's by the Mark I, Mark II, and DELCO detectors [39] . The actual source of D-mesons was the OZI-allowed copious hadronic decay of the ψ'' :

$$\psi''\left(3.77\,GeV/c^2\right) \rightarrow \left\{ \begin{array}{c} D^+\,D^- \\ \\ D^0\,\overline{D}^0 \end{array} \right\}$$

The neutral D-meson showed up as peaks in the invariant mass spectra of the $K^\pm\,\pi^\mp$ and $K^\pm\,\pi^\mp\pi^+\pi^-$ combinations recorded by the SLAC-LBL group with the magnetic detector at SPEAR [40] . Particle I.D. probabilities from time-of-flight measurements (see Section 5.2.7 for example in the context of E531) provided weights which helped in dealing with the large combinatorics involved. The mass of the neutral-D was extracted by fitting the invariant mass spectrum to a Gaussian peak plus linear and quadratic background. The spectra of masses recoiling *against* the neutral combinations mentioned above were also measured and

¶ Actually, the experimental width *is* very broad because of the experimental resolution (e.g. beam-momentum uncertainty). The true width was *inferred* from a simultaneous fit of the experimental total $e^+\,e^-$ annihilation cross-section plot versus center-of-mass energy to the following parameters: m ,Γ_e ,Γ_μ and Γ_h with $\Gamma = \Gamma_e + \Gamma_\mu + \Gamma_h$ and assuming the observed spectrum was the result of the convolution of a Gaussian resolution function and a Breit-Wigner total cross-section form of the following type:

$$\int \sigma_{channel}\,dE = \frac{2\,\pi^2}{m^2}\,(2\,J\,+\,1)\,\frac{\Gamma_e\,\Gamma_{channel}}{\Gamma}$$

for any channel. In the above formula, $\sigma_{channel} \equiv \sigma_{e^+\,e^- \rightarrow \psi \rightarrow channel}$ and $J = 1$, as was determined by the interference effect mentioned earlier [37] .

‡ Actually, the OZI rule was established in the context of $\phi \rightarrow K\,\overline{K}$ decays where ϕ is an $s\,\bar{s}$ state. In that case though, ϕ *does* decay into $K\,\overline{K}$ preferentially over say, to $\pi\pi\pi$, although the latter is phase-space favored. (Note that the two-kaon mass is just below that of the ϕ while the three-pion mass is way below.) Decays of J/ψ thus merely confirm the rule... In addition, the higher-lying ψ'' with a mass of $3.77\,GeV/c^2$ is therefore not kinematically forbidden to decay to charm-anticharm meson pairs, and it does so hadronically (without violating the OZI rule) with typical larger width of $2500\,KeV/c^2$ [32] .

showed no evidence for systems recoiling with masses less than the measured mass of the neutral-D , as it should be, since the neutral-D's were, in that experiment, produced in pairs.

In a later experiment also at the SLAC-LBL magnetic detector at SPEAR [41] , both $D^0\ \overline{D}^0$ and $D^+\ D^-$ were detected. Use was made of the fact that the center of mass of $e^+\ e^-$-collisions is at rest in the laboratory frame of reference when two equal-energy electron-positron beams are collided. Thus, $E_{c.m.} = 2\ E_{beam}$. Since $e^+\ e^- \rightarrow \psi'' \rightarrow D\ \overline{D}$, ie a charmed meson pair, half the center-of-mass energy is available for each D-meson at the resonance. The invariant mass of a D-meson candidate particle combination is thus given by:

$$m = \sqrt{E_{beam}^2 - p^2}$$

where p is the total 3-momentum of the combination. The point in making the beam energy enter the mass calculation was that $\sigma_{E_{beam}} \ll \sigma_{E_{combination}}$ so that, in the end, it turned out that 5 to 10 times more precise mass measurements could be done that way. Thus, each particle combination's energy was required to agree closely with the beam energy and those which didn't were thrown out. In particular, the charged D-meson was clearly seen in the $D^{\pm} \rightarrow K_s^0\ \pi^{\pm}$ channel thus experimentally establishing the state.

Perhaps more interesting is that this collaboration also measured the angular distribution of the D's relative to the incident beams. Now, ψ'' , a spin-one object, was created with its spin parallel (or anti-parallel) to the head-on colliding electron-positron beams. If the two decay products (D^0 and $\overline{D}^0$ or D^+ and D^-) each have zero spins, the distribution of the number of D's in the polar angle θ (with respect to the beam) should take the following form [42] [43] :

$$P_{1^- \rightarrow 0^- 0^-}(\theta) \propto \sin^2\theta$$

while for daughter particles of other spins, it would take the form:

$$P_{1^- \rightarrow else}(\theta) \propto \left(1 + \alpha \cos^2\theta\right) \qquad -1 \leq \alpha \leq 1$$

It was determined that, for neutral and charged D-mesons, $\alpha = -1$ within 10% thus, consistent with zero spin for both species.

Since the early experiments, neutral and charged D mesons have been produced in large numbers with many machines. Yet, it cannot be too emphasized that experiments at $e^+\ e^-$ colliders do *not* actually record the passage and decay of charmed particles through a detector, they merely *infer* their presence from the decay secondaries. The masses extracted from the World data by the Particle Data Group [32] are:

$$M_{D^+ \text{ or } D^-} = 1869.4 \pm 0.6\ MeV/c^2$$

$$M_{D^0 \text{ or } \overline{D}^0} = 1864.7 \pm 0.6\ MeV/c^2$$

Experimental evidence on excited states of the D-mesons ($J^P = 1^-$, see Figure # 4) also comes from $e^+\ e^-$ machines and the Particle Data Group currently lists:

$$M_{D^{*+}} = 2010.1 \pm 0.7\ MeV/c^2$$

$$M_{D^{*0}} = 2007.2 \pm 2.1\ MeV/c^2$$

An additional body of new experimental data on the third member of the top $SU(3)_f$ triplet from the $SU(4)_f$ $J^P = 0^-$ representation, the $F^+_{c\bar{s}}$ (and the corresponding $F^-_{\bar{c}s}$ from the bottom triplet) has, since the very early reports from the DASP collaboration at DESY's DORIS $e^+ e^-$ storage ring [44] of a possible signal of $F^\pm \rightarrow \eta\pi^\pm$, much clarified the situation with respect to the F-meson †. Stronger evidence came from the CLEO group at Cornell's CESR $e^+ e^-$ collider [45] for the decay $F^\pm \rightarrow \phi\,\pi^\pm$ in which ϕ subsequently decays through: $\phi \rightarrow K^+ K^-$. They found the angular distribution of the decay products to be consistent with the decay of a spin zero object. Other groups have now also reported seeing the F-meson decay through that channel and the current Particle Data Group value for its mass [32] is:

$$M_{F+\ or\ F-} = 1971 \pm 6\ MeV/c^2$$

As it is, the mass of the F-meson is based on the $\phi\,\pi^\pm$ channel.

Recently, the ARGUS collaboration at the DORIS II $e^+ e^-$ storage ring at DESY has reported [46] a signal for $F^* \rightarrow F\,\gamma$ where F^* ($J^P = 1^-$) is an excited state of the F-meson at a mass of $2109 \pm 9\ MeV/c^2$.

Experimental evidence for Λ_c^+ , a $c\,u\,d$-baryon with $J^P = \frac{1}{2}^+$ first showed-up [47] at Brookhaven National Laboratory's 7-foot cryogenic bubble chamber back in 1975 . It was observed that, in one event, a high-energy neutrino interacted in the hydrogen and produced a single strange baryon, a Λ^0 with a typical Vee signature. Thus,

$$\nu\,p \rightarrow \mu^-\,\Lambda^0\,\pi^+\,\pi^+\,\pi^+\,\pi^-$$

Knowledge of all momenta and decay-angles (in a bubble-chamber, events are directly *photographed*) of all the visible (including the Vee) particles allowed computing a lower limit to the mass of the incident particle (neutrino) which was found compatible with zero. The vector sum of all visible momenta was found to be compatible with the ν-beam direction. Alternate interpretations of the event were found to have probabilities of 10^{-5} or less.

The existence of the state was further consolidated by the report of a peak in the invariant-mass spectum of the $\bar{\Lambda}\,\pi^-\,\pi^-\,\pi^+$ final state produced in the wide-band photon beam at Fermilab [48] .

Since these early days, the state has been observed in many other experiments and the Particle Data Group [32] now lists it at:

$$M_{\Lambda_c^+} = 2282.0 \pm 3.1\ MeV/c^2$$

It is interesting to notice that the spin of Λ_c^+ is still only based on the quark-model prediction.

Reports of discovery for more exotic charmed baryons have also been made more recently. The $A^+_{c\,s\,u}$ has been seen as a narrow state at 2460 MeV/c^2 in an experiment at the CERN hyperon beam [49] using Cherenkov counters, Multi-Wire Proportional Chambers and magnets. This collaboration sees a statistically

† The F-mesons are not produced as often as D-mesons in $e^+ e^-$ collisions because, in addition to the $c\,\bar{c}$-pair born out of the annihilation, one must pull a heavier $s\,\bar{s}$ quark pair from the ocean instead of the lighter $u\,\bar{u}$ or $d\,\bar{d}$ pairs for D-mesons. It has been estimated [45] that $s\,\bar{s}/total \sim 15\%$

significant peak in the invariant-mass distribution of the $\Lambda\, K^-\, \pi^+\pi^+$ final state produced in

$$\Sigma^-\, Be \rightarrow \left(\Lambda\, K^-\, \pi^+\pi^+\right)\, X$$

and attributes it to the Cabibbo-favored decay of A^+ . The same collaboration [50] even reported in 1984 seeing 3 instances of $T^0_{c\,,\,}$ decaying into $\Xi^-\, K^-\, \pi^+\pi^+$.

Obviously, charmed baryon spectroscopy and that of excited states of charmed mesons is not exhausted (Figure # 4).

2.0) CHARM DECAY: THEORY AND EXPERIMENTS

2.1) Naive Spectator Model of charm decay

Following fragmentation, the charmed hadron lives for some while and then it decays. The simplest view of the charm decay process is that it occurs totally independently of the other quark(s) in its environment. This is known as the Spectator Model of heavy quark decays. Essentially, it involves calculating the transition matrix element for quark transition:

$$T_{if} = \langle f | H_w | i \rangle$$

in which H_w is the effective charged-current weak Hamiltonian in the limit $M_w \rightarrow \infty$. This limit is justified as all weak decay momentum transfers are much smaller than the W-mass. The weak charged-current semi-leptonic decay width of a free charm quark is then given by [51] :

$$\Gamma_{sL}\left(c \rightarrow s\, l^+ \nu_l\right) = \frac{G_F^2\, m_c^5}{192\, \pi^3} \sum_{i=s,d} |V_{ci}|^2 \left(1 - 8\, z_i + 8\, z_i^3 - z_i^4 - 12\, z_i^2 \ln z\right)$$
$$z_i = m_i^2 / m_c^2$$

in which V_{ci} denotes the mass/weak eigenstate mixing and the factor in z_i is due to phase-space. In order to get an order of magnitude estimate, phase-space can be temporarily neglected (until Section 2.3). In this case the sum over s and d is ~ 1 . Since the muon decay width can be estimated in an entirely similar way, one therefore has:

$$\Gamma_{sL}\left(c \rightarrow s\, l^+ \nu_l\right) \approx \left(\frac{m_c}{m_\mu}\right)^5 \Gamma_{sL}\left(\mu \rightarrow e\, \overline{\nu}_e\, \nu_\mu\right)$$

Using $m_c \sim 1.75\ GeV/c^2$ one gets $\Gamma_{sL} \approx 5 \times 10^{11} s^{-1}$. Up to a Cabibbo factor, the weak charged-current also couples to $q\bar{q}$ pairs like $u\bar{d}$. So, it has been estimated that the total charm width in the Naive Spectator Model (NSM) is given by [52] :

$$\Gamma_{all} = \Gamma_{sL}^{NSM} + \Gamma_{NL}^{NSM}$$
$$\Gamma_{all} \approx \underset{(2\ accessible\ leptons)}{2\, \Gamma_{c \rightarrow s\, l^+ \nu_l}} + \underset{(3\ clr\ anti-clr\ of\ u\,\bar{d})}{3\, \Gamma_{c \rightarrow s\, u\, \bar{d}}}$$
$$\approx 5\, \Gamma_{sL} \approx 10^{+12}\ to\ 10^{+13} s^{-1}$$

and hence, on the basis of this model, it can be expected that charmed particle lifetimes are in the order of $\sim 10^{-13}\ sec$.

Certainly, this is not the only prediction one can get from the naive spectator model. Often made (and most useful) predictions are those involving the relative amplitudes of the decays:

$\Delta S = \Delta C = -1$		$\propto \cos^2 \theta_c$	*Cabibbo favored decays*
$\Delta S = 0$	$\Delta C = -1$	$\propto \sin \theta_c \cos \theta_c$	*Singly Cabibbo unfavored decays : suppressed*
$\Delta S = 1$	$\Delta C = -1$	$\propto \sin^2 \theta_c$	*Doubly Cabibbo unfavored decays : strongly suppressed*

See Figure # 5 for the basic quark processes involved in the spectator model of charm decay. If anything, the spectator model of charm decays provides a strongly intuitive yet only semi-quantitative understanding of the processes involved.

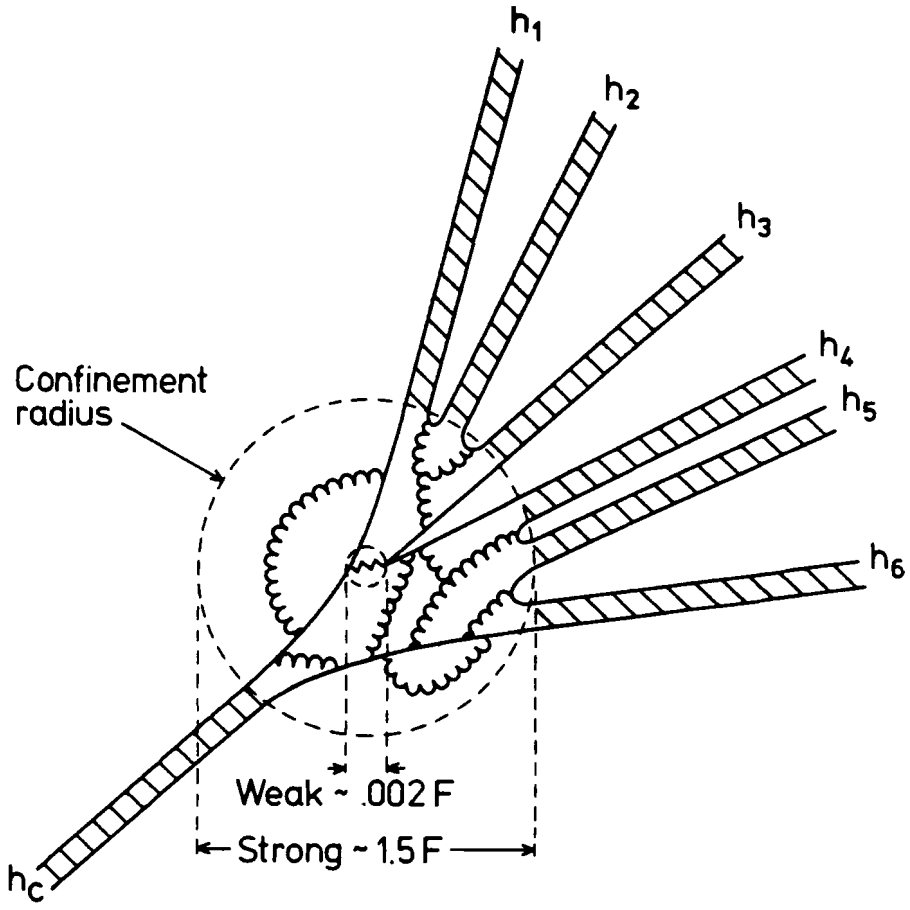

Figure # 6

Qualitative view of a realistic charmed particle decay. The typical ranges of the weak and strong interactions are indicated. The process depicted is $h_c \rightarrow h_1 \ldots h_6$ in which h_1 most likely carries a strange valence quark.

2.2) **Charm decay and strong interactions**

Strong interactions proceed via exchange of QCD's 8 massless (un-broken) $SU(3)$ gauge bosons called gluons between members of color quark triplets $q = (q_{red}, q_{blue}, q_{green})$. Leptons are color-neutral (do not carry any color charge) while hadrons are color-singlets (carry no net color charge) [53] . The coupling strength depends on the momentum transfer Q^2 involved and so perturbation theory is only applicable in certain regimes. The important point is that the QCD coupling constant (α_s) decreases logarithmically as Q^2 increases and thus perturbation theory in QCD is expected to be working *at sufficiently short distances* [54] . Attempts have thus been made to compute hard QCD corrections (HQCDC) to the non-leptonic (NL) decay of the charm quark.

The arguments presented up to now reveal a somewhat qualitative view [55] of the realistic decay of a charmed hadron and this is pictured in Figure # 6 . The charmed hadron (h_c), like other hadrons, is a complex assembly of fluctuating quark-gluon configurations. On the scale of the strong interactions however, the weak decay of the charm quark is almost point-like ($\sim .002\ F$) due to the large mass of the W-boson. After the weak current has acted, the daughter quark (preferably s but sometimes d) travels freely within the the boundaries of the confinement radius. When it reaches this boundary ($\sim 1.5\ F$), color forces start pulling on the $q\,\bar{q}$ pairs in the ocean and physical daughter hadrons materialize ($h_1, h_2, \ldots, h_6$).

In calculating QCD corrections to non-leptonic weak decays of the charm quark, one possible approach thus assumes that it is possible to separate short distance effects from long distance effects. Short distance effects involve hard-gluon exchange and attempts to use perturbation theory at that level have been made. Long-distance effects involve soft-gluon exchange and are then assumed to be embodied in the final states.

In the limit of no short distance QCD corrections, the approach outlined above thus reduces to the familiar 4-quark interaction as is displayed in Figure # 7a . Thus, in this limit (no QCD and $M_W \to \infty$), the weak interactions have reduced to something resembling the old 4-point interaction of Fermi, but for quarks, not nucleons. Figure # 7b shows (only) the one-loop QCD corrections one must bring to the weak-only picture.

The hard QCD corrections to the non-leptonic Hamiltonian have been computed [55] and it turns out that they are characterized by two *numbers* , two *renormalization* factors, which enter the calculation of widths. These factors are:

$$C_- \overset{\text{lead. log approx.}}{\approx} 1/C_+^2 = 1.7 \text{ to } 2.1 \qquad \text{using } m_c = 1.7\ GeV/c^2$$

and, for the purpose of illustration have been reproduced in Appendix 12.5 (taken from *Ref.* 56).

2.3) **Short distance effects and the Spectator Model revisited**

At this point, one can concentrate only on the short distance aspects of the QCD corrections and thus revert to a picture somewhat like the old picture of the Naive Spectator Model (NSM) in which only valence quarks are taken into consideration and soft-gluon corrections are neglected. What is new to this otherwise old picture though is that hard-gluon corrections are taken into account. Thus, while in the NSM one has:

$$\Gamma_{NL}^{NSM} = 3 \cdot \frac{G_F^2\ m_c^5}{192\ \pi^3}$$

in the Naive Spectator Model with Hard QCD Corrections, ($NSM + HQCDC$) one gets

$$\Gamma_{NL}^{NSM+HQCDC} = \left(2C_+^2 + C_-^2\right) \cdot \frac{G_F^2\, m_c^5}{192\,\pi^3}$$

and thus hard QCD corrections *enhance* [56] the non-leptonic rates by a factor of ~ 1.45 . The NSM prediction of equal weak semi-leptonic branching ratios and lifetimes for all single-charm states

$$BR_{SL}^{NSM}(D^{\pm}) = BR_{SL}^{NSM}(D^0) = BR_{SL}^{NSM}(F^{\pm}) =$$

$$BR_{SL}^{NSM}(\Lambda_c^+) = BR^{NSM}(c \to s\, l^+\, \nu_l) = \tau_c\, \Gamma(c \to s\, l^+\, \nu_l) = \frac{\Gamma(c \to s\, l^+\, \nu_l)}{\Gamma_{TOTAL}} = \frac{\Gamma(c \to s\, l^+\, \nu_l)}{\Gamma_{SL} + \Gamma_{NL}}$$

$$\sim \frac{1}{2\ leptons + (\sim 1) \cdot 3\ clr\ anti - clr\ of\ u\,\bar{d}}$$

$$= 20\%$$

are somewhat lowered in the $NSM + HQCDC$ to

$$BR_{c \to s\, l^+\, \nu_l}^{NSM+HQCDC} = \frac{1}{2 + 2\,C_+^2 + C_-^2} \sim 16\%$$

Still within the limits of an analysis focussing on the short distance limit augmented with hard QCD corrections, several improvements can be made to the picture apart from the obvious taking into account of the KM mixing. They include allowing for the bound state properties of the initial charmed hadron. Considerable theoretical uncertainty can be traced back to the ill-determined (determinable) charm quark mass. The details of the actual binding in the charmed hadron *before* its decay determine the effective mass one needs to use. Improvement is also expected to occur if the three-body (as in $c \to s\, l^+\, \nu_l$) phase space ($P.S.$) factors from massive quarks and leptons in the final state is taken into account. Finally, one should also take into account gluon radiation from quarks (Figure # 7c): Radiative QCD Corrections $RQCDC$. ‡ All these corrections to heavy quark decays amount to the following [56] :

$$BR_{c \to s\, l^+\, \nu_l}^{NSM+HQCDC+RQCDC+PS} \sim 13\%\ to\ 20\%$$

Yet, all such corrections, as elaborate as they are, still cannot account for experimental results presented in this thesis (see Section 8) namely that all charmed particles do not have the same lifetime (see next section) and it is also at variance with recent data published on the following electronic branching ratios:

$$BR^{MARK\ II}\left(\Lambda_c^+ \to e^+\, X\right) = 4.5 \pm 1.7\%\ [58]$$

$$BR^{MARK\ III}\left(D^+ \to e^+\, X\right) = 17.0 \pm 1.9 \pm 0.7\%\ [59]$$

$$BR^{MARK\ III}\left(D^0 \to e^+\, X\right) = 7.5 \pm 1.1 \pm 0.4\%\ [59]$$

2.4) **Long distance effects**

Apart from the experimental evidence presented in this thesis (Section 8), there is additional complementary evidence that the lifetime of the charged D-meson is longer than that of its neutral counterpart. If one assumes that the electronic widths of the two species are the same, then:

$$\frac{\tau_{D^+}}{\tau_{D^0}} = \frac{BR_{D^+ \to e^+\, \nu_e\, X}}{\Gamma_{D^+ \to e^+\, \nu_e\, X}} \cdot \frac{\Gamma_{D^0 \to e^+\, \nu_e\, X}}{BR_{D^0 \to e^+\, \nu_e\, X}} \sim \frac{BR_{D^+ \to e^+\, \nu_e\, X}}{BR_{D^0 \to e^+\, \nu_e\, X}} \sim 2.3\ to\ 3.6$$

‡ These are the QCD analogues to QED's first order corrections to muon decay [57] .

where the lower number comes from the MARK III numbers of *Ref.* 58 *Ref.* 59 and the upper number comes from *Ref.* 32 . The $NSM + HQCDC + RQCDC + PS$ model cannot account for this kind of data and as a result, theoretical investigations aimed at explaining the experimental situation have been made in two different types of phenomena: quark-cluster interference effects and weak-annihilation and W-exchange effects. The outcome of these will be described briefly below.

2.4.1) **Quark-cluster interference effects**

2.4.1.1) **Principle**

Concentrating on the Cabibbo-favored processes for a while, one can show [60] [61] [62] that the amplitude for the non-leptonic decays of D^+ and D^0 involve the diagrams displayed on Figure # 8a,b . On these figures, the hatched areas represent color singlets. Each amplitude is the sum of two diagrams. For $D^+_{c\bar{d}}$, both diagrams involve the same final-state quark-clusters: $s\,\bar{d}$ and $u\,\bar{d}$. For $D^0_{c\bar{u}}$ however, the clusters are different: $u\,\bar{d}$ and $s\,\bar{u}$ in the first diagram and $s\,\bar{d}$ and $u\,\bar{u}$ in the second. The details of the calculation show that it is possible for the amplitudes associated with the diagrams of $D^+ \rightarrow hadrons$ to interact *destructively* thus partially cancelling each other. This is not possible in the case of $D^0 \rightarrow hadrons$. The so-called quark cluster interference (QCI) is parametrized by $0 \leq \alpha_P \leq 1$ * and

$$\left[\frac{\tau_{D^+}}{\tau_{D^0}}\right]^{QCI} = \frac{\Gamma_{D^0}}{\Gamma_{D^+}} = \frac{2 + 2\,C_+^2 + C_-^2}{2 + 2(1+\alpha_P)\,C_+^2 + (1-\alpha_P)\,C_-^2}$$

and thus, no interference corresponds to $\alpha_P = 0$ for which the lifetime ratio is 1 while full interference corresponds to $\alpha_P = 1$ in which case the lifetime ratio is predicted to be about 1.5 using $C_+ = .74$ and $C_- = 1.8$ (from Appendix 12.5) at the rough scale of the charm quark mass. Also, the semi-leptonic branching ratio is predicted to be

$$BR^{QCI}\left(D^+ \rightarrow e^+ X\right) = \frac{1}{2 + 2(1+\alpha_P)\,C_+^2 + (1-\alpha_P)\,C_-^2}$$

or a maximum of 24% with the values of C_+ and C_- quoted above and assuming $\alpha_P = 1$.

2.4.1.2) **Non-relativistic approximation**

It is not necessary to go through all the details of the calculations to see what the physical origin of the interference process is; it is due to the Pauli exclusion principle. This can be seen from Figure # 8a . In the case of the D^+ , one is actually trying to force two identical $\bar{d}$-quarks in the final state. Thus, on quite general physical grounds (Non Relativistic Quantum Mechanics: NRQM), one can expect that *how much* interference one eventually gets depends on how *close* , in the final state, one wants these two anti-quarks to be. This is especially obvious when a non-relativistic approximation † is done using NR-wavefunctions for

* It may appear unusual that one needs to *parametrize* the cancellation since, after all, one is dealing with a theoretical result. The reason is that, in order to perform such calculations, theorists assume certain symmetries to be obeyed *exactly* (for example: $SU(6)$). However, such symmetries need not be exact in Nature and how much they are broken is really governed by the data...

† Even in a non-relativistic approximation, the calcualtions are *by no means* trivial; see *Ref.* 63 *Ref.* 64 .

the bound-state meson containing the heavy charm quark. If one makes the simplification $M_D \sim M_c = M$, then it can be shown that [63] :

$$\alpha_P^{NR} \approx 192\,\pi^2 \frac{|\Phi(0)|^2}{M^3}$$

in which $\Phi(0)$ is the meson-wavefunction evaluated at the origin. This equation is revealing that the heavier the meson, the less quark-cluster interference one gets. It has been calculated that the quark-interference effects should not amount for more than about 20% in the case of charmed mesons and should be negligible for beauty mesons [56] [64] .

2.4.2) **Weak-annihilation and W-exchange: flavour annihilation effects**

Flavour annihilation (FA) is a terminology that collectively includes W-exchange and W-annihilation in the limit of large W-boson mass. These topics will be briefly discussed in the following paragraphs.

2.4.2.1) **Principle**

Since it appears that one cannot make the D^+ non-leptonic rate small enough relative to that of the D^0 so that $\tau(D^+) > \tau(D^0)$, theorists have turned to the other possibility which is to try to enhance the D^0 non-leptonic rate relative to that of the D^+ thus making $\tau(D^0) < \tau(D^+)$ ...

The NSM specifically neglects any possible contribution from the other (lighter) quark of a charmed meson. Figure # 9a,b present quark diagrams which do involve the c-quark with the $\bar{u}$-quark in the case of D^0 and the c-quark with the $\bar{d}$ in the case of D^+ . In the case of D^0 , W-exchange is doubly Cabibbo-favored. In the case of D^+ , the W-annihilation process is singly Cabibbo-unfavored thus, to first order, negligible. If W-exchange for D^0 could be made to contribute to the non-leptonic width, it could possibly explain the (comparatively) shorter lifetime of D^0 . The reason such diagrams were initially tossed away by theorists is because it can be argued, on general grounds, that the amplitudes should be very suppressed. Indeed, as is implicit in the form of the Standard Model Lagrangian given in Section 1.2, only (massless) left-handed ‡ leptons and quarks can couple via the weak-charged current. (D^0 like $D^{+\,or\,-}$ and $F^{+\,or\,-}$ are pseudo-scalar mesons.)

In any case, where the argument falls short is that it neglects the presence of the long lived gluons inside the hadronic bound states. These gluons can carry spin and color and that makes a difference. The calculations involving a c-quark and $\bar{u}$ (for D^0) plus some glue are, as can be expected, quite impressive [65] [66] . However, the results are expressed in the following form [67] :

$$\Gamma_{FA}(D^0) = \frac{G_F^2\, M_{D^0}^2}{3\,\pi} \left[(2\,C_+ - C_-)^2\, P_{D^0}^{(1)} + \left(\frac{C_+ + C_-}{2} \right)^2 P_{D^0}^{(8)} \right]$$

where $P^{(1)}$ is the singlet and $P^{(8)}$ the octet contribution to the flavour annihilation (FA) width.

For F^+ , one has:

$$\Gamma_{FA+LA}(F^+) = \frac{G_F^2\, M_{F^+}^2}{3\,\pi} \left[(2\,C_+ + C_-)^2\, P_{F^+}^{(1)} + \left(\frac{C_+ - C_-}{2} \right)^2 P_{F^+}^{(8)} \right] + 2\,\frac{G_F^2\, M_{F^+}^2}{\pi}\, P_{F^+}^{(1)}$$

‡ Left-handed particles have their spin aligned opposite to their direction of motion.

where the last term arises because of the possible purely leptonic annihilation (LA) processes of the $F^+ \to l^+\nu$ and for which one considers only two leptons: e^+ and μ^+ ...

Therefore, the total number of parameters describing long distance effects in the decay of pseudo-scalar mesons is at least three: α_P , $P^{(1)}$ and $P^{(8)}$. That is, assuming the annihilation amplitudes are all the same irrespective of the meson.

2.4.2.2) **Non-relativistic approximation**

In the lowest order (hard) QCD approximation of the decay of D^0 (Figure # 9c), $P^{(1)} = 0$ and upon using, again, a non-relativistic approximation, one can relate $P^{(8)}$ to the square of the wavefunction at the origin [67] . It turns out that

$$P^{(8)}_{D^0} = \frac{\alpha_s}{9\pi}\frac{M^2_{D^0}}{m^2_u}|\Phi(0)|^2$$

The factor $M^2_{D^0}/m^2_u$ is a phase-space suppression factor in the expression for $P^{(8)}$. This shows that flavour annihilation is roughly proportional to the square of the meson mass. In fact, experimentally, the rate of $K^+ \to e^+\,\nu_e$ is much suppressed over $K^+ \to \mu^+\,\nu_\mu$, for example, by about 10^{-5} [32] which is roughly m_e^2/m_μ^2 .

The hard-qluon contribution is not enough to account for the difference of lifetimes between D^+ and D^0 so calculations have been performed including a soft gluon component [68] . The Author of *Ref.* 68 has predicted, using contributions from both the soft and hard gluon emission processes that the ratio of the charged to neutral-D lifetimes is somewhere between 1.2 and 7 .

Theoretical arguments that have been presented up to now have also some bearing on the weak decays of charmed baryons like the Λ_c^+ which has quark content $c\,d\,u$. In particular, the decay process $c \to s\,u\,\bar{d}$ together with the W-exchange $cd \to su$ have been calculated in a non-relativistic approximation of 3-colored-quark states with spin [69] [70] . The result is:

$$\Gamma^{HQODO+NR+NS}_{\Lambda_c^+} = \Gamma_{HQODO} - \Gamma_P + \Gamma_{FA}$$

$$\Gamma_{HQODO} = \frac{G_F^2\,M^5}{192\,\pi^3}\left(2\,C_+^2 + C_-^2\right)$$

$$\Gamma_P = C_+\,(2\,C_- - C_+)\,\frac{G_F^2\,M^2}{4\,\pi}|\Phi(0)|^2$$

$$\Gamma_{FA} = \frac{C_-^2\,G_F^2\,M^2}{2\pi}|\Phi(0)|^2$$

in which $M \sim m_c$ and where P stands for "Pauli" (i.e. interference) effects, FA for flavour annihilation effects and NS stands for "Non-Spectator" effects: interference and flavour annihilation. Using typical values for the parameters, the Author of *Ref.* 69 predicts a lifetime of $\tau \sim 2.6 \times 10^{-13}$ *sec* for the Λ_c^+ .

2.5) **Phenomenological potential models**

The quark model has had a large success at describing hadronic structure in general. (e.g. baryon magnetic moments [71]) It thus provides theorists with an approach to non-perturbative QCD effects which are so important in understanding the decays of charmed particles. Thus, it is not surprising to witness a large theoretical effort in trying to understand heavy meson decays in terms of a basically phenomenological approach and certainly not surprising to see these attempts being very successful.

At the core of the method, lies the form of the QCD potential to be used. There are many forms that have been studied [72] and *fitted* to the observed spectra of excited states of heavy quark mesons like $\psi_{c\bar{c}}$ and $\Upsilon_{b\bar{b}}$. A particularly economical functional form is that of the Cornell parametrization [73] :

$$V_{Cornell}(r) = -a\frac{1}{r} + br + c$$
$$a = \frac{4}{3}\alpha_s \quad \alpha_s = 0.5$$
$$b = 0.18\,GeV^2$$
$$c = -0.84\,GeV$$

In the Cornell potential, the first term is $1/r$-Coulomb-like while the other two terms provide a linearly rising potential. When $r \leq 1/(2\,GeV)$ or $r \leq .1\,fm$, the $1/r$-term dominates and in this regime, it can be shown that this term provides *asymptotic freedom* : that it then goes as $1/r\ln(\Lambda r)$. (Note: α_s depends on r ...) In the other limit, that of $r \geq 1\,fm$, the first term of the Cornell potential is negligible and the linear part provides *confinement*.

Such a potential has been used by the Authors of ***Ref.*** 74 in order to compute the transition matrix element for processes like $D \rightarrow X\,e\,\nu_e$. By using quark-model non-relativistic wavefunctions for the mesons, (actually harmonic-oscillator-like trial-wavefunctions coupled to spin), the Authors of ***Ref.*** 74 predict:

$$\Gamma_{D^0 \rightarrow X\,e^+\,\nu_e} = \Gamma_{D^+ \rightarrow X\,e^+\,\nu_e} = 2.1 \times 10^{11} sec^{-1}$$

2.6) **Charmed particle lifetime measurements**

The first charmed particle decay [75] was recorded in an emulsion exposed to cosmic rays while flown aboard a commercial airliner back in 1971 . It was possible to determine the mass of the particle to be ~ 2 to $3\ GeV/c^2$ and its proper decay time to be $\sim 10^{-14}\ sec$. Since then, several experiments have attempted the task, with different degree of success, of measuring charm particle lifetimes using a variety of experimental methods. These methods, or techniques, can be grouped in perhaps four broad classes according to what kind of vertex detector they use. The first class of experiments regroups those that use nuclear emulsions as very high-resolution vertex detectors. This is the class to which E531 belongs. The second class is comprised of experiments that use bubble-chambers in order to record, with high precision, the charm decay events. The third class of experiments rely on the relatively recent technology of high-resolution solid state vertex detectors to record charm decays. The fourth class regroups all the experiments that, apart from their mainstream business, can also do lifetime measurements but in a somewhat indirect way, that is, those experiments that are essentially blind i.e. that do *not* actually record the decay of charmed particles but merely infer such decays from attributes of the final states. Each of these classes will be briefly described below. More information on each experiment can be obtained from reviews like ***Ref.*** 76 or, of course, from the individual experimental group publications.

2.6.1) **Nuclear emulsion vertex detector experiments**

The techniques related to nuclear emulsions will be described in details in Section 3 when the principle of E531 are exposed. Apart from E531 whose combined results are presented in Section 8, three other groups

have measured lifetimes using nuclear emulsions. The NA15 [77] collaboration exposed an emulsion chamber at CERN's 340 GeV π^- beam. This experiment had limited particle identification ability and no neutral detection capability. None of their events were fully reconstructed. Nevertheless, their result is:

$$\tau_{D^0}^{NA15} = 3.1^{+2.0}_{-1.6} \times 10^{-13} sec \quad 5\ decays$$

Another experiment, WA17 [78] , exposed emulsions to CERN's wideband neutrino beam. This collaboration could only uniquely identify one event and found no F-meson candidate:

$$\tau_{D^0}^{WA17} = 0.53^{+0.57}_{-0.25} \times 10^{-13} sec \quad 3\ decays$$

$$\tau_{D^\pm}^{WA17} = 2.5^{+2.2}_{-1.1} \times 10^{-13} sec \quad 5\ decays$$

$$\tau_{\Lambda_c^+}^{WA17} = 7.3^{+0.1}_{-0.1} \times 10^{-13} sec \quad 1\ decay$$

Finally, the WA58 collaboration [79] [80] [81] [82] exposed emulsions to the $20 - 70$ GeV tagged photon beam at CERN's Ω' spectrometer and obtained:

$$\tau_{D^0}^{WA58} = 3.4^{+1.1}_{-0.8} \pm 0.25 \times 10^{-13} sec \quad 22\ decays$$

$$\tau_{D^\pm}^{WA58} = 5.4^{+1.9}_{-1.2} \pm 0.8 \times 10^{-13} sec \quad 12\ decays$$

$$\tau_{\Lambda_c^+}^{WA58} = 2.22^{+1.34}_{-0.75} \times 10^{-13} sec \quad 8\ decays$$

2.6.2) **Bubble chamber vertex detector experiments**

The NA18 collaboration [83] used the BIBC (Bern Infinitesimal Bubble Chamber) at CERN's 340 GeV π^- beam to study charm decays. The bubble size was 30 μm-diameter. This experiment had no charged particle identification and no π^0-detection ability. Thus, they used only all-charged decays but required them to be fully constrained. They quote:

$$\tau_{D^0}^{NA18} = 4.1^{+2.6}_{-1.3} \pm 0.5 \times 10^{-13} sec \quad 9\ decays$$

$$\tau_{D^\pm}^{NA18} = 6.3^{+4.8}_{-2.3} \pm 1.5 \times 10^{-13} sec \quad 7\ decays$$

Another experiment, BC72-73 [84] [85] [86] with its further run with equipment improvements BC-75 [87] , used SLAC's 1 m-bubble chamber at the 20 GeV backward scattered γ-beam with bubble sizes of 50 μm and 40 μm . A spectrometer allowed momentum measurements, charged particle I.D. determination as well as neutral particle detection. Their result is [82] :

$$\tau_{D^0}^{BC72-73+BC75} = 6.1 \pm 0.9 \pm 0.3 \times 10^{-13} sec \quad 42\ decays$$

$$\tau_{D^\pm}^{BC72-73+BC75} = 8.6 \pm 1.3^{+0.7}_{-0.3} \times 10^{-13} sec \quad 45\ decays$$

Another group, NA16 [88] [89] [90] [91] at CERN's 360 Gev π^- and p beams from the SPS , used the LExan Bubble Chamber (LEBC) together with the European Hybrid Spectrometer (EHS) to measure charmed particle lifetimes. The EHS had magnet-based momentum measurement ability, lead-glass based photon detection ability and some charged particle I.D. (ISIS) ability. Only constrained fits were used in the lifetime calculations done with the help of maximum likelihood fits. Their result is:

$$\tau_{D^0}^{NA16} = 4.1^{+1.3}_{-0.9} \times 10^{-13} sec \quad 16\ decays$$

$$\tau_{D^\pm}^{NA16} = 8.4^{+3.5}_{-2.2} \times 10^{-13} sec \quad 15\ decays$$

The same group of experimentalists improved their bubble chamber to a bubble size of $< 20\ \mu m$ and ran again as NA27 [76] [92] [82] . They quote:

$$\tau_{D^o}^{NA27} = 3.5^{+1.4}_{-0.9} \times 10^{-13} sec \quad 29\ decays$$
$$\tau_{D^\pm}^{NA27} = 10.1^{+5.0}_{-2.8} \times 10^{-13} sec \quad 33\ decays$$

as well as a more recent number

$$\tau_{D^o}^{NA27} = 4.1^{+1.2}_{-0.8} \times 10^{-13} sec$$
$$\tau_{D^\pm}^{NA27} = 14.7^{+7.5}_{-4.2} \times 10^{-13} sec$$

2.6.3) **Solid state vertex detector experiments**

The NA1 [92] collaboration at CERN's 40 *to* 150 *GeV bremsstrahlung* γ-beam has used the FRAMM forward spectrometer coupled to a multilayer active silicon target with typical resolution of $\sim 400\ \mu m$. The equipment allowed momentum measurement, photon detection and particle I.D. . However, because solid-state detectors measure charge multiplicity in a plane, this group's results suffered from some inability to distinguish charged from neutral events. They still managed, using cuts, to quote a result for the "charged" D-meson:

$$\tau_{D^\pm}^{NA1} = 9.5^{+3.1}_{-1.9} \times 10^{-13} sec \quad 98\ decays$$

Another group, the NA11 [93] [94] [95] [82] ACCMOR collaboration at CERN's 200 *GeV* $\pi^\pm$ beam used an electron trigger to select charm candidates produced in:

$$\pi^- Be \rightarrow D\,(eX)\ \overline{D}\,X$$

The group relied on a on a high-resolution micro-strip detector with typical longitudinal resolution of $\sim 150 \mu m$. Some particle I.D. was available and the group quotes the following results:

$$\tau_{D^o}^{NA11} = 3.6^{+0.9}_{-0.7} \pm 0.5 \times 10^{-13} sec \quad 26\ decays$$
$$\tau_{D^\pm}^{NA11} = 11.3^{+4.4}_{-2.8} \pm 1.8 \times 10^{-13} sec \quad 28\ decays$$
$$\tau_{F^\pm}^{NA11} = 3.1^{+1.2}_{-0.8} \times 10^{-13} sec \quad 33\ decays$$

2.6.4) **Other experiments**

Many experiments have equipment set ups which have no hope at directly resolving the actual charm particle or its decay. Yet, they still manage to make measurements by using physics cuts on their large samples of data. The MARK II collaboration [96] used SLAC's PEP $e^+\ e^-$ collider at $\sqrt{s} = 29\ GeV$ to compute charm particle lifetimes by estimating the displacement of secondary vertices from the beam-line. In order to perform this impressive task, they relied on a high precision drift-chamber vertex-detertor coupled to a main-tracking chamber to obtain a $100\ \mu m$ accuracy perpendicular to the beam-direction. Obviously, beam size and beam position must be known very accurately because such numbers enter directly into the lifetime calculations. The beam size was known to be: *horizontal beam size* $= 480 \pm 10\ \mu m$ and *vertical beam size* $= 65 \pm 15\ \mu m$. The average beam position was known to $\pm 20\ \mu m$ both vertically and horizontally. In order to see anything at all among the huge backgroung they experienced, they relied on

the known $D^* - D^0$ mass difference while selecting on the low-background (at high %-energy of the D^* relative to that of the beam):

$$D^{*\,+}_{\ 0} \rightarrow D^0\, \pi^{+}_{0}$$

$$D^{*+} \rightarrow D^+\, \pi^0$$

In any case, their analysis demands convoluting a Gaussian as part of the response function of the detector to charm-decay and they quote [82] :

$$\tau_{D^0}^{MARK\ II} = 4.5^{+0.9}_{-0.8} \pm 0.5 \times 10^{-13} sec \quad 74\ decays$$

$$\tau_{D^\pm}^{MARK\ II} = 8.9^{+3.8}_{-2.7} \pm 1.3 \times 10^{-13} sec \quad 23\ decays$$

Another experiment, the WA62 group [97] [98] using CERN's 135 *Gev* Σ^- beam have measured the lifetime of their own discovery, the A^+-baryon, using extrapolated tracks to the vertex combined with beam information to be:

$$\tau_{A^+}^{WA62} = 4.8^{+2.9}_{-1.8} \times 10^{-13} sec$$

The High Resolution Spectrometer (HRS) at SLAC's PEP $e^+\,e^-$ collider ring measured the lifetime of the neutral D-meson. The spectrometer used a superconducting magnet and provided tracking and time-of-flight measurement abilities. Neutral and charged particle identification was done. This group quotes [82] [99] :

$$\tau_{D^0} = 4.5 \pm 1.4 \pm 0.8 \times 10^{-13} sec$$

Also measuring the lifetime of the neutral D-meson, the TASSO group at DESY's PETRA $e^+\,e^-$ ring used a conventional magnet, had time-of-flight ability and could identify charged and neutral particles. This group quotes [82] [100] :

$$\tau_{D^0} = 4.6^{+2.9+1.0}_{-1.7-1.3} \times 10^{-13} sec$$

The DELCO group at SLAC's PEP $e^+\,e^-$ ring used a detector with open geometry to study neutral D-meson decays. The spectrometer used a conventional magnet and allowed tracking and time-of-flight measurements. Neutral and charged particles could be identified. The group quotes [82] [101] :

$$\tau_{D^0} = 4.6 \pm 1.5^{+0.7}_{-0.6} \times 10^{-13} sec$$

Finally, the CLEO detector at Cornell's CESR $e^+\,e^-$ ring used a superconducting magnet and had neutral and charged particle identification abilities. The group quotes [82] [102] :

$$\tau_{D^0} = 4.1 \pm 1.0 \pm 0.7 \times 10^{-13} sec$$

3.0) FNAL EXPERIMENT E531: EQUIPMENT, BASIC PRINCIPLES AND LOGIC

This section is more concerned with describing motivations behind the type of apparatus used to make short lifetimes measurements together with describing the design principles than it is concerned with explaining the many important related techniques of usage and efficiencies (see Section 5) or the calibration (see Section 4). *

An early † attempt at observing production and decay of charm in the FNAL wide-band ν beam [104] yielded only *one* single candidate with several acceptable decay hypotheses and an average decay time of $\sim 6 \times 10^{-13} sec$. In another set up again located in a ν beam, emulsion stacks were placed outside the Big European Bubble Chamber (CERN WA17) [78] . Multi-Wire Proportional Chambers helped in the connection of tracks between the bubble chamber and the target. An External Muon Identifier was placed downstream of the bubble chamber. The experiment yielded 5 charm decay candidates, ony one of which was fully fitted. At the Fermilab 15 foot bubble chamber, in the ν beam, E564 [105] placed their emulsion *inside* the volume of the deuterium (D_2). An external muon identifier completed the set-up. From its first run, only one event was fully reconstructed. Nuclear emulsion targets have also been used in other types of beams: in a muon beam (FNAL E382 [106]) and in a tagged-photon beam (CERN WA58 with the Ω' spectrometer [107]). This list is not meant to be exhaustive but it hints at the hard-learned lessons from such experiments. These constitute part of the basis for the design and conduct of the first truly successful generation of experiments employing hybrid emulsion-spectrometers, to which FNAL E531 belongs.

Fermilab Experiment 531 consisted of a nuclear emulsion target which was used as a very high-resolution vertex detector and which was followed downstream by an electronic spectrometer thus allowing kinematical measurements to be made on the interaction and secondary particles emerging from the target. The hybrid emulsion-spectrometer took data in FNAL's wide-band neutrino beam in two distinct runs. The first run consisted of a integrated $\sim$ 1488-hour exposure between November 18^{th} 1978 and February 7^{th} 1979 . The second run was a much longer $\sim$ 3816-hour exposure done between November 30^{th} 1980 and May 31^{st} 1981 .

In the vast array of contemporary experimental tools available to the H.E.P. community, the hybrid emulsion-spectrometer is certainly not the most common and perhaps still needs some introduction. The next few paragraphs are devoted to explaining in some details the principles behind E531's set-up.

3.1) The hybrid emulsion-spectrometer principle

A hypothetical detector purporting to measure lifetimes using only nuclear emulsions would face several major problems, if reasonable statistics were to be attained. Emulsions will start to time-integrate informa-

* Some typical resolutions are quoted in this section (from reference works or from internal technical notes) when these are not to be part of the more detailed Section 4 in which the extensive post- and pre-data-taking calibration effort is described. Parts of the apparatus common to both of its runs are already quite extensively described in [103] . In this section, emphasis is put on *new* or *modified* equipment of the 2^{nd} run.

† FNAL E247 used a combination of a nuclear emulsion target and wide-gap optical spark chambers.

tion the moment they are prepared and stop when they are developed and stabilized. Long exposure times are required to maximize the integrated production probability of rare events but excessive accumulated backgrounds can easily make the location and analysis of these events either too time-consuming or simply prohibitively long. Although emulsions have some momentum analysis capability, the sheer effort involved for complete microscope analysis of complex charm production and decay events together with the intrinsic limitations of the methods make their stand-alone use impossible. However, as was mentioned above, nuclear emulsions have excellent single-track spatial resolution (*diameter of one grain* $\sim$ 1 μm) still better than now almost competitive solid-state detectors 3 μm *at* $\theta = 0$ *degree incidence* [108] . Direction slopes dx/dz and dy/dz can be measured with very high precision close to the location the event took place thus reducing the problem of multiple Coulomb scattering associated with slope measurements done far from vertices. Given the momenta of the secondaries at a comparable precision, events can be kinematically reconstructed and even un-seen neutral secondaries inferred. Such qualities make the use of emulsions for reliable lifetime measurements in the order of $10^{-13} sec$ very desirable.

The two major problems that plague the use of a nuclear emulsion target, that of finding a sufficient number of the events it contains and that of determining the momenta of all the secondaries with enough precision in each of the found events, can be solved, at least in priciple, by electronic equipment located *downstream* of the interaction and decay regions. This equipment should comprise means to self-trigger: the ability to recognize that an interesting event (ν production and decay of charm) has occured thus preventing the event-information recording device to saturate. It should also comprise means to reconstruct the trajectories of primary and secondary charged particles emerging from the target and belonging to the event. Also, insuring these particles go through a region of known magnetic field will cause their trajectories to bend and measurements of this will permit determination of the momenta involved. A high ability to detect (ordinary) secondary neutral hadrons before or after their decay should also be part of the equipment because this is necessary to the complete understanding of each event. The ability to tag (to identify) particles emerging from the target should also be as high as possible. Finally, all this equipment is incomplete without the means of reliably and un-ambiguously associating the information it provides with that from the nuclear-emulsion target.

3.2) The FNAL wide-band ν beam

The main characteristics of the neutrino beam incident on the E531 emulsion-target are displayed on Figure # 10 . Schematically, $\sim$ 400 *GeV* protons from the accelerator's Main Ring bash into a $\sim$ 1 interaction length water-cooled BeO cylindrical target. During good running conditions, $\sim$ 1 *to* 2×10^{13} such protons were delivered on target at a machine repetition rate of 10 *to* 15 *sec* . A wide variety of hadrons are created in the complex hadronic interactions taking place inside the target. As these emerge, they are then taken over by the *horn* which creates a region of high magnetic field specially designed to focus positively charged particles (with a $p_\perp$-kick proportional to the particle's transverse momentum) while defocussing negatively charged particles. Among the particles focussed are K^+ and π^+ which then proceed to enter a $\sim$ 343 m

long cylindrical region in which they weakly decay through

$$K^+ \rightarrow \mu^+ \nu_\mu \qquad B.R. = 63.51\% \qquad c\tau = 370.9\ cm$$

$$\pi^+ \rightarrow \mu^+ \nu_\mu \qquad B.R. \sim 100\% \qquad c\tau = 780.4\ cm$$

Hadrons that might have survived the horn and decay pipe then smash into concrete located at the end of the decay region and are absorbed through hadronic showers. At that point, the mostly leptonic beam enters the berm and travels through $\sim 560\ m$ of dirt loaded with $\sim 6000\ t$ of steel and as a result, most but not all muons are absorbed. This new earth-steel shield lowered μ backgrounds in the emulsion to such reasonable levels that it was possible to tolerate an increase of 50 GeV in the incident proton beam energy over the 1^{st} run's 350 GeV without the use of a special toroidal-shaped magnetic field upstream of the spectrometer.

3.3) **The emulsion target**

3.3.1) **Principle and set-up**

Nuclear emulsions like the one used by E531, are suspensions of silver bromide (AgBr) in gelatin. Fuji's ET7B emulsion contains, by weight, 46.1% silver and 33.4% bromine. Other materials like carbon, oxigen, water, nitrogen, iodine, hydrogen and sulphur are also present. Emulsions record the passage of charged particles in latent form. After chemical processing, strings of developed grains remain along the trajectories. A grain is a locally blackened spot-like region of high silver (Ag) density about $10^{-6}m$ in diameter. The use of nuclear emulsions as detectors is nothing new and the lower limit to their ability at measuring short decay distances is well (although somewhat indirectly) examplified by the measurement of the shortest lifetime to be ever determined by means of observation of the track length of secondaries: that of the electromagnetically decaying π^0 from stopped kaons [109] : $K^+ \rightarrow \pi^+ \pi^0$ followed by the Dalitz decay $\pi^0 \rightarrow e^+ e^- \gamma$. However, because the systematic error on this early estimate turned out, using other measurement methods, to be over a factor of 3 , it has been estimated [110] that nuclear emulsions cannot be relied upon to measure track lengths $< 0.1\ \mu m$ even if use is made of large angle secondaries and of several tracks fitted to both the primary and decay vertices.

In the 2^{nd} run of E531, the nuclear emulsion target which occupied a width of 70 mm from $z = -5.53\ mm$ to $z = +64.31\ mm$ † was divided, much as in the 1^{st} run, according to two very distinct methods of mounting. In one method, 600 μm thick pellicles of pure emulsion are stacked flush against each other and wrapped into *modules* ($\sim 177\ pellicles/module$) so that the plane of each pellicle be parallel to the incoming ν beam. Each pellicle is 7 cm along the beam direction and 14 cm high. This emulsion is known as "horizontal" emulsion. A total of 12 such modules (2 rows of 6) were positioned above the experiment's $y = 43.18\ mm$. In this mounting scheme, a ν comes into the pellicle through its side, interacts somewhere along the 7 cm of its width creating secondaries which also travel within the same pellicle before exiting at the downstream edge of the emulsion. Thus events in "horizontal" emulsion have an excellent chance of being fully contained into one single pellicle and have an easily recognizable topology. One horizontal module (# 2) was replaced by an additional module (# 13) early in the run. In the other mounting method used for the rest of the

† Determined from extensive pre and post data-taking optical surveys [111] of the whole apparatus.

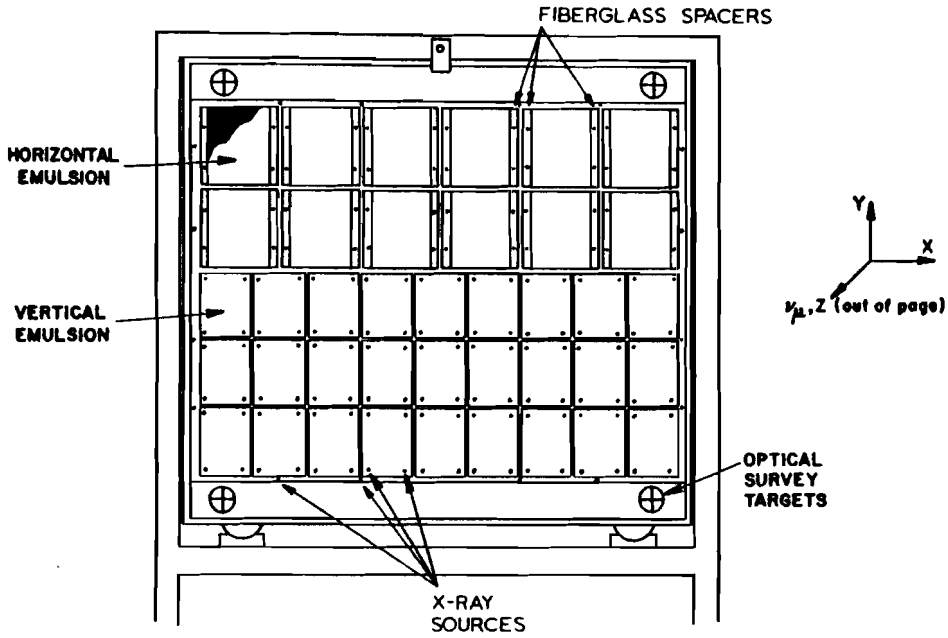

Figure # 11

Emulsion target stand and emulsion modules. This is a view with the neutrino beam coming out of the page. Horizontal emulsion modules are located in the upper part of the target while vertical emulsion modules are located in the lower part. The emulsion stand rests directly on a massive granite block.

emulsion, 27 (3 rows of 9) modules of stacked plates were exposed with the plane of the plates oriented perpendicularly to the direction of the incoming ν beam. Because of this fact, this emulsion was called "vertical" emulsion. These modules were all located below the experiment's $y = 43.18\ mm$ and each were 12 cm along the Y-direction (up-down) and 9.5 cm along the X-direction (across). In vertical mounting, emulsion is deposited on a structural support. Each plate consists of a 70 μm thick polystyrene support sheet coated with two 330 μm thick layers of emulsion, one on each side. Plates are stacked on top of each other and their alignments maintained by support posts in the 4 corners. Obviously, in this mounting scheme, events are not necessarily wholly contained in a single plate. Because the two mounting methods described above are so different, they have led to the development of two very distinct traditions of expertize.

As Figure # 11 shows, all 39 modules were laid in a rectangular pattern and mounted on a light aluminum support Hexcel plate. More details appear on Figure # 12 where the locations of X-ray marking sources for both types of emulsions are shown. Markings from these sources were used for positioning the pellicles during scanning. Figure # 12 shows the location of the *changeable sheet* of emulsion. This 800 μm thick piece of plastic coated on both of its sides with 70 μm emulsion layers extended over the full cross-sectional area of the fiducial volume, downstream of the structurally separate emulsion stacks. This sheet was changed often during data taking so as to provide a low background volume in which the finding of high energy tracks from the spectrometer was made much easier. (200 μ/mm^2 in a module compared to 20 μ/mm^2 in the changeable sheet). The whole assembly of emulsion modules and changeable sheet is mounted on a light aluminium stand; emulsions, drift chambers and spectrometer magnet all rest on a single massive granite block insuring structural integrity.

3.3.2) **Emulsion quality and resolution**

Emulsion quality was monitored during the data taking run. Frequent processing of test samples allowed determination of the optimum development conditions. Careful processing was necessary to minimize fog size as the quality of the 2^{nd} run emulsion was different from that of the 1^{st} run. Emulsion was mixed and poured in a specially built separate facility located $\sim 1\ km$ from the experimental area. Apart from tests, processing was done in another facility located at the University of Ottawa, Canada. Samples were exposed at the M5-multiparticle test-beam facility on January 10^{th} 1981 and some of them processed 4 days later while others were processed 11 days later. The results are summarized below: [112]

Latent time (days)	Processing time (hours)	Surface grain density (grains/100 μm)	Base grain density (grains/100 μm)
4	3.5	26.1 ± 1.2	26.2 ± 1.1
11	3.5	26.1 ± 1.1	24.6 ± 1.1
11	4.5	29.5 ± 1.2	28.2 ± 1.2
11	5.5	30.4 ± 1.2	29.2 ± 1.2

The quality of the emulsion was found to be good (1^{st} run measurements varied from 28.6 ± 0.9 grains per

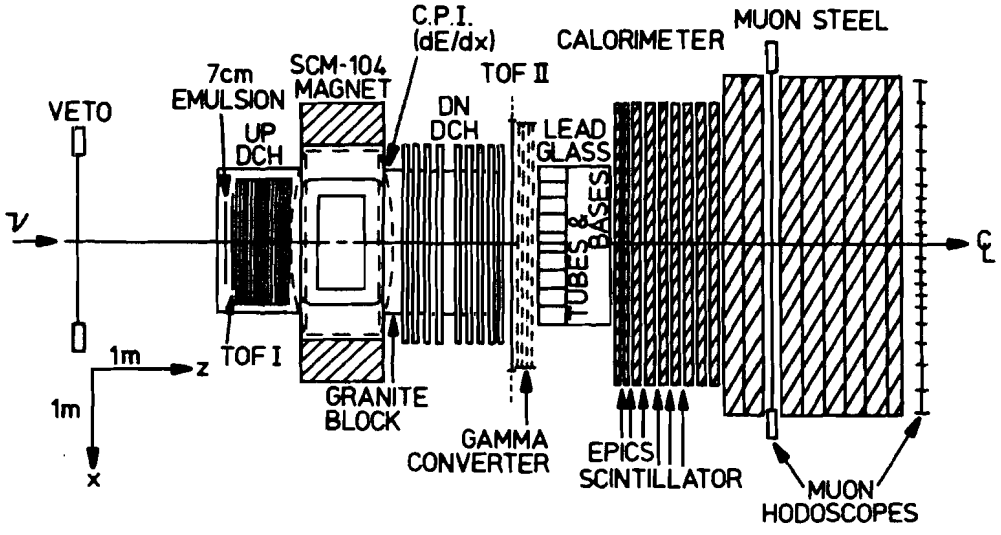

Figure # 13

Plan view (bend-plane) of the E531 spectrometer. The neutrino beam comes from the left. The entire assembly is about 9 *m* long and about 3.5 *m* wide at the downstream end. Primary and secondary particles that leave the high resolution vertex detector (emulsion) may then traverse other pieces of apparatus and be identified. The target, the upstream drift-chambers, the spectrometer magnet and the downstream drift-chambers all rest on a massive granite block.

$100\mu m$ to 31.3 ± 1.2 grains per $100\mu m$ depending on the module) and the exposure carried on.

Although the local spatial resolution of nuclear emulsions is very high, uncertainties due to warpage and shrinkage start, over long distances, to dominate. As the emulsion is used to measure the direction slopes of the charged particles near the vertices, it is the angular resolution that constitutes the most important parameter. The emulsion angular resolution for tracks also seen in the drift chambers is very high as is testified by its measurement in the 1st run [113] :

$$\sigma(\theta) = (0.0015 + 0.01\,\theta)\ \textit{radians} \qquad \textit{Vertical Emulsion}$$

and

$$\sigma\left(\frac{dy}{dz}\right) = 0.5\sigma\left(\frac{dx}{dz}\right) = (0.0033 + 0.02\,\theta)\ (\theta\ \textit{in radians}) \qquad \textit{Horizontal Emulsion}$$

3.4) **The spectrometer**

Figure # 13 shows a plan view of the E531 spectrometer with its second run modifications. The following sections are devoted to briefly describing each of the pieces of apparatus.

3.4.1) **The Veto counters**

The array of veto counters, known as the "Antis", is the most upstream piece of equipment. (1.4 m upstream of Emulsion) The array consists of eight 2×1.78 m long, $25.4cm$ wide, 0.95 cm thick scintillator paddles arranged so as to form a thin wall. The main purpose of the arrray is to provide a "no" signal or $\overline{A}$ signal, indicating that no charged particle are incident on the target during the ν spill (machine delivery of neutrinos). Both ends of each paddle were equipped with photomultiplier tubes. The array and the associated electronics (Figure # 14) are designed to respond to the passage of charged particles in a uniform manner, wherever hits may have occured, over the area it covers. In order to achieve this, signals from opposite ends of paddles were fast mean-timed † by the hardware and fanned-in over the array so that by arranging the signal arrivals (using proper delays) to be in time, an otherwise continually raised flag can be lowered. With proper discriminating levels imposed on the hardware sum of pulses from the 6 middle paddles, this scheme provides $\overline{A}$, part of the neutrino trigger. In addition, A was used as a feed to part of a muon calibration trigger (μ_c) available at the end of each machine spill and recorded as such if no neutrino trigger occured. The efficiency of the array was measured to be 96% relative to both TOF I and II firing simultaneously.

The vetoing of triggers caused by high energy charged particles incident on the target during most of the ν-spill essentially amounts to a hardware physics cut. With high efficiency, only events including a neutral particle incident on the target could proceed further into the fast trigger scheme; an obvious requirement for the succesful observation of the neutrino production of charm and its decay. To complete the trigger scheme, the presence of charged particles produced at the interaction vertex and at any subsequent decay vertices is required. This is achieved through the use of other pieces of equipment which will now be introduced. In

† Hardware mean-timing is a technique by which the light propagation times to opposite ends of a paddle are averaged by the electronics.

Section 3.5, the basic E531 triggers will be presented in term of the signals recorded in these devices as well as in the Veto array.

3.4.2) **The Time of Flight I and II counters**

Downstream of the emulsion target at $z = 7.11\ cm$ (*front face*) was located a large single rectangular (74 *cm* high by 92 *cm* across) piece of 1 *cm* thick Pilot F scintillator (New England Nuclear Corp.: peak fluorescence wavelength: 425 *nm* , 1/2 intensity attenuation distance: 1.35 *m*) instrumented by 12 (3 per side) μ-metal-shielded RCA 8575 photomultiplier tubes fed with 90^0 curved light guides. The physical characteristics of the TOF I counter are essentially unchanged from those of the first run and its dual purpose remains exactly the same: first; provide a "start" signal to be used in computing the flight time difference between this counter and any from an associated array (TOF II) downstream of the spectrometer-magnet and second; provide part of the neutrino trigger. The first feature allows measurement of the speed of a charged particle. Thus by computing β from the flight length and time measurements, charged particle I.D. tagging can be done using the inverse momentum measurement (from the bend in the magnet) through use of $p = m\beta\gamma$ where $\gamma = 1/\sqrt{1-\beta^2}$. In practice, I.D. tagging is achieved by computing the confidence level of the hypothesized particle type being associated with the TOF speed, at the measured inverse momentum. This will be explained in details when dealing with calibration because it required off-line analysis. (Section 4.1) The second feature called for the removal of signal arrival time jitter due to the location of the hit on the area covered by the scintillator. In order to do this, each side's 3 tubes were first OR'ed together. (Figure # 15) Then, after hardware mean-timing of the signals coming from 2 adjacent sides of the array, the two resultant signals were OR'ed and fed to a single AND gate. The other feed to this AND gate came from discriminated analog information on the hardware sum of the pulses from the 12 phototubes. If the sum exceeded twice minimum-ionizing in TOF I, this branch would fire. The output of the AND gate served as feed to the rest of the ν trigger as well as to other signals.

Much more downstream, at $z^{near} = 283.15\ cm$ & $z^{far} = 286.49\ cm$ (*front face*) , beyond the analysing magnet and the last set of drift chambers, were located the 34 1.5 *m* high Pilot F scintillator paddles forming the picket-fence like TOF II array. Pulses from counters of this array were used to achieve two ends: fast trigger timing and to provide a stop signal so as to allow off-line calculation of the flight times of charged particles between TOF I and TOF II (Section 4.1). The array was designed taking into account the expected charged-multiplicity and forwardness of events. In order to minimize the probability of two or more charged particles traversing the same paddle, thus jeopardizing timing within that paddle, 16 narrow 7 *cm* wide counters were centrally located in two slightly overlapping ($\sim 0.64\ cm$) rows of eight (in order to allow some redundancy) while 9 wider 10 *cm* counters were located on each side of this core bringing the total to 34 . All counters were 2.54 *cm* thick. Each paddle was instrumented with Amperex 2230H photomultiplier tubes at both ends which were interfaced with the scintillator, in the case of the 16 narrow paddles, with optical cones and in the case of the 18 wider paddles with light guides and optical cones. In the 2^{nd} run, in order to record more fanning-out charged particles, the X-acceptance of the array was increased by adding four 10 *cm* wide paddles, two on the beam-left and two on the beam-right side, bringing the total width from 2.25 *m* to 2.65 *m* . Each tube on each end of each paddle was instrumented, as in the first run,with Analog

to Digital Converters and Time to Digital Converters.

In order to be part of the fast trigger timing, analog pulses from the TOF II counters were all fanned-in together. Single- and double-hit levels, were monitored closely throughout the run as they had direct input into the ν trigger (see Section 3.5)

3.4.3) **The Upstream and Downstream Drift Chambers**

Drift chambers were required to record the trajectories of charged particles created in the interactions of the incoming neutrinos with nucleons in the target or in the subsequent decays of products of these interactions. Because particles are made to go through a dipole magnetic field in the center region of the E531 spectrometer in order to bend the trajectories of those carrying electric charge, the drift chambers are naturally divided into two sets: those upstream and those downstream of the magnet. Furthermore, because these devices can only measure a distance along a single co-ordinate axis, they must be oriented so as to provide enough measurements for a 5-parameter ($dx/dz|_{origin}$, $dy/dz|_{origin}$, $x|_{origin}$, $y|_{origin}$, and $1/p$) fit to the spatial evolution of the charged particle trajectories to be performed (off-line). As a single multi-cell drift chamber can only measure the *time* the ionization from charged particles takes to drift to one of its accurately surveyed sense wires, it cannot tell which way (+ or −) along the chamber's co-ordinate axis (perpendicular to the direction wires run) this ionization travelled. The position computed through use of the known drift-velocity (*negative* ionization drifts along the direction *opposite* to that of the applied electric field up to terminal speed due to collisions) in the gas of a single chamber is therefore always ambiguous:

$$\bar{d}_{hit} = (d_{sense\ wire} \pm v_{drift}\, t_{drift}) \cdot \bar{1}_d$$

This problem is adressed through shifting sense-wires with respect to each-other by one half a cell on chambers recording in a given view. This has tremendous implications for pattern recognition. (see Section 5.2)

In the 2^{nd} run, 15 upstream drift chambers (as opposed to only 12 in the 1^{st} run) were positioned $\sim 5\ cm$ apart, from $z = 16.79\ cm$, † just behind the TOF I counter, all the way to $z = 82.47\ cm$, flush against the upstream widow of the CPI. (Figure # 16) Chambers were positioned with their plane perpendicular to the $\bar{1}_z$ axis and rested on six 1 inch diameter support rods forming a "V" shape. Each (50-50) Argon-Ethane-filled chamber had 32 20 μm *diam.* sense wires running through 4 cm cells in which cathode-to-cathode wire spacing was 6 mm . The active area covered by any one chamber was 128 $cm \times 128\ cm$. Normal operating bias voltages provided an electric field strength of $E = 700\ V/cm$ and a typical drift velocity of $\sim 50\ \mu m/nsec$. The typical single wire position resolution, obtained from reconstructed beam-muons, was $\sigma = 125\ \mu m$. (More on this and the related subject of muon tunes in Section 4.2) In order to record enough data so as to allow 3-dimensional reconstruction of the charged particles' trajectories while securing a necessary degree of redundancy used for pattern recognition, the upstream drift chambers were oriented so as to measure drift distance along three separate axes labelled V,U and X. The direction $\bar{1}_x$ naturally

† These measurements are really survey averages. Reconstruction programs may use slightly different numbers with proper offsets.

points along the experiment's X-axis. The direction $\bar{l}_u$ is rotated 60^0 anti-clockwise (when looking along the beam's $\bar{l}_z$) from the vertical $\bar{l}_y$ and $\bar{l}_v$ is rotated 60^0 clockwise again from the vertical $\bar{l}_y$. Thus, $\theta_{xu} = 30^0$, $\theta_{uv} = 120^0$ and $\theta_{xv} = 150^0$. All sense wires naturally run perpendicular to the chamber co-ordinate axis. Chambers were distributed among the three orientations in 5 triplets going from upstream to downstream according to the following scheme :

$$VUXVUXVUXVUXVUX$$

The transformation between the co-ordinates is:

$$\begin{pmatrix} \bar{l}_u \\ \bar{l}_v \end{pmatrix} = \begin{pmatrix} \sin\theta_u & \cos\theta_u \\ -\sin\theta_v & \cos\theta_v \end{pmatrix} \begin{pmatrix} \bar{l}_x \\ \bar{l}_y \end{pmatrix}$$

where $\theta_u = \theta_v = 60^0$ from the vertical. Because of this large stereo angle, the propagated uncertainties in the Y-co-ordinates of fits to sets of hits along trajectories of charged particles are lower than if this angle were smaller, as is indeed the case for the downstream drift chambers. The X-co-ordinates, the uncertainty in which most affects the measurement of $1/p$, are very well determined, not exclusively though, by the set of chambers measuring *in the X-co-ordinate*. One slight draw-back to the staggered arrangement described above arises for very steeply sloped tracks and/or for charged particles with very low momentum. These particles can possibly head into the few extreme directions that allow chambers to be skipped in a particular view while still recording hits in other views. This is not expected to be a problem in event reconstruction however; such low momentum secondaries would not have a significant effect on the reconstruction of the parent's momentum and it is not expected that a multi-GeV decay particle goes-off at too large an angle because that would entail an un-physical perpendicular component of momentum on necessarily very forward-going charm parents.

Downstream of the spectrometer magnet, starting from $z = 209.86$ *cm* (flush against the downstream window of CPI) and going all the way to $z = 255.39$ *cm* were located the 9 large active area (203 *cm*$\times$118 *cm*) downstream drift chambers. In the first run, only 8 such chambers were used. These chambers had built-in cell-orientation according to the following sheme:

$$E'_{43}X_{40}D'_{44}X'_{40}X_{40}E_{44}X'_{40}D_{43}X_{40}$$

In this notation, ' indicates 1/2 cell shifts in a view and the subscript is the number of 25 μm *diameter* sense wires spaced 5.08 *cm* apart. A typical drift-field strength of 750 V/cm provided a comparable ionization drift-velocity with the upstream drift chambers. The same (50-50) Argon-Ethane gas mixture as for the upstream drift chambers was circulated in the downstream chambers. The single-wire resolution of these chambers was $\sigma = 175$ μm . The E and D views are *not* the same as the upstream V and U views, the co-ordinate axes transform as follows:

$$\begin{pmatrix} \bar{l}_d \\ \bar{l}_e \end{pmatrix} = \begin{pmatrix} \sin\theta_d & \cos\theta_d \\ -\sin\theta_e & \cos\theta_e \end{pmatrix} \begin{pmatrix} \bar{l}_x \\ \bar{l}_y \end{pmatrix}$$

where $\theta_e = \theta_d = 10.6^0$ from the vertical in the clockwise and anti-clockwise directions respectively. Spacing between the drift chambers was 5 *cm* except for between the two middle X-chambers where it was 10 *cm* .

The smaller stereo angle of the dowstream drift chambers (compared with upstream chambers) was chosen in order to avoid the problem of long wires sagging due to gravity. This resulted, as expected, in a worse Y-resolution of tracks fitted to sets of hits using downstream chambers alone as opposed to tracks in the upstream chambers or traversing both sets of chambers. (Note that it is the X-co-ordinate measurement which has the most effect on the determination of $1/p$ of charged particles.) Still, gravity did cause some problems: the downstream drift chambers warped under their own weight. This was picked-up by the tuning program (Section 4.2) and later (after the 2^{nd} run was over) the bowing was carefully surveyed so it could be taken into account.

3.4.4) **The SCM104 analysing magnet**

In order to bend the trajectories of charged particles traversing the spectrometer, a large water-cooled dipole magnet (maximum field of 6 *kGauss*) occupied the area between the upstream and downstream drift chambers. The magnetic induction field developed by this magnet, the SCM104, was mapped at the nearby Argonne National Laboratory [114] and Figure # 17 summarizes the measurements. Track fitting naturally made use of the exact field table. Often enough though, the following approximate rule of thumb can be used to make estimates on the bends:

$$\theta_{bend} = \frac{\int \overline{B} \cdot \overline{dl}}{p} = \frac{.186}{p}$$

in which if p is expressed in GeV/c then θ_{bend} comes out in *milliradians*. This is quite a reasonable approximation especially in the mid-field XZ-horizontal plane, the bend-plane.

In the 1^{st} run, the volume within the magnet gap (89 *cm* high by 203 *cm* wide by 102 *cm* deep) was filled with a bag containing a low-Z gas (He) in order to minimize multiple Coulomb scattering. In the 2^{nd} run, this space was occupied by a large-volume, long-drift multi-cell chamber equipped with necessary electronics to measure both dE/dx and drift time at several locations along the tracks left by charged particles. The chamber was manufactured using non-magnetic materials.

3.4.5) **The Charged Particle Identifier**

In this section, the motivations for CPI are first exposed. This is then followed by a brief description of the device.

In the 2^{nd} run of E531, an attempt was made to compensate for two design draw-backs associated with the spectrometer. The first problem arises with the intrinsic time resolution limit associated with the TOF system: σ_{TOF} . Given a measured inverse momentum $1/p$, a charged particle can be tagged (at the one-sigma level) by TOF only if the difference in flight times over a given flight path l is greater than the time resolution of the system:

$$\Delta t = t_i - t_j \approx \frac{l}{2c}\frac{m_i^2 - m_j^2}{p^2} \quad must\ be\ > \sigma_{TOF}$$

where m_i and m_j are two different mass tags to be assigned. (p in GeV/c and masses in GeV/c^2) This is only true if

$$l > l_{min} = 2c\,\sigma_{TOF}\,\frac{p^2}{m_i^2 - m_j^2}$$

For typical 2^{nd} run $\sigma_{TOF} = 80\ psec$,

$$l_{min} \approx .2\ p^2 \qquad \pi^{\pm}\ K^{\pm}\ separation$$
$$l_{min} \approx .06\ p^2 \qquad K^{\pm}\ p\ separation$$
$$l_{min} \approx .05\ p^2 \qquad \pi^{\pm}\ p\ separation$$

where l_{min} is in meters. To give an example, if the charged particle were going straight along $\bar{l}_z$, the available distance would then only be 2.76 m which would not allow TOF to distinguish this particle as a pion from say, a kaon, above a momentum $p = 3.71\ GeV/c$. (not a particularly high value; also, see Section 4.1 on TOF calibration for more details) This examplifies the problem: fast charged particles *can* escape tagging by flight-time measurement if they are *fast* enough.

The second problem encountered in the design of the spectrometer has been mentioned before: multiple hits in TOF II paddles render the timing information useless. An alternate way to tag fast charged particles was sought and the (relatively) recently developed technique of Multiple Ionization Sampling on the relativistic rise (particularly in noble gases) [115 to 134] combined with a CCD-based read-out system was chosen. [135] The physical characteristics and design considerations as well as early tests performed (off- and on-site) with CPI are described elsewhere [136 137] . The design of the device essentially relies on a single physical principle: the Most Probable Energy Loss (MPEL) caused by a fast singly-charged particle traversing a gas with high ionization potential depends *only* on the speed of that particle. Furthermore, MPEL rises appreciably (as much as 50%) in appropriate gases (See Appendix 12.6 for more details). As $MPEL < \langle dE/dx \rangle$ and because of the non-negligible probability that any single i^{th} measurement of dE/dx be such that $dE/dx_i \gg MPEL$, a single measurement of dE/dx or even the average of several such measurements is not appropriate for particle identification. The statistical variations on such a quantity would be much too large.

A simple way (which was shown to be statistically un-biased) to reduce the size of the statistical variations is to estimate $MPEL$ by removing the *largest* samples from a set of N measurements of dE/dx and to take the average of the rest.

$$MPEL_{est} = \langle dE/dx \rangle_{cut\ off}$$

Cut-off studies have been made and it was concluded that it is reasonable and sufficient to low-average 70% of the data, thus throwing-out the top 30% . This is the method that was adopted for the analysis of the CPI data. In theory, knowledge of MPEL provides an estimate of the speed of the charged particle and using the inverse momentum measured from the bend in the magnet, a particle I.D. tag can be made. More realistically though, it was chosen to do the following: for a given measurement of $I/I_0 = MPEL\ /\ MPEL_0$ in CPI, a confidence level was assigned for that measurement to be associated with a charged particle of some assumed mass; the momentum being known. This allows probabilities to be associated with I.D. hypotheses on fast charged particles. (see Section 4.3)

The resolution of multiple ionization sampling devices has been measured to be

$$\frac{FWHM(\ MPEL\ )}{MPEL} = 0.96\ N^{-0.46}(tp)^{-0.32}$$

where N is the number of samples of dE/dx used in the determination of MPEL, t is the sample thickness in centimeters and p is the pressure in atmospheres. This formula is for argon and is also a good approximation for other commonly used gases except Xenon. [138] It was prudently decided that CPI should operate at atmospheric pressure. Also, the available space in the SCM104 gap dictated a straight-through total path length of 100 cm . Choosing to collect 50 samples of dE/dx and averaging the 35 lowest samples to extract MPEL, one can expect the device, under ideal conditions, to have a resolution of 15% FWHM, good enough to tell $\pi^{\pm}$ from $K^{\pm}$ over a wide range of momenta.

The CPI (Figure # 18) consisted of a large (88 cm high, 183 cm across, and 100 cm deep) box filled with a mixture of 80% Argon and 20% carbon-dioxide at atmospheric pressure. The gas mixture was dried and oxygen removed with a trap rated at less than 5 ppm . The main purpose for the presence of the molecular gas is to "cool" drifting electrons; to prevent them from diffusing too much over their long $max.$ = 22.5 cm drift distance to one of the 100 amplification cells. A draw back to the admixture of carbon-dioxide is that CO_2 can act as a *catalyst* to electron capture by the oxygen molecule thus resulting in a loss of signal depending on the drift distance. The chamber had to be kept very clean from oxygen contamination. It has been estimated [136] that in the gas mixture that was used, CO_2 would limit the electron-cluster size to about σ = 1 mm after drifting the full 22.5 cm . Each amplification cell was 2 cm deep along the beam direction, 1 cm high in the Y-direction and ran the full length of the 183 cm in the X-direction. The CPI sense-wires ($diam.$ = 25.4 μm , $bias\ voltage$ = +1.6 kV) running along the axis of those cells were thus laid 2 cm apart in two rows of 50 , one at $y^{lower} = -17.04$ cm and the other at $y^{upper} = +28.59$ cm , along the $\overline{1}_y$ direction starting from z = 96.08 cm and going all the way to z = 194.07 cm . This naturally divides the device in 4 *quarters* . In the first and second quarters (starting from the top), ionization drifts to the upper sense-wire plane; there is thus up-down ambiguity about that plane. In the third and fourth quarters, ionization drifts to the lower sense-wire plane and there is also an up-down ambiguity about that plane. However, another symmetry relevant for CPI is that of the magnetic field it sits in; this results in a symmetry about the mid XZ-plane: the first quarter is the analogue of the fourth and the second that of the third. The CPI chamber sat inside the spectrometer's magnet and within its volume, the chamber's electric drift-field and the SCM104's magnetic field were approximately parallel. This drift field of $E = 356\ V/cm$ resulted in measured electron-cluster drift velocity of $\sim 1\ cm/\mu sec$ (see Section 4.3) along the Y-direction.

Each sense-wire was instrumented, at one end only (thus allowing only a single view, the Y-view, to be recorded), with a (LeCroy TRA510) pre-amplifier and the output pulses fed to a specially built CCD-based read-out system described extensively in $Ref.$ 135 . The design, testing and building was entirely done at McGill University. The system, once triggered, integrated (bucket size = 100 $nsec$), digitized and buffered charge above threshold at any of the 100 instrumented channels for a total time of 20 $msec$. The large quantity of data this scheme naturally generates (typically 24k bits) had to be read at the very end of the CAMAC cycle, but the slow repetition rate of the machine left plenty of time to do this.

3.4.6) **The Electromagnetic Shower Detector**

The analysis of the 1st run data revealed a weakness in the reconstruction of π^0-decays. For that data run, the basic spatial resolution for detection of electromagnetic showers was only 19 cm × 19 cm (see next

section) which often caused uncertainties in the pattern recognition. In the second run, it was decided these uncertainties ought to be reduced at the cost, however, of much added analysis time and complications. The basic need of observing electromagnetic showers arises from the fact that E531 strived for full kinematical reconstruction of all its decay hypotheses. The (electromagnetic) decay of the lightest of all neutral hadrons (π^0) involve gamma rays [138] which may be observed through electromagnetic showers they subsequently induce.

$$\begin{aligned} \pi^0 &\rightarrow \gamma\,\gamma \qquad B.R. = 98.80\% \\ \pi^0 &\rightarrow \gamma\,e^+\,e^- \qquad B.R. = 1.198\% \end{aligned} \qquad c\tau = .025\mu m$$

followed by

$$\gamma \rightarrow \textit{Shower of } e^+\,e^-$$

Although gamma rays may simply convert inside the emulsion volume ($\gamma \rightarrow e^+\,e^-$); it is very likely, for example, that the two gamma rays from a π^0 decay produced midway through the 70 *mm*-emulsion do survive traversing the remaining thickness of material without converting. In fact, with a 40 *mm* conversion length, it turns out that the *average* combined survival probability for two gamma rays is: $\langle P_{surv} \rangle = 47\%$; not a small number. Such gamma rays exiting the emulsion then stand a excellent chance of flying right through any further material without converting until they reach the γ-EPIC system.

3.4.6.1) **The γ-EPIC planes**

It was decided to use a γ-ray converter wall just downstream of the TOF II array. The converter was made of 1.59 *cm* thick lead sheets supported by an aluminium backing 0.95 *cm* thick. The lead sheets were actually 54% PbO and 46% SiO_2 by weight. [139] . This resulted in a combined thickness of 2.9 radiation lengths for a single gamma survival probability of only 5% . Immediately downstream of the γ-converter, were three planes of Extruded Proportional Ionization Chambers (EPIC). These chambers were used to measure the position of the developing showers. They were oriented along three different views: a Y-view at $z = 308.71$ *cm* , a U-view at $z = 310.69$ *cm* and a V-view at $z = 312.93$ *cm* . The approximate area covered by the γ EPIC planes was 2.03 *m* high by 2.51 *m* across. * Each chamber contains eight cells (cross-section: 2.381×1.27 cm^2) filled with a 50-50 mixture of argon-ethane. See Figure # 19 . The Y-view used ten chambers for a total of 80 cells in that plane, while the other two views used twelve chambers each, and thus had 96 cells per plane. Each cell was instrumented with amplifier and ADC. This allowed pulse height information to be recorded; a minimum ionizing charged particle would deposit 20 MeV per cell. While the $\bar{1}_y^{EPIC}$ axis was almost straight up, 0.32^0 with vertical, the $\bar{1}_u^{EPIC}$ direction pointed at 60^0 clockwise with respect to the experiment's vertical and the $\bar{1}_v^{EPIC}$ pointed 60^0 anticlockise with the same vertical. This redundant arrangement allowed extensive pattern recognition to be performed. (see Section 5.2.3). The single cell resolution was $\sigma_{xuv} = 7.3$ *mm* while the typical angular resolution of γ's originating at the target was $\sigma_{\frac{dx}{dz}} = \sigma_{\frac{dy}{dz}} = .002$ *radians*

* These low-cost (extruded) multi-cell chambers offered an attractive alternative to a full aperture plastic scintillator hodoscope.

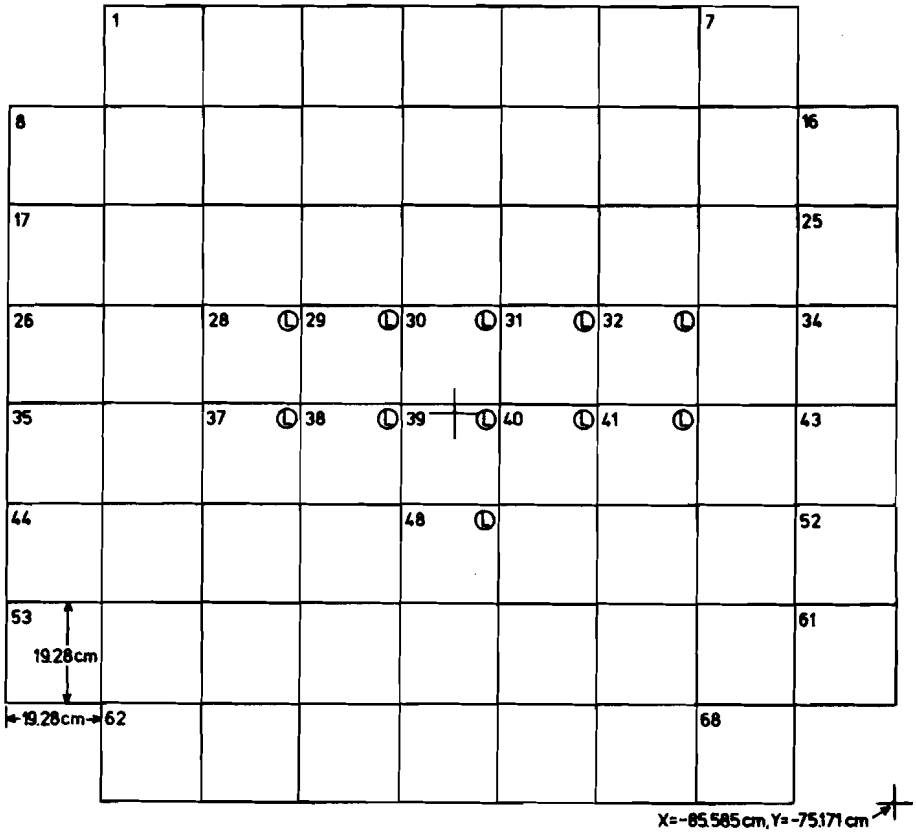

Figure # 20

The lead-glass (PbG) block array. The neutrino beam goes into the picture. Blocks are all 19 $cm \times 19$ cm across the beam direction but come in two different lengths. Long blocks are indicated with the symbol "L", others are all short. The array is square with the four corner blocks removed. All photomultiplier tubes are located behind the blocks and do not show on the picture. The cross in the center of the array shows the center-line of the spectrometer. The entire assembly was mounted on a cart which ran on rails and thus could easily be wheeled out to allow servicing.

3.4.6.2) **The Lead Glass blocks**

While the three planes of γ EPIC's allowed pattern recognition to be done on the developing electromagnetic showers, it provided little information on the total energy of these showers. This task was accomplished by a wall of 68 lead loaded glass blocks. (Figure # 20) Each block was 19 cm × 19 cm across the beam direction and came in two different lengths: 30.5 cm and 35 cm . F2 lead-glass (45% PbO per weight, $r.l. = 3.22\ cm$) was used for the 56 short blocks (9.5 radiation lenghts long) and SF2 lead glass (53% PbO per weight, $r.l. = 2.84\ cm$) was used for the 12 centrally located long blocks (12.3 radiation lengths long). Each individually wrapped block had its downstream end instrumented by EMI 9815 phototubes and each tube was read by two ADC's through a 1 : 20 pulse splitter in order to be able to record both minimum ionizing calibration muons and showering electrons. (Also, note that lead-glass blocks are $\sim 2/3$ absorption length long [140] so hadrons stand about a 50% chance of interacting while traversing them...) The energy response and resolution of the PbG-EPIC system were measured in the M5 multi-particle test beam. (Section 4.4)

3.4.7) **The hadronic shower detector**

Neutral hadrons other than π^0 are expected to be created in the interactions of neutrinos with nucleons from the emulsion target or in the subsequent decay of charmed particles. Such hadrons include, for example, neutrons and K_L^0 . Detection of charged hadrons is straightforward in the drift chambers. However, detection of long-lived neutral hadrons that traverse the spectrometer require the use of dedicated equipment. The calorimeter (Figure # 21) in which *all* hadrons deposited their energy through hadronic showers was a sandwich-type device interspacing 6 read-out planes between 6 10.16 cm-thick walls of steel. In order to record the evolution of hadronic showers, the calorimeter was first instrumented by 3 planes of EPIC's at $z = 4.13\ m$, $z = 4.28\ m$ and $z = 4.42\ m$ which were followed by 3 planes of large area scintillator paddles at $z = 4.57\ m$, $z = 4.72\ m$ and finally at $z = 4.92\ m$.

Each EPIC plane consisted of 11 chambers similar to the ones used upstream of the lead-glass wall. Although each chamber contained 8 sense-wires, every 4 sense wires were OR'ed together by the electronics so that only 22 active "slices" remained. The approximate area covered by each plane was 2.23 m high and 2.26 m accross. All three calorimeter EPIC planes were positioned so that sense-wires ran horizontally. Thus, in the first three planes of calorimeter EPIC's, position along the Y-direction was measured with a resolution of $\sigma_y = 30\ mm$. In addition, both ends of EPIC's were instrumented by ADC's and position of single hits along the X-direction could be achieved through charge division with $\sigma_x = 64\ mm$.

Each of the three downstream planes of the calorimeter were instrumented with four 1.3 cm-thick (NE114 or NE110) scintillator (att. length = 5.0 m) paddles each 244 cm high and 75 cm accross. Only the top end of each paddle was equipped with an Amperex 58DVP phototube optically connected with the paddle through a light guide. As paddles ran vertically, position was only roughly determined along the X-direction to a paddle width affording only paddle-length resolution in the Y-view. Pulses from the phototubes were split (1 : 7) so that both calibration muons and showering hadrons could be recorded on ADC's.

3.4.8) **The muon detector**

One of the most important part of the spectrometer is actually one of the structurally simplest: the two

muon tagging hodoscopes. In the most probable scheme for the neutrino production of charm (Section 1) off quarks inside a target nucleon, an energetic μ^- is expected to come out of the production vertex. (μ^+ is expected for $\overline{\nu}$ production of anti-charm.) Also, semi-leptonic charm decays can include less energetic muons of opposite electric charge to the production muon. Production or decay muons, can be identified with their range in steel.

The muon-front and muon-back hodoscopes used in the 2^{nd} run of E531 are exactly the same pieces of equipment used in its 1^{st} run. [141] The muon-front wall ($z = 5.61\ m$) was made of two side-by-side column arrangements of scintillator paddles. Each column arrangement contained 18 scintillator paddles running horizontally for a total of 36 paddles altogether. The beam-right paddles looked into the beam-left direction ($+\overline{1}_x$) while the beam-left paddles looked into the beam-right direction ($-\overline{1}_x$)... Each paddle was 1.52 m long and instrumented an one end with an AMPEREX AVP 56 phototube whose pulses were split between an ADC and TDC. The resolution in the $\overline{1}_y$ direction was governed only by the variable paddle widths. The 10 most centrally located paddles were 10.16 cm wide. The two paddles on top and two below this core arrangement were 20.32 cm wide. The two top and two bottom paddles completing the muon-front wall were each 27.94 cm wide. Timing allowed distance measurement along $\overline{1}_x$ to within $\sigma_x \sim 13\ cm$. Because of the massive steel wall just upstream of the muon-front hodoscope, muons recording hits in that array had to have $E_{muon} \geq 1.9\ GeV$.

The muon-back hodoscope was located at $z = 7.06\ m$ behind another wall of steel dowstream of the muon-front array, and muons with $E_{muon} \geq 3.4\ GeV$ would record hits in any of its 40 vertically looking paddles. These paddles were of the same type as those of the muon-front hodoscope and were divided in two arrangements of 20 , the top arrangement looked down ($-\overline{1}_y$ direction) and so did the bottom one. Thus the bottom arrangement was offset by one paddle length (w.r.t. the top arrangement) in the $-\overline{1}_y$ direction. The X-resolution was governed by paddle widths. Within either the top or bottom arrangement, the 10 most centrally located scintillators were 10.16 cm wide. The two paddles beam-left and the two paddles beam-right of the central core were 20.32 cm wide. The 3 paddles on the extreme beam-right and the 3 paddles on the extreme beam-left were each 27.94 cm wide. Some efficiencies of the muon counters are presented in Section 4.6 .

3.5) **Gating and triggering**

The output signal of some of the basic devices whose set-up and functions were described in the preceeding sections were combined to provide the main E531 ν trigger as follows:

$$\nu_{trig} = \nu_{gate} \cdot \overline{A} \cdot TOF\ I_{\geq 2\ M.I.} \cdot TOF\ II_{\geq 2\ tracks}$$

In this,

$$TOF\ II_{\geq 2\ tracks} = TOF\ II^{top}_{\geq 2\ M.I.} \cdot TOF\ II^{bot}_{\geq 2\ M.I.}$$

where "top" and "bottom" refers to the independently instrumented top end and bottom end of TOF II counters and "M.I." is a shorthand for "Minimum-Ionizing". Thus, in order to record a neutrino-trigger, it was required that the veto-array be off (ν incident), that TOF I had more than two charged particles

traversing it (ν interacted), that TOF II recorded two distinct charged particles (downstream end reached) and that all of these events happened in time with the neutrino gate.

In addition, a μ trigger was provided:

$$\mu_c = \mu_{gate} \cdot A \cdot TOF\ II^{top}_{\geq 1\ M.I.} \cdot TOF\ II^{bot}_{\geq 1\ M.I.}$$

in which the muon gate opened in the last 20% of the beam spill. This was for the purpose of beam-on device calibration. The relative timing of gates to the horn current is displayed on Figure # 22 .

4.0) DEVICE AND SYSTEM CALIBRATION: RESPONSE AND RESOLUTION.

An extensive device calibration effort immediately followed the second run of E531. Many aspects of the response of devices described in the previous section could only be established, with high statistics, using beam muons recorded with the μ_c trigger. Most of the time, a single muon would traverse the spectrometer per such trigger. For calibration purposes, the reconstructed muons in the drift chambers were required to be tagged by the muon identifier. Figure # 23 presents the reconstructed $q \times p$ of the calibration muons. (Most calibration muons carry negative electric charge q as they are produced by ν interactions in the berm.) The most probable calibration muon is a μ^- with $p \sim 6\ GeV/c$ but as the distribution shows, the momentum range is rather wide. The muons arrive at the E531 spectrometer with $\langle dx/dz \rangle = \langle dy/dz \rangle = 0$ and $\sigma_{dx/dz} = \sigma_{dy/dz} = .013$

4.1) The TOF system

For calibration purposes, the (single) TOF I scintillator was divided in 9 square "regions" of equal area defined by the "intersecting views" of the 3 tubes on each of the 4 sides. Tube efficiencies for the 8 regions having a side immediately viewed by a tube was 97% while the central region had an efficiency of 91% . Centrally located TOF II paddles were very well populated (about 5000 muons for counter 10 through 25) while side counters were less populated. The efficiencies (given μ predicted to go through a paddle; demand TOP and BOT tube fire...) of the TOF II counters were high, $\sim$ 97% for most counters.

Consider one calibration muon whose identification is known by tagging in the muon-front and muon-back hodoscopes (See Section 4.6) . The speed β of that muon can be computed from its momentum measurement in the magnetic field through $p = m\beta\gamma$ and also by use of the TOF system through $\beta = l_{path}/c\, t_{flight}$. (l_{path} is the total path length travelled along the curved trajectory of the muon over the flight time given by the difference between the stop and start times.) A set of *many* such speeds is used to fit the overall parameters describing the TOF system.

A calibration muon records a single hit in TOF I . Although this hit is seen by all 12 phototubes, those tubes directly above, below, to the right and to the left of the hit record the most direct light. These 4 tubes are thus the best to compute the start time for this calibration muon:

$$t^{\mu}_{start} = \frac{1}{4}\sum_{i=1}^{4} t_i$$

$$t_i = t_i^{TDC} - A - \frac{d_i}{c_{eff}} - \frac{B}{\sqrt{PH_i^{ADC}}} \quad .$$

In this expression, t_i^{TDC} is the time read out by the i^{th} TDC, d_i is the distance from the hit to the i^{th} tube, c_{eff} is the effective speed of light in the scintillator A is the time required for propagation through tube bases and cables and PH_i^{ADC} is the pulse height as recorded by the i^{th} tube's ADC. This last term is essential in order to account for jitter that would otherwise be introduced because of the necessary use of a discriminating level on the TOF pulses (one unique shape, finite rise-time).

In a very similar manner, for TOF II,

$$t^{\mu}_{stop} = \frac{1}{2}\sum_{j=1}^{2} t_j$$

$$t_j = t_j^{TDC} - C - \frac{d_j}{c_{eff}} - \frac{D}{\sqrt{PH_j^{ADC}}}$$

In this case, j runs over the top and bottom counters of the TOF II paddle traversed by the muon; t_j^{TDC} is the time recorded by either the top or bottom TDC, d_j the distance from the hit to the top or bottom tube, C the propagation time through the tube bases and cables and D the correction due to the pulse height PH_j^{ADC} . The set of parameters $\{A, B, C \text{ and } D\}$ together with $c_{eff} = 17.132\ cm/nsec$ completely describe the response of the E531 TOF system and muons were used to determine them.

Top minus bottom-tube time resolutions *per paddle* were determined for the TOF II hodoscope using the fitted set of parameters. These were found to be to be $\sigma_{wide} = 100\ psec$ for the (outer) wide TOF II paddles and $\sigma_{narrow} = 75\ psec$ for the (inner) narrow paddles. The unequal resolutions arise because of differences in the optical couplings of photomultiplier tubes to wide and narrow counters.

The TOF parameter-set, determined using calibration muons, was used with neutrino triggers. These have quite a few more tracks going through the spectrometer compared to single-track muon calibration triggers. In an attempt at removing bias on a statistical basis, a correction to the TOF I start-time was applied to take into account the finite *spot* size of the expanding cone of particles traversing the TOF I scintillator. If there are N tracks in a ν-triggered event, the average (over tracks) spot-size radius ρ is given by:

$$\rho = \sqrt{\frac{\sum_{i=1}^{N} \Delta_z^2 S_i^2}{N}}$$

$$S_i^2 = \left(\frac{dx}{dz}\right)_i^2 + \left(\frac{dy}{dz}\right)_i^2$$

in which Δ_z is just the distance, along $\bar{1}_z$, between TOF I and the vertex. This radius was removed from the 4 perpendicular distances light has to travel in order to reach the TOF I phototubes.

An overall check of the TOF system to identify particles in conjunction with the magnetic spectrometer was done for low momentum tracks. Figure # 24 displays the distribution of masses computed using β from TOF and p from the drift chambers. For $p \leq 2\ GeV/c$, the system correctly produces masses and widths without any further ajustment of its parameters.

4.2) **The momentum measurement system**

The inverse momentum of charged particles ($1/p$) was obtained from the fits to tracks recorded by the drift chambers located upstream and downstream of the analysing magnet. Any set of hits constituting a track was fitted to 5 parameters: two co-ordinates at the origin: $x|_0$, $y|_0$; two slopes at the origin: $dx/dz|_0$, $dy/dz|_0$ and the inverse momentum: $1/p$. The precision in $1/p$ depends on whether the track was actually reconstructed as going through the magnet aperture, that is, reconstructed in the upstream and downstream drift chambers (down-to-up track), or merely reconstructed in the upstream chambers but not

in the downstream chambers (up-only track) because either the track wasn't inside the magnet's acceptance or because the track just couln't be found in the downstream chambers. In all cases, the accuracy in $1/p$ strongly depends on pattern recognition. (Section 5.2)

The position of all critical pieces of apparatus of the E531 spectrometer was constantly electronically monitored during the long 2^{nd} run by LVDT sensors read out as part of a dedicated CAMAC calibration cycle. In addition to this warning system, and quite more importantly, key parameters used by the track reconstruction software and related to the performance of the drift chambers were *tuned* (by software) , using calibration muons, as the 2^{nd} run progressed. The calibration muon population was divided in 103 time intervals and a set of *tune* parameters was produced for each interval.

A tune consisted of a list of parameters used by the software for each of the 24 drift chambers. The *geometry* parameters described: the bowing of a drift chamber under its own weight, small changes in the position of the drift chamber primary support rod, small changes in the co-ordinates of the first (reference) wire on the chamber and small rotations of the whole chamber about the $\overline{1}_z$ axis. Another parameter described small changes to the drift velocity in the gas of the chambers and finally, a set of parameters described small changes in key calibration constants of the electronics (TDC response and propagation time).

On a few occasions, calibration muons were recorded with the SCM104 magnet intentionally turned *off*. This was helpful to establish what the contribution of the intrinsic resolution of the chambers was to the $1/p$ measurements. With the magnetic field off, all muons fly straight through the spectrometer. No bend is induced. By further requiring front-back energetic muons, the multiple Coulomb scattering is reduced to a negligible level. The output of track fits, (done with the assumption that the magnetic field is still on) assigns to these tracks an *effective* infinite momentum or $1/p = 0$ with a certain spread (the total contribution of the intrinsic chambers resolution) of $\sigma_{1/p}^{intrinsic} = .004\ .\ (c/GeV)$ On the other hand, multiple Coulomb scattering is accounted for by $\sigma_{1/p}^{M.C.S.} = .118/p\ (c/GeV)$ which was verified to be compatible with the χ^2-per-degree-of-freedom distribution of fitted tracks. Combining the two contributions, for down-to-up tracks:

$$\sigma_p = \sqrt{.014\,p^2 + (.004\,p^2)^2} \qquad Down - to - up\ \ tracks$$

in which p is in GeV/c . In the case of up-only tracks, the resolution was, expectedly, not as good:

$$\sigma_p = 0.08\,p^2 \qquad Up - only\ \ tracks$$

4.3) **The CPI calibration**

Just before the 2^{nd} data taking run started, during the summer of 1980 , the Charged Particle Identifier was put to test, on location, using calibration muons. For the duration of the test, the SCM104 magnet was turned off but the muon hodoscopes turned on. This allowed selecting stiff muons $p \geq 3.4\ GeV/c$. The CCD-based read-out system was *not* used and only the upper sense-wire plane was instrumented with conventional ADC's and TDC's. This test greatly helped in determining several key operational parameters of the new device. The results demonstrated that the device responded to within a few % of design specifications when

traversed by fast single muons. [136] [142] Based on these promising results, it was enthusiastically decided to carry-on with the full-scale implementation of the chamber. The following two sections briefly describe the extensive CPI calibration effort that followed the 2^{nd} run of E531. The work was initiated on Fermilab's Cyber computing facilities then continued on the McGill University Computing Center's Amdahl mainframe and final aspects of it were completed on the E531 On-line machine, a Data General ECLIPSE mini, moved from Chicago to Montreal partly for that purpose.

4.3.1) **The drift parameters**

The first aspect of the calibration deals with the drift of the ionization towards the sense-wire planes. This is characterized by drift velocities and an offsets.

$$d_i^j = {d_0}_i^j + v_{drift}^j \, t_{drift}^i$$

In the above expression, i ($i = 1 \rightarrow 50$) labels the drift-cell number † within the j^{th} ($j = 1 \rightarrow 4$) quarter, d_i^j is the distance between the sense-wire servicing the i^{th} drift-cell and the location of the track along the $\pm\bar{1}_y$ direction. In the second term, v_{drift}^j is the appropriate drift velocity for one of the 4 quarters. From drift studies, it was found that structural differences of the chamber caused the drift velocities in the different quarters to be slightly different and to also exhibit a rough symmetry about the mid XZ-plane. Finally, t_{drift}^i is the arrival time of the *first* non-zero data recorded on the sense-wire servicing the i^{th} drift-cell in the j^{th} quarter. Therefore, the complete set of parameters fully describing the tracking response of the chamber totalled $4 + 4 \times 50 = 204$. These were determined by doing a χ^2 minimization fit using the fully reconstructed calibration muons traversing the chamber. (N_μ = 17 595, 28 661, 30 124, 19 287 *per quarter*) In order to track slight changes in the gas drift velocity over time but still collect enough statistics, typically 2 to 5 runs had to be bunched together and 120 sets of calibration parameters were produced.

The time-averaged fitted drift velocities in the 80-20 Argon-CO_2 gas mixture ($E_{drift} = 356\ V/cm$) were found to be

$$v_{drift}^{j=1,2,3,4} = \{1.082,\ 1.174,\ 1.169,\ 1.099\ (cm/\mu sec)\}$$

and these numbers were stable to $\delta_v/v = 5\%$ over the whole duration of the 2^{nd} run. Residual distributions between tracks found in CPI and tracks predicted by the drift chambers were plotted. Single-wire Y-residuals were found to be $\sigma_y = 1.3\ mm$ while fitted-track dy/dz-residuals were found to be $\sigma_{dy/dz} = .0017$ mid-way through the chamber.

† This is not the gas amplification-cell number; one amplification-cell actually serviced two drift-cells: one above (drift down) and one below (drift up). There were four quarters in the CPI: above (1^{st}) & below (2^{nd}) the upper sense-wire plane, above (3^{rd}) & below (4^{th}) the lower sense-wire plane and 50 drift-cells per quarter, but only 100 sense-wires divided in 2 planes of 50 . This resulted in a stand-alone up-down ambiguity for each amplification-cell. However, the ambiguity could be removed with the help of a match to a drift chamber track.

4.3.2) **The ionization parameters**

The response of each of the 100 electronic read-out channels on the gas-amplification cells of the CPI is characterized by:

$$V_k = g_k \, ADC_k + V_k^0$$

In this formula, V_k is the cell voltage produced on the effective cell capacitance by the total charged collected, g_k is the gain of the k^{th} amplification cell ($mV/ADC\ count$) and V^0 is the voltage below which the channel does not respond. Pulse shape studies revealed that it was necessary to integrate the contents of non-zero charge-buckets for 600 $nsec$. There are therefore 2 parameters per wire and thus a total of 200 parameters that partially describe, up to an absolute calibration, the response of the chamber to ionization; muons had to be used to determine them. Though the gains were measured to vary little over long periods of time, the electronic offsets were not so stable and, because of this, essentially one set of calibration parameters per run was required. Also, full account was taken of several corrections (pressure, drift-distance, geometry, angle) which were first parametrized during the test-run and later confirmed by the calibration data of the 2^{nd} run of E531.

The ionization parameters were fitted with an iterative procedure which equalized single-wire responses. The absolute gain of the chamber was established making use of the theoretically predicted relativistic rise in 80-20 Argon-CO_2 . [118] (50 % from $\beta\gamma = 4.5$ to $\beta\gamma \geq 1500$). The muon dataset available to do this had $\langle\beta\gamma\rangle = 273 \pm 233$ but peaked at $\beta\gamma = 40$. Figure # 25 presents the fully-corrected Most Probable Energy Loss in the chamber for 44 377 muons (integrating over the whole 2^{nd} run) which registered $40 \leq N \leq 50$ hits along their tracks in the CPI. This was fitted to a Gaussian of width $FWHM = 22\%$. The expected $1/\sqrt{N}$-type dependence of the $FWHM$ vs N was observed to be roughly obeyed.

The bottom line really is whether this calibration is adequate to identify particles in ν-triggered events. As was mentioned before in the case of TOF, the μ_c-triggered and ν-triggered datasets are *very* different although, of course, the physics of devices is quite invariant. In order to cross-check this μ-calibration with hadronic data, a reasonable size dataset had to be put together. As CPI allowed only one view (Y), typically busy multi-track ν-triggered events rendered the pattern recognition so complex that it could only be reliably done using an interactive-software algorithm. It required $\sim$ 3 man-months to go through and digitize 77 of the charm candidates. Of the 399 down-to-up tracks that traversed CPI, 120 were matched with a decay track in the emulsion, which was the first requirement imposed. Of these, because of the high hit density and the many track-crossings, only 19 had the required participation $40 \leq N \leq 50$ and only 6 were positively identified by another device. CPI was able to corroborate the identification of half of those, at the 2σ level, while only 1 could be corroborated, at the 1σ level. Of the 13 remaining tracks in need of I.D., 9 ended-up in fitted charm events in the final data-sample. Essentially, it was found to be impossible to cross-check the CPI muon calibration in any statistically meaningful way thus preventing its use for reliable stand-alone particle-identification. The many drift-related qualities of the chamber were, on the other hand, quite helpful in many instances during the course of event analysis.

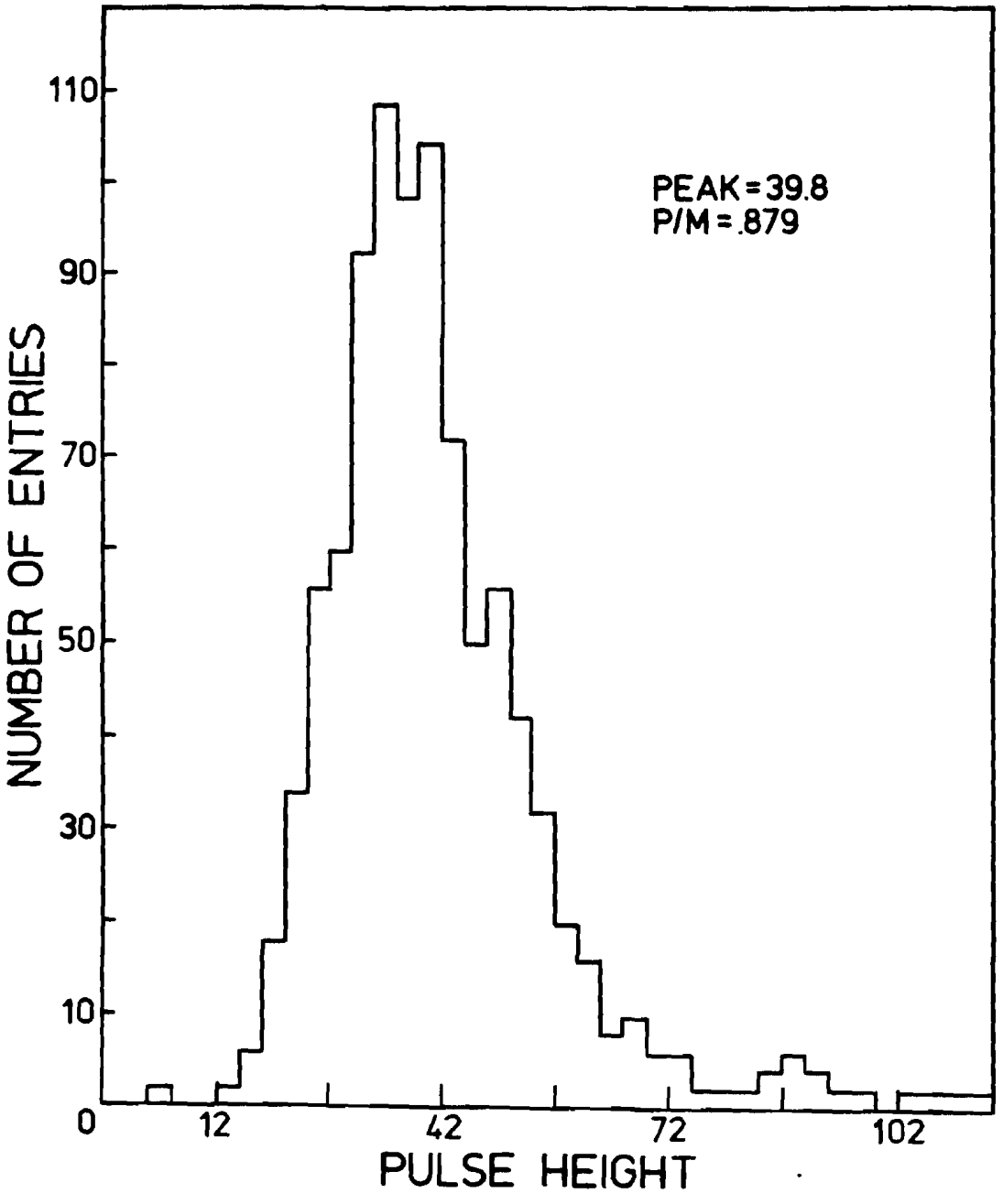

Figure # 26
Distribution of pulse heights in the lead-glass array. The ratio of the peak to the mean is .879 .

4.4) **The PbG/EPIC system calibration**

The response for *on axis* minimum-ionizing pions traversing short and long lead-glass blocks was determined using tagged pions from the FNAL M5 multiparticle ($\pi^{\pm}, \gamma, e^{\pm}$) test beam. Along the axis of the blocks, this turned out to be [143] :

$$E_{long} = 467 \pm 15\ MeV/M.I.$$

$$E_{short} = 392 \pm 15\ MeV/M.I.$$

where *M.I.* stands for Minimum Ionizing. While this established gain, calibration muons recorded during the 2^{nd} run of E531 gave the peak locations of the minimum-ionizing distributions for each block in terms of *ADC counts/M.I.*. Also, the pulse-height varied over the surface of the blocks for off axis and angled tracks. This effect was studied and appropriate corrections were established. Figure # 26 presents the distribution of pulse-heights in the lead-glass block array. The ratio of the peak to the mean of the distribution is $P/M = .879$.

In the 2^{nd} run of E531, the biggest improvement in electromagnetic shower detection was due to the use of the three γ-EPIC planes (to do pattern recognition) upstream of the lead-glass array. Calibration muons recorded during the run were used to fine-tune the survey of the proportional ionization chambers and also to observe the response of each cell in terms of *ADC counts/M.I.* . However, the exact energy correlation between the pulses observed in the EPIC cells and the pulse from one of the downstream lead-glass blocks, in the case of a developing electromagnetic shower, was the object of a pre-run test (1980) done under carefully controlled conditions again at the M5 multi-particle beam line and also of an extensive Monte Carlo simulation. The pattern recognition aspects associated with electromagnetic showers will be discussed in Section 5.2.3 .

The analysis of the M5 test in which the response of the PbG/EPIC system to electron-induced showers was determined is presented in *Ref* 139 . The object of the investigation was three-fold; first to determine the correction to the observed shower energy in the block due to upstream material and second, to determine the spacial resolution of the system while third, it was to determine energy-sharing between neighbouring blocks.

The last objective was fulfilled and a map (Figure # 27) of the energy-sharing was produced. It shows that a shower is 100% contained if it occurs midway across the face of a block and still is 92.5% contained if it occurs 7.620 *cm* off-center in the $\pm\bar{1}_x$ or $\pm\bar{1}_y$ directions (2.54 *cm* from the neighbouring block). However, containment then quickly drops to 50% when the shower occurs exactly on the limit between two blocks. This map was very useful in the partition of energy between block-sharing showers.

The first and second objectives were also adressed by analysis of the M5 data. For electron-induced showers ($E_e = \{5,\ 10,\ 20,\ 30\ GeV\}$), the pulse-height in a lead-glass block was found to be linearly correlated with the pulse-height observed in the EPIC. However, attempts to extrapolate to low energy ($E \leq 1\ GeV$) and to infer the behaviour of γ showers using the results of the test were not satisfactory. Many 2^{nd} run events contain low-energy electromagnetic shower candidates with no EPIC tubes turned-on (indicating no γ interaction or *re-absorbtion* of $e^{\pm}$ in the lead converter) and this behaviour had to be understood before these shower candidates could be included in any further kinematic reconstruction. To extrapolate to lower

energies, the geometry of the converter was fed to a properly modified version of the EGS simulator [144] . Runs were made [145] for several initial energies of the incident γ in the range $E_\gamma = 0.5 \rightarrow 35\ GeV$. In particular, it was shown that the probability that no charged particles from conversions make it out of the lead sheet varies from 9.7% at $E_\gamma = 6\ GeV$ up to 13.6% at $E_\gamma = 0.5\ GeV$. Tracking closely this behaviour was the % of showers with only 1 charged particle emerging from the lead indicating that the other from the pair was absorbed. This turned out to be 0% at $E_\gamma \geq 6\ GeV$ and increased up to $\sim 3\%$ at $E_\gamma = 0.5\ GeV$.

The energy loss in the EPIC planes was studied as a function of the number of outgoing (emerging from lead sheet) charged particles and it was determined that:

$$\langle E_{loss\ in\ EPIC\ cell} \rangle_{E_\gamma = 0.5 \rightarrow 2\ GeV} = 19.5 \pm 2.8\ MeV/M.I.$$

The response of the PbG/EPIC system (in GeV) was therefore:

$$E_\gamma = 0.020\ \langle P.H.^{EPIC} \rangle_{3\ planes}$$

where $P.H.^{EPIC}$ is the pulse-height in a plane in terms of $M.I.$. Overall, the energy-resolution of the PbG/EPIC system was:

$$\frac{\sigma_E^{PBG+EPIC}}{E} = \frac{0.17}{\sqrt{E}}$$

Thus, the electromagnetic shower pattern recognition equipment introduced for the 2^{nd} run resulted in only a small (2%) worsening of the energy resolution.

Another question of great interest regarding the PbG/EPIC system was the situation when some hadron is incident on a lead-glass block and more than 1 $M.I.$ pulse is recorded. The question being asked is: how likely was it for such a hadron to interact in the block, given the observed pulse-height? The answer was derived, again, from data taken at the M5 multiparticle test beam. Experimentally, [146] it is observed that the interacting π^- spectrum falls like $\exp(-.0095\ Q)$ where $Q > 1\ M.I.$ is the observed pulse-height in the block, measured in terms of $M.I.$ equivalents. In addition, there is a minimum-ionizing peak which accounts for 1/2 of the area under the spectrum. Thus, the probability that some hadron with energy E_{had} interacts in a lead-glass block and deposits an amount of energy larger or equal to the one observed in the block (E_{obs}) is given by [147] :

$$P_{Hadron\ exceeds\ observed\ energy} \sim \frac{1}{2} \frac{\int_{Q_0}^{\infty} \exp(-.0095\ Q)\ dQ}{\int_0^{\infty} \exp(-.0095\ Q)\ dQ}$$

$$= \frac{1}{2}\ \exp(-.0095\ Q_0)$$

$$where\ Q_0 = 480\ E_{obs}/E_{had}$$

This probability was routinely computed for tracks traversing lead-glass blocks and the decision to interpret the energy deposited in a block as coming from the sum of $M.I.$-deposition with some γ-induced shower or from only hadronic interaction was based upon it.

Whether the PBG/EPIC system could reconstruct showers from the decay $\pi^0 \rightarrow \gamma\gamma$ was the object of an extensive post-second run analysis [148] . The $\gamma\gamma$-invariant mass was plotted with several cuts imposed on the data. No charged particles were allowed to go through blocks containing candidate showers. The ratio

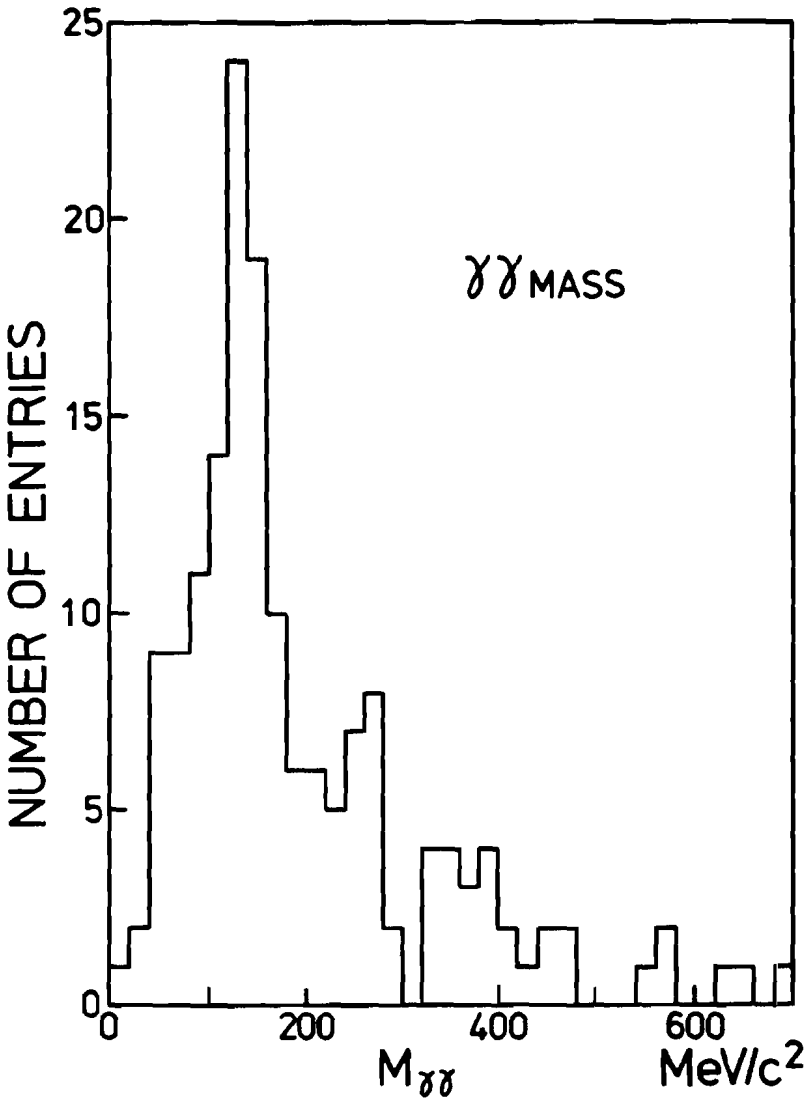

Figure # 28
Gamma-gamma invariant mass distribution from two-shower combinations in the lead-glass EPIC system. Each mass bin is 20 MeV/c^2-wide. The distribution is sharply peaked at the mass of the neutral pion (135 MeV/c^2). This is attributed to the process $\pi^0 \rightarrow \gamma\,\gamma$.

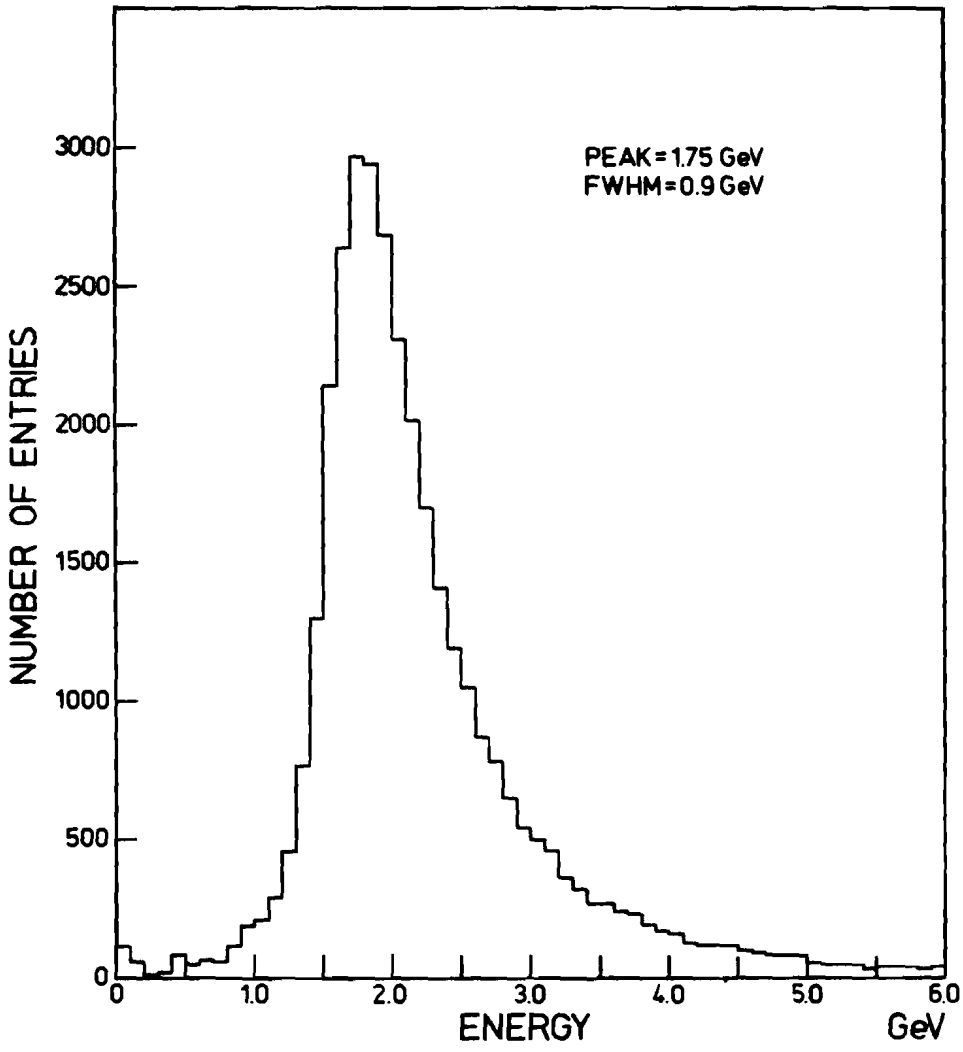

Figure # 30
Hadron calorimeter energy response to minimum-ionizing muons. Each energy bin is 100 *MeV*-wide. The peak occurs at 1.75 *GeV* with a FWHM of 0.9 *GeV* .

$E_{\gamma_1}/E_{\gamma_2}$ was required to be ≥ 0.2 (the most probable value is 1), the individual energies of the showers were required to be $\geq 600\ MeV$. Good geometrical separation of the two showers in the array was also required. Figure # 28 presents the resulting distribution of $\gamma\gamma$-invariant masses which shows a clear signal at $m_{\gamma\gamma} \sim m_{\pi^0} = 135\ MeV$.

Another question was the ability of the PbG/EPIC system at identifying showering electrons and positrons. Studies of the 2^{nd} run ν-triggered data have shown that for single e's hitting lead-glass blocks ($1\ GeV \leq P_{incident} \leq 3\ GeV$), the quantity E/P has a peak at 1 with $\sigma_{E/P} \sim 20\%$. (Figure # 29) The minimum-ionizing peak occurs at $E/P = .2$ and is down to 1/2 its maximum at $E/P = .3$. Therefore, electron/positron hypotheses were not retained as being compatible with otherwise un-identified charged particles traversing in the PbG/EPIC system unless $E/P \geq .3$.

4.5) **The hadron calorimeter calibration**

The hadron calorimeter's spatial resolution was established using neutrino triggered data. Fitted tracks in the drift chambers with $p \geq 2\ GeV/c$ seen to be pointing unambiguously to hadronic showers recorded in the hadron calorimeter EPIC planes were used to determine, in the X-direction, $\sigma_A^{HAD} = 7.1\ cm$, $\sigma_B^{HAD} = 10.1\ cm$ and $\sigma_C^{HAD} = 10.4\ cm$. For each showering charged hadron used in the calibration, a strict requirement of 1 hit per EPIC plane was imposed in order to insure that the device contained no other showering charged or neutral hadron.

The hadron calorimeter's response to minimum-ionizing particles is shown on Figure # 30 . While the raw response of the array is given in terms of *M.I.* equivalent, this is transformed to kinetic energy through the measured *design* [149] calibration function. (see below) Figure # 31 presents the expected number of *M.I.* equivalents for showering hadrons after traversing several 10.16 *cm* steel intervals. The rough E531 equipment location is also shown. The data is from *Ref.* 149 ; see also Appendix 12.7 and Appendix 12.8 .

The kinetic energy response and resolution of the hadron calorimeter is:

$$E_{cal} = \frac{N}{2a}(1 + \sqrt{1 + 4ab/N})$$

$$\frac{\sigma_E}{E} = \frac{1.1}{\sqrt{E}}$$

where N = ***Pulse height*** measured in # of minimum-ionizing equivalents and $a = 5.428\ GeV^{-1}$, $b = 0.721\ GeV$. More on this in Section 4.6 . Pattern recognition aspects are treated in Section 5.2.4 .

4.6) **The muon counters calibration**

The muon-front and muon-back counters were calibrated (M.I. and position response) using beam muons recorded during the 2^{nd} run of E531. Then, the basic muon tag $\mu_{tag} = MF \cdot MB$ was properly examined using muons from ν-triggered data. These muons were selected under the requirements that incident particles have $p \geq 4\ GeV/c$, that the proper TOF II paddle be "on", and that drift-chamber tracks match μ-TDC predictions with $\chi^2 \leq 6.5$ for MF and ≤ 7 for MB . This is actually done in several stages. Initially, best track-paddle associations are made independently in the MF and MB hodoscopes. The only requirement is that the track be *close enough* in space to the predicted paddle, that is, within $2.5\,\sigma$ of the

expected multiple Coulomb scattering:

$$\Delta Y|_{MF}^{2.5\sigma} = \frac{33.27\ cm}{p} \qquad \Delta X|_{MB}^{2.5\sigma} = \frac{76.20\ cm}{p}$$

in which p is in GeV/c . The set of all MF & MB hit (i.e. registered "paddle on") combinations are examined and the total number of them is reduced just by requiring the proper TOF II paddle to fire. Using the individual muon paddle time resolutions σ_t^{MF} and σ_t^{MB} obtained from the μ-calibration, a further cut:

$$\left|(t_{TOFII} + \frac{1}{c}\, d^{flight}_{MF\ or\ MB-TOF\ II}) - t_{MF\ or\ MB}\right| \leq 2.5\ \sigma_t^{MF\ or\ MB}$$

is imposed on the predicted time difference between TOF II and MF and also between TOF II and MB using the known geometry of the arrays. Finally, MF X-predictions (from TDC's & the speed of light in paddles) are required to match the drift chambers predictions with $\chi^2 \leq 6.5$ while similar MB Y-predictions are required to have $\chi^2 \leq 7$.

Under conditions described above, using ν-triggered data, the muon-front array turned out to be 93% efficient in the second run (92% in the first run). Similarly, the muon-back array turned out to be 97% efficient (98% in the first run).

5.0) CHARM CANDIDATES ANALYSIS: TECHNIQUES & ALGORITHMS

This section describes the manner in which the E531 equipment was used for the analysis of charm decay events. In the first half, the very important subject of scanning techniques in the emulsion part of the detector is presented. Several key aspects of pattern recognition in the electronic part of the detector will be discussed in the second half. In some sense however, this is a bit the wrong way around: restricted pattern recognition in the drift chambers led to event and charm decay searches in the emulsion. This was then followed by much more extensive pattern recognition in the drift chambers.

5.1) The Emulsion Target

5.1.1) Scanning methods and efficiencies

Emulsion scanning techniques were used to achieve two basic aims: find ν interaction vertices and find the subsequent decay(s) of any charmed particle(s). It is necessary to include information on the various scanning criteria used both in the 1^{st} and 2^{nd} run of the experiment because the lifetime computations will be based on the combination of the two datasets.

A major part of the emulsion work originated from Japan. The Japanese Groups involved in this work were from the Aichi University of Education, the Faculty of Education of Gifu University, the College of Liberal Arts of Kobe University, the Department of Physics of Kobe University, the Graduate School of Science and Technology of Kobe University, the Department of Physics of Nagoya University, the Physics Department of Okayama University, the Physics Department of Osaka City University, the Science Education Institute of Osaka Prefecture, the Department of Physics of Toho University and the Faculty of Education of Yokohama National University. A significant amount of emulsion work was also performed by the Canadian emulsion group at the University of Ottawa. Finally, emulsion work was also performed by the following groups from Korea: the Department of Physics of the Gyeongsang National University and the Department of Physics of Korea University.

In general, emulsion work is difficult and tedious. Features in the emulsion must be examined with the help of optical microscopes. A non-negligible amount of overhead work must be performed before any reliable measurements can be made in a particular plate or pellicle of emulsion. Even with some degree of automation, emulsion scanning still required the combined effort of a large number of dedicated people.

Some of the features seen in the emulsion and relevant to the experiment include the following: γ-conversions, nuclear interactions, Vee's, single and multi-prong decays. Gamma-conversions originate at a point (the conversion point) and are initially characterized by a single, twice-minimum ionizing track which only opens-up into the electron-positron pair some distance away from the conversion vertex. Nuclear interactions are recognized by their multitude of slow (heavily ionizing) debris tracks all pointing to the interaction vertex. Vee's are pairs of minimum-ionizing tracks that originate from a single location in space. Even-prong events, like vee's, are found when several minimum-ionizing tracks are seen to originate from a single location: the possible decay vertex of a neutral parent. Odd-prong events are just tracks that transform into many minimum-ionizing tracks at a single point: the possible decay vertex of a charged parent. A single-prong event, a kink, is some track which undergoes a significant deflection. This can, in particular, be caused by the decay of a charged parent involving at least one neutral.

Many scanning techniques discussed in this section rely on performing a transfer of track parameters from the spectrometer to the emulsion volume. The transfer was usually made by use of the *changeable sheet* of emulsion where fast tracks could be located in a low muon background (10 *to* 20 μ/mm^2 compared to 200 *to* 250 μ/mm^2 in a module) due to the short exposure times of the sheet. Such transfers from the spectrometer to the changeable sheet and then to the emulsion module were achieved quite reliably. The original alignment of the sheet with respect to a vertical module could be recovered by making use of the X-ray marks caused by the four small sources which were part of the module's 4-post mounting assembly. For horizontal modules, the reference X-ray marks were also used together with two other special X-ray marks located on the edge of the pellicles. These two special line markings (at 45^0 to each other) were originally done with an X-ray generator at Argonne National Laboratory prior to the run. The alignment of the sheet with respect to the spectrometer was recovered by finding a few tracks (from the spectrometer) in the sheet. No ambiguities remained because apart from X and Y predictions, the spectrometer provided θ and ϕ , the polar and azimuthal angles at the sheet location. For each track used in the alignment operation, these predictions were checked in the changeable sheet using the measured angles in the sheet. Because of shrinkage (which occured in the sheet development process) along the Z-direction of both downstream and upstream surfaces of the sheet, more weight was put on the un-affected azimuthal angle ϕ than the polar angle θ .

5.1.1.1) **Charm production vertex finding**

In the 1^{st} run of E531 [150] , ν-interaction vertices were found using two methods: track follow-back (FB) and volume scanning (VS). Follow-back is a method in which typically 1 or 2 fast tracks (μ or fast hadron) from spectrometer predictions are *transferred* into *vertical* emulsion using the changeable sheet and followed all the way to a ν-interaction vertex. In the first run, the FB efficiency $\left(\frac{found}{predicted}\right)$ was 88% while the average time to handle a prediction was roughly one hour. On the other hand, VS for ν-vertex location in the 1^{st} run consisted in scanning a volume ($4 \times 4 \times 20$ mm^3) of *horizontal* emulsion centered on the ν-vertex prediction. This method, which does not rely on any spectrometer information, turned out to be only 55% efficient and required, on average, four hours per prediction. Thus, in the 1^{st} run, the overall † ν-vertex finding efficiency was 72% .

In the 2^{nd} run of E531, the much more efficient FB technique was used by all scanning groups to find the ν-interaction vertices in *both* types of emulsion. The technique remained unchanged and conditions were much improved by a lower muon background. Although the FB efficiency varied from group to group over a range of 20% , the overall ν-vertex finding efficiency was 82% , better than the first run's.

5.1.1.2) **Charm decay vertex finding**

The scanning methods used to find charm decay vertices once the production vertex is found will now be described.

† This excludes the Ottawa group with an efficiency of 82% , where in the 1^{st} run, for the main part, FB was done.

5.1.1.2.1) **Methods and criteria**

5.1.1.2.1.1) **First run**

In the first half of the 1^{st} run of E531, decay vertices were found mostly through VS in the case of neutral parents and mostly through track follow-down (FD) in the case of charged parents.

Volume scanning for decay vertices in the first run's horizontal emulsion was done in a cylinder with radius of 200 μm for a total length of 1 mm downstream of the ν-vertex. In the first run's vertical emulsion, it was done for a volume of $\pm 300\ \mu m \times \pm 300\ \mu m \times 1\ mm$.

Track follow-down is a technique by which each charged track satisfying certain critera is *followed* downstream of the ν-interaction vertex through the emulsion while visually checking for any evidence of decay or interaction. It relies on no spectrometer information. In the first run's horizontal emulsion, all tracks with $200\ mrad \leq |\theta_{x\ or\ y}| \leq 350\ mrad$ were followed-down at least 3 mm from the primary vertex or until the track exited the emulsion stack. Tracks with $|\theta_{x\ and\ y}| \leq 200\ mrad$ were followed-down at least 6 mm or until the emulsion edge was reached. In the first run's vertical emulsion, tracks with $\theta \leq 200\ mrad$ were followed down 7.3 mm (exit of 10^{th} plate), tracks with $200\ mrad < \theta \leq 400\ mrad$ were followed down 3.65 mm (exit of 5^{th} plate) while tracks with $\theta > 400\ mrad$ were followed down 0.73 mm (exit of 1^{st} plate) or until the emulsion edge was reached.

However, yet another technique known as track scan-back (SB) showed much more efficient at finding charm decays, especially neutral decays. This technique, used for the second half of the 1^{st} run (and throughout the 2^{nd} run) is very-much like FB in that it makes use of spectrometer information. Not all tracks were scanned-back though; in the first run, only those with $p > 700\ MeV/c$ and extrapolating to within 2 mm of the primary vertex while not being observed there (not observed is defined as a mismatch of $\Delta\theta_{x\ or\ y} \geq 15\ mrad$) were scanned-back. In the first run, 30% of neutral and 8% of charged decays would have been missed if it hadn't been for use of SB.

5.1.1.2.1.2) **Second run**

In the second run of E531, all tracks with $p \geq 400\ MeV/c$ and with $\theta \leq 300\ mrad$ were scanned-back. Depending on the group, volume scanning was also performed in a 200 μm-radius cylinder 1 mm downstream of the ν-interaction vertex or in a cone of 100 μm-base radius and 300 μm long fanning-out downstream of the ν-interaction vertex. Follow-down was also performed on all charged tracks from the ν-interaction vertex for 6 mm if $\theta < 200\ mrad$ or up to 3 mm at larger angles. In the second run, charged decay events were found mostly through SB and some using FD. Note that it is possible to find a charged decay with VS too. Neutral decay events were also found mostly through SB and some using VS. [151]

5.1.1.2.2) **Track follow-down efficiency**

As explained above, charged secondary particles are followed-down from the production vertex for a certain distance depending on their polar emission angle. The FD efficiency for finding multi-prong and kink

events is therefore defined by:

$$\eta_{FD} = \eta_{det} \cdot \eta_{geo} \quad for\ both\ multi-prongs\ and\ kinks$$

$$\eta_{det}^{multi-p} = 1$$

$$\eta_{det}^{kinks} < 1$$

$$\eta_{geo} = \left(\frac{\#\ of\ tracks\ followed\ all\ the\ way\ down\ to\ a\ certain\ range\ without\ decay}{total\ \#\ of\ tracks\ coming\ out\ from\ \nu - interation} \right)$$

The FD efficiency splits into two parts: detection efficiencies and geometrical cuts. In the expression for η_{geo}, it is assumed that the charm decay lengths are *longer* than the range followed. If the charm decay lengths were shorter than the followed range, neglecting any momentum emission-angle relations, more charm would be found and the above formula would give a lower estimate to the FD efficiency. The detection efficiency for multi-prong events is essentially unity: $\eta_{det}^{multi-p} = 100\%$. In the first run of E531, as well as for its second run, the multi-prong follow-down efficiency was:

$$\eta_{FD}^{multi-p} = \left\{ \begin{array}{lll} 95 \pm 5\% & 0 < \theta \leq .2 & l_{max} = 6\ mm \\ 95 \pm 5\% & .2 < \theta \leq .4 & l_{max} = 3\ mm \end{array} \right\}$$

While it is quite difficult for an alert scanner to miss a single track developing into a multi-prong vertex, it is not impossible to miss a track undergoing a single small deflection: a kink. Therefore: $\eta_{det}^{kinks} \neq 1$ but it can be very high (Nagoya). In fact, in horizontal emulsion, kink candidates with long enough decay lengths (above $20\mu m$ in 1^{st} run) were found by looking for changes in the slopes from straight line fits to tracks at several locations along their lengths resulting in a high detection efficiency independent of the kink angle, above threshold. Below threshold however, another method was used by which the fitted straight line is projected to the ν-vertex location and the distance of closest approach measured. In this range, the kink detection efficiency becomes a function of the product of the decay length and kink angle. In vertical emulsion, the kink finding efficiency is more complicated [152] .

5.1.1.2.3) **Volume scanning efficiency**

The efficiency for VS can be estimated using the expected number of $\gamma \rightarrow e^+ e^-$ conversions as a function of the distance downstream of the interaction vertex:

$$\eta_{VS} = \frac{\#\ found\ e^+ e^-\ pairs\ per\ event}{\#\ expected\ e^+ e^-\ pairs\ per\ event}$$

in which the expected number of pairs was estimated using $2\pi^0$'s per neutrino event [153] . This is an estimate because γ-conversions do not look like charm decays in the emulsion. As γ has zero mass, the initial opening angle of the pair is also zero. The electron and the positron stay over each other for distances larger than the thickness of the field of view of a microscope, ~ 2 *or* $3\ \mu m$, but eventually separate. Charm, on the other hand, opens-up much quicker. Also, tracks from conversions are initially twice-minimum ionizing while those from charm events are minimum ionizing. Some $e^+ e^-$-pairs may not be associated with events hence only those with tracks observed in the spectrometer or pointing to the ν-interaction vertex are counted. The

2^{nd} Run volume scanning efficiencies are as follows:

Group	η_{VS} [%]
Nagoya	34 ± 5
Osaka	17 ± 10
Kobe	12 ± 8
Ottawa (Vertical)	20 ± 9
Ottawa (Horizontal)	0

5.1.1.2.4) **Track scan-back efficiency**

Scan-back (SB) makes the most out of drift-chamber information unlike follow-down (FD) and volume scanning (VS) which have nothing to do with it. In the first half of the first run, the scan-back efficiency for n-prong events η^n_{SB} was given by:

$$\eta^n_{SB} = \frac{1}{N^{(n)}} \left\{ \sum_{i=0}^{n} N_i^{(n)} \left[1 - (1 - \eta_{EM})^i \right] \right\}$$

$$N^{(n)} = \sum_{i=0}^{n} N_i^{(n)}$$

$$\eta_{EM} = \eta_{CS} \cdot \eta_{FB}$$

where η_{CS} is the efficiency for finding a drift chamber track on the changeable sheet of emulsion, η_{FB} is the efficiency for following back a track from the changeable sheet up into the emulsion all the way to a vertex and $N_i^{(n)}$ is the number of n-prong events with i decay tracks found in the drift chambers. This method utilises $N_0^{(n)}$, the number of n-prong events with no decay track found in the drift chambers which, in the first half of the first run, was wholly obtained using VS. From the first run, for tridents, the average scan-back efficiency was $81 \pm 9\%$.

In the second half of the 1^{st} run and throughout the 2^{nd} run, although VS was performed for all events, data recorded by the different scanning groups did not allow $N_0^{(n)}$ to be measured accurately. However, in the hypothesis that each track is independent of others, the n-prong SB efficiency is given by:

$$\eta^n_{SB} = 1 - (1 - \tilde{\eta}_{SB})^n$$

where $\tilde{\eta}_{SB}$ is the SB efficiency ***per track***. This quantity can be understood as being given by

$$\tilde{\eta}_{SB} = \eta_{SPEC} \cdot \eta_{EM}$$

$$\eta_{SPEC} = \eta_{rec} \cdot \eta_{SC} \cdot \eta_{AC}$$

$$\eta_{EM} = \eta_{CS} \cdot \eta_{FB}$$

in which η_{rec} is the combined efficicency for observation and pattern recognition in the drift chambers, η_{SC} is the scanning cuts, η_{AC} is the acceptance cuts, η_{CS} is the efficiency for finding a drift chamber track on the changeable sheet of emulsion and η_{FB} is that efficiency for following back a track from the changeable sheet up into the emulsion all the way to a vertex. Estimates for η_{SPEC} , $N^{(n)}$ and $N_0^{(n)}$ were obtained by counting the number of n-prong charm decays which had no decay tracks found in the spectrometer, one decay track found in the spectrometer and so on; for n-prong events:

$$
\begin{aligned}
N_0^{(n)} &= N^{(n)}\,(1-\eta_{SPEC})^n \\
N_1^{(n)} &= n\,N^{(n)}\,\eta_{SPEC}\,(1-\eta_{SPEC})^{n-1} \\
&\vdots \\
N_i^{(n)} &= \binom{n}{i}\,N^{(n)}\,\eta_{SPEC}^i\,(1-\eta_{SPEC})^{n-i} \\
&\vdots \\
N_n^{(n)} &= N^{(n)}\,\eta_{SPEC}^n \\
N^{(n)} &= \sum_{i=1}^{n} N_i^{(n)}
\end{aligned}
$$

in which $\binom{n}{i} = n!/i!\,(n-i)!$ is the number of ways i tracks can be "missing" from a n-prong event. Actually, because of statistical fluctuations, each $N_i^{(n)}$ $i = 1,\ldots,n$ has an error of $\sqrt{N_i^{(n)}}$ associated with it. The system of $n+1$ equations can be solved or fitted for the unknowns: η_{SPEC} , $N^{(n)}$ and $N_0^{(n)}$. In the second run, using 41 tridents and one 5-prong, $\eta_{SPEC} = 56.5 \pm .5\%$. For neutrals, using 40 vee's and 15 4-prongs, $\eta_{SPEC} = 77 \pm 6\%$.

The remaining contributions to the SB efficiencies were taken from the Nagoya University (Ng) scanning group (1^{st} run) efficiencies: $\eta_{CS}^{Ng} = .96 \pm .02$ and $\eta_{FB}^{Ng} = .98 \pm .01$. Efficiencies for other groups were obtained by simple scaling according to the number of found $e^+\,e^-$ pairs.

$$
\eta_{EM}^{group} = \eta_{EM}^{Ng}\,\frac{[\#\ of\ found\ e^+\ e^-\ pairs\ per\ event]^{group}}{[\#\ of\ found\ e^+\ e^-\ pairs\ per\ event]^{Ng}}
$$

Finally, total charged and neutral SB efficiencies are obtained from n-prong SB efficiencies through:

$$
\begin{aligned}
\eta_{SB}^{charged} &= \frac{1}{N_{tridents} + N_{5-prongs}}\,\left(N_{tridents}\,\eta_{SB}^3 + N_{5-prongs}\,\eta_{SB}^5\right) \\
\eta_{SB}^{kinks} &= \eta_{SB}^1 \\
\eta_{SB}^{neutrals} &= \frac{1}{N_{Vee's} + N_{4-prongs} + N_{6-prongs}}\,\left(N_{Vee's}\,\eta_{SB}^2 + N_{4-prongs}\,\eta_{SB}^4 + N_{6-prongs}\,\eta_{SB}^6\right)
\end{aligned}
$$

For the second run, the charged and neutral scan-back efficiencies are summarized below:

Group	$\eta_{SB}^{charged}$ [%]	$\eta_{SB}^{neutrals}$ [%]
Nagoya	89 ± 3	92 ± 3
Osaka	78 ± 7	81 ± 7
Kobe	60 ± 8	62 ± 8
Ottawa (vertical)	94 ± 6	97 ± 4
Ottawa (horizontal)	96 ± 8	96 ± 8

5.1.1.2.5) **Combined charm-finding efficiency**

5.1.1.2.5.1) **Combination method**

Since SB FD and VS overlap in some regions, all these methods constitute competing ways to find charm and their efficiencies must be combined. First run charm finding efficiencies (per decay regions or decay length bins) were all combined together irrespective of the scanning group. In the second run however, much more methodical procedures allowed enough reliable $e^+ e^-$-pair data from each scanning group to be gathered so that a set of combined (overall) efficiencies could be produced *per* scanning group. For neutral events, the efficiencies for the two possible charm finding methods (SB and VS) are combined through:

$$\epsilon_{neutrals} = \eta_{SB}^{neutrals} + \eta_{VS} \, (1 - \eta_{SB}^{neutrals})$$

The three possible charm finding methods for charged events, (SB, FD and VS), are combined through:

$$\epsilon_{charged} = \eta_{SB}^{charged} + \eta_{FD}^{multi-p} \, (1 - \eta_{SB}^{charged}) + \eta_{VS} \, \left[1 - \eta_{SB}^{charged} - \eta_{FD}^{multi-p} \, (1 - \eta_{SB}^{charged})\right]$$

The combined charm finding efficiencies are very high; for example, at Nagoya University, between 30 μm and 1000 μm , $\epsilon_{neutrals}^{Ng} = 95 \pm 2$ % and $\epsilon_{charged}^{Ng} = 100 \pm .4$ % . All such combined efficiencies, for each scanning group in each of the decay regions, are listed in Appendix 12.9 .

5.1.1.2.5.2) **Uniformity**

In the 2^{nd} run, most events were found through SB and that technique is very much like FB. An excellent appraisal of the uniformity is depicted on Figure # 32a . This shows FB to be on average 82% efficient *flat* right through the fiducial volume of the 2^{nd} run emulsion and most of the apparent 18% inefficiency is due to interactions occuring outside, but near to, the fiducial volume of the emulsion. [154] A cross-check is provided by the efficiency at finding $e^+ e^-$ pairs using SB which is presented on Figure # 32b . This quantity is independent of the conversion distance and thus *flat* right through the fiducial volume of the emulsion.

5.1.2) **Particle identification in the emulsion**

It is possible to extract information on dE/dx (thus speed) of a particle by counting the number of developed grains per unit length along its trajectory. This is done with respect to some nearby minimum-ionizing track in order to minimize the systematic effects (emulsion fading and grain density fluctuations).

The limitations on this method of measuring the ionization relative to minimum ionizing (I/I_0) are, in part, statistical and the size of the error on the grain count goes down as $1/\sqrt{N}$ where N is the total number of grains counted. Also, if the particle is slow enough ($p \leq 700\ MeV/c$), multiple Coulomb scattering is measureable. Estimation of the Gaussian width (θ_0) of the distribution of such deflections yields an estimate of $1/p\beta$ through [138] :

$$\theta_0 = \frac{14.1\ MeV/c}{p\beta}\, Z_{inc}\, \sqrt{L/L_R}\, \left[1 + \frac{1}{9}\log_{10}(L/L_R)\right] \qquad (radians)$$

in which Z_{inc} is the electric charge of the particle, L is the distance travelled through the emulsion after which the measurement of θ_0 is made and L_R is the radiation length of the emulsion: 29.4 mm in horizontal emulsion and 32.0 mm in vertical emulsion. This type of measurement is performed relative to some nearby fast muon or hadron in order to avoid systematic errors due to local warping of the emulsion.

From elementary electromagnetic theory, one can compute the relations between I/I_0 and $p\beta$ in the emulsion for several particle types. Protons can be distinguished from kaons up to $p = 1.5\ GeV/c$ and kaons from pions up to $p = 800\ MeV/c$. If a track is not reconstructed in the spectrometer because it is outside acceptance (emitted at large angles or even backwards in the laboratory!) or it is not recognized among the hits in the drift chambers, or the particle does not make it out of the emulsion volume (hits a post or some other support structure), particle identification can sometimes still be made by combining measurements of I/I_0 and $1/p\beta$, if available. The χ^2 associated with these 2 independent measurements is:

$$\chi^2_{e,\mu,\pi,K,p} = \frac{(I/I_0|_{e,\mu,\pi,K,p} - I/I_0|_{meas})^2}{\sigma^2_{I/I_0}} + \frac{(p\beta|_{e,\mu,\pi,K,p} - p\beta|_{[meas]})^2}{\sigma^2_{p\beta}} \qquad \#d.f. = 2$$

and the decision on the particle i.d. is made on the basis of the associated confidence level. In certain circumstances, if $1/p\beta$ cannot be measured on a track but that track happens to be observed in the spectrometer, one can substitute the computed value of $1/p\beta$ obtained from the spectrometer using an assumed mass.

In other cases, charged particles that are slow enough to *stop* can be identified through their range in the emulsion provided measurements of the energy loss is also made. Particles like π^- and μ^- can sometimes be observed to end their life through orbital capture by some atomic nucleus where they eventually decay.

5.2) **The spectrometer**

5.2.1) **Pattern recognition in the drift chambers I: event-finding**

All data from recorded ν-triggers were analyzed by two independent off-line ν-event finding computer programmes. The purpose of these programmes was to generate the minimum amount of information necessary to hand over to the scanners so that they could find the events responsible for the neutrino triggers (mainly through FB). These programmes rely only on pre-set strategies in the decision making processes involved in pattern recognition and are different from the charm candidate analysis programmes which do the detail charm analysis to be discussed shortly.

Ohio State University (OSU) produced 6361 ν-predictions which were sent to scanner groups in Japan and Canada. Cuts on the ν-event finding analysis required at least one up-to-down track being reconstructed among the hits seen in the drift chambers, at least 2 tracks total, at least 1 vertex without any cuts on the

errors but the location of which had to be within the XY cross-sectional area of the emulsion yet *not* imposing any cut on the Z co-ordinate. The OSU programme would find, on average, 3.49 up-to-down tracks per ν-trigger and that programme's efficiency $\left(\frac{\#\ found}{\#\ predicted}\right)$ was 61% .

The same dataset of ν-triggers was fed to the University of Toronto (UT) ν-event finding programme which proved to be somewhat less efficient: 48% . The UT algorithm included an initial step in which cuts were imposed on the distributions of hits in the three views of the upstream drift chambers and it has been conjectured that this is partly responsible for the difference in efficiencies. The UT programme found, on average, only 2.65 up-to-down tracks per ν-trigger which is consistent with a slight inefficiency at making down-to-up connections between upstream and downstream track segments. The set of common $(OSU \cdot UT)$ predictions was extensively studied. In particular, the agreement in the fitted angles of UT's down-to-up and OSU's up-to-down tracks was very good: $\sigma\left(\Delta\frac{dx}{dz}\right) = .0008$ and $\sigma\left(\Delta\frac{dy}{dz}\right) = .0004$. Differences in the other parameters could be traced back to pattern recognition. In general, both up-to-down and up-only tracks from the two programmes turned out to be very similar.

The distribution of the predicted ν-interactions Z-locations is displayed on Figure # 33 . As can be seen, most predictions were inside the emulsion volume while some came from support structures and other equipment. Some relative inefficiency at reconstructing ν-events is noticeable in the first 20 mm of the emulsion volume with respect to the downstream end. This is not too surprising, in the subsequent kinematical analysis, charm candidates from the volume upstream of $z = 20$ mm were very difficult to fit and eventually had to be removed from the sample.

5.2.2) **Pattern recognition in the drift chambers II: charm-candidate analysis**

The found events, also called charm-candidates, were reconstructed in details. The problem of finding all tracks among the hits in the drift chambers in order to allow full kinematical event reconstruction is much more complex and time consuming than that of producing ν-predictions. At OSU, an essentially batch-oriented algorithm was used. Yet, it was often driven from an appropriate set of parameters decided upon by physicists and complete fits were arrived at in several runs of the track fitter. At McGill University (McG) and at the University of Toronto (UT), a different approach was adopted. Early work on pattern recognition done at UT on ν-produced events had showed that erroneous decision making amidst the multitude of possible hit combinations was the main source of many track fits initially starting out right but eventually going astray. It was estimated that a solution to the problem of finding *all* the possible tracks going through all the hits would be best solved using a hybrid technique combining machine-based computing power with physicist-based decision-making power through use of computer interactive graphics software. Development of this software was far from being a linear process however; the track-finder turned out to be ever evolving over many years (over 2 computers) and the development of many efficient improvements brought to it were heavily dependent on the ability to visually check (on ν-data) the effect of the modifications. From the beginning of the analysis to the end, the compiled code more than tripled in storage size.

The final software used at McG and UT comprized the graphics-assisted semi-automatic mode described above as well as a more conventional fully automatic mode (batch mode).

In the automatic mode, tracks would be independently found in the upstream drift chambers and in the

downstream drift chambers. In the upstream chambers, hits would first be considered in any of the three views: V U or X. In a given view, 5 chambers are available and essentially provide five lists of hits which are narrowly spaced in the most upstream chamber and moderately spaced in the fifth chamber. A hit would be sequentially selected in one chamber and then another. A straight line connecting these two hits would be used to predict the expected location of a third hit on a third chamber. If some hit were found on the third chamber *close enough* to the prediction, a curved line fit in the magnet's fringe field would be made to the three hits. Parameters of this fit were used to predict locations in the remaining other two chambers and a further fit was done including any new hits falling in the predicted road. There are 10 permutations (20 in all) which make the single-view searches in the forward direction and they are:

0 gap spanned	*1 gap spanned*	*2 gaps spanned*
$1,2,\bar{3} : \underline{4},\underline{5}$	$1,3,\bar{4} : \underline{5},\underline{2}$	$1,4,\bar{5} : \underline{2},\underline{3}$
$2,3,\bar{4} : \underline{1},\underline{5}$	$2,4,\bar{5} : \underline{1},\underline{3}$	$1,2,\bar{5} : \underline{3},\underline{4}$
$3,4,\bar{5} : \underline{1},\underline{2}$	$1,2,\bar{4} : \underline{3},\underline{5}$	$1,3,\bar{5} : \underline{2},\underline{4}$
	$2,3,\bar{5} : \underline{1},\underline{4}$	

In this list, each digit represents the drift chamber offset in a given view. For example, in the V-view, chambers 1 ,4 ,7 ,10 and 13 have offsets 1 ,2 ,3 ,4 and 5 . The over-bar means the hit in that chamber is looked for (discriminated against) using its offset from a straight line fit to the two preceding hits while the under-bar indicates hits in these chambers are selected if they are picked-up using the curved line fit to the preceeding three hits. Initially, only a few of the permutations were included but it turned out that more tracks could be found using all of them. Note that a hit is actually the result of a drift time measurement to some drift chamber sense wire and thus all hits come in pairs but each hit is treated independently in the pattern recognition. Half cell shifts of drift chambers in a given (clean) view insures images cannot be lined up to make tracks...

Automatic mode track-fitting then proceeds to attempt to make tracks out of the three sets of single upstream view segments. This is done by running sequentially over the segments in one view and another view. A road ± 1.27 *cm*-wide is opened in the third view using the two selected views and hits are searched for. If enough hits are found ($N_{hits} \geq 10$) in the upstream chambers, the set of data is fitted with 5 parameters: X_0 , Y_0 , $dx/dz|_0$, $dy/dz|_0$ and $1/p$ using the magnetic field table (the subscript $|_0$ means "at the origin of the co-ordinate system"). The permutations used were $1,2;\underline{3}$, $2,3;\underline{1}$ and $3,1;\underline{2}$. A set of hits was accepted as forming a good track if the fit resulted in $\chi^2/\nu \leq 1.5$ or $1.5 < \chi^2/\nu \leq 2.5$ and the worst deviation from the fit was less than $.030 \times 25.4 = .762$ *mm* . Otherwise, the set of hits was attempted to be improved upon. This was done by removing the offending hit and refitting the track again. Although there are only a maximum of 15 upstream hits to use in a track, a 16^{th} point was always tried in an additional fit attempt. This point was initially the rough vertex-position which could iteratively be improved upon using good tracks. So up-only (and also down-to-up) tracks came in two versions: vertex constrained (a misnomer) and vertex un-constrained.

The downstream tracks were found in a similar manner as for the upstream tracks. A minimum of 5

hits and $\chi^2/\nu \leq 1.5$ were required for a fit to be accepted. Cases with $1.5 < \chi^2/\nu \leq 10$ were fitted again after worst-hit deletion if they still had more than the 5 hits required.

The final step in automatic mode track finding consisted of *joining* down tracks with up tracks forming down-to-up tracks. Again, more than one scheme was studied to achieve this task. It was attempted to use stand-alone track finding in the CPI to corroborate possible Y-matches between up and down segments at the mid-magnet location. But without operator intervention, this only made the process less efficient. Thus up and down tracks were only required to have reasonable Y-matches (little bend in Y-view) in the center of the magnet for the combination to be allowed to proceed on any further.

Those up-down combinations which did pass the (very loose) cut were then fed to certainly the most delicate part of the whole track-finding algorithm: the hit-replacement routines. In some sense, this part of the algorithm performed more of a patch-up job to the preceeding sections of the programme than anything else. It attempted to alleviate the consequences of bad decisions made at earlier stages. A candidate set of hits to a down-to-up track consists of the sum of all the hits from its up and down segments. Apart from worst-hit replacement, the software attempted to fill-in any gaps that might have been opened. Thus, in its initial conception, the programme allowed hit-configurations to recur in cycles of varying period. This problem was identified and studied so that corrections to the algorithm could be implemented. The correction involved providing a buffer of 100 hit-configurations from which the best non-recurring one could be selected. Prevention of configuration recurrence was assured by keeping track of the frequency of all hit flips. Moreover, individual chamber resolutions were used in the hit-substitution decision making process.

Finally, only down-to-up track fits involving at least a total of 16 hits (from a maximum of 24) with a minimum of 4 downstream hits, were kept. In addition, in those fits, no single view was allowed to have less than 2 hits except for the downstream D and E views for which these 2 hits were allowed to be shared among the four D+E chambers. Best tracks with $\chi^2/\nu \leq 1.5$ or with $1.5 < \chi^2/\nu < 3$ and worst deviation smaller than $.020 \times 25.4 = .508$ *mm* were retained immediately. Others were relinquished again (provided they still had enough hits) to the hit-replacement routines.

For both up-only and down-only track finding, hit (but not image) entries from the hit buffer were flagged as used if a track finally passed all the cuts. Such hits could not be re-used. This was however not the case for up-to-down tracks where any weak up-down connection in automatic mode at some early stage could have jeopardized making a better one later on if hits had been flagged as used. Automatic mode pattern recognition often provided more than one down-to-up track fit to only slightly different sets of hits. Tracks were thus made to undergo a compression stage to reduce their total number. This was typically done as the first step of the follow-up semi-automatic mode session of the pattern recognition programme. Essentially, it involved keeping all candidates as "different tracks" if they differed on at least a certain number of hits: usually chosen to be 5 , the number of hits in a fully populated upstream view.

In semi-automatic mode track-finding, all views were visually scanned at various magnifications. * Any incomplete pattern recognition was easy to spot. Hit buffers could be set up in any views through interactive

* This is a non-trivial point; such an ability often proved to be the deciding factor between different track interpretations produced by the OSU and McG programmes.

software and delivered to the routines described above. Down-to-up connections using new tracks could be requested. These abilities proved to be very valuable tools to look for specific tracks in the spectrometer. Of course, semi-automatic mode tracks still had to pass exactly the same set of cuts as automatic mode tracks.

When all pattern recognition was found to be complete, matches between the drift chamber tracks and the emulsion-measured tracks were attempted (see Section 5.2.6) . This was done by grading the difference in slopes at the exit of the emulsion volume (if available) between DCH and EMU tracks. If exit angles were not measured in the emulsion, allowances were made for multiple Coulomb scattering and matches attempted at the production and decay vertices. In this way, the best *overall* set of matches could be arrived at. If some emulsion track (preferably with measured EMU exit angles) could not be found in the set of DCH tracks, a projection mode allowed these to be searched for within a wide range of $p \cdot \frac{dx}{dz} \cdot \frac{dy}{dz}$ by opening a road through the drift chambers and selecting proper hits.

While a typical automatic mode charm event candidate analysis required a single batch run of roughly 12 VAX-785 CPU hours (and sometimes over 24), more than one semi-automatic mode session were needed per event and each of these could last several days.

In the 2^{nd} run, all pattern recognition on all charm candidates was done independently at OSU and McG for charged events and OSU and UT for neutral events. Interpretations were all confronted and apparent differences resolved through periodic meetings. All charged charm events were reduced to a single common OSU-McG set of fits.

5.2.3) **Pattern recognition III: The PbG-EPIC system**

Pattern recognition was also performed in the three EPIC planes upstream of the lead-glass array in order to ultimately associate energy depositions in the blocks with electromagnetic showers with increased precision. In automatic mode and semi-automatic mode, showers would be found among the hits remaining in the EPIC tubes once all single minimum-ionizing responses due to reconstructed tracks were removed from the hit buffer. Minimum-ionizing equivalents were also removed from the PbG blocks involved. Some charged tracks (hadrons, electrons) could be accompanied with larger than minimum-ionizing energy depositions ($E \geq p/2$) and, for such cases, the hits and associated energy were not removed from buffers. Resulting showers were tagged as possibly being associated with such tracks.

Automatic mode pattern recognition proceeded to find all the possible clusters independently in all three EPIC views: Y, U and V. Within a view, this was done in order of decreasing EPIC pulse-height response with checks made to detect double peaking. The centroid and width of each cluster was computed. Clusters from different views were then put together by cycling over all 3-cluster combinations. For a given 3-combination, the algorithm assumed the source to be a γ-ray coming from the (known) vertex position. The U and V centroids were then used to compute a prediction Y and this was compared to the current Y-centroid. If the match was good to within 50.8 mm , the triple crossing was accepted. Crossings were then fitted to two parameters: the X- and Y-slopes of the γ-ray by minimizing χ^2 :

$$\chi^2 = \frac{(U - U_{centroid})^2}{\sigma_U^2} + \frac{(V - V_{centroid})^2}{\sigma_V^2} + \frac{(Y - Y_{centroid})^2}{\sigma_Y^2}$$

where

$$\begin{pmatrix} U \\ V \\ Y \end{pmatrix} = \begin{pmatrix} -\cos\theta_U & \sin\theta_U \\ \cos\theta_V & \sin\theta_V \\ -\sin\theta_Y & \cos\theta_Y \end{pmatrix} \begin{pmatrix} (z_{U\ or\ V\ or\ Y} - z_{vtx}) \cdot \frac{dx}{dz}|_{shw} + x_{vtx} \\ (z_{U\ or\ V\ or\ Y} - z_{vtx}) \cdot \frac{dy}{dz}|_{shw} + y_{vtx} \end{pmatrix}$$

where $\frac{dx}{dz}|_{shw}$ and $\frac{dy}{dz}|_{shw}$ are the two parameters to be fitted. The matrix notation is just a convenient way to express the rotations. Triple-crossing parameters were then used to make projections to the PbG wall. Energy in blocks within $\sim$ 1.5 radiation length of the projections was associated with the corresponding crossing. If no PbG energy could be associated with a crossing, the candidate was rejected. However, if the projection fell *outside* of the lead-glass array, it was still accepted. Finally, after pattern recognition in the PbG-EPIC was completed, shower candidates were made using left over lead-glass blocks that remained unmatched to any crossings or charged tracks. Thus, three different kinds of shower candidates were retained: those which involved a lead-glass block and an EPIC crossing (PbG-EPIC), those which involved only an EPIC crossing outside PbG acceptance (EPIC-only) and those which involved the left-over lead-glass blocks (Block-only). Note that shower candidates were dropped if the PbG energy associated with them was much less than that expected from a minimum-ionizing track except for EPIC-only showers for which, by definition, no PbG energy was measured.

Shower candidates from the automatic mode often provided a very good starting point where semi-automatic mode could take over. In a typical semi-automatic mode session, automatic mode shower candidates were interactively displayed. Pattern recognition was then thoroughly checked. All shower candidates from charm events were independently found by the three analysis groups at OSU, McG and UT. Different interpretations were all discussed in full meetings and when ambiguities could not be resolved, all possibilities were retained.

5.2.4) **Pattern recognition IV: The Hadron calorimeter**

In the automatic mode, charged tracks were followed all the way through the hadron calorimeter. Calibration studies have shown that hits falling within a radius as large as 25.4 *cm* from the predictions could be associated with tracks and when such associations were made, the associated hits were removed from the hit buffer. In the calorimeter paddles, energy was removed on the basis of the previously associated EPIC energy and the list of any left-over energy depositions was output in a format convenient for interpretation. Following this, checks were made for any trails of left-over hits in the EPIC planes that might line-up as coming from the vertex location. If any such evidence was found, a χ^2 minimizing fit was made to $\frac{dx}{dz}|_0$ and $\frac{dy}{dz}|_0$ using the known position of the vertex. The total energy of the neutral hadron candidate was set equal to the sum of the observed hits. On occasion, for complex events, it was still necessary to go through the list of all such neutral hadron candidates using the semi-automatic mode but no extensive semi-automatic mode pattern recognition was usually required.

5.2.5) **Pattern recognition V: Track finding and fitting in the CPI**

Track finding in the Y-view among the CPI hits was done on a stand-alone basis. In the automatic mode, this was achieved by using a downstream-to-upstream search technique. Hits and images were treated on an equal basis and searches were performed independently within each of the 4 quarters of the chamber. A hit would be selected sequentially from the list of hits on the most downstream drift-cell of a given quarter.

Another one would also be selected sequentially but, this one, from the list of hits belonging to the most upstream drift-cell. A 15 *mm*-wide road along the straight line connecting the two selected hits was opened and hits (from any drift-cells between the two anchors) falling into that road were picked-up. These were removed from the buffer only if at least a total of $N_{hits} = 5$ could be found and if they lined-up with no gap longer than 8 *cm* between them while spanning at least 25.4 *cm* in the Z-direction. A slope $\frac{dy}{dx}|_0$ and an offset y_0 were fitted to such a set of hits and this constituted a *segment*. If no segment could be found, the downstream anchor was moved one step in the upstream direction and the process was repeated. When the downstream anchor reached the upstream side of the chamber, the upstream anchor was moved dowstream by one step while the dowstream anchor was reset to point at the most dowstream drift-cell. The search was then repeated. This went on until the upstream anchor reached the downstream end of the chamber or until no more hits remained in the hit buffer. The method was observed to be very effective at finding most segments. High-participation straight-through's were picked up first.

Attempts were made to combine segments from different quarters allowing for a small curvature due to the fringe field of the magnet. In the semi-automatic mode, all stand-alone CPI tracks would be displayed and, as for other systems, new ones could be entered while old ones could be removed interactively. In addition, semi-automatic mode allowded completion of the delicate task of associating dE/dx information to close (often overlapping) tracks. All reconstructed tracks in the drift chambers were checked for presence in the CPI. Often, down-to-up connections could be interactively helped using stand-alone tracks in the CPI. Also, the Y-view CPI provided was useful to corroborate charged tracks which did not make it through the magnet's $\frac{dx}{dz} \cdot \frac{dy}{dz} \cdot p$ acceptance.

5.2.6) **Matching emulsion tracks with drift chamber tracks**

When automatic mode and semi-automatic mode pattern recognition in the spectrometer on a given charm candidate was completed, tracks found in the spectrometer were then matched with those found in the emulsion volume. Matching was essentially done by comparing the drift chamber slopes to those measured in the emulsion. If the measurement was done on the changeable sheet, effects of multiple Coulomb scattering were minimized and matching was rendered easier. Still, if this measurement was not done, slopes at the production or decay vertices (depending where the track came from) were used and this was more reliable if the vertices happened not to be too deep in the emulsion volume. In any case, MCS was always taken into account in interpreting the weight given to a match. Automatic mode matches were all examined and revised using the semi-automatic mode. All matches were done independently by the analysis groups and compared. If any matching differences could not be resolved, all possibilities were retained. However, it must be emphasized that the matching ability was very high. This feature of *uniquely* mating spectrometer tracks to emulsion tracks is one of the paramount attributes of E531.

Studies of the distribution of matches (using charm candidates) have been made *for each scanning group*. These showed that corrections (rotations and translations on emulsion module co-ordinates) each scanning group determines in the process of FB and later apply to the measurements of charm candidate emulsion parameters, were generally effective in removing any systematics. Nevertheless, all charm candidates were examined for rotations. No fits are found to be heavily dependent on any. Figure # 34 presents the

distributions (for all scanning groups) of the difference in the X- or Y-slopes between the changeable sheet and the spectrometer measurements:

$$\Delta\frac{d\,x\,or\,y}{dz} = \frac{d\,x\,or\,y}{dz}|_{cs} - \frac{d\,x\,or\,y}{dz}|_{spec}$$

at the changeable sheet. Both X- and Y-slope (no-cuts) distributions have $\sigma_{\frac{dx\ or\ y}{dz}} = 11\ mrad$.

5.2.7) **Particle identification: use of the TOF system**

Probably one of the very last steps in the charm candidate analysis was that of charged particle identification based on the time-of-flight system. In a given event with $N = N_{out\ or\ bad} + N_{in}$ reconstructed charged particle tracks, $N_{out\ or\ bad}$ of them could not possibly be identified by the TOF system because they were outside the acceptance of the TOF II hodoscope or the paddle they hit also happened to be hit by other tracks. The N_{in} remaining tracks with good TOF II hits split into two categories: $N_{in} = N_{fast\ or\ id'ed} + N_?$. The $N_{fast\ or\ id'ed}$ charged particles either had so large momenta that, whatever their ID, their speed was $\beta \sim 1$ *or* they already had some identification using an external piece of equipment other than TOF. The other $N_?$ particles had no ID's at all and the TOF system could be used to determine their identifications.

For each of the $N_?$ particles, a flight time was computed according to:

$$t^i_{flight} = t^i_{stop} - t^{event}_{start} \qquad i = 1, \ldots, N_?$$

$$t^{event}_{start} = \frac{\left(t^{TOF\,I}_{start}/\sigma^2_{t^{TOF\,I}_{start}}\right) + \left(\sum_{j=1}^{N_{fast\ or\ id'ed}} t^j_{start}/\sigma^2_{t^j_{start}}\right)}{\left(1/\sigma^2_{t^{TOF\,I}_{start}}\right) + \left(\sum_{j=1}^{N_{fast\ or\ id'ed}} 1/\sigma^2_{t^j_{start}}\right)}$$

$$t^j_{start} = t^j_{stop} - t^j_{flight} = t^j_{stop} - \frac{l^j}{\beta^j\,c}$$

in which l^j is the integrated path lentgh along the curved trajectory of the j^{th} member of the set of $N_{fast\ or\ id'ed}$ particles and β^j is its speed. The event's start-time t^{event}_{start} was given by a weighted ‡ sum of the TOF I counter contribution and the contributions of all computed start-times from the $N_{fast\ or\ id'ed}$ particles. In a given charm event, these included the ν-interaction muon (for FB muons, $\beta \sim 1$), any particle having $p \geq 10\ GeV/c$ ($\beta \sim 1$) together with a good track-fit ($\chi^2/\nu \leq 2.5$) and finally, any other particles which might have either been identified as electrons/positrons by the PbG-EPIC system or tagged by a conversion in the emulsion or which might have been identified in the emulsion using I/I_0 and $1/p\beta$ ($\beta \neq 1$). All stop-times were given by the appropriate TOF II hit.

Once all flight-times for the $N_?$ particles had been computed, they could be compared to the set of flight-times that would have been observed assuming the particles were electrons, muons, pions, kaons and protons. Thus, for each particle type, one could compute the χ^2 associated with the measurement being compatible with any of these particle types using:

$$\chi^2_{e,\mu,\pi,K,p}{}^i = \left(\frac{t^i_{flight} - t^{comp;\ e,\mu,\pi,K,p\ i}_{flight}}{\sigma_{t^i_{flight}}}\right)^2 \qquad i = 1, \ldots, N_? \qquad \#\,d.f. = 1$$

‡ For the TOF I contribution, the error used depends on the number of phototubes firing: 1 ,2 ,3 or 4 . For the fast or identified particles contribution, each computed start-time carries the error associated with the TOF II paddle that was hit...

and statistically meaningful decisions on which particle identifications to assign (or to allow) were based on the confidence level associated with this quantity.

6.0) SECOND RUN DATA TAKING

6.1) The data acquisition system

Data acquisition proceeded through a CAMAC [155] dataway. The neutrino trigger collected 1000 8-bit words of various ADC's and TDC's and allowed for an additional maximum of 3059 8-bit words of drift chamber data. In addition, typically 3072 8-bit words of CPI data were also read. Thus, roughly 60 *kbits* of data were read in per neutrino trigger and written on magnetic tape. Muon calibration data was read in if no neutrino trigger occured. In addition, sensor and pedestal triggers were also provided. All data was immediately written to magnetic tape at 800 *bpi* at a machine spill rate of once every 10 to 15 seconds. Over the duration of the second run, a total of 374 2400-foot magnetic tapes were written in this manner. On average, $\sim$ 80 neutrino triggers occured during a run for a grand total of $\sim$ 24 000 neutrino-triggers. The average live-time was: $\frac{\#\ \nu\ records}{\#\ \nu\ triggers} = 92 \pm 8\%$. In the first run these numbers were: on average $\sim$ 390 neutrino triggers per run for a total of $\sim$ 61 000 neutrino triggers. The average live-time of the first run was $79 \pm 5\%$.

6.2) The data logging system

All data was logged using a DATA GENERAL [156] ECLIPSE S200 8-bit computer. The data logging programme was a two-task software performing tape writing and equipment monitoring. The highest priority task was to complete a CAMAC read cycle and to write the data to magnetic tape as well as to dump the latest record read onto disk. The lowest priority task was to allow the user to access continually updated statistical information on the spectrometer. For example, various multiplicity distributions could be displayed interactively in table form or at the end of a run as part of a hard-copy run summary. Such run summaries were always examined carefully and many hardware problems were detected in that way. Appropriate curative action could usually be taken right away and the effect confirmed by the end of the next run.

The on-line computer allowed a separate lower-priority background environment to run concurrently with the main foreground environment occupied with the data-logger. These computer cycles were reserved for preventive large-statistics monitoring of data recently written to tape as well as for data compression. Also, a simplified version of the interactive track reconstruction software was available and this was used mainly to perform checks , on location, of the spectrometer equipment behaviour.

6.3) The on-line monitoring system

All throughout both runs of E531, several parameters related to critical pieces of apparatus were constantly monitored and such data read in through CAMAC and written to tape. The magnetic field developed by the SCM104 was monitored by a Hall effect probe and deviations of more than 10% from the nominal value would trigger an on-line alarm. Various critical high-voltage power supplies were also monitored, in a similar manner, and triggered the alarm at the 10% level. Temperature sensors on the emulsion target and CPI were read in and triggered an alarm at the 20% level. Pressure was also constantly monitored in CPI and the drift chambers.

Perhaps the most important parameters monitored in the spectrometer were the positions of each of the 24 drift chambers. The monitoring was achieved with the use of LVDT variable inductors to a rated precision of $14.4 \pm .6\ \mu m/ADC\ count$.

6.4) **The protection systems**

Excessive exposures of the emulsion to muon and neutron backgrounds were avoided by interlocking protection systems on the spectrometer with the only possible high-rate source: the beam halo from the nearby FNAL N7/N3 transported beam-lines. The muon background was monitored with the TOF I counter and if it exceeded more than 100 ***counts/pulse*** , the beam lines would be automatically shut down. The neutron background was measured with a sodium iodide scintillator coupled to a paraffin moderator. If the rate exceeded 3000 ***neutrons/pulse*** , N7/N3 would be automatically shut down.

7.0) CHARM EVENT ANALYSIS: THE METHOD

7.1) Kinematics

Many aspects of the work presented up to now in this thesis had to do with describing how the measurements were made. The preceeding sections dealt with determining the kinematical parameters of all the particles detected by the spectrometer. In this section, the kinematical fitting procedure employed to test hypotheses is first described and then the method in which it was used is explained.

7.1.1) χ^2 minimization algorithm

With all the pattern recognition on a particular charm candidate done, kinematic fits were attempted as part of a totally automatic procedure. This was done in order to minimize the possibility of introducing biases in the analysis. The different types of fits are described in the next sections. The purpose of this section is to briefly mention the mathematical basis on which all kinematic fits rest.

In a typical situation, a set of measurements $m_i \quad i = 1, 2, ..., I$ needs to be confronted with some kinematical hypothesis; for example, a particular charm particle decaying to a particular final state. That hypothesis is characterized by a set of K *constraint* equations which take the form of

$$f_k(x, m) = 0 \qquad k = 1, 2, ..., K$$

In a multi-vertex fit, these equations are the statements of energy-momentum conservation at each of the vertices. Depending on the type of hypothesis tested, there remains a set of J variables $x_j \quad j = 1, 2, ..., J$ from the above equations which essentially are *unknowns* and, therefore, part of the object of the procedure is to determine them. The method of *least squares* in which, the fundamental assumption is that the measured variables m_i distribute according to the normal (Gaussian) probability distribution function, is then used in order to find the set of I quantities $m_i^0 \quad i = 1, 2, ..., I$ that are such that the following variable reaches a *minimum* :

$$\chi^2 = \sum_{j=1}^{I} \sum_{i=1}^{I} (m_i - m_i^0)(G_m)_{ij}(m_j - m_j^0)$$

while still ensuring that

$$f_k(x, m) = 0 \qquad k = 1, 2, ..., K$$

In the above, G_m is the weight matrix, the inverse of which, G_m^{-1} , is the covariance matrix. The elements along the diagonal of the covariance matrix are the variances. The number of degrees of freedom associated with the above problem is $n_f = K - J$. In the case of a multi-vertex fit in which secondary vertices may be included with the charm decay vertex in the hypotesis to be tested thus adding up vertices to a total of $N_v \geq 1$, the number of constraints really is $K = 4 \times N_v$, where the "4" comes from the four-component equation of energy-momentum conservation. In such cases, fits can be performed if $n_f = (4N_v - J) \geq 1$ while calculations remain the only possibility when $n_f \leq 0$. Fits are sometimes classified using the number of degrees of freedom n_f as "$n_f C$ fits" denoting the "effective" or "remaining" number of constraints. The variable χ^2 can be shown to distribute according to

$$f_n(\chi^2) = \frac{(\chi^2)^{1/2(n-2)}}{2^{n/2}\Gamma(n/2)} \exp(-\chi^2/2)$$

in which Γ is the Gamma function. This equation can be used to compute the probability of obtaining χ^2 such that $\chi^2 \geq \chi_0^2$ where χ_0^2 is some experimentally observed value of the variable. This is, of course, the Confidence Level associated with the fit:

$$C.L. = P_n(\chi^2 \geq \chi_0^2) = \int_{\chi_0^2}^{\infty} f_n(\chi^2)\, d\chi^2$$

Which variables x_j are unknown depends on the problem at hand. For example, consider a situation where all kinematical quantities pertaining to a particular decay hypothesis are measured except for the mass and the momentum of the decaying parent. In the case of a one-vertex fit, this would constitute a 2C fit. But a multitude of other situtations can arise in which one or several other quantities like secondary charged particle direction slopes $\frac{dx}{dz}|_i$ and/or $\frac{dy}{dz}|_i$ and/or some inverse momentum $1/p_i$ or other quantity may, for experimental reasons, not be part of the set of measured quantities $m_i \quad i = 1, 2, ..., I$. Also, it is possible that some quantities be measured with such large errors that it is no longer useful for them to be part of the m_i's and so the set of x_j's must be enlarged to include them. Whatever the reason, it is not possible to have the computer symbolically manipulate a different set of equations each time a new charm candidate needs to be fitted in a different way. Fortunately, this is not necessary as the mathematical procedure of Lagrange multipliers can be used [157] to provide a general iterative solution through linearization of the constraint equations.

In order to achieve overall convergence of χ^2 to a stable minimum as the iterative process unfolds, not only should χ^2 generally decrease but the change $\Delta\chi^2$ between two successive iterations should also decrease while the constraint equations and their derivatives should come to zero within some reasonable limit. The automatic mode of kinematical fitting of charm candidates used a very loose cut on the tapering-off of the change in χ^2 between iterations:

$$\Delta\chi^2 \leq 0.3 \longrightarrow \textit{go on to another iteration...}$$

which essentially amounted to, as much as possible, un-restricted minimization of χ^2 . However, energy-momentum balance at all vertices was only assumed to be achieved if all of the following conditions were exactly met:

$$\sum_{i=1}^{I} p_x^i \leq 1\ MeV/c \qquad \sum_{i=1}^{I} p_y^i \leq 1\ MeV/c \qquad \sum_{i=1}^{I} p_z^i \leq 10\ MeV/c$$

In normal circumstances, the procedure would attempt an overall maximum of 30 iterations in order to satisfy the above conditions. If at any point in the course of this, all conditions were met and the Confidence Level associated with the fit was greater or equal to 1% , the fit was accepted and the process stopped. Even if the maximum number of iterations was performed and the process stopped, the Confidence Level would still be checked anyway so as to insure no possible fits be thrown out. As it turned out, the most probable number of iterations required to meet the above conditions for all cases of fits to the *charged* 2^{nd} run charm candidates in which the mass of the parent was constrained to that of a D^{+or-} , an F^{+or-} or Λ_c^+ was 4 while roughly 10% of all fits required more than 10 iterations.

The above procedure was used for automatic large scale fitting and the retaining of acceptable kinematical fits. However, a few pathological cases did occur (particularly for events with a large number of unknowns to determine) for which the iterative fitting process did not converge rapidly or oscillated wildly. Such events were all carefully re-examined outside of the context of the automatic kinematical fitting algorithm and the iterations interactively monitored in order to pinpoint the problems. Often, these rare cases resulted from proportionally large steps in one or many of the quantities to be fitted and a common cure was simply to cut the size of any such ovesized step, in any given quantity, even if called-for by the procedure. In some others of these rare cases, quantities to be fitted would step outside of their allowed physical range. That problem too could be detected by proper interactive monitoring and appropriate action could then be taken.

7.1.2) **Types of fits and systematic use of the algorithm**

The automatic kinematical fitting procedure used for large scale fitting of the charm candidates consisted of two main parts. The first task to perform was to try the allowed topologies to be confronted with the set of experimental measurements. By topology, one means whether an all-charged, one-neutral or two-neutral fit was to be performed. For each of these three general topologies, the procedure would try all allowed secondary charged particle identifications. If no external device provided positive identification of a charged secondary, the prong would be sequentially assigned the mass of π^{+or-} , K^{+or-} or that of p . This method was used for fitting all non-leptonic decays. Semi-leptonic decay hypotheses were not tested for in this way because of the necessarily undetected neutrino. Section 7.1.5) describes the procedure used for those cases. The only restrictions applied when selecting a set of decay particle identifications in a particular hypothesis to be tested was that of electric charge and total baryon number conservation.

The first topology to be tested is the all-charged hypothesis:

$$X \rightarrow N_p \; charged \; particles \begin{cases} \pi^{+or-} \\ K^{+or-} \\ p \end{cases}$$

In principle, if the decay contained N_p prongs, (for N_p even, the parent is neutral otherwise it is charged) one could expect at the very most 3^{N_p} all-charged decay hypotheses to be tested for non-leptonic decays. In the best cases, for each prong, two direction slopes $\frac{dx}{dz}|_i$ and $\frac{dy}{dz}|_i$ were available from measurements in the emulsion while the inverse momentum $\frac{1}{p_i}$ was available from the spectrometer. Occasionally, unambiguous charged particle identification was available from the TOF measurement combined with the inverse momentum. In such cases, that decay prong's cycled id's were restricted only to the allowed ones.

Next in line among the different topologies tested is the one-neutral hypothesis. This is really a misnomer as the actual hypothesis tested is, of course, charged particles together with a neutral particle.

$$X \rightarrow N_p \; charged \; particles \begin{cases} \pi^{+or-} \\ K^{+or-} \\ p \end{cases} + \; one \; neutral \begin{cases} K^0_{S \; or \; L} \; \pi^0 \\ \Lambda^0 \\ n \end{cases}$$

The addition of an observed neutral particle in a hypothesis to be tested through a fit does not necessarily imply that the number of vertices in the fit, N_v , increases. Only so-called *reconstructed* neutrals will cause N_v to do so. It is important to notice that both re-constructed and un-reconstructed types of neutrals are *observed* , the difference in terminology has to do with *what* is actually obeserved.

Reconstructed neutrals are secondary (i.e. coming from the charm decay vertex) neutrals that decay within the volume of the emulsion or in the spectrometer. Their decay products must kinematically *reconstruct* to any of the parent's measured quantities (the mass of the decaying neutral being constrained) in fits that determine whether that neutral together with its decay products can be part of the tested charm decay hypothesis. Un-reconstructed neutrals consist of observed quantities of neutral hadronic energy deposited in the calorimeter in a pattern compatible with showering neutral hadrons. These are tested as being part of the fits to charm decays in a similar way as the reconstructed neutrals. Yet, since no secondaries are observed, they remain *un-reconstructed.*

In all fits to decays of the second run, all two-electromagnetic-shower combinations $\gamma_i\gamma_j$ that reconstructed into an invariant mass such that

$$m_{\pi^0} - 3\sigma_{m_{ij}} \leq m_{ij} \leq m_{\pi^0} + 3\sigma_{m_{ij}}$$

or

$$|m_{\pi^0} - m_{ij}| \leq 60\ MeV/c^2$$

where $m_{\pi^0} = 135\ MeV/c^2$ were tested as to be coming from the electromagnetic decay

$$\pi^0 \rightarrow \gamma\gamma \qquad 98.8\%$$

This was done by including, one after the other, those two-gamma combinations that passed the loose cuts as part of the attempted one-neutral fits; the "one-neutral" being the decaying neutral pion. In doing so, 4 constraints are gained at the additional vertex but the two decay angles and the momentum of the neutral pion are un-observed so that vertex contributes $4 - 3 = 1C$ to the total fit. The mass of the neutral pion is constrained to 135 MeV/c^2 . In the First run, as the EPIC system whose function is to improve location of electromagnetic showers was not part of the apparatus, consideration had to be given to single PbG-block electromagnetic energy depositions large enough to be equal or exceed the energy deposition of a single $\pi^0 \rightarrow \gamma\gamma$ for which the distance between the two impact points of the γ rays at the location of the lead-glass block array was less or equal to the size of a single block. In the π^0 center-of-mass frame, because of phase space, the most probable decay configuration of $\pi^0 \rightarrow \gamma\gamma$ is the one in which the direction of flight of the π^0 and the direction defined by the 2 back-to-back gamma rays are perpendicular to each other. In such cases

$$\theta_{op}^{MPV} \sim \frac{m_{\pi^0}}{p_\gamma}$$

which translates into a minimum electromagnetic energy deposition of $\sim$ 4.4 GeV above which a single π^0 whose 2 gamma rays hitting the same PbG block could be hypothesised. This type of un-reconstructed neutral pion decays did not increase the total number of vertices in the fit and was included as one additional particle. Because of the much improved electromagnetic shower location capability of the 2^{nd} run apparatus, all neutral pion decays could be resolved in the range of observed energies.

Neutrals like K^0 and Λ^0 may belong to either the category of reconstructed or un-reconstructed neutrals. Because of the fact that for

$$K_S^0 \rightarrow \pi^+\ \pi^- \qquad 68.6\%$$

the quantity $(\langle p/m \rangle = 5.6) \cdot (c\tau = 2.675\ cm) = 14.9\ cm$ in our data, it is likely that such decays be observed as "Vee's" downstream of the charm decay vertex within the emulsion volume or as a secondary vertex in the upstream drift chambers. The same is also true for

$$\Lambda^0 \rightarrow p\,\pi^- \qquad 64.2\%$$

for which $(\langle p/m \rangle = 2.4) \cdot (c\tau = 7.89\ cm) = 19.2\ cm$. If such strange particle decays were observed, a secondary vertex was included in the charm decay hypotheses to be tested by the fitting procedure. Because these strange decays have long lifetimes compared to the electromagnetic decay of the neutral pion, direction slopes $\frac{dx}{dz}|_i$ and $\frac{dy}{dz}|_i$ could easily be measured with typical high precision of a few milliradians between the two well separated charm decay and strange decay vertices. Such re-constructed neutrals, for which only the momentum remained un-constrained, contributed a much more sturdy $4 - 1 = 3C$ to the overall fit. Now, hadronic showers in the hadron calorimeter can certainly be interpreted as K_L^0 for which $(\langle p/m \rangle = 5.6) \cdot (c\tau = 1554\ cm) = 87\ m$ or as Λ^0 or as neutrons. Such un-reconstructed neutrals did not increase the number of vertices and were simply added to the fit as single additional particles.

Finally, the last of the topologies confronted with data through fit attempts was that of the two-neutral fit, again a misnomer as the charged particles obviously are part of the fit too. These fits were of the type

$$X \rightarrow N_p\ charged\ particles \left\{ \begin{matrix} \pi^{+or-} \\ K^{+or-} \\ p \end{matrix} \right. + first\ neutral \left\{ \begin{matrix} K_{S\ or\ L}^{0\ or\ 0} \\ \Lambda^0 \\ n \end{matrix} \right. + second\ neutral \left\{ \begin{matrix} K_{S\ or\ L}^{0\ or\ 0} \\ \Lambda^0 \\ n \end{matrix} \right.$$

Most of the fits were simply those including two neutral pions, that is:

$$(\pi^0 \rightarrow \gamma_i\gamma_j)\,(\pi^0 \rightarrow \gamma_k\gamma_l)$$

combinations. Such combinations contributed at most $2 \times 4 - 6 = 2C$ to the overall fit. The contributions of other combinations depend on the experimental details of each case.

Fit attempts involving three or more neutrals were not done as such topologies account for a very small fraction of the decay modes.

7.1.3) χ^2 **Freed and unknown quantities**

The actual number of degrees of freedom n_f of any of the fits described above really depends on the particular experimental status of each event. Although measured, some quantities were sometimes freed (and thus become part of the set $x_j \quad j = 1, 2, ..., J$) in fits because the errors associated with them were too large. This happened for a few of the upstream-only drift-chamber tracks whose inverse momentum measurements from the fringe-field of the analyzing magnet were not assigned a typical error. It also happened that charged decay secondaries were very fast and that their large measured inverse momenta carried such large errors that again considering such poorly measured quantities as un-measured was warranted. There remains, however, truly un-measured quantities. The invariant mass of the decaying parent is such a quantity as are direction slopes and momenta of certain neutrals (see preceeding section).

7.1.4) **Cuts, requirements and progression of algorithm**

As is apparent from the last section, the large number of fits to attempt can rapidly get out of hand. In order for this not to happen, minimum bias cuts had to be applied so that this task did not demand an inordinate amount of computing time.

For a given topology to be confronted with data and a given set of particle identifications, fits in which the charm parent-mass was left as an un-constrained variable to be calculated by the automatic procedure were attempted first. A loose cut was applied at that level which dealt with the likelihood of the hypothesis not including the correct set of neutrals or at least an incomplete set of neutrals. Let $\overline{l}_c$ stand for a unit vector pointing into the direction of flight of the decaying charm particle and let $\overline{P}^{tot}$ be the vector sum of all the charmed particle decay products † momenta:

$$\overline{P}^{tot} = \sum_{i=1}^{N_p} \overline{P}_p^i + \sum_{j=1}^{N_{neut}} \overline{P}_{neut}^j$$

where N_p is the number of decay prongs and N_{neut} is the number of neutrals included in the fit. Then, $P_\perp^{tot}$, computed through

$$P_\perp^{tot} = \sqrt{\overline{P}^{tot} \cdot \overline{P}^{tot} - \left(\overline{l}_c \cdot \overline{P}^{tot}\right)^2}$$

is the amount of perpendicular momentum the proposed fit would have to reduce to zero for part of the constraint equations to be satisfied at the charm decay vertex. The cut used was:

$$P_\perp^{tot}\ (before\ the\ fit) \leq 500\ MeV/c$$

above which no fits with the parent-mass left un-constrained would be attempted. As the charm parent direction $\overline{l}_c$ was measured with high precision in the emulsion, $P_\perp^{tot}$ could be computed using spectrometer measurements with a typical precision of 40 MeV/c . So the $P_\perp^{tot}$ (*before the fit*) cut was very loose, its purpose being only to prevent the automatic algorithm spending too much time attempting fits whose negative outcome was certain. At the same level, another cut was applied on the parent's computed invariant mass before the mass-unconstrained fit was tried. No fits were attempted for which this mass exceeded 3 GeV/c^2 .

If the parent-mass-unconstrained fit to the hypothesis resulted in a Confidence Level $C.L. \geq 1\%$, the algorithm would then consider attempting a parent-mass-constrained fit to the same data using known charmed mesons or baryon masses as well as those of the strange K^0 and Λ^0 particles. ‡ This would be done only if the following conditions were met:

$$\frac{|M_{physical} - M_{inv}(fitted)|}{\sigma_{M_{inv}(fitted)}} \leq 2$$

otherwise, the fit would be skipped.

---

† Including both charged and neutral decay products...

‡ D^0 and $\overline{D}^0$ were constrained to a mass of 1864.7 MeV/c^2 , D^{+or-} to 1869.4 MeV/c^2 , F^{+or-} to 1971 MeV/c^2 and Λ_c^+ to 2282 MeV/c^2 [138] while A^+ was constrained to 2460 MeV/c^2 [158]

Then, the automatic algorithm would proceed to consider fits to resonant states both produced and decaying immediately at the primary vertex such as

$$D^{*+or-} \rightarrow D^0\ \pi^{+or-}$$
$$D^{*+or-} \rightarrow D^{+or-}\ \pi^0$$
$$D^{*+or-} \rightarrow D^{+or-}\ \gamma$$
$$D^{*0} \rightarrow D^0\ \pi^0$$
$$D^{*0} \rightarrow D^0\ \gamma$$
$$F^{*+or-} \rightarrow F^{+or-}\ \gamma \qquad 159$$

on the basis of a similar 2σ cut. When successful, these were used as further constraints to the fits.

7.1.5) **"Zero-constraint" calculations**

So called "zero-constraint" calculations refer to cases when the hypothesis is made that some additional totally un-detected decay particle is part of an event. The un-detected particle must carry zero electric charge otherwise it would have been seen as a decay prong in the emulsion. All semi-leptonic decays in which one of the decay prongs is identified as e^{+or-} or μ^{+or-} were "fitted" in this way because ν or $\bar{\nu}$ necessarily escaped detection. There is, however, another class of events for which the results of such calculations were retained. These are some of the non-leptonic events for which the result of the calculation indicates that the hypothesized un-detected particle heads in a direction that brings it outside the acceptance of the PbG-EPIC γ-ray detection system or of the hadron calorimeter. Depending on the location of the decay vertex within the fiducial volume of the emulsion, it is also possible that such a neutral heads in the direction that does not even pass the acceptance cuts imposed by the analysing magnet aperture. It was therefore important that "zero-constraint" fits be performed not only on semi-leptonic decays but also on all candidates and that the acceptance be carefully checked for all cases. This was routinely done as part of the automatic fitting procedure described in previous sections.

The 4 equations of energy-momentum conservation at the charm decay vertex provide 4 constraints. The un-detected neutral's two direction slopes $\frac{dx}{dz}|_{und}$ and $\frac{dy}{dz}|_{und}$ together with its mass M_{und} and momentum P_{und} as well as the charm parent's mass M_{par} and momentum P_{par} all constitute unknowns. In order to proceed, one assumes both the charm parent's and the un-detected neutral's masses are known which means the procedure must run over all possible combinations of the two. With the inclusion of the un-detected neutral particle it may be possible to *exactly* solve the constraint equations at the charm decay vertex:

$$\overline{P}_c = \overline{P}_{det} + \overline{P}_{und}$$

So, one refers to the "zero-constraint" fits as balancing the remaining amount of momentum in the direction defined by

$$\overline{l}_\perp \sin\Omega = \overline{l}_c \times (\overline{l}_{P_{det}} \times \overline{l}_c)$$

where Ω is the angle between the direction of flight of the charm particle $\overline{l}_c$ and the direction in which the sum of all detected momenta points $\overline{l}_{P_{det}}$. Clearly, because of conservation of momentum in a decay, the

sum of all momenta along $\overline{1}_\perp$ must vanish. Note that the quantity $\overline{P}_{det} \cdot \overline{1}_\perp$ is a Lorentz invariant against boosts in the charm parent direction.

The parent mass is given by the following expression:

$$\begin{aligned} M_{par}^2 &= (E_{det} + E_{und})^2 - (\overline{P}_{det} + \overline{P}_{und})^2 \\ &= E_{det}^2 + 2E_{det}E_{und} + M_{und}^2 - 2\overline{P}_{par} \cdot \overline{P}_{det} + \overline{P}_{det} \cdot \overline{P}_{det} \end{aligned}$$

with

$$E_{und} = E_{par} - E_{det} = \sqrt{M_{par}^2 + P_{par}^2} - E_{det}$$

where the subscript "det" stands for detected, "und" for un-detected and "par" for parent. By detected, one really means all quantities that are measured and included in the hypothesis; "zero-constraint" calculations were routinely performed on decays already involving an observed neutral. The assumed parent's momentum can then be varied over its physical range and the set of possible parent masses plotted. Figure # 35 presents a sketch of the four possible cases one can encounter in such calculations. The curve labelled "A" depicts the case when no possible value in the physical range of P_{par} brings $M_{par} \leq M_0$ where M_0 is the current charm parent mass. Such cases are not strictly hopeless, as it may appear. Sometimes, the measurement errors allow the minimum of the envelope of error-propagated curves to go down close enough to $y = M_0$ so that it be within some reasonable value, say within 2σ , (sigma being the propagated error on the computed parent mass at the minimum of the curve). Curve "B"presents this situation. In such cases, within errors, only one "solution" can be contemplated: that at the minimum of the curve. Curve "C" presents the case where there is only one single solution to the problem as it intersects $y = M_0$ at only one point while curve "D" shows the most common case where there are two well separated solutions to the problem. In one solution, the slow un-detected neutral usually goes-off at a wide angle with respect to the direction of flight of the charm particle. In the other solution, the fast un-detected neutral usually goes-off at small angle with respect to the flight direction of the charm particle. In principle, the ambiguity cannot be removed unless it turns out that one of the solutions points inside the acceptance of the spectrometer and the observed electromagnetic or hadronic energy rules it out. Propagation of measurement errors on the output of "zero-constraint" calculations was routinely done. As a general rule, the direction of the slow un-detected neutral is much less well-known than that of the fast one.

Using the current cycled parent mass in the procedure, cases "C" and "D" can be solved for by finding the roots of the following quadratic equation in P_{par} :

$$\begin{aligned} &4\left(P_{det}^2 \cos^2\Omega - E_{det}^2\right) P_{par}^2 + \\ &4P_{det}\cos\Omega\left(M_{par}^2 + E_{det}^2 - M_{und}^2 - P_{det}^2\right) P_{par} + \\ &[M_{par}^4 + E_{det}^4 + M_{und}^4 + P_{det}^4 - 2M_{par}^2\left(E_{det}^2 + M_{und}^2\right) - \\ &2M_{und}^2 E_{det}^2 + 2P_{det}^2\left(M_{und}^2 - M_{par}^2 - E_{det}^2\right)] = 0 \end{aligned}$$

where again, Ω is just the angle between $\overline{1}_c$ and $\overline{1}_{P_{det}}$.

When the ambiguity could not be removed, both solutions to the "zero-constraint" calculations were kept and given equal weight in the calculation of the lifetime. However, in cases when one or more fully

constrained fits could be found, possible additional "zero-constraint" solutions were *not* included in the calculation of the lifetimes.

7.1.6) **Gamma conversions inside the emulsion volume**

High energy gamma rays can convert within the emulsion volume. Such conversions in which $\gamma \rightarrow e^+ e^-$ are easily recognized (see Section 5.1) by emulsion scanners because of their peculiar topology. As γ is massless, the initial opening angle between the electron and the positron is zero. Thus, certainly for horizontal emulsion, conversions initially appear as *single* (yet twice minimum-ionizing) tracks which eventually separate into two oppositely diverging ones. The e^+ and e^- then proceed to travel through the emulsion volume and the changeable sheet while undergoing some multiple Coulomb scattering. In best cases, both are within the acceptance of the spectrometer and are recorded as tracks through the drift-chambers often to be associated with electromagnetic showers in the PbG-EPIC system. Gamma conversions may be an extremely important part of any single charm event. These gammas, when reconstructed with a typical fitted invariant mass of $m_{e^+ e^-} \lesssim 40\ MeV/c^2$, must be combined with each other (if there are more than one in an event) and with other gammas that did not convert and were observed to initiate electromagnetic showers in the PbG-EPIC system. This is because when $\pi^0 \rightarrow \gamma\gamma$, either gamma may convert, or even both. All possible combinations were tried by the automatic procedure described in the preceeding sections. Sometimes, if the conversion vertex is well downstream of the charm decay vertex and/or the charm decay length is long; because of the particular topology of γ conversions in which e^+ and e^- initially point along the direction of flight of the gamma-ray, it may be possible to un-ambiguously determine which vertex the photon originates from. If it originates from the ν-interaction vertex or is upstream of the charm decay vertex, the importance of the conversion may be lessened, at least in terms of the analysis of the charm decay vertex.

An important feature of kinematical fits of γ conversions is that their output is particularly sensitive to a number of rather important corrections that must be applied on the observed input measurements and also on the input errors. The most important such corrections are described in the following sections.

7.1.6.1) **Bremsstrahlung correction**

As e^+ and e^- fly through the emulsion volume, the Coulomb field of atoms will cause them to change direction and, as a result, undergo accelerations which will cause some of their energy to be radiated away. For the reconstruction of gamma conversions to be effective, this energy-loss must be taken into account. The process of Bremsstrahlung and that of gamma conversion only differ by kinematical factors so:

$$1\ \textit{Conversion length} = \frac{9}{7}\ \textit{Radiation length}$$

The radiation lengths in horizontal and vertical emulsion are $d^H_{rad} = 29.4\ mm$ and $d^V_{rad} = 32.0\ mm$ [150] . Using these values, one can correct the energy of the e^+ and e^- using

$$E^{e^+ or -}_{corr} = E^{e^+ or -}_{obs} \exp\left(\frac{d_{obs}}{d_{rad}}\right)$$

in which d_{rad} is the radiation length, E_{obs} the energy computed from the observed momentum of e^+ or e^- and d_{obs} is the distance travelled from the conversion vertex all the way to the downstream edge of

the emulsion including the changeable sheet. If the conversion vertex has been found in the emulsion by scan-back or otherwise, this distance is straight-forward to compute. However, if conversion products are only observed in the spectrometer, d_{obs} is set equal to one conversion length when that distance is less than the one between the charm decay vertex and the downstream edge of the emulsion. Otherwise the conversion is hypothesized to have occured midway between the charm decay vertex and the downstream edge of the emulsion.

7.1.6.2) **EGS Monte Carlo simulation**

In the 2^{nd} Run, the maximum emulsion thickness was 7 *cm* ($\sim$ 2.3 *radiation length*) so Bremsstrahlung corrections are non-negligible, especially for events deep in the emulsion. The effective kinematical reconstruction of gamma conversions critically depends on the size of errors associated with the corrected electron or positron energy. This error was computed using:

$$\sigma^2_{E^{e^+ or -}_{corr}} = \sigma^2_{E^{e^+ or -}_{obs}} + \sigma^2_{Brem}$$

The first term, the error on the observed energy of the electron or positron, is just the error on the momentum measurements associated with their tracks in the spectrometer. The second term is the contribution from Bremsstrahlung. This contribution is the variation in the initial energy of e^+ or e^- given some observed final energy and distance travelled inside the emulsion volume. This quantity depends on the particular details of the emulsion composition and was estimated by a Monte Carlo simulation. The SLAC Electron-Gamma Shower simulator package [144] was used to generate distributions [160] of initial energies as a function of d_{obs} for different values of observed final energies $E^{e^+ or -}_{obs}$. The widths of these distributions were retained as best estimates of the error on the initial energy of e^+ or e^- . Appendix 12.10 reproduces these values. See also *Ref.* 144 for many more details.

7.1.6.3) **Multiple Coulomb scattering correction**

In some cases, the conversion vertex was not found by the emulsion scanners and no emulsion measurements of angles are available for e^+ or e^- . One is then forced to rely on on drift-chamber track-fits. This is only effective if account is taken for the multitude of randomly occuring small deflections in the direction of flight of e^+ or e^- as they traverse the emulsion volume. As fits to the direction slopes of each track are made in the x and y planes of the experimental set-up (z being along the ν beam direction), the Multiple Coulomb scattering contributions in either of these projected planes is [138] :

$$\sigma^{MCS}_{dx/dz \text{ or } dy/dz} = \frac{14.1\ MeV/c}{p\beta}\sqrt{d_{obs}/d_{rad}}\left\{1 + \frac{1}{9}\log_{10}(d_{obs}/d_{rad})\right\} \qquad (radians)$$

for particles carrying unit electric charge. In this equation, $p\beta$ is the measured momentum (in MeV/c) times the speed of the particle ($\beta = v/c$).

7.2) **2^{nd} Run event selection and statistics**

In the second run of E531, the thickness (7 *cm*) of the emulsion exposed to the ν beam was increased by 2 *cm* over that of the first run (5 *cm*) in the hope of observing more events. However, it turned out (as will be detailed below) that events contained in the most upstream 2*cm* of the second run emulsion were much

more difficult to fit due to multiple Coulomb scattering, to the high probability of secondary interactions and to gamma conversions. In order to eliminate any possibility of lifetime bias from these events, all second run events produced in the first 2 *cm* of emulsion were removed from the sample. Thus, both first and second run exposures had the same fiducial volume. Compared with the first run's 1248 , a total of 2638 second run neutrino interactions were observed to have occured within that fiducial volume. Scanners from emulsion groups † communicated to analysis groups ‡ a grand total of 207 second run charm event candidates. Of these, 79 were neutral candidates (N_p even), 43 were charged (N_p odd but $\neq 1$) and 85 were kinks ($N_p = 1$). A large number (76) of these kinks were not analysed any further: only events for which

$$P_{\perp}^{kink} = P_{charged} \cdot \sin\Theta_{kink} \geq 400\ MeV/c$$

were considered likely charm decay candidates. There remained 131 events for which kinematical fits were attempted: 96 of these were constrained while 35 were "zero-constrained".

Of the 131 events, 46 could be classified as *non-charmed* : 17 were consistent with strange decays (6 K_S^0 , 8 Λ^0 and 3 vees ambiguous between K_S^0 and Λ^0 .), 20 were unfittable § , 5 were gamma conversions, 2 were later not considered as charm by emulsion-groups, 1 turned out with $P_{\perp}^{kink} \leq 400\ Mev/c$ while 1 was vee or trident ambiguous. The remaining 85 of the 131 events, could be classified as *charmed.* These included 50 constrained and 35 "zero-constraint" fits. A total of 35 events were charged : 31 were tridents, 3 were kinks and 1 event had 5 prongs. A total of 50 events were neutrals: 34 were vees while 16 had four prongs.

A complete kinematical fit was attempted for each of the 131 events mentioned above. These attempts were distributed among the three analysis groups roughly as follows: all fits were attempted by the Ohio State University group. All charged fits and some neutrals were attempted both at McGill and by the Ohio State University group while neutrals and some charged fits were attempted both by the Ohio State University group and the University of Toronto group. In the case of the charged fits, all candidates were independently fitted in parallel at OSU and McGill, using different * computer codes. These fits were

† All Japanese groups, one Korean group and one group at the University of Ottawa, Canada.

‡ McGill University, Ohio State University and the University of Toronto.

§ The is no single experimental reason for the "unfittability" of a few of the charm candidates. Often, fits to such events were very underconstrained: no neutrals were present to balance $P_{\perp}$, one or more decay tracks would point outside the spectrometer acceptance, the parent invariant mass was too low ($M \leq 1\ GeV/c^2$) or too high (M $\geq 3\ GeV/c^2$), critical emulsion measurements could not be made, etc..., Some were classified "unfittable" for other reasons: one $3\mu m$ event, E11581349, at which decay length the efficiency is unknown was consistent with having a proton and and anti-proton in the final state, E01585775 was too slow and messy: it had 6 gamma conversions within the emulsion volume. Others had un-physical $P_{\perp} \sim 1\ GeV/c$ ...

* The McGill algorithm heavily used interactive reconstruction, the OSU algorithm did not.

compared to each other and a great deal of care was taken to critically review all details of all computations. Fits were considered "suspect" unless the same results were obtained independently by both groups. In this way, a unique set of charged decay hypotheses was arrived at in which all numbers pertinent to the extraction of charged particle lifetimes from the data are consistent.

As was mentioned at the beginning of this section, a cut on the z of the charm production vertex was imposed: $z_{prod}^{emu} \geq 2\ cm$ such that both first and second run fiducial volume were the same. From the list of 85 charm candidates, this cut removed 14 neutrals, 10 of which are un-constrained or un-fittable and also removed 14 charged events of which 13 are un-constrained or un-fittable. Many of the events removed were hopelessly complicated.

7.3) **A complete example of charm event analysis**

As far as the analysis is concerned, there really are no events more typical than any other. To be fair, one would have to include a detailed list of all the steps taken in the analysis of all of the charm events. In fact, this list exists but little information can be gained from its inclusion here. Instead, this section purports to provide an *example* of the sequence of tasks that was performed in order to arrive at a fitted charm event. The event chosen is 1050 2844 mainly because of its moderate degree of complication. It would have been misleading to choose an *easy* (short) event because most weren't. The outcome of the fit (ambiguous between D^+ and F^+ meson) is only typical of the ambiguous sample but that shouldn't cause any worry because the outcome of a fit was obviously *never* known *a priori* !

1050 2844 (scanning tag: Kobe 1129, Figure # 36a,b,c,d,e,f,g and h) was first entered on the E531 database in September 1982 . The event is a trident in horizontal emulsion. The production vertex was measured in absolute co-ordinates while as usual, the decay vertex was measured in relative co-ordinates (to the production). In this event, the measured number of nuclear recoil and breakup tracks seen in the emulsion is $N_h = 4$ and and the number of showering or minimum ionizing tracks is $N_s = 3$. A total of 7 emulsion tracks (including the charm parent's) were measured in the emulsion. These are: 3 production tracks (including the expected μ^- ,see later...), the charm parent, and 3 decay tracks from the charm vertex. As charm does not exit the emulsion volume, 5 (including all decay tracks) out of a possibility of 6 tracks had their exit angles dx/dz and dy/dz measured in the emulsion. No emulsion measurement of I/I_0 and/or $1/p\beta$ are available for any of the emulsion tracks. The computed (from the location of vertices) decay length of the trident is $1292 \pm 4\ \mu m$ while the distance from the production vertex to the downstream edge of the emulsion or *potential path* is $17096\ \mu m$. As a whole, the emulsion situation is quite un-eventful.

The situation in the drift-chambers is not so simple. A total of 7 tracks have been found (using a mixture of the automatic and the operator-aided modes of the re-construction programme) of which 6 are of the down-to-up type while the remaining 1 is of the up-only type. The average number of hits on those down-to-up tracks is 21 ± 1 (maximum is 24). None of the drift chamber tracks present any particular problem. However, it is known that the pattern recognition in the drift chambers is not completly efficient. Graphics display of the event reveals un-mistakable well separated strings of hits in two of the upstream drift-chamber views (V and U). In the V-view, the first three drift chambers are hit while the last two are not, an indication that the particle may be going-off at such a steep angle that it misses those two. This is

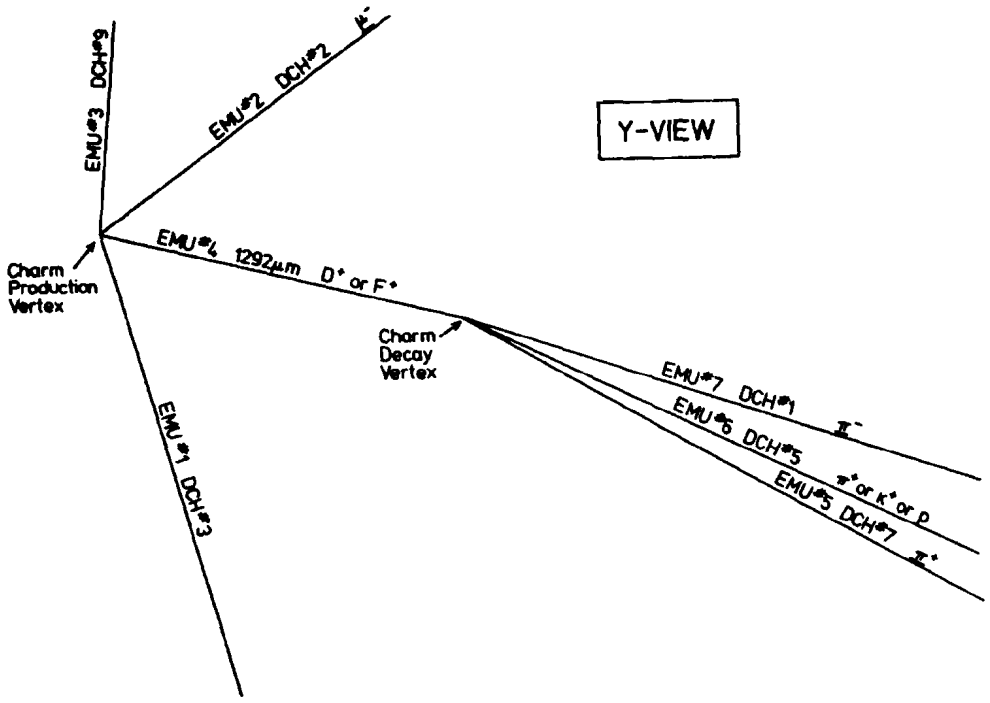

Figure # 36b
Event 1050 2844. This picture shows a Y-view of the event as depicted from the emulsion measurements. The neutrino beam is incident from the left. As is clearly evident from the picture, the charm decay is at least a four body decay involving at least one neutral.

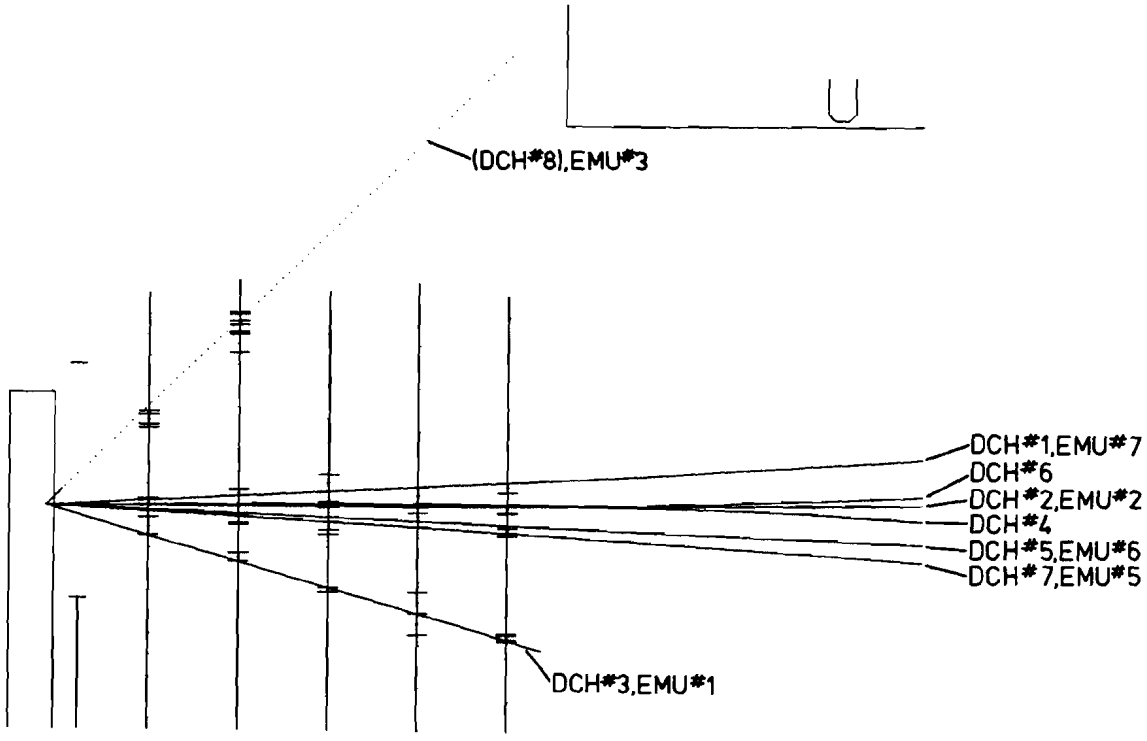

Figure # 36d
Event 1050 2844. This picture shows a computer-generated U-view of the event as seen in the upstream U drift-chambers. The neutrino beam is incident from the left. The projection DCH # 8 of EMU # 3 is seen to go through the unused hits in the first two chambers.

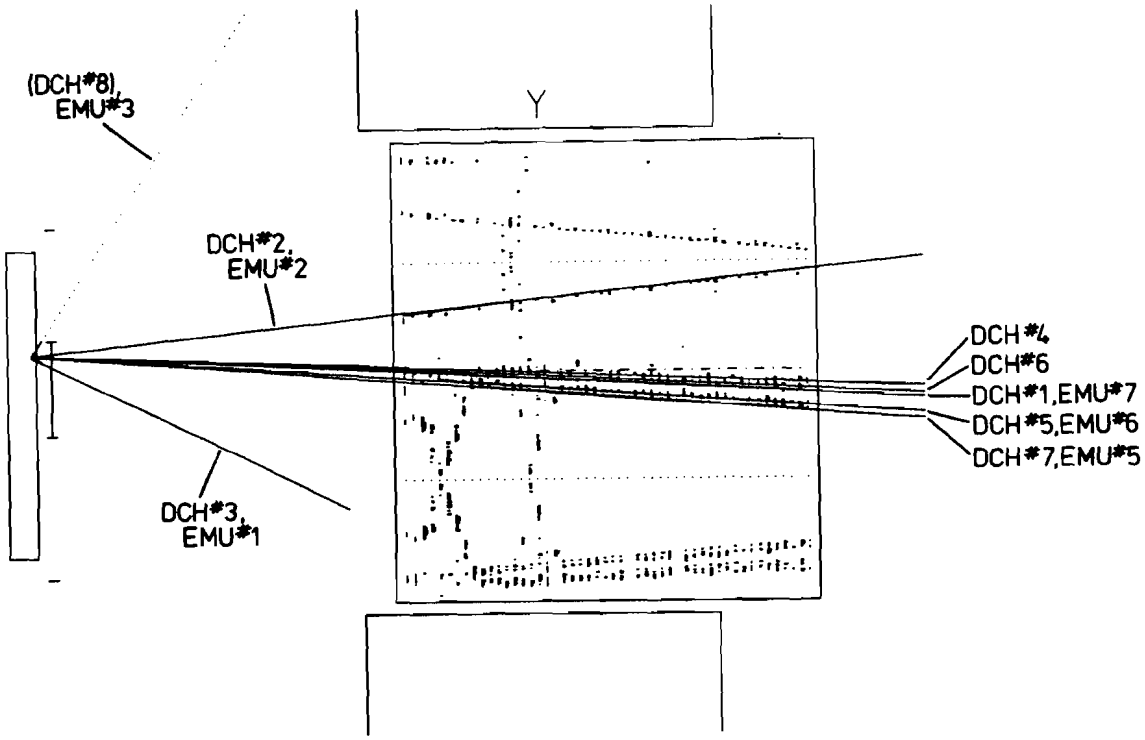

Figure # 36f

Event 1050 2844. This picture shows a computer-generated Y-view of the event as seen in the upstream part of the spectrometer. The neutrino beam is incident from the left. The CPI drift chamber hits (with images) are displayed. DCH track # 2 matched to EMU track # 2 is the only track which is well separated from the others and this happens to be the production μ^- . DCH track # 3 matched to EMU track # 1 is seen to be pointing out of the Y-acceptance of the spectrometer. This is the reason why the track was reconstructed as an upstream-only track in the spectrometer. (See other views.) The projection of EMU track # 3 (DCH # 8) is also seen to point outside the Y-acceptance of the spectrometer.

particularly evident in the U-view in which only the first two drift chambers are hit and and the last three are not. The steep angle is clearly seen. In the third upstream view, the X-view, the situation is much more confused. The tracks in this view form a narrow cone and there is no clear evidence of an un-reconstructed segment. Most likely, these strings of hits belong to a single track and that track must have a fairly small dx/dz but rather large dy/dz . The situation in the downstream drift-chambers is quite clean. A total of 6 un-ambiguous track segments could be found and all of them could be connected to upstream track segments resulting in the 6 excellent down-to-up fits. There are no additional track segments observed nor any extra hits to make them from. This suggests that the unique up-only drift chamber track is a *genuine* up-only track: that it is outside the acceptance of the analysing magnet. An interactive check on this shows that it is well within the X-view acceptance as well as the U-view acceptance but obviously heading into the magnet return yoke in the V-view. There is no clear confirmation of this in the CPI's unique Y-view. In that view, particles making their way through the acceptance of the magnet are found to gather into a narrow bundle of tracks above the lower sense-wire plane of the chamber. Only one particle is observed to go through, very well separated from the others, below the upper sense-wire plane of the device. In all, 4 CPI tracks could be fitted in the operator-aided mode of the programme.

Of the 6 emulsion tracks exiting the target, 5 could be un-ambiguously matched with drift-chamber tracks. Of these, 4 were down-to-up tracks and the fifth one is the up-only track directed into the magnet yoke. All three decay tracks from the trident were matched with down-to-up spectrometer tracks. This is *not* so typical, tridents may have tracks that either remain un-matched altogether or are matched to up-only spectrometer tracks. Usage of the interactive programme was made to project out the only emulsion track that could not be matched to any drift chamber track. As emulsion exit angles were not measured, production angles had to be used and an infinite momentum had to be assumed. This method can only give a crude approximation of where the track might have headed in the spectrometer as it neglects any curvature due to the magnetic field and does not take any multiple Coulomb scattering into account.§ Nevertheless, this projection (of EMU # 3) for which $dx/dz|_{prod} = .048 \pm .005$ and $dy/dz|_{prod} = +1.328 \pm .002$ clearly goes through the un-used strings of hits (described above) in the upstream U and V views. In the X-view, the projecion is in mid acceptance. In the V-view, the projection is still inside acceptance. In the U-view though, the projection is well outside acceptance as it heads for the magnet return yoke.

All of the 6 down-to-up drift-chamber tracks are observed to go through TOF II scintillator paddles. There are no additional un-matched TOF II hits. All paddle hits are single and one track (un-matched) even goes through the corner of a second side (and slightly more downstream) paddle (# 16) so that two single

§ The projection mode of the interactive programme was equipped with the software necessary to project tracks out of the emulsion and through the magnetic field. This was a very valuable tool in looking for tracks in busy areas or for tracks with special problems or for establishing limits to various parameters. As a general rule however, the simpler-minded infinite-momentum (straight-out) projections were always among the first things attempted for un-matched emulsion tracks.

TOF II hits are associated with it. This situation is, again, not so typical. More often than not, because of the high multiplicity of charged tracks in events, a single TOF II paddle will get hit sometimes with 2 but often with more than 2 tracks. † Also, it sometimes happens that there are additional TOF II paddles turned-on upstream of which there is only evidence of slow (curving in the low magnetic field region of the downstream drift-chambers) track segments for which all down-to-up connection attempts failed. These hits, usually well out-of-time with the rest of the event, can often be associated with electromagnetic energy deposited in the EPIC-PbG system and are very good candidates for electromagnetic-shower debris going *backwards* in the laboratory ("back-splash"). In that respect, this event is somewhat cleaner than usual.

Emulsion track # 2 which goes through two TOF II paddles, 16 and 17 , cannot be assigned an un-ambiguous particle-ID by TOF. In the case of the paddle 16 hit, the difference between the flight time calculated from the top tube timing information and the flight time derived from the known location of the hit in the paddle is 4.250 ***nanoseconds*** , more than one order of magnitude above the typical resolution of the system. This measurement is un-physical and it wasn't used. In order to compute the flight time, only the bottom tube timing measurement was then used. This measurement is compatible with a light particle going at $\beta = 1$ but no un-ambiguous I.D. can be obtained. The top and bottom timing measurements in paddle 17 which track # 2 also hits yield the same information: a fast light particle but no positive I.D. . In fact, there is nothing surprising with all this: the particle is a $p = 14.3\ GeV/c$ negatively charged (from bend in magnet) object coming from the primary vertex; a prime candidate for μ^- in $\nu\ nucleon \rightarrow \mu^- Charm$. The particle is not a hadron: it is minimum-ionizing in the three un-ambiguous views of the EPIC-PbG tubes, minimum-ionizing in the singly-hit PbG block behind it (S21, no evidence of initiation of hadronic shower), minimum-ionizing throughout the calorimeter (no evidence of hadronic shower: a 14 GeV/c hadron would, on average, record $\sim 28\ MI$, $\sim 23\ MI$ and $\sim 11\ MI$ after traversing $4\ in = 10.16\ cm$, $8\ in = 20.32\ cm$ and $12\ in = 30.48\ cm$ of steel.(See Section 4.6)) and turns both the muon-front and muon-back muon-tagging paddles on. On the basis of this evidence, this track was assigned the un-ambiguous I.D. of μ^- .

Emulsion track # 5 , the first trident track, goes through singly-hit TOF II paddle 13 . This $p = 1.5\ GeV/c$ track with positive electric charge is well within the TOF system resolution. If the particle were a π^+ , there is a 94% chance that it would have recorded a stop-time as measured in TOF II. Similarly, this probability is less than 1% if it were a K^+ or p . The kaon and proton ID's are therefore ruled-out. EPIC-PbG measurements (block L38) assign $E/P \sim .2 \ll 1$ so the e^+ I.D. is also ruled-out. Calorimeter EPIC planes are not of any use for this track because there is also a very-high energy track through the tubes involved. Also, if the particle were a μ^+ , thus not hadronically interacting, its momentum is too small for it to reach the muon-front paddle assembly and it would not have been expected to be record hit there. On the basis of these data, the I.D. can only be reduced to μ^+ / π^+ ambiguous. However, it turns

† The situation is not necessarily hopeless even if two charged particles go through a single paddle. Since the Y-location of the hits are known, independently instrumented top-tube and bottom-tube timing can be done. If more than 2 particles hit the same paddle, timing information is un-available.

out (see below) that the two down-to-up un-matched tracks can be tagged as e^+ and e^- . The inclusion of this constraint (in the determination of the start time of the event) in a re-fit of the TOF data rules the μ^+ I.D. out. So, finally, the particle is un-ambiguously identified as a $\underline{\pi}^+$ where the underline labels that un-ambiguous identification. This is a nice example of the non-linear nature of event fitting.

Emulsion track # 6 goes through TOF II paddle # 10. However, at $p = 7.7\ GeV/c$, the particle is too fast, whatever its ID, to be tagged by TOF. The EPIC-PbG system records $E/P \sim .5$, still too small for an electron but yet too large for a hadron, of that momentum, simply interacting in PbG block L37. So, after one minimum-ionizing worth of dE/dx energy is removed (to take the charged track into account) , a (block-only) gamma shower is hypothesised to have occured in L37. This accounts for the extra energy recorded. The energy of the γ involved is computed to be $2.92 \pm 0.27\ GeV$. Roughly 62% of the charged hadron's energy is deposited in the first calorimeter EPIC plane downstream of the PbG wall, which is quite typical of an $\sim 8\ GeV$ hadron. Neither mu-front nor mu-back counters aimed at recorded any signals, which, at this momentum, rules the muon I.D. out. All these data tag the particle as a hadron; the assigned I.D. is $\pi^+ \,/\, K^+ \,/\, p$ ambiguous.

Emulsion track # 7 goes through TOF II paddle #4 . This negatively charged particle with momentum of 3.1 GeV/c is, according to TOF measurements, very fast, so much that K^- and anything heavier is ruled out. There is only a 1% chance the measurements be compatible with a π^- but, although the track does not hit a PbG block as it is well outside acceptance of the PbG wall, it does fire two EPIC tubes. Both views pulse heights are consistent with minimum-ionizing which is very un-likely for a $p = 3.1\ GeV/c$ electron, ruling this I.D. out. No calorimeter energy can be associated with this track. The muon I.D. is also ruled out because, at that momentum, were the particle a μ^- , it whould have registered a muon-front hit. None was observed in the paddle it should have gone through. All these measurements force a unique ID; the particle is identified as a $\underline{\pi}^-$.

This does not exhaust all tracks. There remains 2 down-to-up un-matched tracks from oppositely charged particles. The positively charged particle goes through TOF II paddle #15 and TOF measurements for this soft ($p = 0.4\ GeV/c$) track are only compatible with a light mass particle, incompatible with any of the heavier $\pi^+ \,/\, K^+ \,/\, p$. This particle hits PbG block L39 and is tagged as e^+ with $E/P = 0.8$, a bit low but not inconsistent with a $p = 0.4\ GeV/c$ positron. The other un-matched track left by a negatively charged ($p = 0.7\ GeV/c$) particle, goes through TOF II paddle #5 and TOF measurements are incompatible with a particle of heavier mass than a pion, ruling-out the kaon (and anti-proton) I.D. Unfortunately it hits well outside of the PbG wall X-acceptance but still inside that of the EPIC planes upstream of it in which it records, on average, $\sim$ 10 times minimum-ionizing, quite compatible with a showering electron. In all likeliness, this particle is an electron. This is further supported by kinematical reconstruction of the hypothesis $\gamma \rightarrow e^+\ e^-$ for which the fitted invariant mass, using data from the two un-matched tracks, is $20 \pm 10\ MeV/c^2$. Scanbacks, to attempt to locate the conversion in the emulsion, on both of these tracks were requested and done. As it turned out, however, the conversion vertex could not be found and the location of the conversion still remains unknown. As was explained in the section dealing with gamma conversions, for purposes of corrections, it was hypothesised that this conversion occured halfway between

the charm decay vertex location and the downstream edge of the emulsion. This is because one *conversion length* is *outside* the emulsion volume. The fitted energy of this gamma turned out to be 1.43 ± 0.14 *GeV* .

The conversion and the block-only gamma discussed above are not the only gammas in this event. In fact, including these two, there is evidence for a total of 6 gammas in the event. The remaining 4 are discussed below.

There is an un-mistakable (no charged track nearby, no hadronic energy of neutral origin behind) EPIC-PbG gamma in block S27 with $E_{gamma} = 8.3 \pm 0.5$ *GeV* . Then, there is a much less energetic EPIC-PbG γ with $E_{\gamma} = 0.5 \pm .1$ *GeV* located in block S1. This gamma shares one EPIC V-view with another one in block S26 with $E_{gamma} = 1.1 \pm .2$ *GeV* . The last gamma observed is formed by a three-EPIC-only grouping slightly to the left of block S26 (outside the PbG wall X-acceptance). This grouping is consistent with a gamma because no charged tracks can be seen pointing in that direction and there are no un-used down-only segments in the drift-chambers nor is there any evidence for un-reconstructed ones. The energy of this γ is not measured but its spatial direction is very well known ($\pm.002$ *radian*). At best, by assuming it comes from the most probable decay configuration of $\pi^0 \rightarrow \gamma\gamma$, it is only possible to make an *estimate* of this energy to which a large error must be assigned. There is no other evidence for any additional γ in this event.

All two-gamma combinations (Section 4.4.4) are then computed and a total of 11 candidates for $\pi^0 \rightarrow \gamma\gamma$ are retained. Of these, 6 have their computed invariant mass between 100 MeV/c^2 and 200 MeV/c^2 and they constitute the best candidates. The energies of the 11 cover the range from just over 1 *GeV* to slightly above 11 *GeV* .

It is typical, at this stage of the analysis of an event, to proceed to checking the hadron calorimeter for evidence of hadronic showers of neutral origin: so-called neutral-showers. The hadron calorimeter is a very crude energy-measuring device (see Section 4.6). It is not much better at pattern recognition, but augmented with external information (from drift-chambers, PbG-EPIC, etc...), it can sometimes provide enough information for neutral-showers to be un-ambiguously detected. In this event, all bunched calorimeter EPIC's can be associated with close-by charged tracks except for three: A11, A12 and the one behind it B12. These form a close grouping consistent with a $E_{had} = 4.4 \pm 2.2$ *GeV* neutral hadron.

At this point, the analysis of the emulsion and spectrometer data is complete. The event is fed, as is, to the automatic kinematical fitting procedure. Fits are cycled over as is described in Section 7.1 . The first successful mass-constrained constrained fit † is:

$$D^+ \rightarrow \pi^+_{[7,5]}\ \pi^+_{[5,6]}\ \pi^-_{[1,7]}\ \pi^0_{[1(4)]}\ \pi^0_{[2(5)]}$$

$$\pi^0_{[1(4)]} \rightarrow \gamma(1)\ \gamma(5)$$

$$\pi^0_{[2(5)]} \rightarrow \gamma(2)\ \gamma(3)$$

† Labels of the type [i, j] subscripting charged tracks indicate spectrometer charged track "i" (McGill programme) matches emulsion track "j"while labels in parentheses subscripting neutrals are McGill labels and others refer to the equivalent OSU fit.

for which

$$P_{\perp}\ (with\ 2\ \pi^0) = 301 \pm 188\ MeV/c$$

$$\#\ of\ iterations = 4$$

$$C.L. = [Kinematics:\ .67, Kinematics\ \&\ TOF:\ .15]$$

$$P_{charm} = 23.148 \pm .375\ GeV/c$$

$$Proper\ decay\ time = (\ 3.48 \pm .06\ ) \times 10^{-13} sec$$

$$M_{unconstrained} = 1868 \pm 47\ MeV/c^2$$

$$Cabibbo\ factor = sc$$

while the second successful constrained fit is:

$$F^+ \rightarrow \pi^+_{[7,5]}\ \pi^+_{[5,6]}\ \pi^-_{[1,7]}\ \pi^0_{[1(4)]}\ \pi^0_{[2(5)]}$$

$$\pi^0_{[1(4)]} \rightarrow \gamma_{(1)}\ \gamma_{(5)}$$

$$\pi^0_{[2(5)]} \rightarrow \gamma_{(2)}\ \gamma_{(3)}$$

for which

$$P_{\perp}\ (with\ 2\ \pi^0) = 301 \pm 188\ MeV/c$$

$$\#\ of\ iterations = 6$$

$$C.L. = [Kinematics:\ .19, Kinematics\ \&\ TOF:\ .04]$$

$$P_{charm} = 24.631 \pm .425\ GeV/c$$

$$Proper\ decay\ time = (\ 3.45 \pm .06\ ) \times 10^{-13} sec$$

$$M_{unconstrained} = 1868 \pm 47\ MeV/c^2$$

$$Cabibbo\ factor = cc$$

In addition to these, Cabibbo favored "zero-constraint" calculations were done for the following hypotheses:

$$I: \quad F^+ \rightarrow \pi^+\ \pi^+\ \pi^-\ (\pi^0)$$

$$II: \quad F^+ \rightarrow \pi^+\ K^+\ \pi^-\ (\overline{K}^0)$$

$$III: \quad D^+ \rightarrow \pi^+\ \pi^+\ \pi^-\ (\overline{K}^0)$$

$$IV: \quad \Lambda_c^+ \rightarrow \pi^+\ p\ \pi^-\ (\overline{K}^0)$$

in order to determine the momenta and directions of the neutrals and to check these informations against the experimental evidence. In case # I, there were two solutions: in the first, one needs a fast ($p = 16\ GeV/c$) π^0 which should have been seen in the EPIC-PbG system but wasn't while in the second solution, one needs a slow ($p = 1\ GeV/c$) π^0 which is un-observable. In all other cases (II III & IV), the minimum mass allowed by the "zero-constraint" curve was above the mass of the hypothesised parent and neutrals required by all "solutions" *at* the minimum of the curves should have been observed in the spectrometer, but weren't.

In view of all the facts outlined ‡ above, only the two fully constrained fits were retained and the event

‡ All data measured by E531 on this event (and every other event recorded during both runs) are stored on an easily accessible magnetic information library (database). Fits to the charged sample are stored in a similar fashion and are also software-accessible.

is D^+ F^+ ambiguous. The D^+ fit is singly Cabibbo un-favored while the F^+ fit is doubly Cabibbo favored. These fits are listed as entries 13, 1, 1 and 13, 1, 2 in the Table of Charged Ambiguous Decays (Part II) Section 10.3 ...

8.0) COMBINED FIRST AND SECOND RUN ANALYSIS: LIFETIMES

In this section, the analysis of the charged datasets for lifetimes of charmed particles is described. The results from both runs of E531 together with the results from the combination of the datasets of the two runs will also be given. A large amount of attention will be given to exposing the exact details of the statistical procedures used for extraction of lifetimes from the pure and contaminated samples. The statistical soundness, that is, the applicability of the methods will be demonstrated via Monte Carlo techniques.

The combined charged dataset of the First and Second run is presented in Section 10 . A total of 6 $F^{+\,or\,-}$ mesons were re-constructed and all of these are fully constrained and none have more than one hypothesis. Also, a total of 13 decays of Λ_c^+ were re-constructed. Of these, 8 are fully constrained, only two decays have more than one hypothesis (none have more than two) and all have an identified baryon in the final state. One decay of a D^- was un-ambiguously re-constructed. It has two D-meson hypotheses. A total of 27 other charged decays have hypotheses which are ambiguous between $D^{+\,or\,-}$, $F^{+\,or\,-}$ and Λ_c^+ . Most of the 27 charged ambiguous events are two- or three-fold ambiguous. It will be shown in the next few sections that a majority of these are charged D-meson decays. Finally, 58 decays of the neutral D-meson were re-constructed.

Pure samples of $F^{+\,or\,-}$, Λ_c^+ and D^0 are each fitted using a single-parameter: the lifetime of the decaying state. The ambiguous charged sample is fitted using two-parameters: the lifetime of the main contributor to the sample and the fraction of shorter-lived contaminant. The following sections explain each of the methods.

8.1) The single-parameter fits to the un-ambiguous samples

8.1.1) Single-parameter maximum log-likelihood method

Let p_j be the probability distribution function of all the H_j hypotheses of a given event j . It is appropriate to write this quantity first because of the fact that the un-ambiguous sample is comprised of a set of events each having one or more different hypotheses to decays of a single species. The very fact that it is not known *a priori* what the probability distribution function for the whole event j is, forces one into the palliative method of assigning weights. [161] So, let f_{ij} be the probability distribution function of the i^{th} hypothesis in the j^{th} event while w_{ij} is the weight associated with that i^{th} hypothesis of the same j^{th} event. Then one can write

$$p_j = \sum_{i=1}^{H_j} w_{ij}\, f_{ij}$$

where H_j is the number of different hypotheses for the j^{th} event. Since the events are assumed to be independent of each other, the total probability of observing a set of N_{evts} such events, the *likelihood*, is the product of all the individual probabilities:

$$L = \prod_{j=1}^{N_{evts}} p_j$$

and in accordance to the log-likelihood method, the log-likelihood function is

$$\ln L = \sum_{j=1}^{N_{evts}} \ln p_j$$

or

$$\ln L = \sum_{j=1}^{N_{evts}} \ln \left(\sum_{i=1}^{H_j} w_{ij} f_{ij} \right).$$

At this point, the experimental probability distribution function f_{ij} should be defined in more details. It is formed by the combination integral of three independent probability density distributions. The first part is given by:

$$\tilde{f}_1(t_{ij}) = \frac{1}{\tau} \exp\left(\frac{-t_{ij}}{\tau}\right)$$

which is re-written in terms of the experimentally determined quantities with the help of $l = \beta\gamma ct$ and $p = m\beta\gamma$ as

$$\tilde{f}_1(m, p_{ij}, c; l_j) = \frac{1}{\tau} \exp\left(\frac{-ml_j}{p_{ij}c\tau}\right)$$

which is just the probability distribution function of the proper decay times in the rest frame of a quantum state expressed in terms of the observed variables l_j and p_{ij} . These are respectively the decay length and the fitted momentum of the i^{th} hypothesis in the j^{th} event. The known parameters are m , the constrained mass of the particle and c , the speed of light. The other parameter: τ , the mean proper decay time of that particle in its rest frame (the *lifetime*) , is the only unknown parameter and is to be determined by the method of maximizing the log-likelihood function.

The second part is given by:

$$\tilde{f}_2(l_j) = \epsilon(l_j)$$

where $\epsilon(l_j)$ is the experimental charm finding efficiency and is a function of the decay of length l_j . This function, as described elsewhere, depends on the scanning group and the method of search employed.

The third part is given by:

$$\tilde{f}_3(l^j_{short}, l^j_{long}; l_j) = \theta(l^j_{short}, l^j_{long}; l_j)$$

where θ is a cut-off function such that:

$$\theta = 0 \qquad for\ l_j < l^j_{short}\ \ or\ \ l_j > l^j_{long}$$

while

$$\theta = 1\ \ otherwise.$$

The cut-off function is really very distinct from the charm finding efficiency function although the efficiency may also exhibit similar behaviour at long and short decay lengths, but for other reasons. The function θ is meant to represent the effect of the shortest and the longest possibly observable decay lengths in a particular event. The shortest possible decay length l^j_{short} in the j^{th} event reflects the apparent size of the primary vertex and also the forwardness of the vertex. The region close to the production vertex is known as the *confusion region.* As all the tracks come to one single point where the incoming ν or $\overline{\nu}$ interacted with a

nucleon, it becomes difficult to tell one track from another due to the finite resolution of the emulsion. In this experiment, this has been parametrized as [162] :

$$l^j_{short} = \left[\frac{(N_h{}^j + N^j_s/2)}{4} + 1.80\right] \mu m$$

where N^j_h is the number of nuclear recoil and breakup tracks and N^j_s the number of showering tracks in the j^{th} event. The first term describes the interaction's apparent size while the second term, a constant, describes the forwardness of ν-interactions. The longest possible decay length l^j_{long} essentially reflects the location of the production vertex in the emulsion volume: the emulsion stack is finite in its extent along the direction of flight of the decaying charmed particle. The distance l^j_{long} is known as the *potential path* as it is the amount of track length the charmed particle would have travelled in the emulsion if it had not decayed. Care is taken to remove any inter-module gaps and to add the distance travelled inside the changeable sheet.

It could possibly be argued that there should be a fourth part to the combination integral namely one that takes care of the measurement error associated with the decay lenght l_j . However, this potential additional complication is not significant since the statistical errors on the lifetimes are much bigger than the measurement errors associated with each of the individual proper decay times. A Monte Carlo procedure by which the input decay lengths and momenta of all events have been varied within their assumed Gaussian errors has shown that measurement errors have negligible effect on the lifetime. See *Ref.* 163 and Section 8.1.5.2 .

So, the combination integral reads:

$$f_{ij} = -K\int_0^\infty \tilde{f}_1(m, p_{ij}, c; (l_j + l')) \; \tilde{f}_2(l_j + l') \; \tilde{f}_3(l^j_{short}, l^j_{long}; (l_j + l')) \; dl'$$

or

$$f_{ij} = -\frac{K}{\tau}\int_0^\infty \exp\left(\frac{-m\;(l_j + l')}{p_{ij}\;c\tau}\right) \; \epsilon(l_j + l') \; \theta(l^j_{short}, l^j_{long}; l_j + l') \; dl'$$

where K is the normalization constant and f_{ij} really stands for $f_{ij}(l^j_{short}, l^j_{long}, m, c, \tau; l_j, p_{ij})$. For the sake of convenience only, this can be re-written in terms of $t = ml/pc$ so that now one has:

$$f_{ij}(t^j_{short}, t^j_{long}; t_{ij}) = -\frac{K}{\tau}\int_0^\infty \exp\left(\frac{-t_{ij} + t'}{\tau}\right) \; \epsilon(t_{ij} + t') \; \theta(t^j_{short}, t^j_{long}; t_{ij} + t') \; dt'.$$

This simplifies into:

$$f_{ij}(t^j_{short}, t^j_{long}; t_{ij}) = -\frac{K}{\tau}\,\theta(t^j_{short}, t^j_{long}; t_{ij}) \; \epsilon(t_{ij}) \; \exp\left(\frac{-t_{ij}}{\tau}\right) \; I(t^j_{short}, t^j_{long})$$

where

$$I(t^j_{short}, t^j_{long}) = \int_0^\infty \epsilon(t') \; \exp\left(\frac{-t'}{\tau}\right) \; \theta(t^j_{short}, t^j_{long}; t') \; dt' = \int_{t^j_{short}}^{t^j_{long}} \epsilon(t') \; \exp\left(\frac{-t'}{\tau}\right) \; dt'.$$

In practice, the quantity $I(t^j_{short}, t^j_{long})$ is computed from the efficiency function $\epsilon(t = ml/pc)$. As is explained in Section 5.1.1 , this function is known in N^j_{eff} *efficiency regions* of different but constant efficiencies ϵ_n . Thus, $I(t^j_{short}, t^j_{long})$ is obtained in the following way:

$$I(t^j_{short}, t^j_{long}) \approx \sum_{n=1}^{N^j_{eff}} \int_{t^n_{short}}^{t^n_{long}} \epsilon_n \; \exp\left(\frac{-t'}{\tau}\right) \; dt' = \sum_{n=1}^{N^j_{eff}} \epsilon_n \int_{t^n_{short}}^{t^n_{long}} \exp\left(\frac{-t'}{\tau}\right) \; dt'.$$

This becomes:

$$I(t^j_{short}, t^j_{long}) \approx \tau \sum_{n=1}^{N^j_{eff}} \epsilon_n \left[\exp\left(\frac{-t^n_{short}}{\tau}\right) - \exp\left(\frac{-t^n_{long}}{\tau}\right) \right] = \tau S(N^j_{eff})$$

where $S(N^j_{eff})$ is just a shorthand for the sum. So the combination integral now reads:

$$f_{ij}(t^j_{short}, t^j_{long}; t_{ij}) = -K\, S(N^j_{eff})\, \theta(t^j_{short}, t^j_{long}; t_{ij})\, \epsilon(t_{ij})\, \exp\left(\frac{-t_{ij}}{\tau}\right).$$

The usual nomalization condition

$$\int_0^\infty f_(t^j_{short}, t^j_{long}; t)\, dt = 1$$

being imposed sets the value of K such that:

$$\frac{1}{K} = -S(N^j_{eff}) \int_{t_{short}}^{t_{long}} \epsilon(t)\, \exp\left(\frac{-t}{\tau}\right)\, dt = -\tau S^2(N^j_{eff}).$$

Finally, one can substitute for K in the original expression of the probability density function so that

$$f_{ij}(t^j_{short}, t^j_{long}; t_{ij}) = \frac{\theta(t^j_{short}, t^j_{long}; t_{ij})\, \epsilon(t_{ij})\, \exp\left(\frac{-t_{ij}}{\tau}\right)}{\tau\, S(N^j_{eff})}$$

or

$$f_{ij}(t^j_{short}, t^j_{long}; t_{ij}) = \frac{\epsilon(t_{ij})\, \exp\left(\frac{-t_{ij}}{\tau}\right)}{\tau\, S(N^j_{eff})} \quad for\ t^j_{short} \le t_{ij} \le t^j_{long}\ \ and\ 0\ otherwise.$$

Note that if all the $\epsilon_n = 1$,that is if the charm finding efficiency is unity everywhere, then one has:

$$\lim_{\epsilon_n \to 1\ \forall n} f_{ij}(t^j_{short}, t^j_{long}; t_{ij}) = \frac{\exp\left(\frac{-t_{ij}}{\tau}\right)}{\tau \left[\exp\left(\frac{-t^j_{short}}{\tau}\right) - \exp\left(\frac{-t^j_{long}}{\tau}\right) \right]} \quad for\ t^j_{short} \le t_{ij} \le t^j_{long}$$

$$= 0 \qquad otherwise.$$

This form is the *double truncated* exponential distribution [164] . Furthermore, in the limit of an infinite emulsion resolution and width:

$$\lim_{\substack{\epsilon_n \to 1\ \forall n \\ t^j_{short} \to 0 \\ t^j_{long} \to \infty}} f_{ij}(t^j_{short}, t^j_{long}; t_{ij}) = \frac{1}{\tau} \exp\left(\frac{-t_{ij}}{\tau}\right) .$$

one recovers the familiar exponential distribution.

Given the appropriate form for $f_{ij}(t^j_{short}, t^j_{long}; t_{ij})$, the principle of Maximum-Likelihood calls for finding τ_{mle} , the maximum-likelihood estimate of the single unknown parameter τ such that:

$$\frac{\partial}{\partial \tau} \ln L\,|_{\tau_{mle}} = 0 \quad and \quad \frac{\partial^2}{\partial \tau^2} \ln L\,|_{\tau_{mle}} < 0$$

This is readily done numerically by varying τ over its physical range by small finite steps of size $\Delta\tau = .005 \times 10^{-13} sec$ and by looking for an absolute maximum in $\ln L(\tau)$. In principle, care must be taken to avoid selecting a local maximum over some absolute maximum out of the currrent search range. However, in practice, none of the first run nor of the second run data exhibit any multiple maxima over a range of lifetimes rougly one order of magnitude smaller or bigger than the expected value for the maximum-likelihood estimate of the lifetime.

So called, *one-sigma* errors on the maximum likelihood estimate of the lifetime are computed by numerically solving the following equations for $\tau^{1\sigma}_{low}$ and $\tau^{1\sigma}_{high}$:

$$L(\tau^{1\sigma}_{low}) = exp(-1/2)L(\tau_{mle}) \qquad for\ \tau^{1\sigma}_{low} \leq \tau_{mle}$$

and

$$L(\tau^{1\sigma}_{high}) = exp(-1/2)L(\tau_{mle}) \qquad for\ \tau^{1\sigma}_{high} \geq \tau_{mle}.$$

The *two-sigma* errors are found by numerically solving:

$$L(\tau^{2\sigma}_{low}) = exp(-2)L(\tau_{mle}) \qquad for\ \tau^{2\sigma}_{low} \leq \tau_{mle}$$

and

$$L(\tau^{2\sigma}_{high}) = exp(-2)L(\tau_{mle}) \qquad for\ \tau^{2\sigma}_{high} \geq \tau_{mle}.$$

The reason for this is better seen if the likelihood function happenened to be Gaussian (as in the hypothetical limit of infinite statistics). The solutions would correspond exactly to one and two-sigma errors since for such a Gaussian distribution $G(x) \equiv G(\overline{x}, \sigma; x)$:

$$\ln G(\overline{x} + n\sigma) = \ln(G(\overline{x})) - n^2/2$$

or

$$\ln G(\overline{x} + n\sigma) = \ln((G^{max})) - n^2/2$$

where $\overline{x}$ is the expectation value of x and n is the number of σ away from $\overline{x}$. It is well known that the Gaussian integral probability $P_G(\overline{x} - n\sigma \leq x \leq \overline{x} + n\sigma) = \Gamma$ gives, for $n = 1$, $\Gamma = 68.3\%$ and for $n = 2$, $\Gamma = 95.4\%$ while for $n = 3$, it is up to $\Gamma = 99.7\%$. However, in our case, the likelihood function is not Gaussian and the corresponding log-likelihood function typically has a long tail extending to high values of τ such that:

$$(\tau_{mle} - \tau^{1\sigma}_{low}) \leq (\tau^{1\sigma}_{high} - \tau_{mle})$$

and

$$(\tau_{mle} - \tau^{2\sigma}_{low}) \leq (\tau^{2\sigma}_{high} - \tau_{mle}).$$

Still, the integral or probability content of the n-sigma interval is approximately the same [165] .

Asymmetric errors are to be expected because of the nature of the exponential probability density function. This will be illustrated below by way of an example. For the sake of argument only, make the

simplifications that there is a single hypothesis to any j^{th} event and that all efficiencies are unity everywhere in an emulsion stack infinite in extent and resolution, then:

$$f_j = \frac{1}{\tau} \exp\left(\frac{-t_j}{\tau}\right).$$

The joint probability, is then simply

$$L = \prod_{j=1}^{N_{evts}} \frac{1}{\tau} \exp\left(\frac{-t_j}{\tau}\right).$$

and the log-likelihood function is:

$$\ln L = -N_{evts} \ln \tau - \sum_{j=1}^{N_{evts}} \left(\frac{t_j}{\tau}\right).$$

Applying the principle of Maximum-Likelihood as described before, yields the intuitive result

$$\tau_{mle} = \frac{1}{N_{evts}} \sum_{j=1}^{N_{evts}} t_j = \bar{t}.$$

In such a simple case, the maximum-likelihood estimate of τ is the average of the proper decay times. Upon using this result in the n-sigma equation,

$$L(\tau_{n\sigma}) = \exp\left(\frac{-n^2}{2}\right) L(\tau_{mle})$$

one eventually gets

$$\frac{1}{\zeta} + \ln \zeta = 1 + \frac{n^2}{2N_{evts}}$$

where $\zeta = \tau_{n\sigma}/\tau_{mle}$. Figure # 37 depicts the quantity

$$f(\zeta) = \frac{1}{\zeta} + \ln \zeta - 1 - \frac{n^2}{2N_{evts}}$$

for $N_{evts} = 6, 13$ *and* 28 ; $n = 1$. The two intersections of $f(\zeta)$ with $y = 0$ yield the two solutions for the 1-sigma errors. For the case of $N_{evts} = 6$, as it is for F-meson sample for example, one has

$$\frac{\tau_{low}^{1\sigma}}{\tau_{mle}} \approx 0.68 \quad \textit{and} \quad \frac{\tau_{high}^{1\sigma}}{\tau_{mle}} \approx 1.55$$

so that

$$(\tau_{mle} - \tau_{low}^{1\sigma})/\tau_{mle} \approx 1.00 - 0.68 = 0.32$$

$$(\tau_{high}^{1\sigma} - \tau_{mle})/\tau_{mle} \approx 1.55 - 1.00 = 0.55$$

which supports the previous observation:

$$(\tau_{mle} - \tau_{low}^{1\sigma}) \leq (\tau_{high}^{1\sigma} - \tau_{mle}).$$

The above example is an indication of what to expect from the statistics of the problem. In all cases, the described behaviour continues for higher sigma-errors but is certainly less pronounced as the number of data increases.

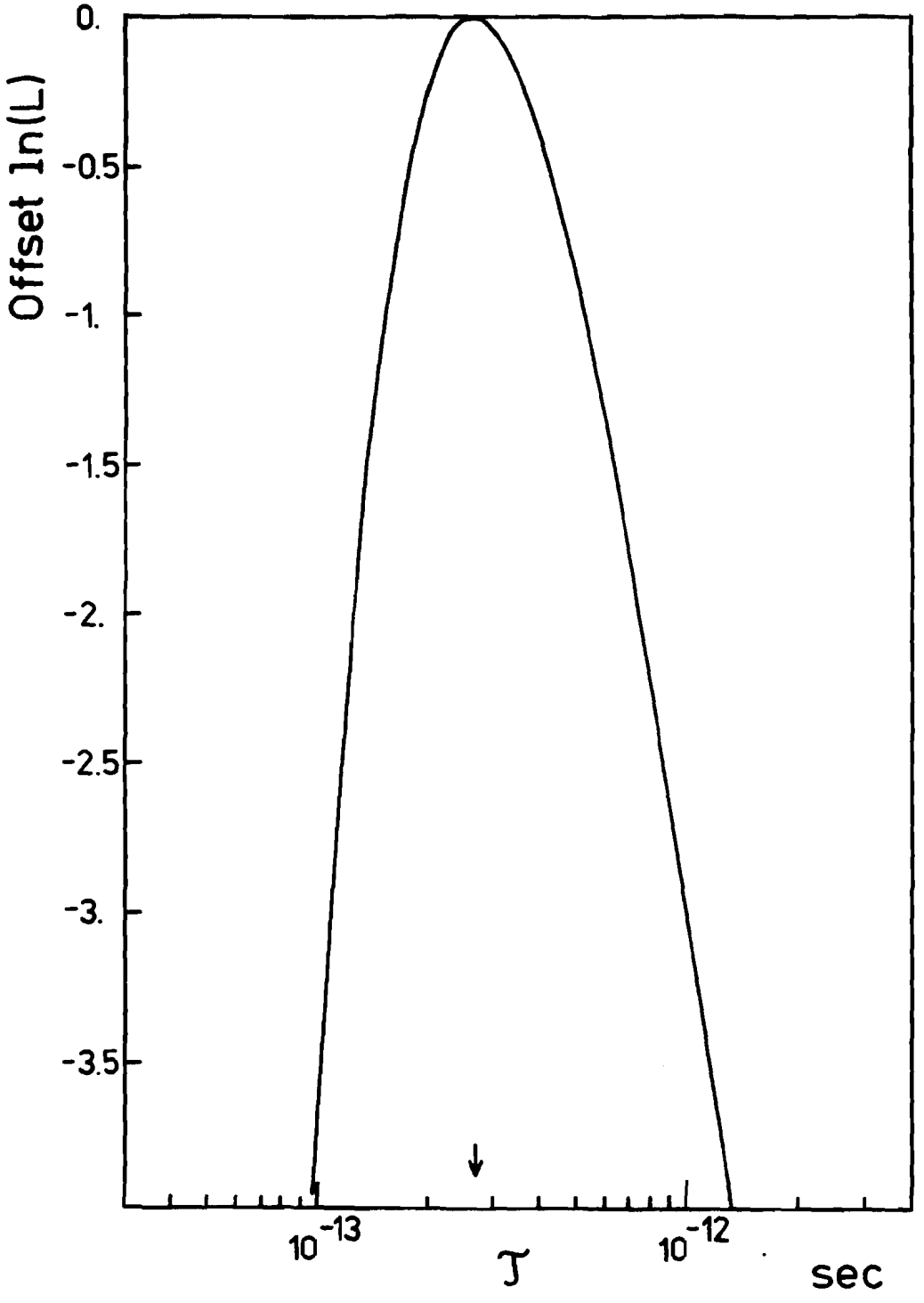

Figure # 38
Log-likelihood function for the 6 F-mesons plotted against its unique parameter: τ . The function is *offset* by the value at its maximum. The location of the maximum is indicated by the arrow.

8.1.2) **The lifetime of the F^{+or-} meson**

The method described in the previous section was applied only to the sum of the 1^{st} and 2^{nd} Run data. † From Section 10 the total number of un-ambiguous F meson decays from the 1^{st} and 2^{nd} run is $4+2=6$. The result is:

$$\tau_{F^{+or-}} = 2.6^{+1.6+4.8}_{-0.9-1.4} \times 10^{-13} sec$$

where the first and second errors quoted are both *statistical* and are respectively the one-sigma and two-sigma equivalent errors. Figure # 38 depicts the F meson Log-Likelihood function offset by the value at its maximum. Thus, one-sigma equivalent errors are located at $y=-1/2$ and two-sigma equivalent errors are located at $y=-2$ on this figure. All the F^{+or-} events are fully constrained.

As all the fits were always separately performed with the mass of the charm parent constrained and then un-constrained, it is possible to quote a mass for the F-meson. The weighted average of the un-constrained masses of the 6 un-ambiguous F^{+or-} decays is $1974 \pm 14\ MeV/c^2$.

8.1.3) **The lifetime of the Λ_c^+ baryon**

The result of the one-parameter maximum-likelihood fit to the subset of the 5 events from the 2^{nd} Run alone is

$$\tau_{\Lambda_c^+} = 1.6^{+1.0+3.0}_{-0.6-0.9} \times 10^{-13} sec$$

The same one-parameter maximum-likelihood method applied to the total of 13 1^{st} + 2^{nd} Run un-ambiguous Λ_c^+ baryon decays gives:

$$\tau_{\Lambda_c^+} = 2.0^{+0.7+1.7}_{-0.5-0.8} \times 10^{-13} sec$$

using the usual notation for one-sigma and two-sigma *statistical* errors. Figure # 39 depicts the Λ_c^+ baryon Log-Likelihood function offset by its maximum value. As always, one-sigma equivalent errors are located at $y=-1/2$ and two-sigma equivalent errors are located at $y=-2$ on the figure. The weighted average of the un-constrained masses from 8 fits out of the 13 Λ_c^+ fits is $2267 \pm 13\ MeV/c^2$, the other fits are "zero-constrained".

8.1.4) **Single-parameter Monte Carlo simulation**

The one-parameter maximum-likelihood method to extract lifetimes out of pure samples of particles like F^{+or-} and Λ_c^+ is a well travelled route. [166] It would be of great interest be able to make some independent check of the output of such a method of calculation. However, as this is quite impossible one must resort to the well known method of random sampling. This section describes a Monte Carlo procedure by which the output of the single-parameter maximum log-likelihood method can be checked.

The object of this particular *simulation* is limited to providing the statistical significance of the output of the one-parameter Maximum-Likelihood estimation. No attempt was made to reproduce the actual raw data

† There were only 2 second run un-ambiguous F^{+or-} decays. Trying to extract the lifetime from too small a sample could lead to erroneous conclusions just because of statistical fluctuations in the sample. Thus, for the F-meson, only the combined 1^{st} and 2^{nd} run dataset is considered.

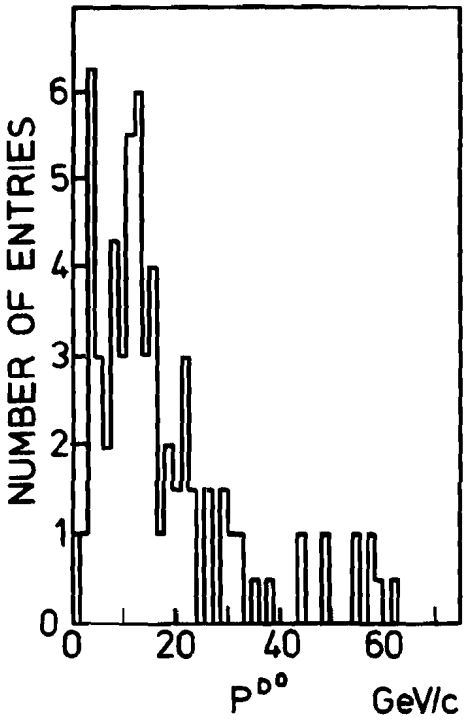

Figure # 40
Distribution of the weighted D^0 momenta. The momentum bin width is 1.5 GeV/c .

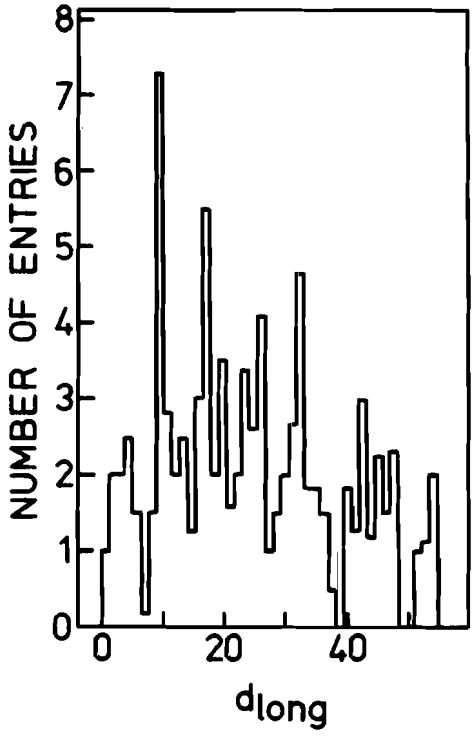

Figure # 42
Potential path distribution of all charm decays. The bin width is 1250 μm .

like the momentum distributions in the drift chambers or the distributions of other key variables. Rather, since these distributions were measured by this experiment and are therefore known, use was made of them. Thus, the simulation could be enacted at a much later stage where already several key variables have been integrated over their respective response function.

To illustrate this, consider the distribution of measured momenta P_{msrd} . Schematically one can write:

$$P_{msrd} = \int_D g(x)\, p(x)\, dx$$

where $p(x)$ is the *physical* distribution of momenta while $g(x)$ is the *response* of the spectrometer-emulsion over all possible relevant experimental variables collectively denoted by x while D stands for their collective range. The integral is over all variables belonging to the set x . Even if $p(x)$ had been available, the formidable task of determining $g(x)$ is, in the present context, not really justified; P_{msrd} is simply obtained from the data. More explicitly, a pseudo-random variable $\tilde{P}$ is generated from the experimental distribution of P_{msrd} such that in the limit of infinite statistics, all moments of the distribution of $\tilde{P}$ are numerically equal to those of the distribution of P_{msrd} . This procedure has been referred to, in another context, as a *hybrid* Monte-Carlo method [167] . In this section, "~" stands for variables that are generated from experimental distributions.

The only parameters that are input to the procedure, that is to say, *a priori* known are: the mass M_c of the decaying particle, its mean proper decay time τ , and N_{evts} , the total number of events to be generated. The algorithm then proceeds to randomly sample several variables from the sum of the 1^{st} and 2^{nd} run data. The charm momentum $\tilde{P}_c^j$ as measured in the spectrometer is first sampled. If the particle is a meson, the weighted D^0 momentum spectrum (Figure # 40) † is used and the momentum is scaled according to

$$\tilde{P}_{\substack{D^{+\,or\,-} \\ F^{+\,or\,-}}} = M_{\substack{D^{+\,or\,-} \\ F^{+\,or\,-}}} \times \frac{\tilde{P}_{D^0}}{M_{D^0}}.$$

This is done in order to avoid small sample size problems in the case of the $F^{+\,or\,-}$ or possible short-lived contamination in the case of $D^{+\,or\,-}$ (more on this later...). If the particle is a baryon, the Λ_c^+ weighted momentum spectrum is used (see Figure # 41). The weight used in both Figure # 40 and Figure # 41 is $W = w_{ij}$ using the notation of Section 8.1.1 . Also sampled from the data are the shortest and longest possible decay lengths $\tilde{l}^j_{short}$ and $\tilde{l}^j_{long}$. The distribution of $\tilde{l}^j_{long}$ is displayed on Figure # 42 . In addition, the *scanning group and emulsion type* is randomly selected according to the frequency of contribution as different scanning groups entail different charm finding efficiency functions ϵ . Figure # 43 shows the distribution of found events among the different scanning groups and emulsion types.

At this point, a pseudo-random variable $\tilde{t}_j$ is generated such that its distribution will satisfy

$$f_j(\tilde{t}^j_{short}, \tilde{t}^j_{long}; \tilde{t}_j) = \frac{\epsilon(\tilde{t}_j)\, \exp\left(\frac{-\tilde{t}_j}{\tau}\right)}{\tau\, S(N^j_{eff})} \; for \; \tilde{t}^j_{short} \leq \tilde{t}_j \leq \tilde{t}^j_{long} \; and \; 0 \; otherwise$$

† The analysis of the E531 D^0 *and* $\overline{D}^0$ data can be found in *Ref.* 168

where, for convenience, all lengths have been converted to times. In order to do this, the generator relies on the following method: a pseudo-random number ς_j with flat (equally probable) distribution in the interval $[0, 1]$ is first generated and then, the following equation is solved:

$$\varsigma_j = \int_{\tilde{t}^j_{short}}^{\tilde{t}^j} f_j(\tilde{t}^j_{short}, \tilde{t}^j_{long}; t)\, dt.$$

This is

$$\varsigma_j = \int_{\tilde{t}^j_{short}}^{\tilde{t}^j} \frac{\epsilon(t)\, \exp\left(\frac{-t}{\tau}\right)}{\tau\, S(N^j_{eff})}\, dt$$

which can be re-written in terms of the efficiency regions as

$$\varsigma_j = \sum_{n=1}^{l-1} \left[\frac{\varepsilon_n}{S(N^j_{eff})} \int_{t^n_{short}}^{t^n_{long}} \frac{1}{\tau} \exp\left(\frac{-t}{\tau}\right)\, dt \right] + \frac{\varepsilon_l}{S(N^j_{eff})} \int_{t^l_{short}}^{\tilde{t}_j} \frac{1}{\tau} \exp\left(\frac{-t}{\tau}\right)\, dt$$

where l denotes that particular efficiency region for which $t^l_{short} \leq \tilde{t}_j \leq t^l_{long}$. Performing integrations yields:

$$\varsigma_j = \sum_{n=1}^{l-1} \left\{ \frac{\varepsilon_n}{S(N^j_{eff})} \left[\exp\left(\frac{-t^n_{short}}{\tau}\right) - \exp\left(\frac{-t^n_{long}}{\tau}\right) \right] \right\} + \frac{\varepsilon_l}{S(N^j_{eff})} \left[\exp\left(\frac{-t^l_{short}}{\tau}\right) - \exp\left(\frac{-\tilde{t}_j}{\tau}\right) \right]$$

which can be re-written as

$$\varsigma_j = T(l-1) + \frac{\varepsilon_l}{S(N^j_{eff})} \left[\exp\left(\frac{-t^l_{short}}{\tau}\right) - \exp\left(\frac{-\tilde{t}_j}{\tau}\right) \right]$$

where $T(l-1)$ is just a shorthand for the sum. The solution is:

$$\tilde{t}_j = -\tau \ln \left\{ \exp\left(\frac{-t^l_{short}}{\tau}\right) - \frac{S(N^j_{eff})}{\varepsilon_l} [T(l-1) - \varsigma_j] \right\}$$

In the limit of charm-finding efficiency ϵ being unity everywhere

$$S(N^j_{eff}) = \left[\exp\left(\frac{-\tilde{t}^j_{short}}{\tau}\right) - \exp\left(\frac{-\tilde{t}^j_{long}}{\tau}\right) \right]$$

and the sum " T " reduces to a single term so that

$$\lim_{\epsilon_n \to 1\ \forall n} \tilde{t}_j = -\tau \ln \left\{ \exp\left(\frac{-\tilde{t}^j_{short}}{\tau}\right) - \varsigma_j \left[\exp\left(\frac{-\tilde{t}^j_{short}}{\tau}\right) - \exp\left(\frac{-\tilde{t}^j_{long}}{\tau}\right) \right] \right\}$$

That situation would correspond to a simple cut-off exponential distribution of the proper decay times. In order to check this, using the same method as above, one solves:

$$\varsigma_j = \int_{\tilde{t}^j_{short}}^{\tilde{s}_j} \frac{\exp(-t/\tau)}{\tau \left[\exp\left(-\tilde{t}^j_{short}/\tau\right) - \exp\left(-\tilde{t}^j_{long}/\tau\right) \right]}\, dt$$

to find

$$\tilde{s}_j = -\tau \ln \left\{ \exp\left(-\tilde{t}^j_{short}/\tau\right) - \varsigma_j \left[\exp\left(-\tilde{t}^j_{short}/\tau\right) - \exp\left(-\tilde{t}_{long}/\tau\right) \right] \right\}$$

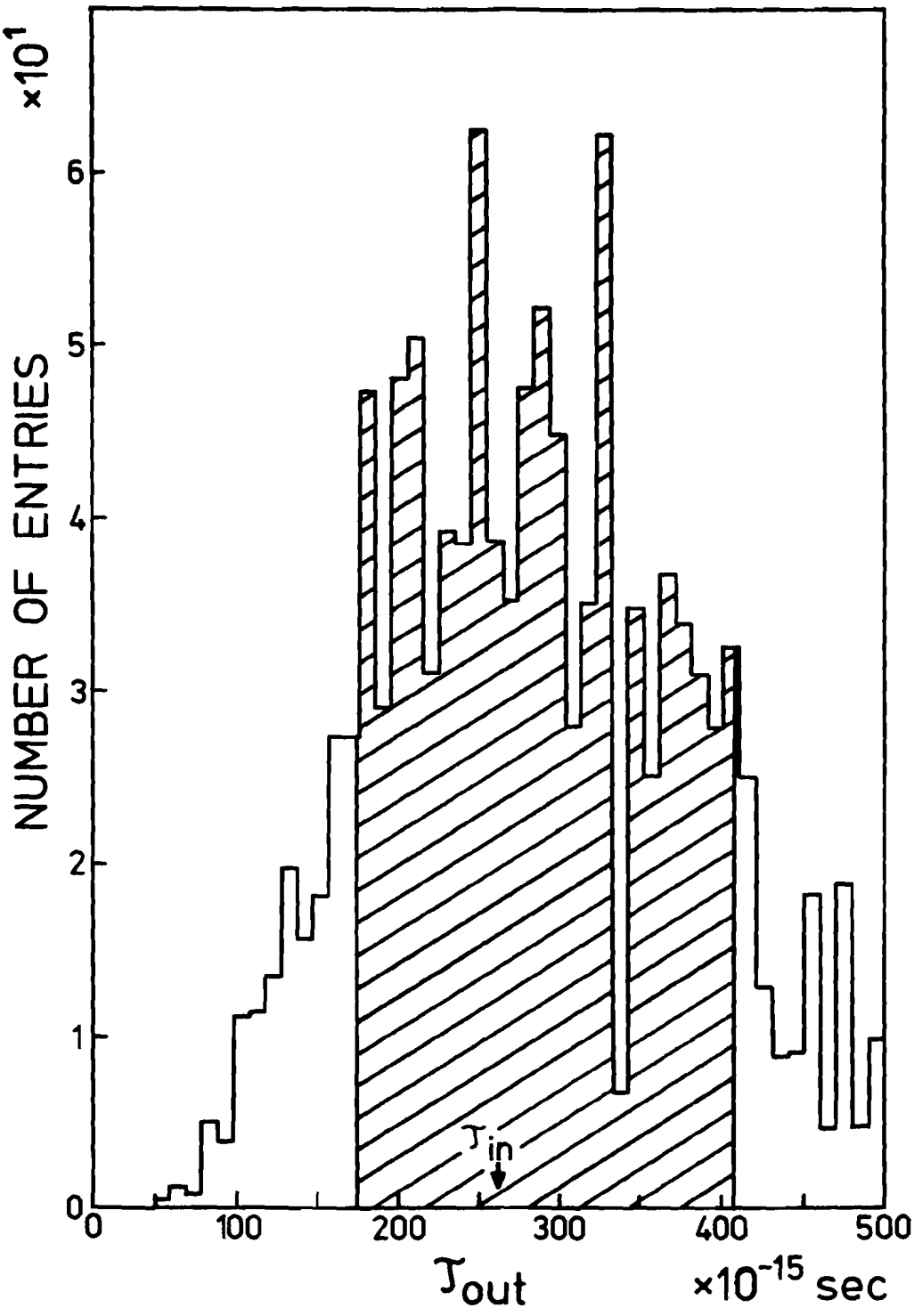

Figure # 44

Monte Carlo distribution of τ_{out} . The bin width is $9.8 \times 10^{-15} sec$. The histogramme depicts the distribution of one-parameter maximum likelihood estimates to simulated data. Each entry is obtained from a fit to a Monte Carlo generation of 6 $F^{+\,or\,-}$ with $\tau_{in} = 2.6 \times 10^{-13} sec$. The hatched area corresponds to one-sigma equivalent errors.

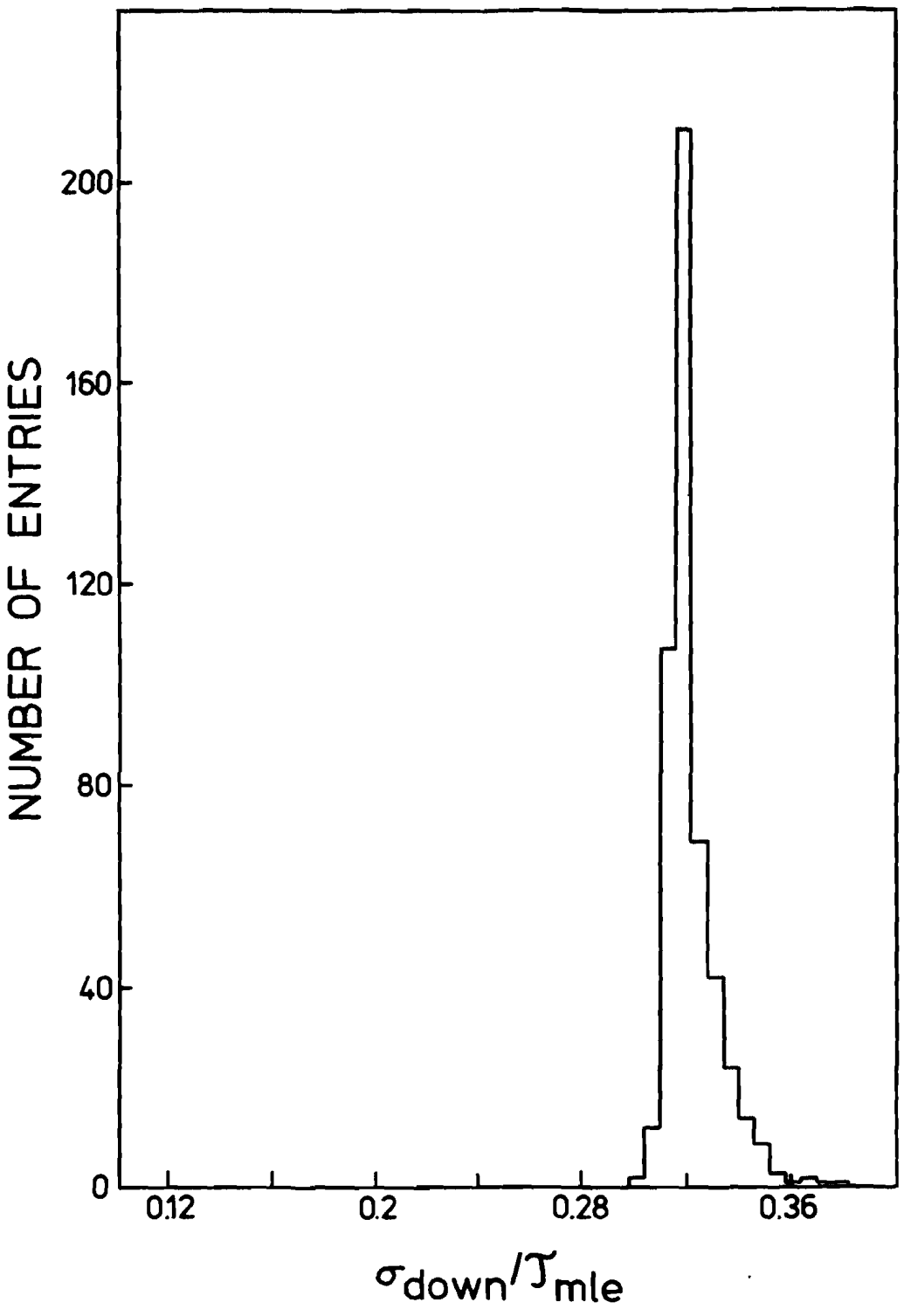

Figure # 46

Monte Carlo distribution of the fractional lower error: $\left(\tau_{out} - \tau_{out}^{-1\sigma}\right)/\tau_{out}$. The bin width is .006 . The histogramme depicts the distribution of the lower fractional one-sigma error on the one-parameter maximum likelihood estimates to simulated data. Each entry is obtained from a fit to a Monte Carlo generation of 6 $F^{+\,or\,-}$ with $\tau_{in} = 2.6 \times 10^{-13} sec$.

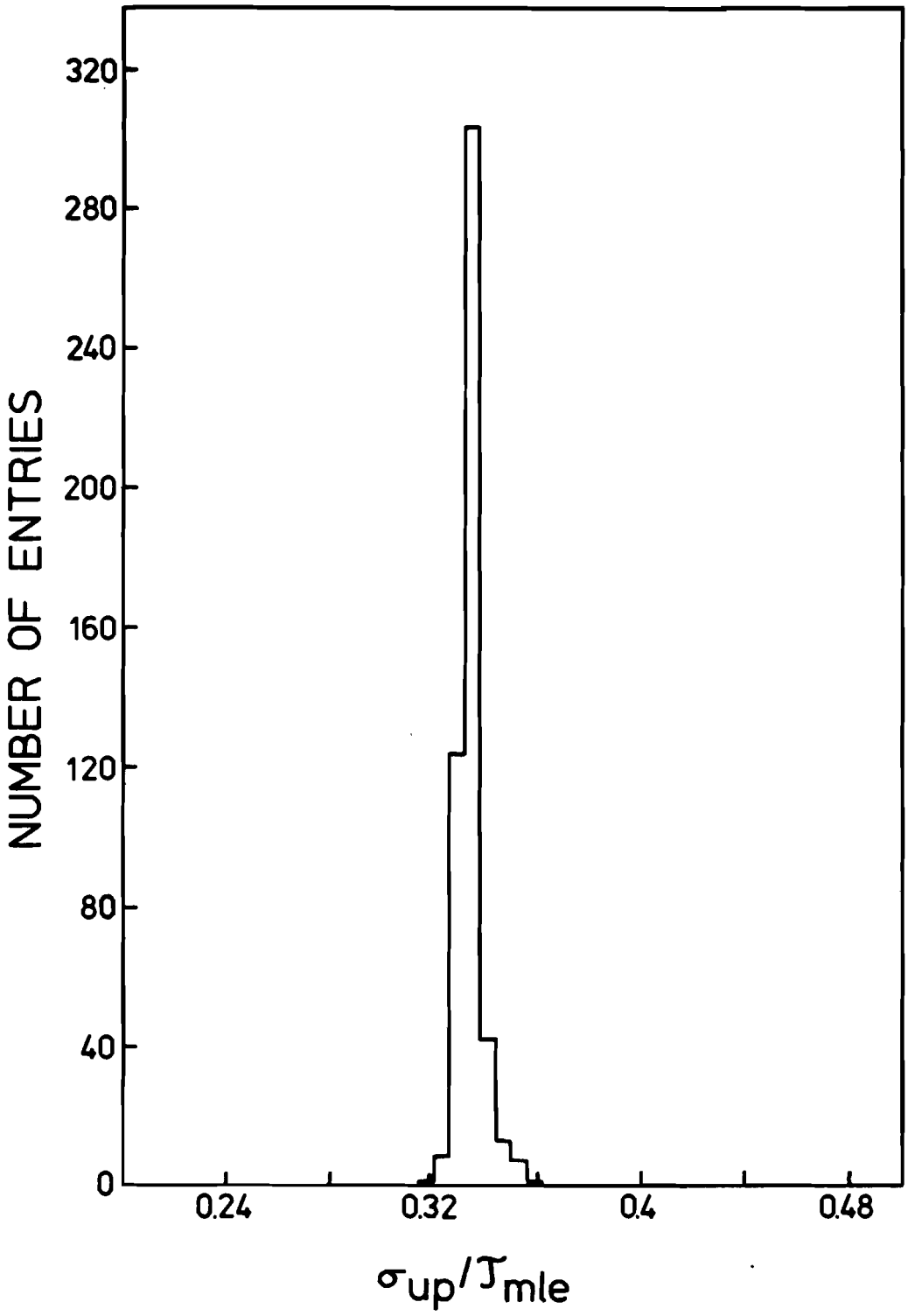

Figure # 48

Monte Carlo distribution of the fractional upper error: $\left(\tau_{out}^{+1\sigma} - \tau_{out}\right)/\tau_{out}$. The bin width is .006 . The histogramme depicts the distribution of the upper fractional one-sigma error on the one-parameter maximum likelihood estimates to simulated data. Each entry is obtained from a fit to a Monte Carlo generation of 13 Λ_c^+ with $\tau_{in} = 2.0 \times 10^{-13} sec$.

which confirms the limit found above:

$$\lim_{\varepsilon_n \to 1 \; \forall n} \tilde{t}_j = \tilde{s}_j .$$

In the further limit of vanishing $\tilde{t}^j_{short}$ and that of $\tilde{t}^j_{long}$ extending all the way to infinity one has

$$\lim_{\substack{\varepsilon_n \to 1 \; \forall i \\ t^j_{short} \to 0 \; \forall j \\ t^j_{long} \to \infty \; \forall j}} \tilde{t}_j = -\tau \ln(1 - \zeta_j).$$

This is what one would expect as in the case of the simple exponential distribution one would solve

$$\zeta_j = \frac{1}{\tau} \int_0^{\tilde{u}_j} \exp\left(\frac{-t}{\tau}\right) dt$$

for $\tilde{u}_j$ to yield

$$\tilde{u}_j = -\tau \ln(1 - \zeta_j).$$

Again,

$$\lim_{\substack{\varepsilon_n \to 1 \; \forall i \\ t^j_{short} \to 0 \; \forall j \\ t^j_{long} \to \infty \; \forall j}} \tilde{t}_j = \tilde{u}_j$$

Finally, the generated proper decay time $\tilde{t}_j$ is converted to a decay length using $\tilde{l}_j = (\tilde{P}^j_c / M_c) \times c\, \tilde{t}_j$. Note that no event degeneracy was generated and this was checked to be of no consequence.

The Monte Carlo result is summarized by Figure # 44 . In this case, the procedure was made to generate a total of 500 datasets with $N_{evts} = 6\, F^{+or-}$ with $\tau_{in} = 2.6 \times 10^{-13} sec$. The histogrammed quantity is τ_{out} which is the *output* maximum-likelihood estimate of the lifetime. The hatched area represents $\sim$ 68.3% of the data, the one-sigma equivalent. Figure # 45 depicts the distribution of the fractional upper one-sigma error: $(\tau^{+1\sigma}_{out} - \tau_{out})/\tau_{out}$. The most probable value of this quantity is 56% with a non-negligible probability of higher values while the fit to the data gives 62% (Section 8.1.2) . The fractional lower one-sigma error: $(\tau_{out} - \tau^{-1\sigma}_{out})/\tau_{out}$ is plotted on Figure # 46 . The most probable value is 32% and the fit to the data gives 35% . There is excellent agreement between the Monte Carlo results for the F-meson and the output of the analysis of the F-meson data.

Figure # 47 , Figure # 48 and Figure # 49 present the result of a similar Monte Carlo run for a total of 500 datasets with $N_{evts} = 13\, \Lambda_c^+$ *with* $\tau_{in} = 2.0 \times 10^{-13} sec$. Here, the most probable value of the upper fractional one-sigma error: $(\tau^{+1\sigma}_{out} - \tau_{out})/\tau_{out}$ is 33% while the fit gives 35% and the most probable value of the lower fractional one-sigma error: $(\tau_{out} - \tau^{-1\sigma}_{out})/\tau_{out}$ turns is 23% while the fit gives 25% . Note that both Figure # 44 and Figure # 47 exhibit the expected non-negligible probability that $\tau_{out} \gg \tau_{in}$. Thus, there is also excellent agreement between the Monte Carlo results for the Λ_c^+-baryon and the output of the analysis of the Λ_c^+-baryon data.

These Monte-Carlo simulations, which are examples from many done with several input lifetimes, clearly demonstrate that the maximum-likelihood method is sound and applicable to the data collected by the sum of both runs of E531.

8.1.5) **Errors on the one-parameter fits**

8.1.5.1) **Statistical errors**

It is a well-known fact [169] that if each of some n observations x_j are distributed with Gaussian statistics $G_j(\mu,\sigma)$, then the sample mean of these observations

$$\overline{x} = \left(\frac{1}{n}\right)\sum_{j=1}^{n} x_j$$

will be distributed according to

$$G(\mu, \sigma/\sqrt{n})$$

where μ and σ stand, respectively, for the expectation value and variance of x . In fact, this property can be used to check that systematic errors are not concealed in the data (or that there are non-Gaussian errors).

Such a test cannot be performed directly on the one-parameter fits to the F^{+or-} and Λ_c^+ samples because the statistics are not Gaussian. The expected behaviour of the *percentage* upper and lower one-sigma equivalent errors on the maximum-likelihood estimates of τ must be generated via the hybrid Monte-Carlo method of Section 8.1.4 .

Figure # 50 presents data from several Monte-Carlo runs for different values of N_{evts} for two particle types: F^{+or-} and Λ_c^+ . Results for runs of 500 datasets generated at $N_{evts} = 5, 10, 20, 40$ *and* 80 are plotted using light symbols while the percentage errors obtained from fits to the actual experimental data (including D^0) are plotted using dark symbols. As can be seen, the behaviour of the size of the errors on the maximum-likelihood estimates of the lifetimes by the one-parameter method is as expected. It follows that other errors (see below) must be much smaller than the statistical errors.

8.1.5.2) **Measurement errors**

In order to appreciate the contribution of the intrumental errors to the determination of the lifetimes of the F^{+or-} meson and Λ_c^+ baryon, a hybrid Monte-Carlo procedure was adopted. As was mentioned in Section 8.1 , the *ultimate* method would have been to write down a likelihood function containing a part reflecting measurement errors [170] . Yet, the Monte-Carlo method provides a good indication of the contribution.

The principal sources of measurement errors are $\sigma_{P_c^j}$, the error on the reconstructed charm-particle momentum, and σ_{l_j} , the error on the charm-particle decay length. The average error on either of these quantities is $\sim 3\%$. The fundamental assumption here is that these errors are *Gaussian* distributed. Each basic cycle in the repetitive procedure generates N_{evts} values from the experimental data according to:

$$dist.\ \tilde{P}_c^j \equiv G(P_c^j, \sigma_{P_c^j})$$

and

$$dist.\ \tilde{l}^j \equiv G(l_j, \sigma_{l_j})$$

where G is a pseudo-Gaussian number generator [171] . The equivalence of the two distributions is understood to mean numerical equality of all moments, in the limit of infinite statistics. Then, each time around the

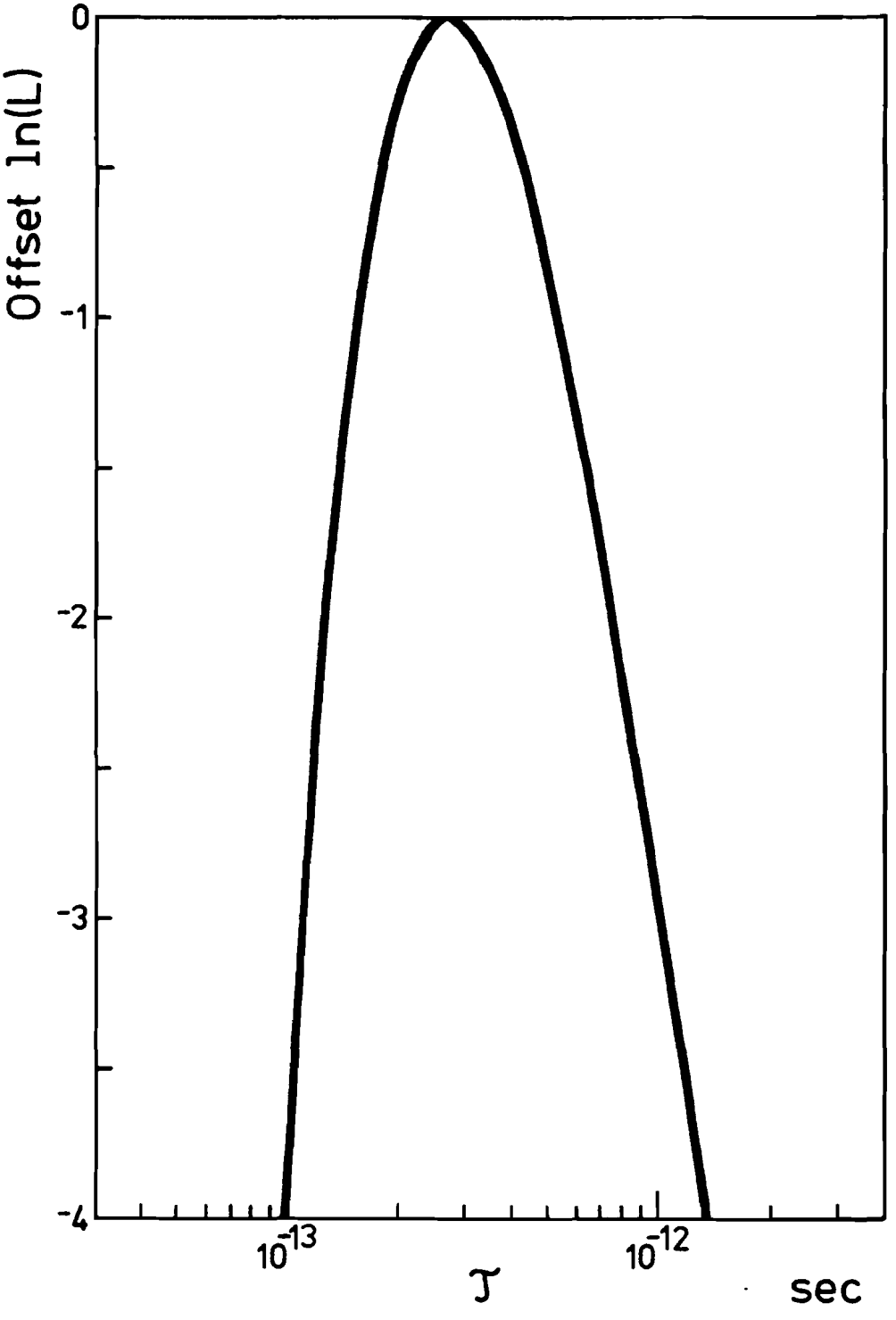

Figure # 51
Effect of propagating the measurement errors on the offset log-likelihood function for the 6 F-mesons. The left and right sides of the thick line represent the minimum and maximum extents of the envelope of all the log-likelihood functions each one of which is computed by fitting the experimental data varied within its assumed Gaussian instrumental errors.

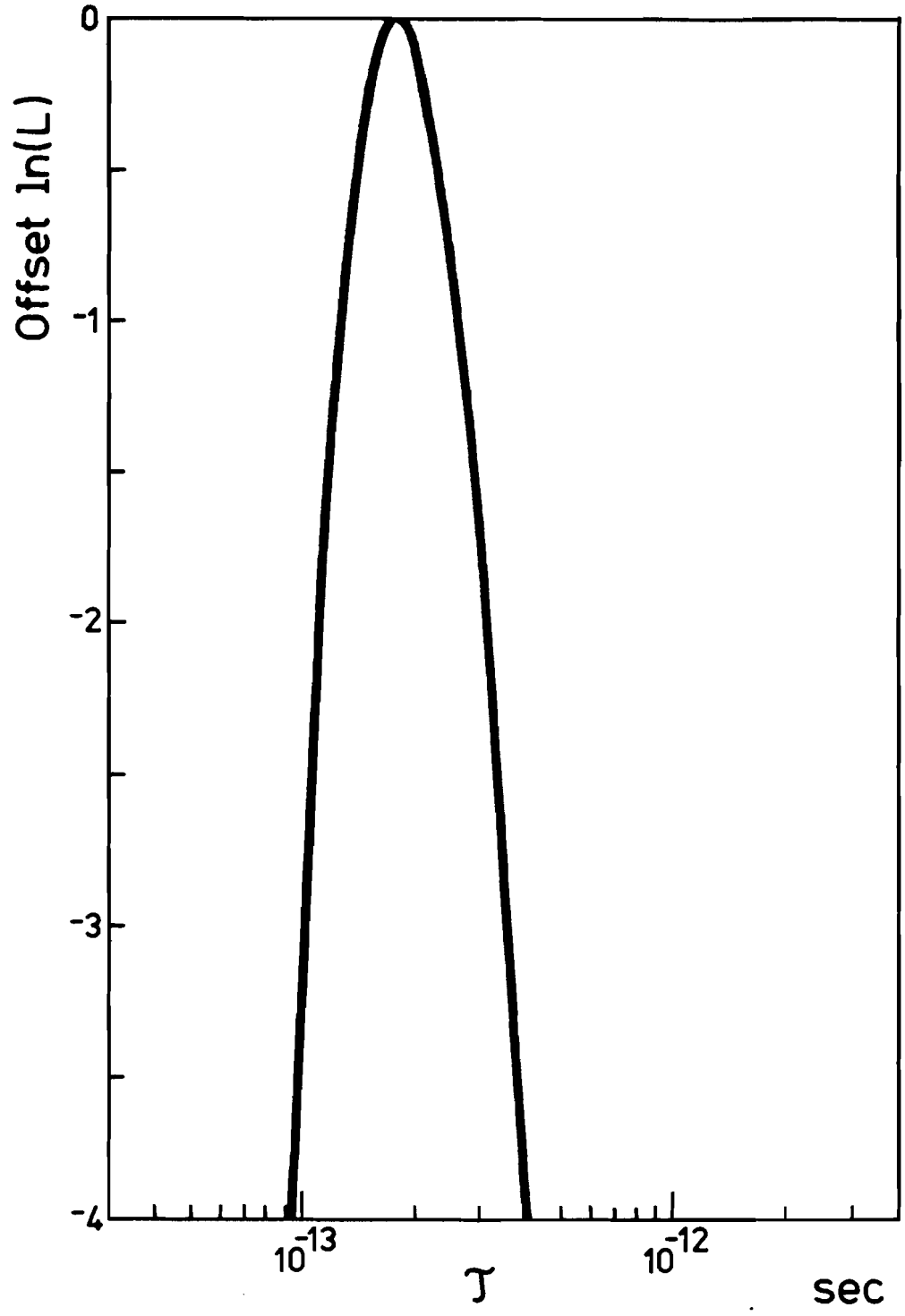

Figure # 53
Effect of propagating the measurement errors on the offset log-likelihood function for the 13 Λ_c^+ baryons. The left and right sides of the thick line represent the minimum and maximum extents of the envelope of all the log-likelihood functions each one of which is computed by fitting the experimental data varied within its assumed Gaussian instrumental errors.

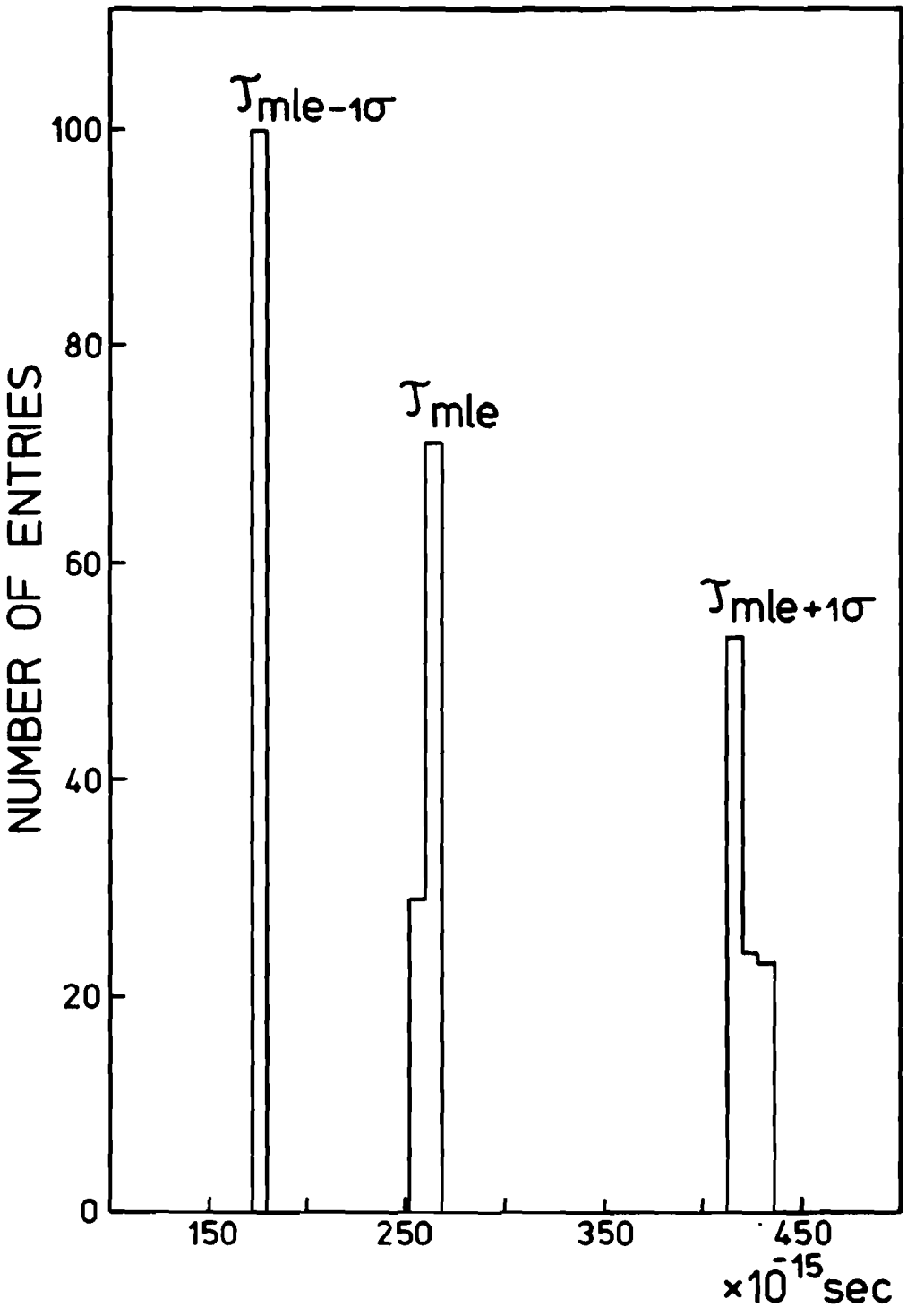

Figure # 55
Distributions of $\tau_{mle}^{-1\sigma}$, τ_{mle} and $\tau_{mle}^{+1\sigma}$ due to the propagation of hypothetical worst-case systematic errors for the 6 $F^{+\ or\ -}$ mesons. The bin width is $8.0 \times 10^{-15} sec$.

loop, the one-parameter maximum-likelihood fit is performed. Figure # 51 depicts the envelope of the log-likelihood functions obtained in this manner for 100 cycles of the procedure applied to the 6 F^{+or-} decays. Again, the log-likelihood functions are offset by their maximum. Figure # 52 shows the distribution of $\tau_{mle-1\sigma}$, τ_{mle} and $\tau_{mle+1\sigma}$. The central peak has

$$\sigma_{meas}\,\tau(F^{+or-}) = 0.06 \times 10^{-13}\ sec.$$

In terms of the lifetime of the F ,

$$\frac{\sigma_{meas}\,\tau(F^{+or-})}{\tau(F^{+or-})} = 2\%$$

Figure # 53 and Figure # 54 are the equivalent plots for the Λ_c^+ baryon and:

$$\sigma_{meas}\,\tau(\Lambda_c^+) = 0.03 \times 10^{-13}\ sec$$

with

$$\frac{\sigma_{meas}\,\tau(\Lambda_c^+)}{\tau(\Lambda_c^+)} = 2\%$$

Thus, measurement errors are much smaller than statistical errors. (See Section 8.1.2 and 8.1.3)

8.1.5.3) **Systematic errors**

In general, sources of systematic errors are hard to identify. Moreover, the very presence of the systematic errors can be hard to witness specially if the *precision* of measurements is not large.

There are no signs of systematic errors in any emulsion measurements. However, the charm-finding efficiency has large errors associated with it and it is not inconceivable that these mask the presence of systematic effects. Therefore, it is worthwhile to check the implication of worst-case effects. The charm-finding efficiency is $\epsilon(l_j)$, where l_j is the decay length of the j^{th} event. Using a Monte-Carlo method, a systematic shift of this efficiency was hypothesized to have the following form:

$$\epsilon(l_j)_{true} = \epsilon(l_j)_{meas} \ + \ or \ - \ \kappa \times [1 - (l_j - l^j_{min})/(l^j_{max} - l^j_{min})]$$

where l^j_{min} and l^j_{max} are the minimum and maximum decay lengths for which there is reliable charm-finding efficiency information (Section 5.1.1) . Here, κ represents the maximum systematic charm-finding efficiency shift that can be considered: $\kappa \leq .20$. When $l_j = l^j_{min}$ then the maximum shift of 20% is applied. When $l_j = l^j_{max}$, no shift is applied. The way, up or down, this shift is being applied is selected at random.

This form of the hypothesized variation of efficiency with decay length was chosen because it would have the most catastrophic effects on the determination of the lifetimes. Upon using a ~flat charm finding efficiency in the analysis while if the true efficiency for finding charm were really dropping with increasing decay length, too many short-lived events would be found and the extracted lifetime would be biased towards low values. Conversely, if the efficiency for finding charm was dropping with decreasing decay length, too many long-lived events would be found and the extracted lifetime would be biased towards longer values.

The results for 100 rounds of the procedure using the experimentally observed $N_{evts} = 6$ F^{+or-} and $N_{evts} = 13$ Λ_c^+ are depicted on Figure # 55 and Figure # 56 respectively. From these, one can conclude

that:

$$\sigma^{eff}_{sys}(\tau_{mle+1\sigma}) \leq 0.1 \times 10^{-13}\ sec$$

$$\sigma^{eff}_{sys}(\tau_{mle}) \leq 0.1 \times 10^{-13}\ sec$$

$$\sigma^{eff}_{sys}(\tau_{mle-1\sigma}) \leq 0.2 \times 10^{-13}\ sec$$

So, on the average,

$$\frac{\sigma^{eff}_{sys}\,\tau_{F^+}}{\tau(F^+)} = 8\% \quad and \quad \frac{\sigma^{eff}_{sys}\,\tau_{\Lambda_c^+}}{\tau_{\Lambda_c^+}} = 10\%$$

No other emulsion related possible sources of systematic errors are expected to have any effect on the lifetimes.

There are no signs of any systematic errors in the measurements made by the spectrometer. In particular, the TOF mass-spectrum testifies of the accuracy of the combination of momentum and time-of-flight measurements. (See Section 4.1) However, neutral particles like π^0 and K^0 when seen in the spectrometer and used to balance the perpendicular component of the all-charged momentum in the laboratory, $p_\perp$, sometimes have large uncertainties associated with their momentum and energy. It could be argued that some systematic errors might have have gone un-noticed. If systematics were present say among the π^0 it could not have caused the selection of a particular neutral pion over another resulting in a different fit because the cut on confidence level was very loose: $C.L. \geq 1\%$, and all versions of a particular hypothesis were kept if no clear choice could be made between them. No such case ever arose with K^0 in the calorimeter.

Systematics might however be present in the data sample due to to *un-constrained* events (see Section 7.1.4) . In fact, some of the events could contain more than one un-detected neutral particles.

8.2) **A lower estimate of the $D^{+\,or\,-}$ meson lifetime**

Part of the charged sample consists of events with ambiguous fits between D^+'s, F^+'s and Λ_c^+'s ; 27 events have fits consistent with at least one charged D-meson decay. In addition, there is one un-ambiguous fit to a charged D-meson decay.

In the section below, it will be argued that some large fraction of the events with ambiguous fits are really D-meson decays. The ambiguous charged sample will then be analysed on the hypothesis that all ambiguous events are really D-meson decays. This however can only be an over-simplification and proper steps to adapt the statistical analysis will be taken in Section 8.3 .

Once the charm quark c has been produced by weak interaction of the ν with some other quark contained in the target nucleon (see Section 1), the process of fragmentation takes over and essentially determines the identity of the outgoing charmed particle. Assuming that $u\,\bar{u}$ and $d\,\bar{d}$ quark pairs are produced with equal probability in this process and that there are no dynamical effects in matrix elements for production of specific charmed particles (thus that *spin counting* statistics applies); total production rates of charged and neutral D-mesons ought to be equal [172] . Given the large number of neutral D-mesons we observe, this simple argument, even if it were not entirely accurate, makes one expect that a majority of the ambiguous events be D^{+or-}'s.

As the identity of a decaying charmed particle is unique, one can select out the fits to D^{+or-} and, at the same time, simply exclude from consideration any of the other fits to F^{+or-} or Λ_c^+ . This, of course,

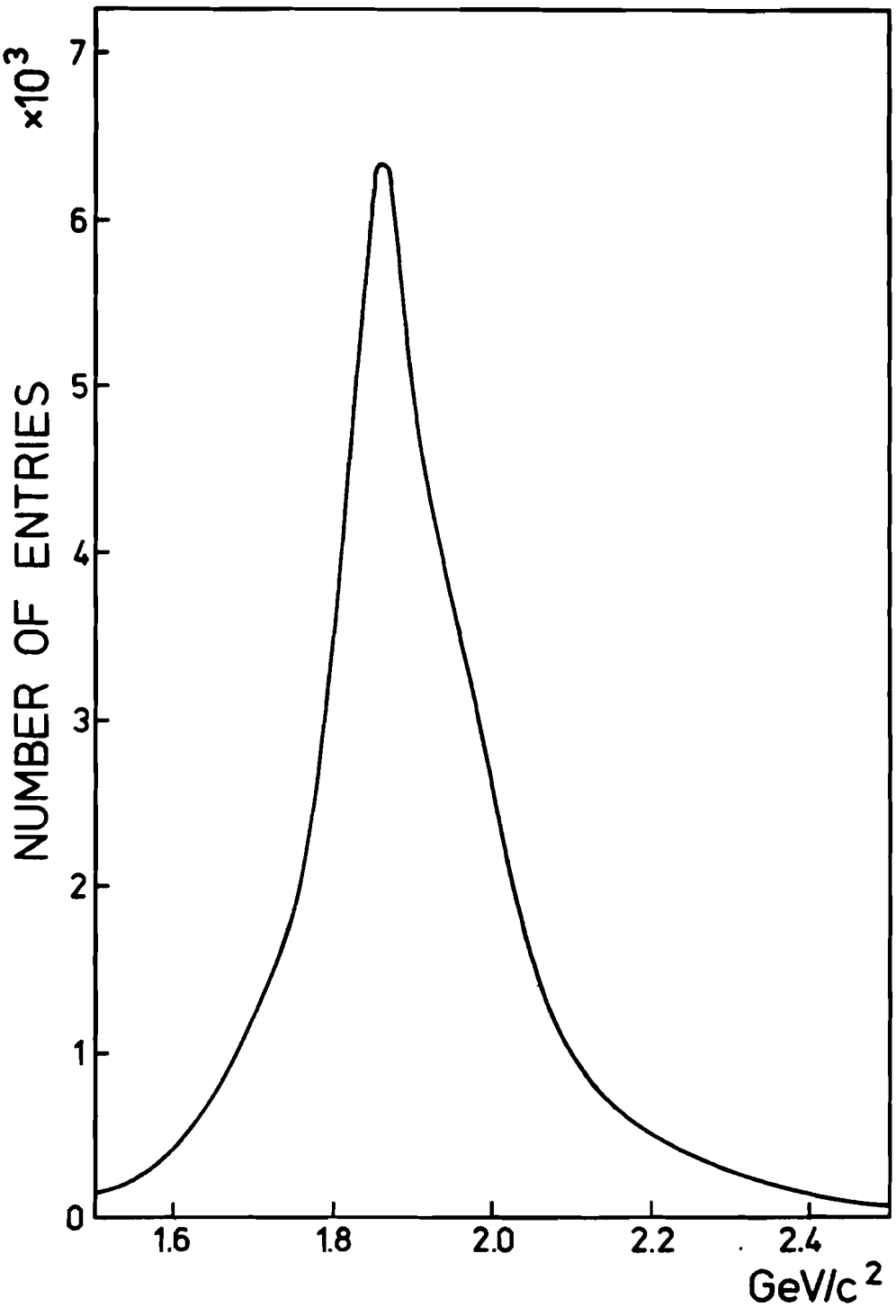

Figure # 57
Charged D-meson Gaussian mass ideogram.

constitutes an entirely arbitrary cut because there is no *a priori* reason for absolutely all of these events to be charged D^{+or-} . A few most likely are F-mesons or Λ_c^+ baryons. Now, since F^{+or-} and Λ_c^+ are much shorter-lived than D^{+or-} , performing a one-parameter fit to this data sample provides *at best* a lower estimate to the actual lifetime of the D^{+or-} . The result (assuming all ambgiguous events are D's) is:

$$\tau_{D^{+or-}} \geq 9.4^{+2.4+5.8}_{-1.8-3.1} \times 10^{-13} sec$$

The upper and lower one-sigma equivalent errors are therefore:

$$\frac{\sigma(\tau_{mle+1\sigma})}{\tau_{mle}} = 26\% \quad and \quad \frac{\sigma(\tau_{mle-1\sigma})}{\tau_{mle}} = 19\%$$

These results are arrived at using $N_{evts} = 28$.

The weighted average of the un-constrained masses from 18 out of 28 fits to D^{+or-} is $1862 \pm 14\ MeV/c^2$, the others are "zero-constraint" fits. Figure # 57 presents a Gaussian *ideogram* † generated from the 18 fully constrained fits. The most probable value is $\sim 1855\ MeV/c^2$. The plot features non-Gaussian wings and a shoulder around $\sim 1900\ MeV/c^2$. This is a further hint that some of these events are really F^{+or-} mesons or Λ_c^+ baryons.

Since there are no reasons to expect the ambiguous sample to be exclusively composed of D^{+or-} , it is interesting to try to understand the above one-parameter lifetime result in terms of the possible amount of short-lived contamination present in the ambiguous sample. A method to do so consists in generating Monte Carlo datasets of 28 events that are not entirely $D^{+\ or-}$ of some input lifetime, but contain a *known* percentage of shorter-lived F^{+or-} and Λ_c^+ events. This Monte Carlo "data" can then be fed to the one-parameter maximum-likelihood algorithm. Much more details on this Monte Carlo procedure will given in Section 8.3.3 in the context of a more elaborate two-parameter procedure to extract the lifetime of the D^{+or-} from the ambiguous sample. Figure # 58 presents Monte Carlo results where $N_{evts} = 28$ and where the *a priori* known amount of F^{+or-} and Λ_c^+ contamination in the sample is varied from 0% to 50% . All charmed particle lifetimes in this procedure are parameters that are set to their experimental values; it is only the percentage of non-D^{+or-} mesons (F^{+or-} or Λ_c^+) that is varied. Each bar on the graph summarizes 500 one-parameter fits to this contaminated Monte Carlo "data" and displays the distribution of the ratios $\tau_{out}^{1-parm}/\tau_{D^{+or-}}^{in}$ where $\tau_{D^{+or-}}^{in} = 11.1 \times 10^{-13} sec$. ‡ Also input to the procedure are $\tau_{F^{+or-}} = 2.6 \times 10^{-13} sec$ and $\tau_{\Lambda_c^+} = 2.0 \times 10^{-13} sec$.

These Monte Carlo runs clearly demonstrate that the presence of short-lived contamination in the ambiguous sample will lower, in a statistically significant way, the one-parameter maximum-likelihood estimate

† A Gaussian mass ideogram is obtained by addition of several Gaussian distributions centered on the different un-constrained masses. The widths of the distributions are set equal to the different sigmas associated with each of the un-constrained masses.

‡ The lifetime of the D^{+or-} meson is obtained in Section 8.3.2 while the procedure leading up to it is described in details in Section 8.3.1 .

of the lifetime of the *main contributor* to this sample: the D^{+or-} . As the figure shows, the amount by which the under-estimate occurs varies strongly with the percentage of shorter-lived contamination. It is therefore obvious that the one-parameter maximum-likelihood method can only provide a biased estimate of the lifetime of D^{+or-} in the ambiguous sample that should only be interpreted as a lower estimate of the lifetime of the charged D-meson. Thus, a more elaborate method involving two parameters had to be used to extract the lifetime of the $D^{+\,or\,-}$ form that sample.

8.3) **The two-parameter fit to the ambiguous sample**

This section explains the two-parameter maximum-likelihood method which was used to extract the lifetime of the charged D-meson from the ambiguous charged sample.

8.3.1) **The two-parameter maximum log-likelihood method**

The objective of the two-parameter maximum likelihood method is to extract, from the data and within errors, not only the maximum-likelihood-estimate lifetime of the D^{+or-} but also the *fraction* of all ambiguous events most likely not to be D^{+or-} mesons that is, the fraction of shorter-lived contaminants. Since the experimental lifetimes of F^{+or-} and Λ_c^+ are very close to each other: $\tau(F^{+or-}) \approx \tau(\Lambda_c^+)$, the lifetime of the short-lived contaminants (labelled "X") was set to:

$$\tau_X = 2.1 \times 10^{-13} sec$$

where τ_X is the *weighted* average of the experimental lifetimes of F^{+or-} and Λ_c^+ . Thus, F-mesons and Λ_c^+ baryons are treated as a single short-lived contaminant.

It can be expected that greater statistical significance is obtained by restricting the question being asked from: *How many F^{+or-} and how many Λ_c^+ and thus how many D^{+or-} are there in the ambiguous sample?* to a much simpler one: *How many F^{+or-}* **or** *Λ_c^+ are there in the ambiguous sample?* or equivalently to: *How many D^{+or-} are there in the ambiguous sample?* Here, "greater statistical significance" is intended to mean "with smaller statistical uncertainty".

With the arguments presented above, one can think of the ambiguous sample as being made out of a short-lived component "X" and perhaps (i.e. to be determined) of a much longer-lived D^{+or-} component. However, this analogy was not carried too far: experimentally obtained fits to F^{+or-} and Λ_c^+ were used in the analysis: decay times for these fits are still computed using the known F^{+or-} and Λ_c^+ masses.

In the following treatment, the sample of ambiguous events is characterized by a quantity which could be called the *charmed particle identification degeneracy.* This should not be confused with the TOF ID's which are quantities associated not with the decaying charm particle but rather with its charged decay products. Thus, the charmed particle identification degeneracy will be referred to simply as the particle identification degeneracy. This quantity $P_j^{I.D.} = 1, 2$ *or* 3 depending on whether the j^{th} event is one, two or three-fold ambiguous between D^{+or-} , F^{+or-} *and* Λ_c^+ . There should be no confusion with the the actual *hypothesis degenaracy* of any single event. The j^{th} event's hypothesis degeneracy splits into a total of $P_j^{I.D.}$ contributions. For example, if the n^{th} event were $D^+D^+F^+F^+F^+\Lambda_c^+$ ambiguous, then one would have $P_n^{I.D.} = 3$, with D^+ , F^+ and Λ_c^+ hypothesis degeneracies respectively equal to 2 , 3 and 1 .

In order to proceed with such a programme, one can immediately divide all hypotheses of any given ambiguous event into two classes. In the j^{th} event, one counts $H_j^{D^{+or-}}$ hypotheses for which the parent particle is D^{+or-} while there are $H_j^X = H_j^{F^{+or-}} + H_j^{\Lambda_c^+}$ hypotheses for which the parent particle is either F^{+or-} or Λ_c^+ . As was mentioned before, there is only one single case for which $H_j^X = 0$. This happens for 1^{st} run event E05804508 in which case $H_j^{D^{+or-}} = 2$.

Irrespective of how many hypotheses of a particular class there may exist in any ambiguous event, the total probability associated with any such event is made out of the sum of the two probabilities corresponding to two non-independent occurances: the probability that the event be a D^{+or-} and the probability that the event be an $X \equiv F^{+or-}$ *or* Λ_c^+ .

$$P_j = P_{D^{+or-}}^j + P_X^j$$

Independently of any measurement on any event, there is a probability $f_{D^{+or-}}$ that any event be a D^{+or-} . Likewise, there is a probability f_X that any event be an $X \equiv F^{+or-}$ *or* Λ_c^+ . Since a fitted event from the ambiguous sample is either one or the other

$$f_X + f_{D^{+or-}} = 1.$$

The probability that the j^{th} event be a D^{+or-} is therefore made out of the product of two probabilities of independent occurances: that there be a D^{+or-} in the j^{th} event and that the proper decay times of the D^{+or-} hypotheses $t_{ij}^{D^{+or-}}$ belong to a sample of D^{+or-} and thus distribute accordingly. This can be written schematically and somewhat informally as:

$$P_{D^{+or-}}^j = f_{D^{+or-}} \times \sum_{i=1}^{H_j^{D^{+or-}}} w_{ij}\, P\left[t_{ij}^{D^{+or-}} \; sampled\, from\; \mathcal{T}(D^{+or-})\right]$$

or

$$P_{D^{+or-}}^j = (1 - f_X) \times \sum_{i=1}^{H_j^{D^{+or-}}} w_{ij}^{D^{+or-}} P\left[t_{ij}^{D^{+or-}} \; sampled\, from\; \mathcal{T}(D^{+or-})\right]$$

where $\mathcal{T}(D^{+or-})$ represents the distribution of all proper decay times of a D^{+or-} meson. Quite similarly, one has

$$P_X^j = f_X \times \sum_{i=1}^{H_j^X} w_{ij}^X\, P\left[t_{ij}^{F^{+or-}} \; or\; t_{ij}^{\Lambda_c^+} \; sampled\, from\; \mathcal{T}(X)\right].$$

Summing up, one has

$$P_j = (1 - f_X) \sum_{i=1}^{H_j^{D^{+or-}}} w_{ij}^{D^{+or-}} P\left[t_{ij}^{D^{+or-}} \; sampled\, from\; \mathcal{T}(D^{+or-})\right] +$$
$$f_X \sum_{i=1}^{H_j^X} w_{ij}^X P\left[t_{ij}^{F^{+or-}} \; or\; t_{ij}^{\Lambda_c^+} \; sampled\, from\; \mathcal{T}(X)\right].$$

The probabilities that measured proper decay times from different hypotheses in the two classes belong to the parent particle associated with that class can be taken from Section 8.1.1 . It should be

$f_{ij}(t^j_{short}, t^j_{long}; t_{ij})$. However, one must remember that the proper decay times are but mere shorthands for $t = ml/pc$ and that since we deal with the ambiguous sample, it *matters* which parent mass is being used to compute proper decay times. Hence

$$P\left[t_{ij}^{D^{+or-}} \text{ sampled from } \mathcal{T}(D^{+or-})\right] = f_{ij}\left(\tau_{D^{+or-}}, t^{j\,D^{+or-}}_{short}, t^{j\,D^{+or-}}_{long}; t_{ij}^{D^{+or-}}\right).$$

The additional argument "τ" refers to which lifetime is being used; in this case, that of the D^{+or-} . Quite similarly one has

$$P\left[t_{ij}^{F^{+or-}} \text{ or } t_{ij}^{\Lambda_c^+} \text{ sampled from } \mathcal{T}(X)\right] = f^X_{ij}\left(\tau_X, t^X_{short}, t^{j\,x}_{long}; t^X_{ij}\right).$$

The superscript "X" on the proper decay times refers to using the known F^{+or-} or Λ_c^+ mass depending on whether the fit is to the meson or to the baryon. Substituting from Section 8.1.1 one has:

$$f_{ij}\left(\tau_{D^{+or-}}, t^{j\,D^{+or-}}_{short}, t^{j\,D^{+or-}}_{long}; t_{ij}^{D^{+or-}}\right) = \frac{\epsilon(t_{ij}^{D^{+or-}})\ \exp\left(\frac{-t_{ij}^{D^{+or-}}}{\tau_{D^{+or-}}}\right)}{\tau_{D^{+or-}}\ S^{D^{+or-}}(N^j_{eff})}$$

for

$$t^{j\,D^{+or-}}_{short} \leq t_{ij}^{D^{+or-}} \leq t^{j\,D^{+or-}}_{long}$$

and

$$f_{ij}\left(\tau_{D^{+or-}}, t^{j\,D^{+or-}}_{short}, t^{j\,D^{+or-}}_{long}; t_{ij}^{D^{+or-}}\right) = 0 \ \textit{otherwise.}$$

Also,

$$f_{ij}\left(\tau_X, t^{j\,x}_{short}, t^{j\,x}_{long}; t^X_{ij}\right) = \frac{\epsilon(t^X_{ij})\ \exp\left(\frac{-t^X_{ij}}{\tau_X}\right)}{\tau_X\ S^X(N^j_{eff})}$$

for

$$t^{j\,x}_{short} \leq t^X_{ij} \leq t^{j\,x}_{long}$$

and

$$f_{ij}\left(\tau_X, t^{j\,x}_{short}, t^{j\,x}_{long}; t^X_{ij}\right) = 0 \ \textit{otherwise.}$$

Dropping the references to the range of proper decay times, the total probability associated with the j^{th} ambiguous event is just:

$$P_j = (1 - f_X) \sum_{i=1}^{H_j^{D^{+or-}}} w_{ij}^{D^{+or-}} \frac{\epsilon(t_{ij}^{D^{+or-}})\ \exp\left(\frac{-t_{ij}^{D^{+or-}}}{\tau_{D^{+or-}}}\right)}{\tau_{D^{+or-}}\ S^{D^{+or-}}(N^j_{eff})} + f_X \sum_{i=1}^{H_j^X} w_{ij}^X \frac{\epsilon(t^X_{ij})\ \exp\left(\frac{-t^X_{ij}}{\tau_X}\right)}{\tau_X\ S^X(N^j_{eff})}$$

Also, one has the normalization condition satisfied:

$$\int_0^\infty P(\tau_{D^{+or-}}, f_X; t)\ dt = (1 - f_X) + f_X = 1$$

Now, the event weights must, by definition, add up to unity. In the total particle identification degeneracy $P_j^{I.D.}$ of an event, "1" is taken up by the D^{+or-} : there must be a D^{+or-} among the fits otherwise such an event wouldn't be in this sample. So

$$\sum_{i=1}^{H_j^{D^{+or-}}} w_{ij}^{D^{+or-}} + \sum_{i=1}^{H_j^{F^{+or-}}} w_{ij}^{F^{+or-}} + \sum_{i=1}^{H_j^{\Lambda_c^+}} w_{ij}^{\Lambda_c^+} = P_j^{I.D.}$$

reduces to

$$1 + \sum_{i=1}^{H_j^{F^{+or-}}} w_{ij}^{F^{+or-}} + \sum_{i=1}^{H_j^{\Lambda_c^+}} w_{ij}^{\Lambda_c^+} = P_j^{I.D.}$$

This is

$$\sum_{i=1}^{H_j^{F^{+or-}}} w_{ij}^{F^{+or-}} + \sum_{i=1}^{H_j^{\Lambda_c^+}} w_{ij}^{\Lambda_c^+} = P_j^{I.D.} - 1$$

Now, since all F^{+or-} and Λ_c^+ are taken as being of a single short-lived origin "X" one must have:

$$\sum_{i=1}^{H_j^X} w_{ij}^X = 1$$

The former equation can be obtained from the latter provided that:

$$w_{ij}^X = \frac{w_{ij}^{F^{+or-} \text{ or } \Lambda_c^+}}{(P_j^{I.D.} - 1)} = \frac{\tilde{w}_{ij}^X}{(P_j^{I.D.} - 1)}$$

where it is understood that which hypothesis weight is being used on the right side of the equation, depends on whether the i^{th} hypothesis is a fit to F^{+or-} or Λ_c^+ . This simplifies the expression of the total probability associated with the j^{th} ambiguous event to:

$$\mathcal{P}_j = (1 - f_x) \sum_{i=1}^{H_j^{D^{+or-}}} w_{ij}^{D^{+or-}} \frac{\epsilon(t_{ij}^{D^{+or-}}) \exp\left(\frac{-t_{ij}^{D^{+or-}}}{\tau_{D^{+or-}}}\right)}{\tau_{D^{+or-}} S^{D^{+or-}}(N_{eff}^j)} + \left(\frac{f_x}{P_j^{I.D.} - 1}\right) \sum_{i=1}^{H_j^X} \tilde{w}_{ij}^X \frac{\epsilon(t_{ij}^X) \exp\left(\frac{-t_{ij}^X}{\tau_X}\right)}{\tau_X S^X(N_{eff}^j)}$$

The likelihood function for the N_{evts} ambiguous events is then:

$$L = \prod_{j=1}^{N_{evts}} \mathcal{P}_j$$

It is important to notice that, in this likelihood function, there are only *two* unknown parameters to be determined by the method of maximum-likelihood: the lifetime of D^{+or-} : $\tau_{D^{+or-}}$ and the fraction of the total sample that are *not* D^{+or-} : f_x . Note that the fraction of D^{+or-} is simply $f_{D^{+or-}} = 1 - f_x$. Also, a reminder about the meaning of the superscript "X" on the proper decay times: experimental decay times obtained from fits to F^{+or-} and Λ_c^+ must be used.

The method of maximum-likelihood in the two-parameter case boils down to numerically solving the follwing set of equations:

$$\frac{\partial}{\partial \tau_{D^{+or-}}} \ln L \Big|_{\tau_{mle}^{D^{+or-}}} = 0 \qquad \frac{\partial^2}{\partial \tau_{D^{+or-}}^2} \ln L \Big|_{\tau_{mle}^{D^{+or-}}} < 0$$

$$\frac{\partial}{\partial f_x} \ln L \Big|_{f_{mle}^X} = 0 \qquad \frac{\partial^2}{\partial f_x^2} \ln L \Big|_{f_{mle}^X} < 0$$

This was done by lookup of a computed map of the function with appropriate grid size and extent. The grid size was chosen to be $\Delta\tau_{D^+\sigma\tau^-} = .02 \times 10^{-13} sec$ and $\Delta f_x = .01$ while its extent was covering the entire physical ranges of the parameters.

Extracting errors from the two-parameter log-likelihood function is slightly more involved than for the one-parameter case. Again, however, this is best explained by resorting to the hypothetical case of infinite statistics where the form of the likelihood is exactly known to be *bi-normal or normal two-dimensional* , that is, two-dimensional Gaussian. † The solution to the n-sigma integral probability equation which reads

$$P_G(\overline{X} - n\sigma_X \leq X \leq \overline{X} + n\sigma_X, \overline{Y} - n\sigma_Y \leq Y \leq \overline{Y} + n\sigma_Y) = \Gamma(\rho, n)$$

may be found numerically and is tabulated [174] . This quantity is plotted on Figure # 59 . The following table lists a few relevant quantities:

ρ	n	Γ	ρ	n	Γ
0	1	.466	1	1	.683
0	2	.911	1	2	.954
0	3	.995	1	3	.997

The log equation for the errors is obtained much as in the case of the one-dimensional Gaussian distribution and reads:

$$\ln G(\overline{X} \pm n\sigma_X, \overline{Y} \pm n\sigma_Y) = \ln G(\overline{X}, \overline{Y}) - \frac{n^2}{1+\rho}$$

This defines cuts at specific values of probability below the function's maximum, the set of all X and Y satisfying the equation form ellipses while $\overline{X} \pm n\sigma_X$ and $\overline{Y} \pm n\sigma_Y$ are tangents to these forming a circumscribing rectangle. For $\rho = 1$, subtracting 1/2, 2 and 9/2 from the function's maximum gives exactly the same probability content as the one-dimensional Gaussian distribution: 68.3 % , 95.4 % and 99.7 % for $n = 1, 2$ and 3 ...

Of course, the likelihood function for the sample of ambiguous events

$$L = \prod_{j=1}^{N_{evts}} P_j$$

† As reminder [173] , the two-dimensional Gaussian distribution is given by

$$G(X,Y) = \frac{1}{2\pi\sigma_X\sigma_Y\sqrt{1-\rho^2}} \exp\left[-\frac{1}{2(1-\rho^2)}\left\{\frac{(X-\overline{X})^2}{\sigma_X^2} - 2\rho\frac{(X-\overline{X})(Y-\overline{Y})}{\sigma_X\sigma_Y} + \frac{(Y-\overline{Y})^2}{\sigma_Y^2}\right\}\right]$$

where expectation values of X and Y are $\overline{X}$ and $\overline{Y}$, while standard deviations are σ_X and σ_Y and ρ is the *correlation* coefficient...

is not exactly two-dimensional Gaussian with $\rho = 1$ and cuts through it are not ellipses so that the $n\sigma$ interval probability content is only approximatively given by the above values.

8.3.2) **The lifetime of the D^{+or-} meson**

When a two-parameter fit, as described in the previous section, is performed on the subset of $N_{evts} = 17$ events from the 2^{nd} run alone, the result is:

$$\tau_{D^{+or-}} = 11.5^{+6.2+19.0}_{-3.6-5.8} \times 10^{-13} sec$$

and

$$f_x = .26^{+.21+.40}_{-.26-.26}$$

where a short-lived contamination with $\tau_x = 2.1 \times 10^{-13} sec$ was assumed.

All 27 events (from both 1^{st} and 2^{nd} runs) that are ambiguous between a D^{+or-} hypothesis and F^{+or-} or Λ_c^+ hypotheses together with the one single event (from the 1^{st} Run) that is un-ambiguously D^- ‡ have also been fitted using this two-parameter maximum-likelihood method described in the previous section. It is convenient to display the one-sigma and two-sigma cuts through the log-likelihood function in terms of its two parameters: the lifetime of D^{+or-} and the fraction f_x of short-lived ($\tau_x = 2.1 \times 10^{-13} sec$) contaminant in the $f_x, \tau_{D^{+or-}}$ plane. The location of the maximum of the function should also be displayed. Figure # 60 is such a plot. Note that both the one and two-sigma contours extend in the *un-physical* region of $f_x < 0$ where they are drawn in dashed line. There is, in fact, no probability content in this region so that two (one one-sigma and one two-sigma) asymptotes to the contours must be made to coincide with $f_x = 0$. The other asymptotes determining the errors are displayed. The maximum of the function occurs at the center of the small circle. Therefore,

$$\tau_{D^{+or-}} = 11.1^{+4.4+12.1}_{-2.9-4.6} \times 10^{-13} sec$$

and

$$f_x = .17^{+.18+.35}_{-.17-.17}$$

From this, the fraction of D^{+or-} in the ambiguous sample is just:

$$f_{D^{+or-}} = .83^{+.17+.17}_{-.18-.35}$$

which translates into

$$N_{D^{+or-}} = 23^{+5+5}_{-5-10} \; events$$

All quoted errors are *statistical*. The result using only the 1^{st} Run data is $\tau_{D^{+or-}} = 11.5^{+7.5}_{-3.5} \times 10^{-13} sec$ and $f_{D^{+or-}} = .97^{+.03}_{-.29}$. Thus, the charged D-meson lifetime measurements from the 1^{st} Run, 2^{nd} Run and both runs of E531 are, within statistical errors, the same while the sample size has more than doubled. The estimate of the short-lived contamination has increased but the increase is less than one sigma.

‡ The event is E05804508

8.3.3) **The Monte Carlo simulation of the ambiguous charged dataset**

8.3.3.1) **Event generation**

The mathematical soundness of the two-parameter maximum-likelihood method is concurrent with its derivation from first principles as was done in Section 8.3.1 . However, the range of sound statistical applicability of this method is not so obvious, although there is nothing in the results of Section 8.3.2 that would suggest this range be exceeded in any way. In order to demonstrate applicability, many tests can be devised if one can simulate a sample of ambiguous events such as the one described in Section 10 . No bias must enter the idealization of what this sample really is. In this section, a Monte Carlo simulation of the charged ambiguous sample will be described.

Any of the several (500) Monte-Carlo samples that were generated comprised a total of $N_{evts} = 28$ events among wich one could find $N_x = N_{F^{+or-}} + N_{\Lambda_c^+}$ events that were drawn from a sample of decaying F^{+or-} or Λ_c^+ with experimentally known lifetimes of $2.6 \times 10^{-13} sec$ and $2.0 \times 10^{-13} sec$ respectively. The remaining $N_{D^{+or-}} = N_{evts} - N_x$ events were drawn from a sample of decaying charged D-meson. The quantities $N_{F^{+or-}}$, $N_{\Lambda_c^+}$, N_{evts} and thus $N_{D^{+or-}}$ are all input parameters to the procedure so that the fraction of short-lived contaminants

$$f_x = \frac{(N_{F^{+or-}} + N_{\Lambda_c^+})}{N_{evts}} = \frac{N_x}{N_{evts}}$$

also contitutes an (indirect) input to the procedure. The remaining $N_{D^{+or-}} = N_{evts} - N_x$ events are drawn from a sample of decaying D^{+or-} with some input lifetime $\tau_{D^{+or-}}$. The actual proper decay times are generated using the method described in details in Section 8.1.4 . The only difference is that the correct known mass of the parent used in $t = ml/pc$ must change depending on whether it is a D^{+or-} being generated or an F^{+or-} or a Λ_c^+ . Using a similar notation as in Section 8.1.4 the j^{th} Monte-Carlo'ed sample will contain N_{evts} events for which the proper decay time is generated through

$$\tilde{t}_j^{k_j=1} = -\tau_j \ln \left\{ \exp\left(\frac{-t^l{}_{short}^{\,j}}{\tau_j} \right) - \left(\frac{S(N_{eff}^j)}{\varepsilon_l} \right) [T_j(l-1) - \zeta_j] \right\}$$

where

$$\tau_j = \tau_{D^{+or-}} \quad for \;\; 1 \leq j \leq N_{D^{+or-}}$$

and

$$\tau_j = \tau_{F^{+or-}} \quad for \;\; N_{D^{+or-}} + 1 \leq j \leq N_{D^{+or-}} + N_{F^{+or-}}$$

and

$$\tau_j = \tau_{\Lambda_c^+} \quad for \;\; N_{D^{+or-}} + N_{F^{+or-}} + 1 \leq j \leq N_{evts}$$

An additional superscript "k_j" was added to indicate the event *degeneracy* , and its value is set to $k_j = 1$, by convention, to remind one that this is the proper decay time that is truly sampled from decaying D^{+or-} , F^{+or-} or Λ_c^+ populations. Another subscript "j" was added to the lifetime being used or to quantities whose computation require use of the lifetime. This is to indicate that in $N_{evts} - N_x$ events, the $k_j = 1$ proper decay time will be sampled from a decaying D^{+or-} parent population while in $N_{F^{+or-}}$ events this $k_j = 1$

proper decay time will come from a decaying F^{+or-} population and that in $N_{\Lambda_c^+}$ events, the $k_j = 1$ proper decay time is drawn from a Λ_c^+ parent population.

Up to now, no hypothesis degeneracy is taken into account nor is any $D/F/\Lambda_c$ particle identification degeneracy (see Section 8.3.1) . The most important feature of the ambiguous sample is not the individual hypothesis degeneracies of the various fits. It is, rather, what makes the sample ambiguous in the first place: the $D/F/\Lambda_c$ particle identification degeneracy. Thus, in order to simplify the procedure, the hypothesis degeneracy H_j of all three particle types was set to a fixed value:

$$H_j^{D^{+or-} \text{ or } F^{+or-} \text{ or } \Lambda_c^+} = 1$$

The procedure will therefore generate events such as D^+F^+ or $D^+F^+\Lambda_c^+$ or D^-F^- but will not generate events such as $D^+D^+F^+\Lambda_c^+\Lambda_c^+$.

The set of N_{evts} ($k_j = 1$) events does *not* constitute yet an accurate idealization of the ambiguous sample without including the $D/F/\Lambda_c$ particle identification degeneracy which will generate $k_j = 1,...,\tilde{P}_j^{I.D.}$ "ambiguous" candidates for the j^{th} event. The $D/F/\Lambda_c$ particle identification degeneracy $\tilde{P}_j^{I.D.}$ is a rather complicated quantity to model. It can be conjecturized that this quantity depends mostly on the topology of the event and the acceptance of the detector. The events of the charged ambiguous sample are ambiguous because of lack of particle identification of the decay products. This is sometimes due to the excessive speeds of these secondaries for time-of-flight identification or to the presence of multiple hits in in the TOF II paddle assembly. Whatever the actual reasons giving rise to $P_j^{I.D.} \neq 1$, it is not necessary to have knowledge of their exact nature. The input $D/F/\Lambda_c$ particle identification degeneracy for the j^{th} Monte-Carlo'ed event can be sampled directly from the ambiguous data so that

$$dist.\ \tilde{P}_j^{I.D.} \equiv dist.\ P_j^{I.D.}$$

where the equivalence of the distributions really means numerical equality of all moments in the limit of infinite statistics.

As explained in Section 8.1.4 , the various momenta are sampled from appropriate experimental distributions depending on whether the event is a charmed meson or baryon. That takes care of the $k_j = 1$ hypothesis. But the remaining $\tilde{P}_j^{I.D.} - 1$ hypotheses must also be generated. A simple method, which was adopted in the end, is to assume the ambiguous parent particles have equal speed, that is, to *scale* the momenta according to

$$\tilde{P}_j^{k_j=2,3} = M_{k_j=2,3} \times \frac{\tilde{P}_j^{k_j=1}}{M_{k_j=1}}$$

where $k_j = 1$ stands for D^{+or-} when $1 \leq j \leq N_{D^{+or-}}$, for F^{+or-} when $N_{D^{+or-}} + 1 \leq j \leq N_{D^{+or-}} + N_{F^{+or-}}$ or for Λ_c^+ when $N_{D^{+or-}} + N_{F^{+or-}} + 1 \leq j \leq N_{evts}$. Also, $k = 2$ and $k = 3$ stand for F^+ and Λ_c^+ when $1 \leq j \leq N_{D^{+or-}}$, for D^+ and Λ_c^+ when $N_{D^{+or-}} + 1 \leq j \leq N_{D^{+or-}} + N_{F^{+or-}}$, and for D^{+or-} and F^{+or-} when $N_{D^{+or-}} + N_{F^{+or-}} + 1 \leq j \leq N_{evts}$.

The approach presented in the last paragraph may, at first sight, appear to be somewhat of an oversimplification. Several ambiguous fits ($P_j^{I.D.} \neq 1$) do not make use of the same combinations of (or single)

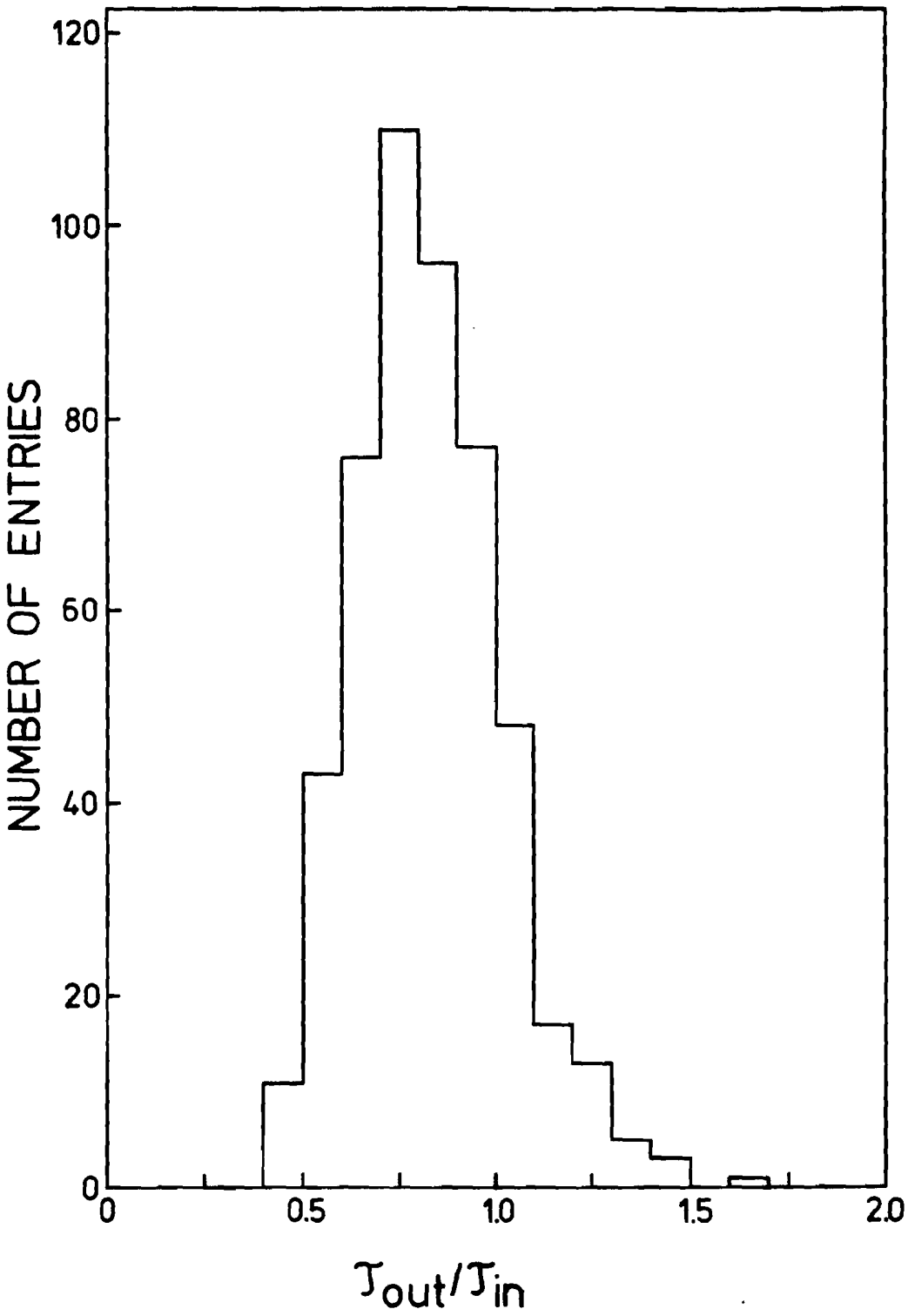

Figure # 61

Monte Carlo distribution of the ratio τ_{out}/τ_{in} . The bin width is 0.04 . Each entry in the histogramme is obtained from a one-parameter fit to the $D^{+\,or\,-}$ candidates from a simulated ambiguous sample. Each simulated ambiguous sample is a Monte Carlo generation of 23 $D^{+\,or\,-}$ with $\tau_{D^{+\,or\,-}} = 11.1 \times 10^{-13} sec$, 3 $F^{+\,or\,-}$ with $\tau_{F^{+\,or\,-}} = 2.6 \times 10^{-13} sec$ and 2 Λ_c^+ with $\tau_{\Lambda_c^+} = 2.0 \times 10^{-13} sec$. together with appropriate ambiguous alternates.

π^0 in order to balance the $p_\perp$ of the charged secondaries in the event, so that the parent momenta need not be related in any such simple way as in the above equation. In order to investigate this further, a method by which the distribution of the ratios $r_j = \left(\frac{P_j^1}{P_j^2 \text{ or } P_j^3}\right)$ of the different parent momenta of all ambiguous events was sampled in order to obtain the degenerate momenta, was devised. In that case,

$$\tilde{P}_j^{k_j=2,3} = \tilde{P}_{k_j=1} \times \tilde{r}_j$$

where

$$dist.\, \tilde{r}_j \equiv dist.\, r_j$$

in the usual sense. This additional complication was checked to have no effect on the results of the Monte-Carlo procedure and was therefore not included in the final version of the algorithm.

The j^{th} Monte-Carlo'ed sample generated with this procedure thus contains N_{evts} events each having k_j particle identification degeneracy such that $\sum_{j=1}^{N_{evts}} k_j \leq 3 \times N_{evts}$. A total of $N_{D^{+or-}}$, $N_{F^{+or-}}$ and $N_{\Lambda_c^+}$ of these events are drawn from pure D^{+or-} , F^{+or-} and Λ_c^+ parent populations respectively. Their proper decay times are distributed according to the probability density function of Section 8.1.1 . The remaining $\sum_{j=1}^{N_{evts}} k_j - N_{evts}$ others are generated so that this does not happen. A typical run of the Monte-Carlo algorithm would generate 500 such samples.

8.3.3.2) **One-parameter fit to the ambiguous Monte Carlo dataset**

The datasets generated in the manner described in the preceeding section were first fed to the one-parameter maximum-likelihood program, for analysis. The results are presented on Figure # 58 . This plot was already referred to in Section 8.2 in connection with the *lower* limit to the D^{+or-} lifetime. It is useful to investigate the effect of including hypotheses of shorter-lived origin than D^{+or-} (but ambiguous with D^{+or-}) into the one-parameter fit used for pure samples such as that of F^{+or-} or Λ_c^+ . To do so, one arbitrarily selects out all the generated decays of D^{+or-} in the Monte-Carlo'ed datasets disregarding all others. Because of the way it was generated, such a subset of the ambiguous events contains $N_{D^{+or-}}$ "true" D^{+or-} coming from sampling a distribution with the parent lifetime $\tau_{D^{+or-}}$ and, in addition, contains $N_X = N_{F^{+or-}} + N_{\Lambda_c^+}$ events, also called D^{+or-} but for which the proper decay times would not distribute according to the lifetime of the charged D-meson or any other lifetime. †

As is seen on the figure, the short-lived events bring down the one-parameter maximum-likelihood estimate of the lifetime by a significant amount. Figure # 58 displays the most-probable value of the distribution of ratios τ_{out}/τ_{in} together with the one-sigma equivalent errors as a function of f_X . The input D^{+or-} lifetime was set to $11.1 \times 10^{-13} sec$. The point for which the short-lived contamination was closer to $f_X = 17\%$ (computed using the two-parameter method) is indicated by the arrow. At that point $N_{D^{+or-}} = 23$, $N_{F^{+or-}} = 3$ and $N_{\Lambda_c^+} = 2$ and the most-probable value of the τ_{out}/τ_{in} ratio is $0.78^{+.19}_{-.14}$. Figure # 61 presents the actual distribution of the ratios τ_{out}/τ_{in} , at that point, while Figure # 62 and

† For these events, it would be the proper decay times of the rejected F^{+or-} or Λ_c^+ fits that would, depending on the case, distribute according to $\tau_{F^{+or-}}$ or $\tau_{\Lambda_c^+}$.

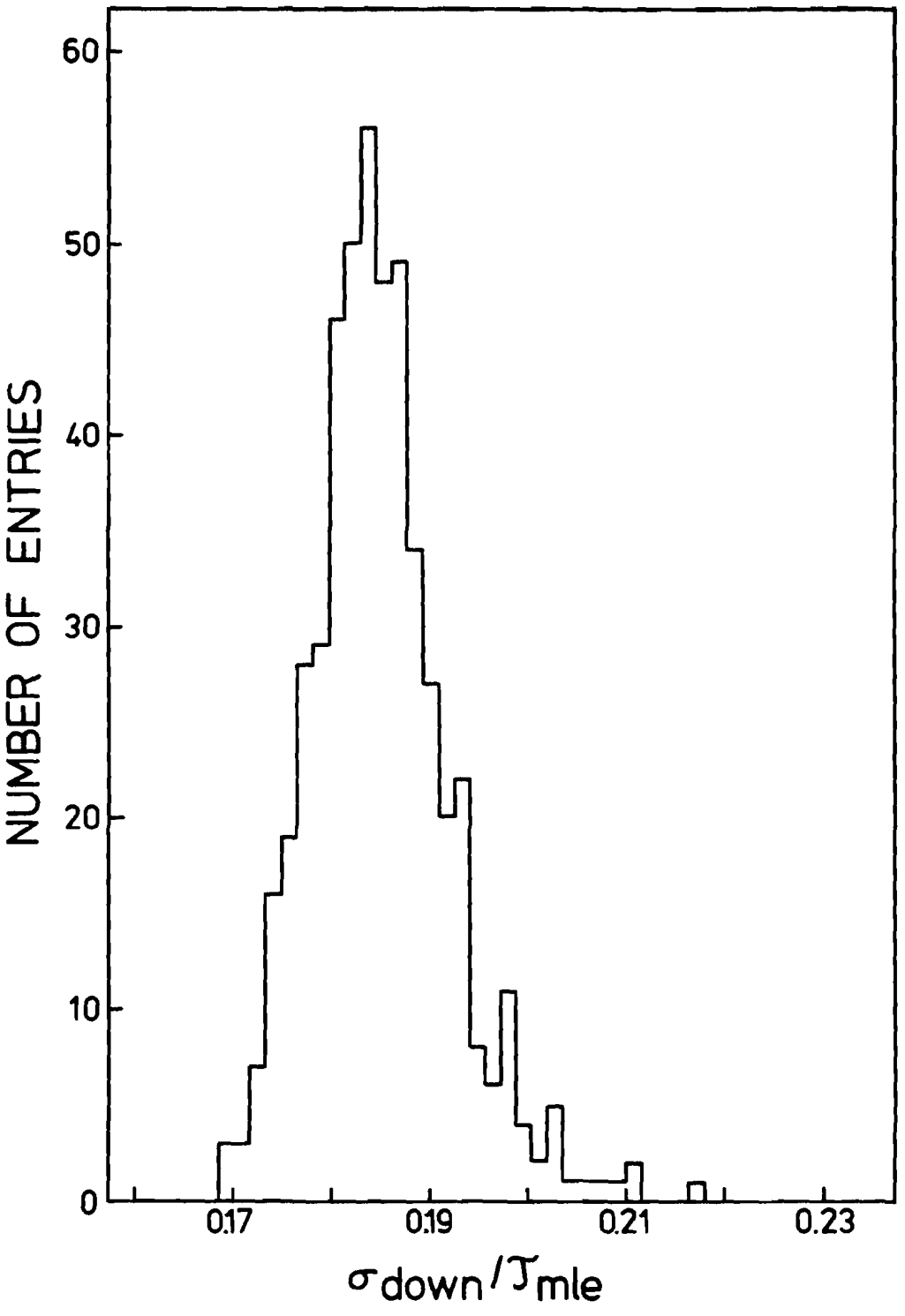

Figure # 63

Monte Carlo distribution of the lower fractional one-sigma equivalent error $(\tau_{out} - \tau_{out}^{-1\sigma})/\tau_{out}$. The bin width is 0.0016 . Each entry in the histogramme is obtained from a one-parameter fit to the $D^{+\,or\,-}$ candidates from a simulated ambiguous sample. Each simulated ambiguous sample is a Monte Carlo generation of 23 $D^{+\,or\,-}$ with $\tau_{D^{+\,or\,-}} = 11.1 \times 10^{-13} sec$, 3 $F^{+\,or\,-}$ with $\tau_{F^{+\,or\,-}} = 2.6 \times 10^{-13} sec$ and 2 Λ_c^+ with $\tau_{\Lambda_c^+} = 2.0 \times 10^{-13} sec$. together with appropriate ambiguous alternates.

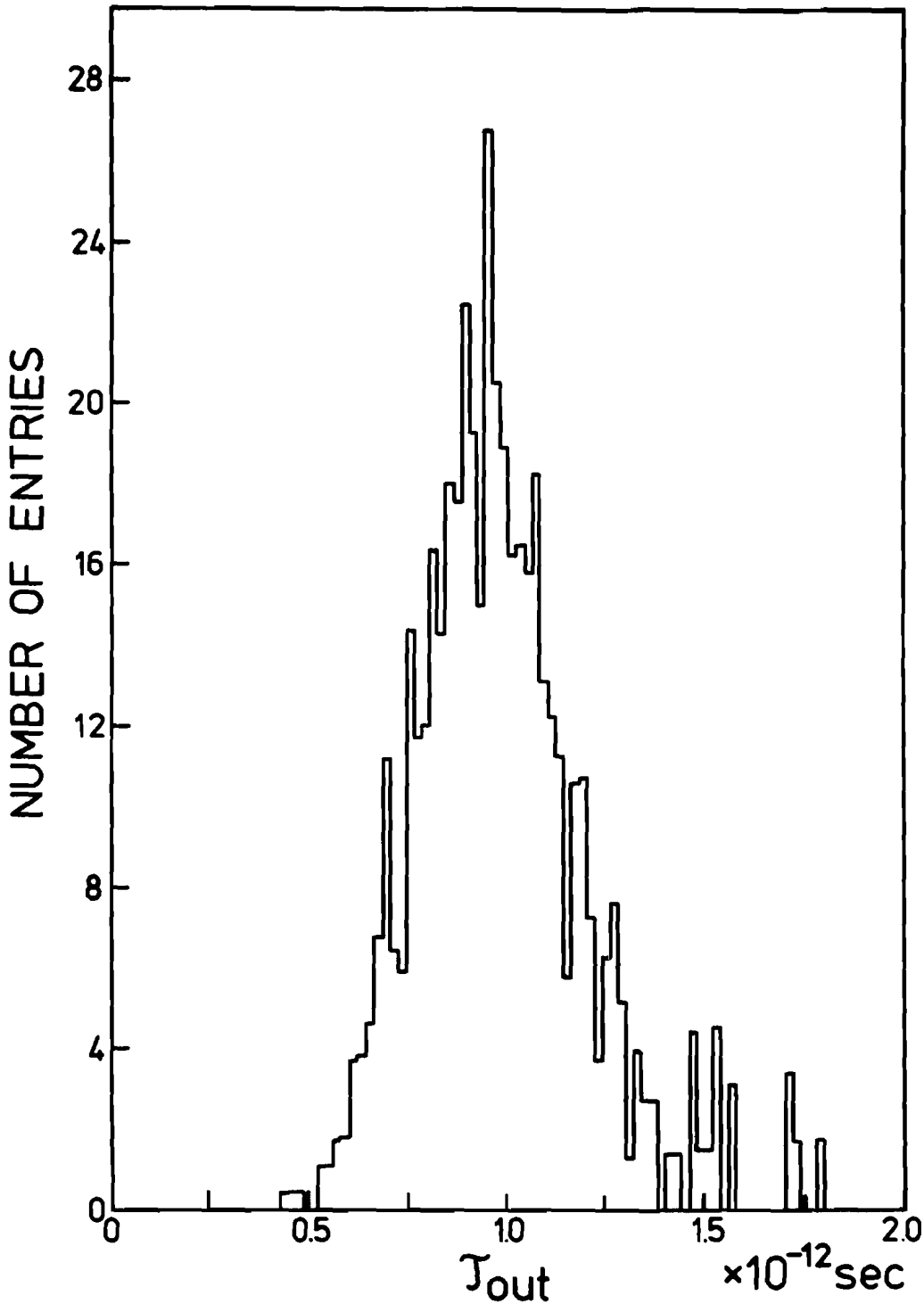

Figure # 65

Monte Carlo distribution of the one-parameter maximum likelihood estimates τ_{out} . The bin width is $0.2 \times 10^{-13} sec$. Each entry in the histogramme is obtained from a one-parameter fit to the $D^{+\,or\,-}$ candidates from a simulated ambiguous sample. Each simulated ambiguous sample is a Monte Carlo generation of 28 $D^{+\,or\,-}$ with $\tau_{D^{+\,or\,-}} = 9.4 \times 10^{-13} sec$, no $F^{+\,or\,-}$ and no Λ_c^+ together with appropriate ambiguous alternates. Thus, each generated sample contains no input short-lived contamination.

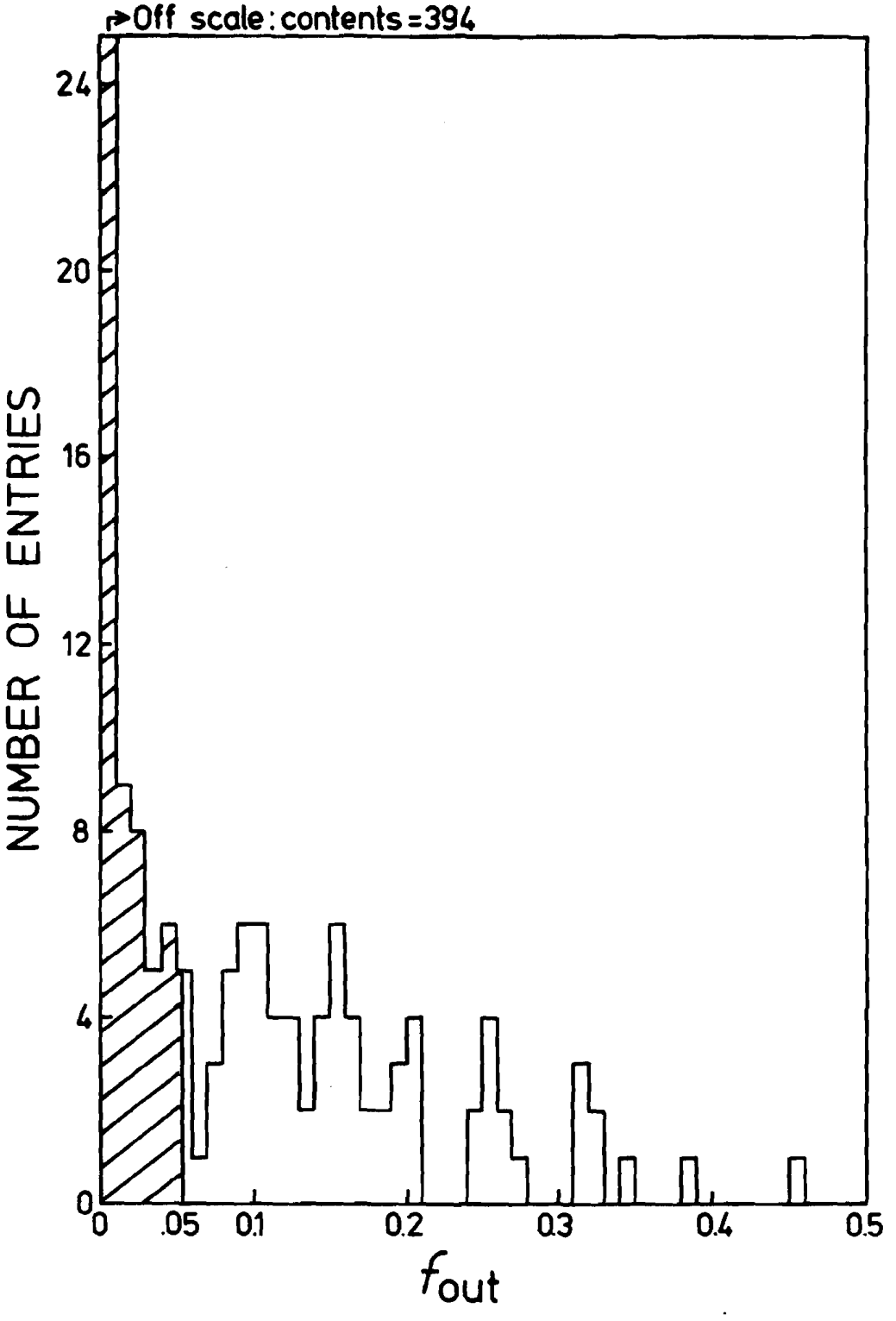

Figure # 67

Monte Carlo distribution of the two-parameter maximum likelihood estimates f_{out} . The bin width is 0.01 . Each entry in the histogramme is obtained from a two-parameter fit to all candidates from a simulated ambiguous sample. Each simulated ambiguous sample is a Monte Carlo generation of 28 $D^{+\,or\,-}$ with $\tau_{D^{+\,or\,-}} = 9.4 \times 10^{-13} sec$, no $F^{+\,or\,-}$ and no Λ_c^+ together with appropriate ambiguous alternates. Thus, each generated sample contains no input short-lived contamination. The first bin is deliberately off-scale.

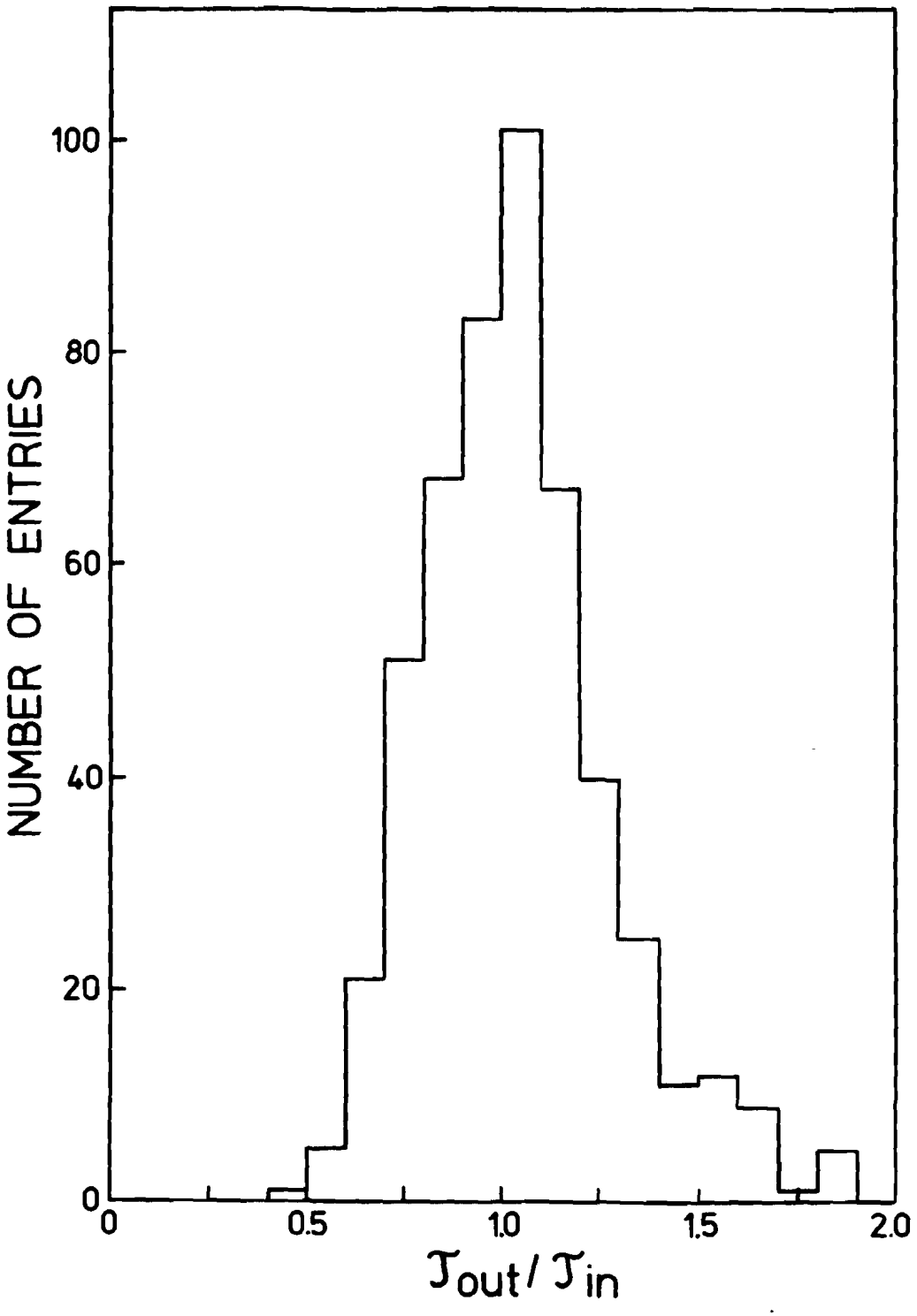

Figure # 69

Monte Carlo distribution of the two-parameter ratios τ_{out}/τ_{in} . The bin width is 0.1 . Each entry in the histogramme is obtained from a two-parameter fit to the $D^{+\,or\,-}$ candidates from a simulated ambiguous sample. Each simulated ambiguous sample is a Monte Carlo generation of 28 $D^{+\,or\,-}$ with $\tau_{D^{+\,or\,-}} = 9.4 \times 10^{-13} sec$, no $F^{+\,or\,-}$ and no Λ_c^+ together with appropriate ambiguous alternates. Thus, each generated sample contains no input short-lived contamination.

Figure # 63 present the distributions of the upper and lower fractional one-sigma equivalent error. Figure # 64 presents the distribution of the one-parameter maximum-likelihood estimates of τ_{out} and one finds that $\tau_{out}^{mle} = 8.7^{+2.2}_{-1.6} \times 10^{-13} sec$ while $\tau^{in}_{D^{+or-}} = 11.1 \times 10^{-13} sec$.

Now, the experimental ratio of the one-parameter lower estimate of the D^{+or-} lifetime to the two-parameter maximum-likelihood estimate of this lifetime is 9.4/11.1 = 0.85 , that is, $\sim .4\sigma$ above what could be expected from the Monte Carlo results presented in the last paragraph. The ratio between the one-parameter estimate and the two-parameter estimate of the lifetime of the charged D-meson is now understood, in a statistically significant way, in terms of a short-lived contamination component.

8.3.3.3) **One- vs two-parameter fit to the ambiguous Monte Carlo dataset**

8.3.3.3.1) **Zero input short-lived contamination fraction**

The Monte-Carlo'ed sets of ambiguous events were fed *simultaneously* to both the one-parameter and two-parameter algorithm for a range of input short-lived contamination. The basic motivation behind all the studies which will be described below always remained the same: to establish the statistical soundness of the two-parameter method under the actual conditions that it was used. In other words, to verify the applicability of the method.

At the bottom of the range of possible input short-lived contamination ($f_x^{in} = 0\%$), one can ask whether the two-parameter log-likelihood method gives a reasonable result: i.e. the same as the one-parameter fit would give. This is a measure of how trustworthy the two-parameter method is if the short-lived contamination happened to be negligible. A total of 500 datasets with $N_{D^{+or-}} = 28$ $\tau^{in}_{D^{+or-}} = 9.4 \times 10^{-13} sec$, $N_{F^{+or-}} = 0$ and $N_{\Lambda_c^+=0}$ ‡ were generated and fitted simultaneously with the one- and two-parameter methods. Figure # 65 presents the distribution of the one-parameter maximum likelihood estimates of the input lifetime. Figure # 66 presents a similar distribution but this time using the two-parameter maximum-likelihood method. Figure # 67 shows the distribution of the output maximum-likelihood estimates of the short-lived contamination fraction f_x^{out} . On this last plot, one finds that 84% of the times (hatched area), $f_x^{out} \leq 5\%$ with $f_x^{in} = 0\%$. (The first bin is deliberately off-scale to show that by the time the second bin is reached, the ratio of contents is already down to 9/394 = 2%) As for the lifetime estimates, ratio distributions summarize best the previous lifetime distributions. Figure # 68 and Figure # 69 display the distributions of τ_{out}/τ_{in} for the one- and two-parameter fits respectively. In this case, both distributions peak at 1 and have similar FWHM showing that, in the hypothetical case of $f_x^{in} = 0\%$, the one- and two-parameter methods yield the same answer.

8.3.3.3.2) **Non-zero input short-lived contamination fraction**

In several other runs, the range of possible input short-lived contamination was extensively covered. Results pertaining to the important cases of $f_x^{in} = 0\%$ 17% and 35% are presented on Figure # 70, Figure

‡ This will provide, by no means, a trivial result. Although, in the Monte-Carlo sample, there are no hypotheses for which the parent distribution sampled was that of an F^{+or-} or Λ_c^+ , F^{+or-} and Λ_c^+ hypotheses were indeed a major part of the data sample. In terms of the previous notation, $P_j^{I \cdot D \cdot} \neq 1 \; \forall j$ ...

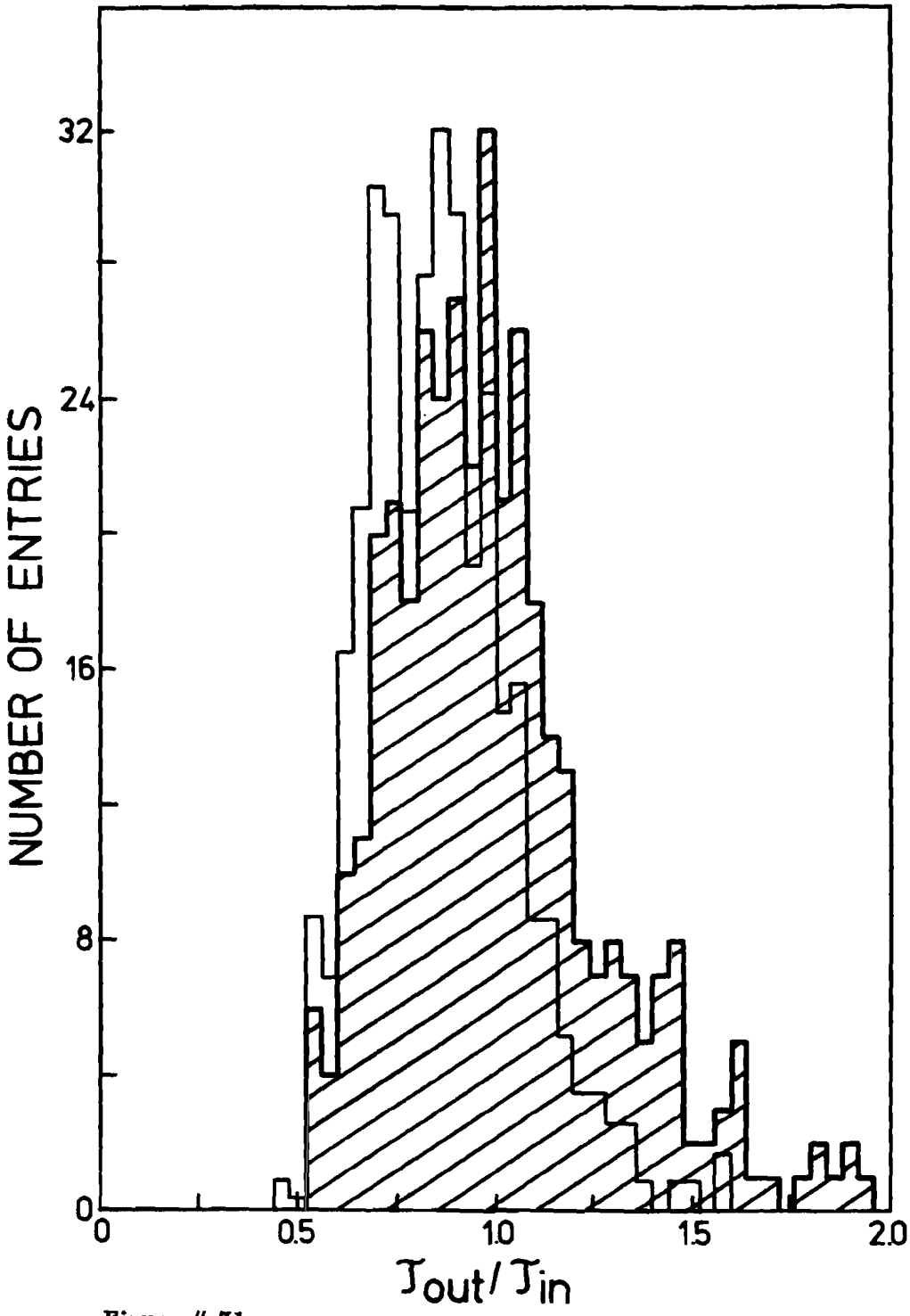

Figure # 71

Monte Carlo distribution of the, one-parameter in the background and two-parameter in the foreground, ratios τ_{out}/τ_{in} . The bin width is 0.04 . Each entry in the histogrammes is obtained from a one-parameter fit to the $D^{+\,or\,-}$ candidates and a two-parameter fit to all candidates from a simulated ambiguous sample. Each simulated ambiguous sample is a Monte Carlo generation of 23 $D^{+\,or\,-}$ with $\tau_{D^{+\,or\,-}} = 11.1 \times 10^{-13} sec$, 3 $F^{+\,or\,-}$ with $\tau_{F^{+\,or\,-}} = 2.6 \times 10^{-13} sec$, and 2 Λ_c^+ with $\tau_{\Lambda_c^+} = 2.0 \times 10^{-13} sec$ together with appropriate ambiguous alternates. This corresponds to about 17% short-lived contamination.

71 and Figure # 72 . Thus, the situation depicted by Figure # 71 is that when the input contaminant fraction to the Monte-Carlo procedure f_x^{in} is given by the maximum-likelihood estimate of f_x using, as data, the sum of the 1^{st} and 2^{nd} run ambiguous datasets while Figure # 70 and Figure # 72 correspond to situations where f_x^{in} is equal to that maximum-likelihood estimate minus its lower and plus its upper one-sigma errors respectively... In all three cases $N_{evts} = 28$, $\tau^{in}_{D^+or^-} = 11.1 \times 10^{-13} sec$, $\tau^{in}_{F^+or^-} = 2.6 \times 10^{-13} sec$ and $\tau^{in}_{\Lambda_c^+} = 2.0 \times 10^{-13} sec$. On Figure # 70, $N_{F^+or^-} = N_{\Lambda_c^+} = 0$, on Figure # 71, $N_{F^+or^-} = 3$ $N_{\Lambda_c^+} = 2$ and on Figure # 72, $N_{F^+or^-} = 5$ $N_{\Lambda_c^+} = 5$. The histogramme in the background represents the distribution of the ratios τ^{one-p}/τ_{in} . The histogramme in the foreground represents the distribution of τ^{two-p}/τ_{in} . The "one-p" and "two-p" superscripts denote which (one- or two-parameter) method was used to fit the Monte-Carlo data. As †

$$M.P.V.\ dist.\ \frac{\tau^{two-p}}{\tau_{in}} = 1 \qquad in\ all\ three\ cases$$

while

$$M.P.V.\ dist.\ \frac{\tau^{one-p}}{\tau_{in}} \leq 1 \qquad in\ the\ last\ two\ cases,$$

it is clear that the two-parameter method removes the short-lived contamination from the Monte Carlo ambiguous samples. The price one has to pay for this benefit is a slight increase in the upper and lower fractional error on the output lifetime; but this is not un-expected as an additional parameter (the short-lived contaminant fraction f_x) was introduced.

The Monte-Carlo simulations presented in this section demonstrate the statistical soundness of the two-parameter maximum-likelihood method as well as its applicability to the E531 data.

8.3.4) **Errors on the two-parameter fit**

Arguments that were raised in the understanding of the error on the one-parameter fits (Section 8.1.5) to pure samples are no less valid in the case of the two-parameter fit to the ambiguous charged sample. As the hypothesized worst-case systematic errors together with the real measurement errors did not account for much in the case of the analysis to pure samples, they would not either in the case of the charged ambiguous sample.

8.4) **The one-parameter fit to the cut ambiguous sample**

8.4.1) **The cut method and Monte Carlo expectations**

The shorter-lived components of the ambiguous sample are expected to preferentially populate shorter proper decay time bins rather than longer proper decay time bins which ought to contain, preferentially, the longer-lived component of the sample. This is a fact that only depends on

$$\tau_X \ll \tau_{D^+or^-}$$

a condition which should be fulfilled as we have

$$2.1 \times 10^{-13} sec < 11.1 \times 10^{-13} sec$$

† M.P.V. stands for Most Probable Value...

Because of this difference in lifetime, one can expect the one-parameter maximum-likelihood fit to a selection of D^{+or-} hypotheses † from the ambiguous sample to progressively reflect more accurately the lifetime of the longer-lived main contributor D^{+or-} *provided* events with increasingly longer proper decay times be systematically excluded from the time-ordered sample. This *cut* preferentially removes the shorter-lived contaminants. Note that, in this case, the value of t_{short} in the one-parameter method of Section 8.1.1 is given by the cut: $t^{ij}_{short} = t_{cut\ off} \quad \forall i,j$.

This method will be checked against Monte Carlo data before using it to extract the lifetime of the charged D-meson.

As was explained in Section 8.2 and Section 8.3.3 , Monte Carlo datasets of a total number of events $N_{evts} = 28$ were generated containing $N_{D^{+or-}} = 23$ with $\tau_{D^{+or-}} = 11.1 \times 10^{-13} sec$, $N_{F^{+or-}} = 3$ with $\tau_{F^{+or-}} = 2.6 \times 10^{-13} sec$ and $N_{\Lambda_c^+} = 2$ with $\tau_{\Lambda_c^+} = 2.0 \times 10^{-13} sec$. This amounts to a weighted average short-lived contamination of $\tau_x = 2.1 \times 10^{-13} sec$ in the order of 17% . These datasets were fed, with no events removed, to the one-parameter algorithm. The ratios of the difference between the output maximum-likelihood estimate and the main contributor's lifetime over this main-contributor's lifetime were plotted yielding an average of

$$\left.\frac{\tau^{one-p}_{out} - \tau^{in}_{D^{+or-}}}{\tau^{in}_{D^{+or-}}}\right|_{avg} = -.17 \pm .24 \quad F.W.H.M.$$

Then, similar datasets were generated and fitted in a similar way except that a required 7 ‡ events with proper decay times $t_{ij} < t_{cut\ off} = 1.19 \times 10^{-13} sec$ were systematically removed from the data. As was explained above, t^{ij}_{short} was set to $1.19 \times 10^{-13} sec$. In this case,

$$\left.\frac{\tau^{one-p}_{out} - \tau^{in}_{D^{+or-}}}{\tau^{in}_{D^{+or-}}}\right|_{avg} = -.09 \pm .29 \quad F.W.H.M.$$

Then, again, datasets were generated and fitted similarly but now with a required 20 events with proper decay times $t_{ij} < t_{cut\ off} = 8.08 \times 10^{-13} sec$ being systematically removed from the data. In this case, t^{ij}_{short} was set to $8.08 \times 10^{-13} sec$. One finds:

$$\left.\frac{\tau^{one-p}_{out} - \tau^{in}_{D^{+or-}}}{\tau^{in}_{D^{+or-}}}\right|_{avg} = -.02 \pm .32 \quad F.W.H.M.$$

The results of this simulation are clear. They indicate that one-parameter fits performed on selections of D^{+or-} hypotheses from Monte Carlo data with known short-lived contamination and long-lived main contribution will provide a statistically significant non-biased maximum-likelihood estimate of the lifetime of the main contributor as long as the adequate $t_{cut\ off}$ is used. So, even in the limit of this experiment's

† As explained elsewhere, such a selection from the ambiguous sample will not yield a pure sample of D^{+or-} .

‡ This corresponds to the actual distribution of proper decay times of the selection of D^{+or-} hypotheses from the ambiguous sample.

limited statistics, this cut method still constitutes an excellent approach to extract the lifetime of D^{+or-} from the ambiguous sample.

8.4.2) **The lifetime of the D^{+or-} meson**

The procedure described in the previous section was applied to the sum of the 1^{st} and 2^{nd} run datasets. Kinematic fits to D^{+or-} hypotheses from the total of 28 events (only one of which is known to be uniquely consistent with a charged D meson) were selected out from the ambiguous sample. Hypotheses with proper decay times smaller than preset values of $t_{cut\ off}$ were then systematically removed from the selection to produce *reduced* samples that were then fitted using the one-parameter method.

A total of 14 such removals and fits were done. Each time one hypothesis had to be removed from the sample, care had to be taken to re-adjust the event weights w_{ij} such that for the j^{th} event,

$$\sum_{i=1}^{H_j^{D^{+or-}}} w_{ij}^{H_j^{D^{+or-}}} = 1$$

still applied. The values of $t^k_{cut\ off}$ were chosen so that

$$t^k_{cut\ off} = s^{D^{+or-}}_{k-1} \quad k = 2, 14$$

and

$$t^1_{cut\ off} = 0 \times 10^{-13} sec$$

In the above, $s_k^{D^{+or-}}$ is simply a notation for the set of the first 13 proper decay times $t_{ij}^{D^{+or-}}$ *ordered* in increasing order. Hypotheses were removed provided

$$t_{ij}^{D^{+or-}} \leq t^k_{cut\ off} \quad k = 1, 14$$

hence, in the first fit, no hypotheses were removed while in the last one-parameter fit, 13 hypotheses were removed.

The results of this procedure applied to the E531 data are displayed on Figure # 73 . The error bars extend as far as the upper and lower one-sigma equivalent errors on the one-parameter maximum-likelihood estimate of the main contributor's lifetime. As can be seen one the figure, by progressively increasing $t_{cut\ off}$ from zero up to slightly above $4.0 \times 10^{-13} sec$ the one-parameter maximum-likelihood estimate of the lifetime of the main contributor increases from about $9 \times 10^{-13} sec$ to roughly $11 \times 10^{-13} sec$ where a *plateau* is reached. The two-parameter result of $11.1 \times 10^{-13} sec$ is indicated on the right hand side of the figure.

The result of the cut method, which is essentially like waiting for the shorter-lived component to die-off while the longer-lived component lives-on, is in excellent agreement with that of the two-parameter method.

8.5) **The lifetime of the D^0 meson**

The E531 experiment has measured and published a lifetime of the D^0 meson using data from its first run. [175] Additional data collected in the 2^{nd} run can be merged with that of the 1^{st} run to provide an overall sample of $N_{evts} = 39 + 19 = 58$ un-ambiguous ‡ neutral D meson decays.

‡ In the sense that no fits to any other charmed of strange parent can be made to any of the D^0 candidates. Note that in the context of this section, D^0 also stands for $\overline{D}^0$ meson decays.

Although some details of the analysis of the neutral sample differ from that of the charged sample, most of these pertain to techniques used in finding the candidates in the emulsion and the related efficiencies. Much more detail on several important aspects of this part of the analysis of the data collected by E531 can be found in ***Ref.*** 168 . The lifetime of the D^0 meson was extracted from the data in exactly the same way the lifetimes of the F^{+or-} and Λ_c^+ were computed using pure data samples: by using the method of the one-parameter maximum-likelihood estimate described in Section 8.1.1 .

The result of such a fit to the subset of $N_{evts} = 39$ second run events is

$$\tau_{D^0} = 4.8^{+.9+2.1}_{-.7-1.3} \times 10^{-13} sec$$

while the fit to the total of $N_{evts} = 58$ combined first and second run events is

$$\tau_{D^0} = 4.3^{+.7+1.5}_{-.5-1.0} \times 10^{-13} sec$$

All errors are statistical. Figure # 74 present the two-sigma offset plot of the ln L function for this last fit.

8.6) **The D^{+or-} to D^0 lifetime ratio**

Several methods have been proposed and used to extract the ratio $\rho = \tau_{D^{+or-}}/\tau_{D^0}$ from the data collected by the 1^{st} Run of E531. [176] These methods are still applicable to the sum of the 1^{st} and 2^{nd} run data. Their purpose is more to estimate the errors associated with the arithmetical ratio of the maximum-likelihood estimates of each of the two particle types rather than estimating the ratio directly.

As it was, experiment 531 was not set up to, and did not, measure *directly* the ratio of the two lifetimes in question. However, and quite more importantly, data collected by both runs can be used to compute this ratio together with an estimate of the error associated with the simple and straightforward calculation $\rho = \tau_{D^{+or-}}/\tau_{D^0} = 11.1/4.3 = 2.6$. In this ratio, the two-parameter maximum-likelihood estimate of the lifetime of the D^{+or-} for a total of $N_{evts} = 28$ ($1^{st} + 2^{nd}$ Run) events is used in the numerator while the the one-parameter maximum-likelihood estimate of the lifetime of the D^0 for a total of $N_{evts} = 58$ ($1^{st} + 2^{nd}$ Run) events is used in the denominator.

As was explained in Sections 8.1) and 8.3), the likelihood function L is constructed as essentially being a measure of the probability of observation, under experimental conditions pertaining to E531, of particular sets of decay times associated with certain decaying states. This function is:

$$L = \prod_{j=1}^{N_{evts}} p_j$$

In the case of D^0 , the likelihood function is obtained by substituting the sum of the 1^{st} and 2^{nd} run data in the one-parameter function of 8.1.1):

$$L^{D^0}(\tau_{D^0}) = \prod_{j=1}^{N_{evts}=58} \left(\sum_{i=1}^{H_j^{D^0}} w_{ij}\, f_{ij}\,(\tau_{D^0} | t^j_{short}, t^j_{long}; t_{ij}) \right)$$

The location where the D^0 likelihood function peaks in terms of its single parameter τ_{D^0} provides the most likely estimate of the lifetime of the D^0 . At other values of this parameter, say τ^* , the likelihood function

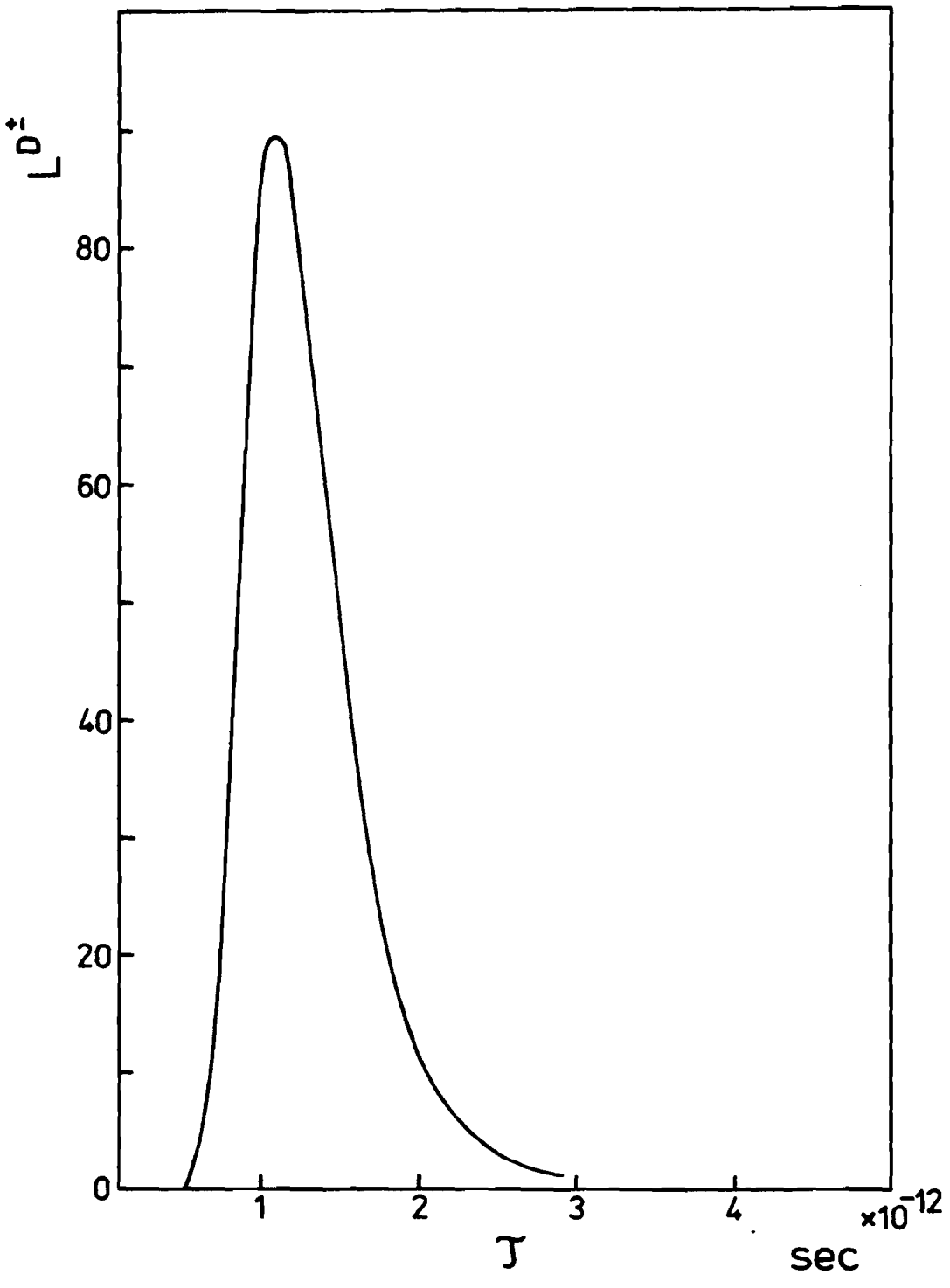

Figure # 76
Probability distribution for the charged D-mesons versus τ . This distribution is obtained from a cut through the two-parameter likelihood function.

provides values of the probability that, given the set of *observed* D^0 decays, the lifetime of the neutral D meson be $\tau_{D^0}^{true} = \tau^*$. Figure # 75 displays the value of $L(\tau_{D^0})$ in the range of $0\,sec \leq \tau^* \leq 10.0 \times 10^{-13} sec$.

In the case of D^{+or-} , the likelihood function has not one, but two parameters and, on using the notation of Section 8.3.1), reads:

$$L^{D^{+or-}}(\tau_{D^{+or-}}) = \prod_{j=1}^{N_{evts}=28} P_j\left(\tau_{D^{+or-}}, f_x = f_x^{mle} | \tau_x = 2.1 \times 10^{-13} sec, \ ...\right)$$

that is:

$$L^{D^{+or-}}(\tau_{D^{+or-}}) = \prod_{j=1}^{N_{evts}=28} P_j\left(\tau_{D^{+or-}}, f_x = 0.17 | \tau_x = 2.1 \times 10^{-13} sec, \ ...\right)$$

where "..." refers to all the observed variables (see Section 8.3.1). This is essentially taking a cut through Figure # 60 at the maximum-likelihood estimate of the short-lived contaminant fraction: 17 % and using each of the data points to evaluate the probability along the cut. Figure # 76 displays this function.

Armed with the probability distributions for D^0 and D^{+or-} , it is now possible to sample (generate) *lifetimes* $\tilde{\tau}^*$ from the data using hybrid Monte Carlo methods, such that

$$dist.\ \tilde{\tau}^*_{D^{+or-}} \equiv L^{D^{+or-}}(\tau^*)$$

and

$$dist.\ \tilde{\tau}^*_{D^0} \equiv L^{D^0}(\tau^*)$$

where the equivalence is meant to mean numerical equality of all moments of the distributions. The usefulness of such a procedure is that while the above distributions can be generated from the data, so can the following:

$$dist.\ \tilde{\rho} = dist.\ \left(\frac{\tilde{\tau}^*_{D^{+or-}}}{\tilde{\tau}^*_{D^0}}\right)$$

Such a distribution for a very large number of entries was generated and plotted on Figure # 77 . From such a plot, one can numerically determine one-sigma equivalent errors on the value of $\rho = 11.1/4.3 = 2.6$ by requiring that 68.3% of the data be included. The result is

$$\rho = \frac{\tau_{D^{+or-}}}{\tau_{D^0}} = 2.6^{+1.0}_{-0.9}$$

where all errors are statistical. Other methods at extracting the lifetime ratio (some of which are more complicated) essentially give similar results.

9.0) CONCLUSIONS

The lifetimes obtained from combining two runs of E531 are [177] :

$$\tau_{F^{+ or -}} = 2.6^{+1.6}_{-0.9} \times 10^{-13} sec \qquad 6 \quad decays$$

$$\tau_{\Lambda_c^+} = 2.0^{+0.7}_{-0.6} \times 10^{-13} sec \qquad 13 \quad decays$$

$$\tau_{D^{+ or -}} = 11.1^{+4.4}_{-2.9} \times 10^{-13} sec \qquad 23 \pm 5 \quad decays$$

and [178] [168]

$$\tau_{D^0 \, or \, \overline{D}^0} = 4.3^{+0.7}_{-0.6} \times 10^{-13} sec \quad 58 \quad decays$$

in which the quoted errors are all statistical. In addition, the lifetime of the charged D-meson was extracted using two different and independent methods. The results were found to be similar.

The ratio of the charged D-meson to neutral D-meson lifetimes was extracted from the charged and neutral samples. The result is:

$$\frac{\tau_{D^{+ or -}}}{\tau_{D^0 \, or \, \overline{D}^0}} = 2.6^{+1.0}_{-0.9}$$

The World data on the charged and neutral D-mesons is summarized on Figure # 78 . World Averages are indicated but these should be taken with extreme caution. Recent experimental results from NA27 clearly support a long-lived charged D-meson as the results presented in this thesis also indicate. On the other hand, it appears that much of the uncertainty concerning the lifetime of the neutral D-meson is now merely statistical. Some implications of the ratio of the charged to neutral D-meson lifetimes are clear. Certainly, in view of the arguments presented in Section 2.0, the Naive Spectator Model of charmed particle decay constitutes an incomplete view. Unfortunately, the theoretical techniques proposed to palliate the shortcomings of the NSM do not permit a model independent prediction of charmed particle lifetimes. In some sense however, there is now qualitative theoretical understanding of why one shouldn't expect mesons or baryons carrying a heavy quark to all have the same lifetimes.

Using the formalism of Section 2 , the ratio of the charged to neutral D-meson lifetimes can be expressed as follows:

$$\rho = \frac{\tau_{D^+}}{\tau_{D^0}} = \frac{\Gamma^{SL+NL}_{D^0} + \Gamma^{FA}_{D^0}}{\Gamma^{SL+NL(QOI)}_{D^+}}$$

Figure # 79 presents the ratio of the flavour annihilation width of the neutral D-meson $\Gamma^{FA}_{D^0}$ to the total width of the charged D-meson $\Gamma^{SL+NL(QOI)}_{D^+}$ as a function of the Pauli interference parameter α_P over its range of 0 to 1 . This was computed using the value of the ratio of the charged to neutral D lifetimes measured by this experiment and using $C_+ = 0.74$ and $C_- = 1.8$. Thus,

$$\frac{D^0 \textit{ annihilation width}}{D^+ \textit{ total width}} = \frac{\Gamma^{FA}_{D^0}}{\Gamma^{SL+NL(QOI)}_{D^+}} = \left(\frac{\tau_{D^+}}{\tau_{D^0}}\right) - \frac{2 + (2\,C_+^2 + C_-^2)}{2 + [2\,(1 + \alpha_P)\,C_+^2 + (1 - \alpha_P)\,C_-^2]}$$

Numerically,

$$\frac{D^0 \textit{ annihilation width}}{D^+ \textit{ total width}} = 1.6^{+1.0}_{-0.9} \qquad \alpha_P = 0$$
$$\frac{D^0 \textit{ annihilation width}}{D^+ \textit{ total width}} = 1.4^{+1.0}_{-0.9} \qquad \alpha_P = 1/2$$
$$\frac{D^0 \textit{ annihilation width}}{D^+ \textit{ total width}} = 1.1^{+1.0}_{-0.9} \qquad \alpha_P = 1$$

In other words, if there are no quark cluster interference effects (Pauli effects), a rather large neutral D annihilation width is required to account for the E531 result. The neutral D-meson annihilation width must then be 60% larger than the total charged D-meson width. If, on the other hand, there are maximum interference effects, then the neutral D-meson annihilation width must only be 10% larger than the total charged D-meson width to account for the E531 data. Although it is not ruled out that the ratio of the charged to neutral D-meson lifetimes measured by E531 be entirely due to quark cluster interference, this is not very likely. As was mentioned in Section 2 , the maximum effect QCI alone can have is to bring the charged to neutral D-meson lifetime ratio up from 1 to 1.5 . This is still 1.2σ below $2.6^{+1.0}_{-0.9}$. Therefore, it can be concluded from our data, that flavour annihilation effects, i.e. Cabibbo-favored W-exchange D^0 decays, contribute significantly to the total decay width of the neutral D-meson. This conclusion is independently supported by recent data [179] from the ARGUS collaboration which has measured the branching ratio for the W-exchange process: $D^0 \rightarrow \overline{K}^0 \phi$ to be $(0.99 \pm 0.32 \pm 0.17)\%$. This branching ratio has also been measured by the CLEO group [201] to be $(1.18 \pm 0.40 \pm 0.17)\%$.

The World data on the F-meson or even on the Λ_c^+-baryon is not as large as it is for the charged and neutral D-mesons. The results presented in this thesis together with other data indicate that the F-meson is longer-lived than the Λ_c^+ baryon and shorter-lived than the neutral D-meson. From Section 2 , in the hypothesis that the annihilation amplitude components $P^{(1)}$ and $P^{(8)}$ are the same for the neutral D meson and charged F meson, the D^0, $D^{+ \textit{ or } -}$ and $F^{+ \textit{ or } -}$ lifetimes measured by E531 indicate that $4.25 \leq P^{(8)}/P^{(1)} \leq 5.4$ for $0 \leq \alpha_P \leq 1$. This result is not inconsistent with a picture of the annihilation mechanism where all colour states contribute with roughly equal probabilities [180] .

Finally, combining E531's lifetimes with recently measured semi-leptonic branching ratios shows a rough equality of the semi-leptonic decay rates of $D^{+ \textit{ or } -}$, D^0 and Λ_c^+ which can be interpreted in terms of W-boson radiation contributing equally to the semi-leptonic decays of these species [178] .

$$R^{sl}_{D^{+ \textit{ or } -}} = 1.7 \pm 0.5 \times 10^{11} s^{-1}$$
$$R^{sl}_{D^0 \overline{D}^0} = 1.5^{+0.4}_{-0.6} \times 10^{11} s^{-1}$$
$$R^{sl}_{F^{+ \textit{ or } -}} = 2.3^{+1.0}_{-1.2} \times 10^{11} s^{-1}$$

This result indicates that the Naive Spectator Model constitutes an adequate but only partial view of charmed particle decays roughly applicable to semi-leptonic decays.

From the results presented in this thesis, a picture of charmed meson decays is emerging. The naive spectator model appears to go a long way towards the understanding of semi-leptonic decays. To complete the picture however, significant corrections to the NSM approach to non-leptonic decays must be made. From lifetime measurements alone, it is not possible to determine the absolute contributions of the possible

mechanisms of QCI and FA. However, from a measurement of the semi-leptonic branching ratio of charged D-mesons, it is possible to estimate the value of the Pauli interference parameter α_P through the formalism of Section 2 . When using the latest MARK III result of

$$BR^{MARK\ III}\left(D^+ \rightarrow e^+ X\right) = 17.0 \pm 1.9 \pm 0.7\%\ ^{59}$$

in

$$BR^{QCI}\left(D^+ \rightarrow e^+ X\right) = \frac{1}{2 + 2\left(1+\alpha_P\right) C_+^2 + \left(1-\alpha_P\right) C_-^2}$$

one obtains:

$$\alpha_P = .21^{+.28}_{-.21}$$

This is displayed on Figure # 80 . The range of α_P is also indicated by arrows on Figure # 79 . This *experimental* value of the Pauli interference parameter is rather moderate and thus, to account for the E531 result on the charged to neutral D-meson lifetimes, it is required that the neutral D-meson flavour annihilation contribution (Cabibbo favored W-exchange D^0 decays) be of the order of about 50% larger than the total charged D-meson width.

Given the current status of the World Dataset on charm decays, it is clear that one of the immediate task to perform is to design and run high-statistics experiments with very high-resolution vertex detectors coupled to spectrometers allowing the best possible charged and neutral particle identification possible. Such experiments are already in the planning stage or underway.

10.0) **THE FIRST AND SECOND RUN CHARGED DECAYS DATASET**

10.1) **TABLE OF F^{+or-} DECAYS**

j	Run	Rec.	Emu. type	N_h^j	N_e^j	$q_\mu^j P_\mu^j$ GeV/c	l_j μm	l_{long}^j μm	$\epsilon(l_j)$ %	P_c^j GeV/c	M_c^j MeV/c^2	t_j $\times 10^{-13} sec$	Decay	Cabibbo factor §	w_j
1†	527	3682	HV	7	5	30	670	4884	95	12.200	2026 ± 56	$3.61 \pm .09$	$F^- \to \underline{\pi}^+ \underline{\pi}^- \pi^- \pi^0$	cc	1.00
2	597	1851	HV	0	5	‡	130	15121	95	9.300	2057 ± 110	$0.92 \pm .09$	$F^+ \to \underline{K}^+ \underline{\pi}^- \underline{\pi}^+ \overline{K}^0$	cc	1.00
3	638	9417	HV	1	3	−9	153	42903	95	6.000	2050 ± 45	$1.68 \pm .09$	$F^+ \to \underline{K}^+ K^- \pi^+ \pi^0$	cc	1.00
4	671	7015	HV	–	–	−7	65	25000	95	2.800	2055 ± 94	$1.53 \pm .12$	$F^+ \to \underline{K}^+ \overline{K}^0$	cc	1.00
5*	1222	281	NV	2	2	−45	1051 ± 28	10814	99	$9.310 \pm .040$	1968 ± 17	$7.42 \pm .21$	$F^+ \to K^+ K^- \underline{\pi}^+$	cc	1.00
6	1340	1667	NV	3	2	−5.3	134 ± 9	1282	100	$13.600 \pm .300$	1919 ± 34	$0.65 \pm .05$	$F^+ \to K^- K^+ \underline{\pi}^+ \pi^0$	cc	1.00

†: First Run data starts here ‡: Primary muon not seen * : Second Run data starts here
§ : $c \equiv \cos\theta_c$ $s \equiv \sin\theta_c$

10.2) **TABLE OF Λ_c^+ DECAYS**

j,i	Run	Rec.	Emu. type	N_h^j	N_s^j	$q_\mu^j P_\mu^j$ GeV/c	l_j μm	l_{long}^j μm	$\epsilon(l_j)$ %	P_c^{ij} GeV/c	M_c^{ij} MeV/c^2	t_{ij} $\times 10^{-13} sec$	Decay	Cabibbo factor §	w_{ij}
1,1†	476	4449	HV	20	12	−59	27.7	27998	76	2.700	*	$0.78 \pm .08$	$\Lambda_c^+ \to \underline{p}\,\underline{\pi}^+\,\underline{\pi}^-\,(\overline{K}^0)$	cc	0.50
1,2	476	4449	HV	20	12	−59	27.7	27998	76	4.800	*	$0.44 \pm .05$	$\Lambda_c^+ \to \underline{p}\,\underline{\pi}^+\,\underline{\pi}^-\,(\overline{K}^0)$	cc	0.50
2,1	498	4985	HV	0	6	−15	180	19526	95	8.400	2274 ± 41	$1.63 \pm .05$	$\Lambda_c^+ \to \underline{\Lambda}^0\,\underline{\pi}^+\,\underline{\pi}^-\,\underline{\pi}^+$	cc	1.00
3,1	499	4713	HV	6	6	−189	366	16330	95	4.170	2269 ± 17	$6.68 \pm .19$	$\Lambda_c^+ \to \underline{\Sigma}^0\,\pi^+$	cc	1.00
4,1	549	4068	HV	4	8	−11	20.6	13367	76	1.900	*	$0.83 \pm .07$	$\Lambda_c^+ \to \underline{p}\,K^-\,\underline{\pi}^+\,(\pi^0)$	cc	0.50
4,2	549	4068	HV	4	8	−11	20.6	13367	76	2.500	*	$0.63 \pm .07$	$\Lambda_c^+ \to \underline{p}\,K^-\,\underline{\pi}^+\,(\pi^0)$	cc	0.50
5,1	567	2596	HV	6	6	−6	175	3370	95	5.800	2204 ± 207	$2.30 \pm .08$	$\Lambda_c^+ \to \underline{p}\,\overline{K}^0$	cc	1.00
6,1	610	4088	HV	2	2	−8	221	17664	95	4.700	2374 ± 62	$3.58 \pm .19$	$\Lambda_c^+ \to \underline{\Lambda}^0\,\underline{\pi}^+\,\underline{\pi}^-\,\underline{\pi}^+$	cc	1.00
7,1	602	2032	HV	10	4	−20	282.5	19198	95	6.300	*	$3.41 \pm .10$	$\Lambda_c^+ \to \underline{p}\,\underline{\pi}^+\,\underline{\pi}^-\,(\overline{K}^0)$	cc	1.00
8,1	650	6003	HV	0	7	−15	40.6	9845	95	5.730	2131 ± 63	$0.54 \pm .03$	$\Lambda_c^+ \to \underline{\Lambda}^0\,\underline{\pi}^+\,\pi^-\,\underline{\pi}^+$	cc	1.00
9,1‡	1089	5646	O3	1	5	−11	275 ± 5	53596	99	$5.220 \pm .030$	2309 ± 207	$4.01 \pm .08$	$\Lambda_c^+ \to \underline{p}\,\underline{K}^-\,\pi^+$	cc	1.00
10,1	1195	4860	VK	1	2	−3	182 ± 17	26152	86	$4.900 \pm .200$	*	$2.83 \pm .31$	$\Lambda_c^+ \to \underline{\Lambda}^0\,\underline{\pi}^+\,(\pi^0)$	cc	1.00
11,1	1198	3153	NV	6	2	−9	82 ± 9	30318	100	$7.100 \pm .300$	2266 ± 30	$0.88 \pm .10$	$\Lambda_c^+ \to p\,\pi^+\,\pi^-\,\overline{K}^0$	cc	1.00
12,1	1215	4119	2O	8	7	−9	$62.8 \pm .2$	32722	99	$3.230 \pm .020$	2261 ± 97	$1.48 \pm .01$	$\Lambda_c^+ \to \underline{p}\,\underline{\pi}^+\,K^-$	cc	1.00
13,1	1277	2257	2N	0	2	−9	18 ± 3	7756	75	$3.670 \pm -$	*	$0.37 \pm -$	$\Lambda_c^+ \to \underline{p}\,\underline{\pi}^-\,\underline{\pi}^+\,(\overline{K}_L^0)$	cc	1.00

†: First Run data starts here ‡: Second Run data starts here * : $0C$ Calculation

§ : $c \equiv \cos\theta_c$ $s \equiv \sin\theta_c$

10.3) **TABLE OF CHARGED AMBIGUOUS DECAYS (PART I)**

j,i,k	Run	Rec.	Emu. type	N_h^j	N_s^j	$q_\mu^j P_\mu^j$ GeV/c	l_j μm	l_{long}^j μm	$\epsilon(l_j)$ %	P_c^{ijk} GeV/c	M_c^{ijk} MeV/c^2	t_{ij}^k $\times 10^{-13} sec$	Decay	Cabibbo factor §	w_{ij} **
1,1,1†	656	2631	HV	6	5	−150	570	31072	95	32.600	1933 ± 73	1.09	$D^+ \to \pi^+ K^- \pi^+ \pi^0$	cc	1.00
1,1,2	656	2631	HV	6	5	−150	570	31072	95	32.400	2099 ± 73	1.16	$F^+ \to K^+ K^- \pi^+ \pi^0$	cc	1.00
1,1,3	656	2631	HV	6	5	−150	570	31072	95	31.700	2317 ± 76	1.37	$\Lambda_c^+ \to p\ K^- \pi^+$	cc	1.00
2,1,1	547	3192	HV	1	11	−16	185	21011	95	9.400	1717 ± 260	1.23	$D^+ \to \pi^+ K^- \pi^+$	cc	0.50
2,2,1	547	3192	HV	1	11	−16	185	21011	95	9.700	2036 ± 231	1.19	$D^+ \to \pi^+ K^- \pi^+ \pi^0$	cc	0.50
2,1,2	547	3192	HV	1	11	−16	185	21011	95	10.800	2209 ± 323	1.13	$F^+ \to \pi^+ \pi^- \pi^+ \pi^0$	cc	1.00
3,1,1	512	5761	HV	0	4	> 150	457	46314	95	10.400	1829 ± 35	2.74	$D^+ \to K^- \pi^+ \underline{\pi}^+ \pi^0$	cc	1.00
3,1,2	512	5761	HV	0	4	> 150	457	46314	95	10.300	2011 ± 33	2.92	$F^+ \to K^- K^+ \underline{\pi}^+ \pi^0$	cc	1.00
4,1,1	598	1759	HV	1	2	−11	1802	6438	95	17.400	1862 ± 25	6.46	$D^+ \to K^- K^+ \underline{\pi}^+ \pi^0$	cs	1.00
4,1,2	598	1759	HV	1	2	−11	1802	6438	95	17.900	2179 ± 38	7.66	$\Lambda_c^+ \to K^- p\ \underline{\pi}^+ \pi^0$	cc	1.00
5,1,1	493	1235	HV	3	4	−7	2203	31668	95	11.900	2061 ± 156	11.54	$D^+ \to \pi^+ \pi^+ \pi^- \overline{K}^0$	cc	1.00
5,1,2	493	1235	HV	3	4	−7	2203	31668	95	11.700	22.46 ± 166	12.38	$F^+ \to \pi^+ \pi^+ K^- \overline{K}^0$	cc	1.00
5,1,3	493	1235	HV	3	4	−7	2203	31668	95	13.300	2330 ± 123	12.61	$\Lambda_c^+ \to \pi^+ \pi^+ K^- n$	cc	1.00
6,1,1	529	271	HV	0	5	−57	2547	20923	95	55.400	*	2.87	$D^+ \to \pi^+ \pi^0 (\overline{K}^0)$	cc	1.00
6,1,2	529	271	HV	0	5	−57	2547	20923	95	43.100	*	3.89	$F^+ \to K^+ (\overline{K}^0)$	cc	0.50
6,2,2	529	271	HV	0	5	−57	2547	20923	95	38.400	*	4.36	$F^+ \to K^+ \pi^0 (\overline{K}^0)$	cc	0.50
7,1,1	663	7758	HV	0	6	> 150	13000	17832	59	114.300	*	7.09	$D^+ \to K^- \pi^+ \underline{e}^+ (\nu_e)$	c	1.00
7,1,2	663	7758	HV	0	6	> 150	13000	17832	59	96.800	*	8.83	$F^+ \to \pi^- \pi^+ \underline{e}^+ (\nu_e)$	c	1.00
8,1,1	546	1339	HV	7	5	−7	2150	41514	95	16.600	*	8.08	$D^+ \to K^- \pi^+ \underline{\mu}^+ (\nu_\mu)$	c	1.00
8,1,2	546	1339	HV	7	5	−7	2150	41514	95	13.300	*	10.63	$F^+ \to \pi - \pi^+ \underline{\mu}^+ (\nu_\mu)$	c	0.50
8,2,2	546	1339	HV	7	5	−7	2150	41514	95	36.800	*	3.84	$F^+ \to \pi - \pi^+ \underline{\mu}^+ (\nu_\mu)$	c	0.50

†: First Run data starts here ‡: Second Run data starts here * : $0C$ Calculation ** : See text for usage of weights in different fits...

§ : $c \equiv \cos\theta_c$ $s \equiv \sin\theta_c$

TABLE OF CHARGED AMBIGUOUS DECAYS (PART II)

j,i,k	Run	Rec.	Emu. type	N_h^j	N_s^j	$q_\mu^j P_\mu^j$ GeV/c	l_j μm	l_{long}^j μm	$\epsilon(l_j)$ %	P_c^{ijk} GeV/c	M_c^{ijk} MeV/c^2	t_{ij}^k $\times 10^{-13} sec$	Decay	Cabibbo factor §	w_{ij} **
9,1,1	533	7152	HV	5	6	−9	5246	39939	85	40.100	*	8.16	$D^+ \to \pi^+ \pi^0 (\overline{K}^0)$	cc	1.00
9,1,2	533	7152	HV	5	6	−9	5246	39939	85	34.800	*	9.91	$F^+ \to K^+ (\overline{K}^0)$	cc	1.00
10,1,1	580	4508	HV	3	4	+7	2307	10733	95	9.500	*	15.14	$D^- \to \pi^- \underline{K}^+ \underline{e}^- (\overline{\nu}_e)$	c	0.50
10,2,1	580	4508	HV	3	4	+7	2307	10733	95	10.000	*	14.39	$D^- \to \pi^- \underline{K}^+ \underline{e}^- (\overline{\nu}_e)$	c	0.50
11,1,1	522	2107	HV	14	4	−51	13600	31270	59	23.500	*	36.09	$D^+ \to \pi^+ \underline{\pi}^+ K^- (\pi^0)$	cc	0.50
11,2,1	522	2107	HV	14	4	−51	13600	31270	59	31.700	*	26.75	$D^+ \to \pi^+ \underline{\pi}^+ K^- (\pi^0)$	cc	0.50
11,1,2	522	2107	HV	14	4	−51	13600	31270	59	22.500	*	39.74	$F^+ \to K^+ \underline{\pi}^+ K^- (\pi^0)$	cc	0.50
11,2,2	522	2107	HV	14	4	−51	13600	31270	59	32.700	*	27.34	$F^+ \to K^+ \underline{\pi}^+ K^- (\pi^0)$	cc	0.50
11,1,3	522	2107	HV	14	4	−51	13600	31270	59	22.500	*	46.01	$\Lambda_c^+ \to p \underline{\pi}^+ K^- (\pi^0)$	cc	0.50
11,2,3	522	2107	HV	14	4	−51	13600	31270	59	31.500	*	32.86	$\Lambda_c^+ \to p \underline{\pi}^+ K^- (\pi^0)$	cc	0.50
12,1,1‡	1046	2977	NV	8	2	−3	154 ± 5	34860	100	10.700 ± .200	1807 ± 83	0.90 ± .04	$D^+ \to \pi^+ \pi^- \pi^+ \pi^0$	sc	1.00
12,1,2	1046	2977	NV	8	2	−3	154 ± 5	34860	100	11.000 ± .200	1855 ± 86	0.92 ± .04	$F^+ \to \pi^+ \pi^- \pi^+ \pi^0$	cc	1.00
12,1,3	1046	2977	NV	8	2	−3	154 ± 5	34860	100	10.800 ± .300	2204 ± 75	1.09 ± .05	$\Lambda_c^+ \to p \pi^- \pi^+ \pi^0$	sc	1.00
13,1,1	1050	2844	KH	4	3	−15	1292 ± 4	17096	98	23.000 ± .500	1868 ± 47	3.50 ± .08	$D^+ \to \underline{\pi}^+ \pi^+ \underline{\pi}^- \pi^0 \pi^0$	sc	1.00
13,1,2	1050	2844	KH	4	3	−15	1292 ± 4	17096	98	24.600 ± .600	1868 ± 47	3.45 ± .08	$F^+ \to \underline{\pi}^+ \pi^+ \underline{\pi}^- \pi^0 \pi^0$	cc	1.00
14,1,1	1068	5090	KH	3	4	−12	827 ± 3	36006	98	13.700 ± .800	*	3.76 ± .22	$D^+ \to \underline{\pi}^+ K^- \pi^+ (\pi^0)$	cc	1.00
14,1,2	1068	5090	KH	3	4	−12	827 ± 3	36006	98	12.800 ± .600	*	4.25 ± .20	$F^+ \to \underline{\pi}^+ \pi^- \pi^+ (\pi^0)$	cc	1.00
15,1,1	1073	192	KH	2	2	−16	927 ± 1	23901	98	6.800 ± .500	*	8.50 ± .67	$D^+ \to \pi^+ \pi^+ \pi^- (\overline{K}^0)$	cc	0.50
15,2,1	1073	192	KH	2	2	−16	927 ± 1	23901	98	6.000 ± .400	*	9.63 ± .72	$D^+ \to \pi^+ \pi^+ K^- (\pi^0)$	cc	0.25
15,3,1	1073	192	KH	2	2	−16	927 ± 1	23901	98	4.700 ± .300	*	12.30 ± .79	$D^+ \to \pi^+ \pi^+ K^- (\pi^0)$	cc	0.25
15,1,2	1073	192	KH	2	2	−16	927 ± 1	23901	98	4.400 ± .300	*	13.85 ± .87	$F^+ \to \pi^+ \pi^+ \pi^- (\pi^0)$	cc	0.48
15,2,2	1073	192	KH	2	2	−16	927 ± 1	23901	98	6.000 ± −	*	10.16 ± −	$F^+ \to K^+ \pi^+ \pi^- (\overline{K}^0)$	cc	0.26
15,3,2	1073	192	KH	2	2	−16	927 ± 1	23901	98	5.600 ± .300	*	10.88 ± .50	$F^+ \to K^+ \pi^+ K^- (\pi^0)$	cc	0.13
15,4,2	1073	192	KH	2	2	−16	927 ± 1	23901	98	4.700 ± .300	*	12.97 ± .71	$F^+ \to K^+ \pi^+ K^- (\pi^0)$	cc	0.13

†: First Run data starts here ‡: Second Run data starts here * : $0C$ Calculation ** : See text for usage of weights in different fits...

§ : $c \equiv \cos\theta_c$ $s \equiv \sin\theta_c$

TABLE OF CHARGED AMBIGUOUS DECAYS (PART III)

j,i,k	Run	Rec.	Emu. type	N_h^j	N_s^j	$q_\mu^j P_\mu^j$ GeV/c	l_j μm	l_{long}^j μm	$\epsilon(l_j)$ %	P_c^{ijk} GeV/c	M_c^{ijk} MeV/c^2	t_{ij}^k $\times 10^{-13} sec$	Decay	Cabibbo factor §	w_{ij} **
16,1,1	1080	2521	KH	0	4	~ -40	188 ± 4	24980	98	$22.500 \pm .700$	1693 ± 675	$0.52 \pm .02$	$D^+ \to \pi^+ K^- \pi^+ \pi^0$	cc	1.00
16,1,2	1080	2521	KH	0	4	~ -40	188 ± 4	24980	98	20.600 ± 1.000	1883 ± 37	$0.60 \pm .03$	$F^+ \to \pi^+ K^- K^+ \pi^0$	cc	0.33
16,2,2	1080	2521	KH	0	4	~ -40	188 ± 4	24980	98	$17.700 \pm .400$	2026 ± 109	$0.70 \pm .02$	$F^+ \to K^+ K^- \pi^+ \pi^0$	cc	0.33
16,3,2	1080	2521	KH	0	4	~ -40	188 ± 4	24980	98	$20.700 \pm .400$	1801 ± 102	$0.60 \pm .02$	$F^+ \to K^+ K^- \pi^+$	cc	0.33
16,1,3	1080	2521	KH	0	4	~ -40	188 ± 4	24980	98	18.300 ± 2.000	2319 ± 115	$0.78 \pm .08$	$\Lambda_c^+ \to \pi^+ K^- p \pi^0$	cc	0.33
16,2,3	1080	2521	KH	0	4	~ -40	188 ± 4	24980	98	18.500 ± 2.000	2146 ± 120	$0.77 \pm .09$	$\Lambda_c^+ \to \pi^+ K^- p$	cc	0.33
16,3,3	1080	2521	KH	0	4	~ -40	188 ± 4	24980	98	$14.000 \pm .400$	2495 ± 147	$1.02 \pm .03$	$\Lambda_c^+ \to p K^- \pi^+$	cc	0.33
17,1,1	1080	7420	KH	2	4	-4	354 ± 1	31350	98	$25.000 \pm .600$	1889 ± 110	$0.88 \pm .02$	$D^+ \to \pi^- \pi^+ \pi^+ \pi^0 \pi^0$	sc	1.00
17,1,2	1080	7420	KH	2	4	-4	354 ± 1	31350	98	$26.700 \pm .700$	1889 ± 110	$0.87 \pm .02$	$F^+ \to \pi^- \pi^+ \pi^+ \pi^0 \pi^0$	cc	1.00
17,1,3	1080	7420	KH	2	4	-4	354 ± 1	31350	98	$26.600 \pm .700$	2222 ± 98	$1.01 \pm .03$	$\Lambda_c^+ \to \pi^- \pi^+ p \pi^0 \pi^0$	sc	1.00
18,1,1	1105	4668	HK	4	4	~ -21	321 ± 2	32188	87	$12.500 \pm .600$	1877 ± 62	$1.60 \pm .08$	$D^+ \to \pi^+ \pi^0 \overline{K}^0$	cc	1.00
18,1,2	1105	4668	HK	4	4	~ -21	321 ± 2	32188	87	$11.700 \pm .500$	2037 ± 61	$1.80 \pm .08$	$F^+ \to K^+ \pi^0 \overline{K}^0$	cc	1.00
18,1,3	1105	4668	HK	4	4	~ -21	321 ± 2	32188	87	$13.000 \pm .800$	2209 ± 46	$1.88 \pm .12$	$\Lambda_c^+ \to \pi^+ \pi^0 n$	sc	1.00
19,1,1	1194	807	NV	2	3	-31	14015 ± 759	40008	89	$22.700 \pm .300$	1958 ± 91	38.50 ± 1.993	$D^+ \to K^- \pi^+ \pi^+$	cc	1.00
19,1,2	1194	807	NV	2	3	-31	14015 ± 759	40008	89	$22.300 \pm .300$	2088 ± 86	41.32 ± 2.47	$F^+ \to K^- \pi^+ K^+$	cc	1.00
19,1,3	1194	807	NV	2	3	-31	14015 ± 759	40008	89	$23.200 \pm .300$	2327 ± 79	45.98 ± 2.60	$\Lambda_c^+ \to \pi^- \pi^+ p$	sc	1.00
20,1,1	1198	3877	OV	1	3	-79	2280 ± 148	32790	100	$15.500 \pm .500$	1783 ± 57	$9.17 \pm .65$	$D^+ \to \pi^+ K^- \pi^+ \pi^0$	cc	1.00
20,1,2	1198	3877	OV	1	3	-79	2280 ± 148	32790	100	$13.100 \pm .300$	1955 ± 57	$11.44 \pm .81$	$F^+ \to K^+ K^- \pi^+ \pi^0$	cc	1.00
20,1,3	1198	3877	OV	1	3	-79	2280 ± 148	32790	100	$9.900 \pm .100$	2513 ± 67	17.53 ± 1.20	$\Lambda_c^+ \to p \pi^- \pi^+ \pi^0$	sc	1.00
21,1,1	1256	2092	NV	0	11	-38	3965 ± 216	11146	99	$16.100 \pm .600$	1716 ± 76	15.36 ± 1.00	$D^+ \to \pi^+ \pi^+ K^- \pi^0 \pi^0$	cc	1.00
21,1,2	1256	2092	NV	0	11	-38	3965 ± 216	11146	99	$15.900 \pm .600$	1942 ± 65	16.40 ± 1.00	$F^+ \to K^+ \pi^+ K^- \pi^0 \pi^0$	cc	0.44
21,2,2	1256	2092	NV	0	11	-38	3965 ± 216	11146	99	$15.300 \pm .800$	1924 ± 60	17.04 ± 1.35	$F^+ \to \pi^+ \pi^+ K^- \pi^0 \overline{K}^0$	cc	0.44
21,3,2	1256	2092	NV	0	11	-38	3965 ± 216	11146	99	$15.400 \pm .800$	1858 ± 66	16.93 ± 1.28	$F^+ \to K^+ \pi^+ \pi^- \pi^0 \overline{K}^0$	cc	0.12
21,1,3	1256	2092	NV	0	11	-38	3965 ± 216	11146	99	$16.000 \pm .600$	2236 ± 56	18.86 ± 1.24	$\Lambda_c^+ \to p \pi^+ \pi^- \pi^0 \pi^0$	sc	1.00

†: First Run data starts here ‡: Second Run data starts here * : $0C$ Calculation ** : See text for usage of weights in different fits...

§ : $c \equiv \cos\theta_c$ $s \equiv \sin\theta_c$

TABLE OF CHARGED AMBIGUOUS DECAYS (PART IV)

j,i,k	Run	Rec.	Emu. type	N_h^j	N_s^j	$q_\mu^j P_\mu^j$ GeV/c	l_j μm	l_{long}^j μm	$\epsilon(l_j)$ %	P_c^{ijk} GeV/c	M_c^{ijk} MeV/c^2	t_{ij}^k $\times 10^{-13} sec$	Decay	Cabibbo factor §	w_{ij} **
22,1,1	1261	5401	NV	0	6	−3	3896 ± 211	14810	99	14.800 ± 1.300	*	16.41 ± 1.84	$D^+ \to K^- \pi^+ \underline{\mu}^+ (\overline{\nu}_\mu)$	c	0.50
22,2,1	1261	5401	NV	0	6	−3	3896 ± 211	14810	99	10.300 ± .500	*	23.59 ± 1.66	$D^+ \to K^- \pi^+ \underline{\mu}^+ (\overline{\nu}_\mu)$	c	0.50
22,1,2	1261	5401	NV	0	6	−3	3896 ± 211	14810	99	19.800 ± 1.900	*	12.94 ± 1.34	$F^+ \to \pi^- \pi^+ \underline{\mu}^+ (\overline{\nu}_\mu)$	c	0.50
22,2,2	1261	5401	NV	0	6	−3	3896 ± 211	14810	99	10.100 ± .400	*	25.36 ± 1.67	$F^+ \to \pi^- \pi^+ \underline{\mu}^+ (\overline{\nu}_\mu)$	c	0.50
23,1,1	1263	3857	2K	28	5	+9	94 ± 1	24558	98	6.500 ± .400	2109 ± 159	0.90 ± .06	$D^- \to \pi^- \pi^- K^+ \pi^0$	cc	1.00
23,1,2	1263	3857	2K	28	5	+9	94 ± 1	24558	98	8.700 ± .100	1895 ± 198	0.71 ± .01	$F^- \to \pi^- \pi^- \pi^+ \pi^0$	cc	1.00
24,1,1	1263	5821	NV	1	10	−6	1281 ± 59	33135	99	14.100 ± .300	1955 ± 58	5.67 ± .28	$D^+ \to \pi^+ \pi^+ K^-$	cc	1.00
24,1,2	1263	5821	NV	1	10	−6	1281 ± 59	33135	99	14.100 ± .300	2046 ± 55	5.97 ± .32	$F^+ \to \pi^+ K^+ K^-$	cc	1.00
24,1,3	1263	5821	NV	1	10	−6	1281 ± 59	33135	99	14.500 ± .300	2286 ± 47	6.72 ± .34	$\Lambda_c^+ \to \pi^+ p K^-$	cc	1.00
25,1,1	1296	2462	NV	2	2	−65	2891 ± 92	43620	99	9.600 ± .200	*	18.78 ± .66	$D^+ \to \pi^+ \pi^- \pi^+ (\overline{K}^0)$	cc	1.00
25,1,2	1296	2462	NV	2	2	−65	2891 ± 92	43620	99	8.500 ± .200	*	22.36 ± 1.03	$F^+ \to \pi^+ \pi^- \pi^+ (\pi^0)$	cc	0.33
25,2,2	1296	2462	NV	2	2	−65	2891 ± 92	43620	99	9.800 ± .200	*	19.39 ± .77	$F^+ \to \pi^+ \pi^- K^+ (K^0)$	cc	0.33
25,3,2	1296	2462	NV	2	2	−65	2891 ± 92	43620	99	9.900 ± .300	*	19.20 ± .85	$F^+ \to K^+ \pi^- \pi^+ (K^0)$	cc	0.33
25,1,3	1296	2462	NV	2	2	−65	2891 ± 92	43620	99	11.700 ± .200	*	18.81 ± .69	$\Lambda_c^+ \to \pi^+ \pi^- p (\overline{K}^0)$	cc	0.50
25,2,3	1296	2462	NV	2	2	−65	2891 ± 92	43620	99	10.600 ± .300	*	20.76 ± .90	$\Lambda_c^+ \to \pi^+ \pi^- p (\overline{K}^0)$	cc	0.50
26,1,1	1305	5297	NV	7	10	−5	164 ± 17	23908	100	32.200 ± 2.000	1839 ± 132	0.32 ± .04	$D^+ \to K^- \pi^+ \pi^+ \pi^0$	cc	1.00
26,1,2	1305	5297	NV	7	10	−5	164 ± 17	23908	100	31.900 ± 2.000	1980 ± 126	0.34 ± .04	$F^+ \to K^- K^+ \pi^+ \pi^0$	cc	0.50
26,2,2	1305	5297	NV	7	10	−5	164 ± 17	23908	100	33.600 ± 2.000	1724 ± 144	0.32 ± .04	$F^+ \to \pi^- \pi^+ \pi^+ \pi^0$	cc	0.50
26,1,3	1305	5297	NV	7	10	−5	164 ± 17	23908	100	31.300 ± 2.000	2436 ± 117	0.40 ± .04	$\Lambda_c^+ \to K^- p \pi^+ \pi^0$	cc	1.00

†: First Run data starts here ‡: Second Run data starts here * : $0C$ Calculation ** : See text for usage of weights in different fits...

§ : $c \equiv \cos\theta_c$ $s \equiv \sin\theta_c$

TABLE OF CHARGED AMBIGUOUS DECAYS (PART V)

j,i,k	Run	Rec.	Emu. type	N_h^j	N_e^j	$q_\mu^j P_\mu^j$ GeV/c	l_j μm	l_{long}^j μm	$\epsilon(l_j)$ %	P_c^{ijk} GeV/c	M_c^{ijk} MeV/c^2	t_{ij}^k $\times 10^{-13} sec$	Decay	Cabibbo factor §	w_{ij} **
27, 1, 1	1311	3060	OH	2	4	−7	944 ± 10	52860	100	$8.600 \pm .400$	*	$6.84 \pm .36$	$D^+ \to \pi^+ K^- \pi^+ (\pi^0)$	cc	0.50
27, 2, 1	1311	3060	OH	2	4	−7	944 ± 10	52860	100	$9.400 \pm .500$	*	$6.26 \pm .37$	$D^+ \to \pi^+ \pi^- \pi^+ (\overline{K}^0)$	cc	0.50
27, 1, 2	1311	3060	OH	2	4	−7	944 ± 10	52860	100	$8.100 \pm .300$	*	$7.66 \pm .31$	$F^+ \to \pi^+ \pi^- \pi^+ (\pi^0)$	cc	0.25
27, 2, 2	1311	3060	OH	2	4	−7	944 ± 10	52860	100	$9.900 \pm .600$	*	$6.27 \pm .38$	$F^+ \to K^+ \pi^- \pi^+ (\overline{K}^0)$	cc	0.25
27, 3, 2	1311	3060	OH	2	4	−7	944 ± 10	52860	100	$9.800 \pm .500$	*	$6.33 \pm .31$	$F^+ \to \pi^+ K^- \pi^+ (K^0)$	cc	0.25
27, 4, 2	1311	3060	OH	2	4	−7	944 ± 10	52860	100	$8.800 \pm .400$	*	$7.05 \pm .31$	$F^+ \to K^+ K^- \pi^+ (\pi^0)$	cc	0.25
28, 1, 1	1322	1554	NV	5	7	−33	1791 ± 74	4570	99	$20.100 \pm .400$	1925 ± 95	$5.56 \pm .27$	$D^+ \to K^- \pi^+ \pi^+$	cc	1.00
28, 1, 2	1322	1554	NV	5	7	−33	1791 ± 74	4570	99	$23.800 \pm .500$	1852 ± 99	$4.95 \pm .23$	$F^+ \to \pi^- \pi^+ \pi^+$	cc	1.00

†: First Run data starts here ‡: Second Run data starts here * : $0C$ Calculation ** : See text for usage of weights in different fits...

§ : $c \equiv \cos\theta_c$ $s \equiv \sin\theta_c$

11.0) REFERENCES

1) Glashow, S.L., J. Iliopoulos, L. Maiani. Phys. Rev. D3 (1981) p1043.

2) Weinberg, S. Phys. Rev. Lett. 19 (1967) p1264.

3) Salam, A. Elementary Particle Theory. ed. N. Scartholm Almqvist, Forlag A B. (1968)

4) Glashow, S.L. Rev. Mod. Phys. 53, (1980) p539.
Weinberg, S. Rev. Mod. Phys. 52, (1980) p515.
Salam, A. Rev. Mod. Phys. 52, (1980) p525.

5) 't Hooft, G. Nuclear Physics, B35, (1971) p167.

6) 't Hooft, G. Nuclear Physics, B33, (1971) p173.

7) Glashow, S.L., J. Iliopoulos and L. Maiani. Phys. Rev. D2 (1970) p1285

8) Huang, Kerson. Quarks Leptons & Gauge Fields. Singapore: World Scientific Publishing, (1982) p117.

9) Bilenky, S.M., and B. Pontecorvo. Phys. Rept. 41, No. 4 (1978).

10) Ushida, N., *et al.* Phys. Rev. Lett. 47 # 24 (1981) p1694.

11) Wohl, C.G., *et al.* Rev. Mod. Phy. 56 # 2 Part II, April (1984) pS43.

12) Chau, Ling-Lie. Phys. Rep. 95 # 1 (1983) p6.

13) Kobayashi, M., and K. Maskawa. Prog. Theo. Phys. 49 (1975) p652.

14) See 11 pS297.

15) Chau, Ling-Lie. Phys. Rep. 95 # 1 (1983).

16) Cabibbo, N. Phys. Rev. Lett. 10 (1963) p531.

17) Roos M. Nucl. Phys. B77 (1974) p420.

18) Hasert, F.J., *et al.* Phys. Lett. 46B (1973) p121.

19) Aubert *et al.*. Phys. Rev. Lett. 33, (1974) p1404.

20) Augustin *et al.*. Phys. Rev. Lett. 33, (1974) p1406.

21) Drell, S., and T.M. Yan. Phys. Rev. Lett. 25, (1970) p316.

22) See 11 pS43.

23) Arnison *et al.*, (UA1). Phys. Lett. 122B (1983) p103 and 129B (1983) p273.
Bagnaia *et al.*, (UA2). Phys. Lett. 129B (1983) p130.
Banner *et al.*, (UA2). Phys. Lett. 122B (1983) p476.

24) Arnison *et al.* (UA1). Phys. Lett. 126B (1983) p398 and 129B (1983) p273.
Bagnaia *et al.* (UA2). Phys. Lett. 129B (1983) p130.

25) van der Meer, S. Rev. Mod. Phy. 57 # 3 Part I (July 1985) p689.
Rubbia, Carlo. Rev. Mod. Phy. 57 # 3 Part I (July 1985) p699.

26) Wahl, Horst D. CERN-EP/84-127.

27) Bailey, David. Ph.D. thesis, McGill University (1983) p19ff.

28) See 11 pS41.

29) Georgi, H., and H.D. Politzer. Phys. Rev. D14 (1976).

30) Campbell, Bruce A. Ph.D. thesis, McGill University (1980).

31) Abramowicz H., *et al.* Zeit. Phys. C17 (1983) p283.

32) See 11 pS62.

33) Diemoz, M., *et al.* Phys. Rep. 130, # 5 & 6 (1986).

34) See 27 p128.

35) Ushida, N., *et al.* Phys. Lett. 121B # 4 (1983).

36) Cheng, D.C., and G.K. O'Neil. Elementary Particle Physics.
Reading: Addison-Wesley (1979) p29 & p80.

37) Boyarski *et al.* Phys. Rev. Lett. 34 (1975) p1357.

38) Okubo, S. Phys. Lett. 5 # 2 (1963) p165.

39) Trilling, G.H. Phys. Rep. 75 # 2 (1981).

40) Goldhaber, G., *et al.* Phys. Rev. Lett. 37 # 5 (1976) p255.

41) Peruzzi, I., *et al.* Phys. Rev. Lett. u39 # 21 (1977) p1301.

42) Pilkuhn, H.M. Relativistic Particle Physics. New York: Springer-Verlag (1979) p194ff.

43) Perl, Martin L. High Energy Hadron Physics. New York: John Wiley (1974) p277.

44) Brandelik, R., *et al.* Phys. Lett. 70B # 1 (1977) p132.

45) Chen, A., *et al.* Phys. Rev. Lett. 51 # 8 (1983) p634.

46) Albrecht, H., *et al.* Phys. Lett. 146B (1984) p111.

47) Cazzoli, E.G., *et al.* Phys. Rev. Lett. 34 # 17 (1975) p1125.

48) Knapp, B.,*et al.* Phys. Rev. Lett. 37 # 14 (1976) p882.

49) Biagi, S.F. *et al.* CERN-EP/83-09 (January 1983).

50) Biagi, S.F. *et al.* CERN-EP/84-154 (November 1984).

51) Rosner, Jonathan L. Charmed particle lifetimes.
School of Physics and Astronomy, University of Minnesota preprint, FNAL # 33831 (1978).

52) Sidwell, R.A., *et al.* Ann. Rev. Nucl. Part. Sci. 33 (1983) p539-568.

53) Quigg, C. Introduction to Gauge Theories of the Strong, Weak and Electromagnetic Interactions.
FNAL-Conf-80/64-THY. (1980)

54) Altarelli, G. Phys. Rep. 81 (1982)1.

55) Rückl, Reinhold. CERN Preprint (1983) 83-1063.

56) Rückl, Reinhold. CERN Preprint (1984) CERN-TH.4013/84.

57) Commins, E.D. Weak Interactions of Leptons and Quarks.
Cambridge: Cambridge University Press (1983) p101.

58) Vella, E., *et al.* Phys. Rev. Lett. 48 #22 (1982) p1515.

59) Baltrusaitis, R.M., *et al.* Phys. Rev. Lett. 54 #18 (1985) p1976.

60) Guberina, B., *et al.* Phys. Lett. 89B, # 1 (1979).

61) Jagannathan, K., and V.S. Mathur. Phys. Rev. D21 # 11 (1980) p3165.

62) Koide, Yoshio. Phys. Rev. D20 # 7 (1979) p1739.

63) Peccei, R.D., and R. Rückl. MPI-PAE/PTh 75/81 (November 1981),
Ahrenshoop Symposium, East Germany, (Nov 8-13 1982).

64) Altarelli G., and L. Maiani. Ref.TH.3367-CERN 23 (July 1982).

65) Shizuya K. Phys. Lett. 100B # 1 (1981) p79.

66) Shizuya K. Phys. Lett. 105B # 5 (1981) p407.

67) See 55 p83.

68) Shizuya K. Phys. Lett. 100B # 1 (1981) p82.

69) Rückl, R. Phys. Lett.120B (1983) p449.

70) Barger, V., *et al.* Phys. Rev. Lett. 44 # 4 (1980) p226.

71) Hayne, C., and N. Isgur. Phys. Rev. D25 (1982) p1944.

72) Chanowitz, M.S. Proceedings of Summer Institute on Particle Physics. SLAC Rep. 245 (Jan. 1982) p65.

73) Eichten, E., *et al.* Phys. Rev. D21 (1980) p203.

74) Grinstein B., M. Wise, and N. Isgur. Phys. Rev. Lett. 56 , 298 (1986).

75) Niu, K., *et al.* Prog. Theor. Phys. 46 1644 (1971).

76) Caso C., and M.C. Touboul. CERN/EP 85-176 (Oct. 1985).

77) Fuchi, H., *et al.* Lett. Nuovo Cimento 31 (1981) p199.

78) Allasia, D., *et al.* Nucl. Phys. B176 13 (1980).

79) Adamovich, M.I., *et al.* Lett. Nuovo Cimento 30 (1981) p166.

80) Adamovich, M.I., *et al.* Phys. Lett. 139B (1984) p199.

81) Adamovich, M.I., *et al.* Phys. Lett. 140B (1984) p123.

82) Thorndike, E.H. Proceedings of the 1985 International Symposium on Lepton and Photon Interactions at High Energy. Kyoto, Japan (1985).

83) Badertscher A., *et al.* Phys. Lett. 123B (1983) p471.

84) Abe, K., *et al.* Phys. Rev. Lett. 48 (1982) p1526.

85) Abe, K., *et al.* Phys. Rev. Lett. 51 (1983) p156.

86) Abe, K., *et al.* Phys. Rev. D30 (1984) p1.

87) Abe, K., *et al.* Proceedings of the XXII International Conference on HEP. Leipzig (July 1984).

88) Aguilar-Benitez, M., *et al.* Phys. Lett. 122B (1983) p312.

89) Aguilar-Benitez, M., *et al.* Phys. Lett. 123B (1983) p98.

90) Aguilar-Benitez, M., *et al.* Phys. Lett. 123B (1983) p103.

91) Aguilar-Benitez, M., *et al.* Phys. Lett. 135B (1984) p237.

92) Albini, E., *et al.* Phys. Lett. 110B (1982) p339.

93) Bailey, R., *et al.* Phys. Lett. 132B (1983) p230.

94) Bailey, R., *et al.* Phys. Lett. 132B (1983) p237.

95) Bailey, R., *et al.* Nucl. Phys. B239 (1984) p15.

96) Gladney, L.D. SLAC Rep. 279 (March 1985).

97) Biagi, S.F., *et al* Phys. Lett. 122B (1983) p455.

98) Biagi, S.F., *et al* Phys. Lett. 150B (1985) p230.

99) HRS result quoted in 82.

100) TASSO result quoted in 82.

101) Yamamoto, H.,*et al.*, (DELCO). SLAC-PUB-3628, (April 1985).

102) Behrends, S., *et al.* Proceedings of the 1985 International Symposium on Lepton and Photon Interactions at High Energy. Kyoto, Japan (1985).

103) See 27 p37.
Pitman, Dale. Ph.D. thesis, University of Toronto (1982) p42,
Errede, S.W. Ph.D. thesis, The Ohio State University (1981) p14.

104) Burhop *et al.* Phys. Lett. 65B (1976) p299.

105) Ammar, R., *et al.* Phys. Lett. 94B (1980) p118.

106) Hand, L., *et al.* Nucl. Instr. Meth. 167 (1979) p261.

107) Adamovich, M.I., *et al.* Phys. Lett. 99B (1981) p271.

108) Damerell, C.J.S. Proc. 12th SLAC Summer Institute on Particle Physics. SLAC Rep. 281, (July 1984).

109) Koller, E.L., *et al* Nuovo Cimento 27 (1963) p1405.

110) Prentice, J.D. Physics Reports 83 # 1 (1982) p85.

111) Lovatt, Ian A. E531 Survey, (Nov 1980,Jun 1981), (Private communication).

112) E531 internal note: Log Book V p36.

113) See 27 p58.

114) Piatak, D. E531 internal note, Nov (1965).

115) Ramana Murthy, P.V., and G.D. Demeester. Nucl. Inst. Meth. 56 (1967) p93.

116) Allison, W.W.M, *et al.*, (ISIS). Nucl. Inst. Meth. 119 (1974) p499.

117) Cobb, J.H. Ph.D. thesis. Wolfson College, Oxford University (1975).

118) Bunch, J.N. Ph.D. thesis, Keble College. Oxford University (1976).

119) Cobb, J.H., W.W.M. Allison and J.N. Bunch. Nucl. Inst. Meth. 133, (1976) p315.

120) Cobb, J.H., W.W.M. Allison and J.N. Bunch. Nucl. Inst. Meth. 133, (1976) p325.

121) Pleming, R.W. Ph.D. thesis. St. John's College, Oxford University (1977).

122) Sauli, F. CERN Yellow Report 77-09 (May 1977).

123) Allison, W.W.M. and J.H. Cobb. Oxford University Preprint 13/80. (1980)

124) Allison, W.W.M., *et al.* Nucl. Inst. Meth. 163 (1979) p331.

125) Walenta, A.H., *et al.* Nucl. Inst. Meth. 161 (1979) p45.

126) Talman, R. Nucl. Inst. Meth. 159 (1979) p189.

127) Walenta, A.H. Proceedings of International Conference on Experimentation at LEP. Uppsala, Sweden (June 1980).

128) Marx, Jay N. Proceedings of the 1980 SLAC Summer Institute. SLAC Rep. 224 (July 1980).

129) Allison, W.W.M. Physica Scripta 23 (1980).

130) Sadoulet, B. Physica Scripta 23 (1980).

131) Allison, W.W.M., and J.H. Cobb. Ann. Rev. Nucl. Sci. 30 (1980) p253.

132) Walenta, A.H. Physica Scripta 23 (1981) p334.

133) Shapiro, A.M., *et al.* Rev. Sci. Instrum. 53(4) (Apr. 1982).

134) Peisert, A. and F. Sauli. CERN Yellow Report 84-08 (July 1984).

135) Kuchela, K.S. and J. Trischuk. IEEE Transactions on Nuclear Science, Vol. NS-29, No. 1, (Feb. 1982) p286.

136) Lovatt, Ian A. M.Sc. thesis. University of Toronto, (1982).

137) Turcotte, M. Contribution to the Canadian Association of Physicists 1981 Annual Meeting

138) See 11 pS48.

139) McKeil, G. M.Sc. thesis, University of Toronto (1982).

140) See 27 p49.

141) Pitman, Dale. Ph.D. thesis, University of Toronto (1982) p62.

142) Trischuk, John. E531 internal note. (Private communication).

143) Errede, S.W. Ph.D. thesis, The Ohio State University (1981) p25.

144) Ford, R.L., and W. R. Nelson. SLAC Pub. 210, UC-32, (June 1978).

145) Olynick, Gene. E531 internal note. (Private communication).

146) See 143 p185.

147) Frederiksen, S. E531 internal note. (Private communication).

148) McKeil, G. E531 internal note. (Private communication).

149) Bodek, A., *et al.* Proceedings of Calorimeter Workshop. FNAL (May 1975), p 235.

150) Ushida, N., *and al.* Nucl. Inst. Meth. 224 (1984) p50-64.

151) Kuramata, S. E531 internal note; Gauthier, A. E531 internal note; (Private communications).

152) See 27 p66.

153) See 143 p47.

154) Ushida, N., *et al.* Phys. Rev. Lett. 56 # 17 (1986) p1767.

155) CAMAC Instrumentation and Interface Standards. Published by The Institute of Electrical and Electronics Engineers, New York: Wiley & Sons, (1982).

156) DATA GENERAL Corporation (1975), Southboro, Massachusetts.

157) Proceedings of the 1964 Easter School for Physicists.

158) Biagi, S.F., *et al.* CERN-EP/83-09. (1983)

159) Albrecht, H., *et al.* Phys. Lett. 146B (1984) p111.

160) Gauthier, A. E531 Internal note. (Private communication, Nov. 1984).

161) Frodesen, A.G., O. Skjeggestad and H. Tøfte. Probability and Stastistics in Particle Physics. Bergen: Universitetsforlaget, (1978) p159.

162) See 143 p46.

163) Frederiksen, S. Private communication.

164) Chernyavsky, M.M., *et al.* Nucl. Inst. Meth. 228 (1984) p133.

165) See 161, p.235.

166) Ushida, N., *et al.* Phys. Rev. Lett. 51 # 26 (1983) p2362.

167) See 27 p102.

168) Lovatt, Ian A. Ph. D. thesis, University of Toronto, (1986).

169) See 161 p109.

170) Gladney, L.D. SLAC Rep. 279, (March 1985) p55.

171) Eadie, W.T., *et al.* Statistical Methods in Experimental Physics.
Amsterdam: North Holland (1977) p43.

172) See 27 p27.

173) Abramowitz, M., and A. Stegun. Handbook of Mathematical Functions.
New York: Dover, (1964) p936.

174) See 161 p243.

175) Ushida, N., *et al.* Phys. Rev. Lett. 48 # 13 (1982) p844.

176) See 143 p72ff.

177) Ushida, N., *et al.* Phys. Rev. Lett. 56 # 17 (1986) p1767.

178) Ushida, N., *et al.* Phys. Rev. Lett. 56 # 17 (1986) p1771.

179) Albrecht, H., *et al.*. Phys. Lett. 158B (1984) p525.

180 See 55 p112.

181) Quigg, C. Gauge Theories of the Strong, Weak and Electromagnetic Interactions.
Reading: Benjamin/Cummings. (1983), p26ff.

182) Abers, S., and Benjamin W. Lee. Phys. Rep. 9 No 1(1973).

183) Georgi, H. Weak Interactions and Modern Particle Theory. Reading: Benjamin/Cummings, (1984).

184) See 181.

185) Aitchison, I.J.R., and A.J.G. Hey. Gauge Theories in Particle Physics.
Bristol: Adam Hilger Ltd in association with the University of Sussex Press, (1982).

186) Halzen, F., and A.D. Martin. Quarks & Leptons. New York: John Wiley & Sons, (1984).

187) Lie, Sophus, and G. Scheffers. *Vorlesungen über contunuierliche Gruppen,*
Leipzig: Teubner verlagsgesellschaft, (1938); For a comprehensive treatment, see:
Racah, Gulio. Group Theory and Spectroscopy
Notes from the Institute of Advanced Studies, Princeton (1951).

188) Hammermesh, M. Group Theory. Reading: Addison-Wesley, (1964).

189) Fermi, Enrico. Z. Phys. 88 (1934) p161.

190) Breit, G., E.U. Condon and R.D. Present. Phys. Rev. 50 (1936) p825.

191) Rochester G.D. and C.C. Butler. Nature 160 (1947) p855.

192) Eisenberg, Y. Phys. Rev. 96 541 (1954).

193) Gell-Mann, M. Phys. Lett. 8 214 (1964).

194) Zweig, G. CERN Report 8182/Th.401 (1964).

195) Gaillard, M.K., and B.W. Lee. Rev. Mod. Phys. 47 # 2 (1975).

196) Einhorn, M.B. FERMILAB-LECTURE-75/1-THY/EXP. (1975)

197) Close, F.E. An Introduction to Quarks and Partons London: Academic Press, (1979) p51.

198) See 181 p15.

199) See 198 p65.

200) Landau, L., J. Phys. USSR 8 (1944), p201.

201) Bebek, C., *et al.* Phys. Rev. Lett. 56 # 18 (1986), p1893.

12.0) APPENDICES

12.1) The E531 Collaboration

N. Ushida
Department of Physics, Aichi University of Education, Igaya-cho,
Kariya-shi, Aichi 448, Japan.

T. Kondo [a]
Fermi National Accelerator Laboratory, Batavia, Illinois 60510, U.S.A.

S. Tasaka
Faculty of Education, Gifu University, Gifu 501-11, Japan.

I. G. Park and J. S. Song
Department of Physics, Gyeongsang National University, Jinju 620, Korea.

T. Hara, Y. Homma [b] and Y. Tsuzuki [c]
College of Liberal Arts, Kobe University, Tsurukabuto, Nada-ku, Kobe 657,
Japan.

G. Fujioka, H. Fukushima, Y. Takahashi, S. Tatsumi [d] and C. Yokoyama
Department of Physics, Kobe University, Rokkodai-cho, Nada-ku, Kobe 657,
Japan.

K. Fujiwara and K. Taruma
Graduate School of Science and Technology, Kobe University, Rokkodai-cho,
Nada-ku, Kobe 657, Japan.

S. Y. Bahk, [e] C. O. Kim and J. N. Park [f]
Department of Physics, Korea University, Seoul 132, Korea.

D. C. Bailey, [g] S. Conetti, P. Mercure, J. Trischuk and M. Turcotte
Department of Physics, McGill University, Montréal, Québec H3A 2T8, Canada.

S. Aoki, K. Chiba, H. Fuchi, [h] K. Hoshino, K. Kodama, R. Matsui,
M. Miyanishi, M. Nakamura, K. Nakazawa, K. Niu, K. Niwa, M. Ohashi,
H. Sasaki, Y. Tomita, N. Torii, O. Yamakawa, and Y. Yanagisawa [i]
Department of Physics, Nagoya University, Furo-cho, Chikusa-ku, Nagoya 464, Japan.

G. J. Aubrecht II, S. Errede, [i] A. Gauthier, M. J. Gutzwiller, [k]
S. Kuramata, G. Oleynik, N. W. Reay, K. Reibel, R. A. Sidwell,
and N. R. Stanton
Physics Department. The Ohio State University, Columbus, Ohio 43210, U.S.A.

K. Moriyama and H. Shibata
Physics Department, Okayama University, Tsushimanaka, Okayama 700, Japan.

O. Kusumoto, Y. Noguchi, T. Okusawa, M. Teranaka and J. Yamato
Physics Department, Osaka City University, Sugimoto, Sumiyoshi-ku,
Osaka 558, Japan.

H. Okabe and J. Yokota
Science Education Institute of Osaka Prefecture, Karita, Sumiyoshi-ku,
Osaka 558, Japan.

S. G. Frederiksen, C. J. D. Hébert, J. Hébert, and B. McLeod
Department of Physics, University of Ottawa, Ottawa, Ontario K1N 6N5, Canada.

M. Kazuno, H. Shibuya
Physics Department, Toho University, Funabashi-shi, Chiba 274, Japan.

I. A. Lovatt, J. F. Martin, D. Pitman, J. D. Prentice, B. J. Stacey,
and T.-S. Yoon
Physics Department, University of Toronto, Toronto, Ontario M5S 1A7, Canada.

Y. Maeda
Faculty of Education, Yokohama National University, Tokiwadai, Hodogaya-ku,
Yokohama 240, Japan.

a Now at KEK, Oho-machi, Tsukuba-gun, Ibaraki-ken 305, Japan.
b Now at School of Allied Medical Sciences, Kobe University, Tomogaoka, Suma-ku, Kobe 654, Japan.
c Also at the Graduate School of Science and Technology, Kobe University.
d Now at Sumitomo Heavy Industries Ltd., Chiyoda-ku, Tokyo 101, Japan.
e Now at Department of Physics, College of Education, Wonkwang University, Iri 510, Korea.
f Now at Department of Computation and Statistics, Sookmyong Woman's University, Seoul 140, Korea.
g Now at University of Toronto, Toronto, Ontario, Canada.

h Now at Eda High School, Yokohama 227, Japan.

i Now at Hamamatsu Photonics Co. Ltd., Hamamatsu 435, Japan.

j Now at University of Illinois, Urbana-Champaign, Illinois, U.S.A.

k Now at Texas Instruments Inc., Houston, U.S.A.

12.2) BASIC FACTS OF GAUGE THEORY

12.2.1) Symmetries, currents & locality

The fact that to symmetries of quantum systems correspond conserved quantities is a consequence of basic single-particle quantum mechanics. In this context, symmetry of wavefunctions with respect to translation in 3-space for instance, leads to conservation of 3-momentum. Symmetry with respect to time (time-invariance) leads to conservation of energy. Symmetry with respect to space-time transformations or invariance of 4-vector lengths leads to energy-momentum conservation etc...

Field theories which are designed to handle many particles instead of just one (as in elementary quantum physics) are no different. There, the basic underlying idea really is that of Noether's [181]: to every symmetry of the Lagrangian of the theory, corresponds a conserved current. If ψ is some multi-component field which exhibits some symmetry [182] [183] [184] [185] [53] such that:

$$\mathcal{L}(\psi + \delta\psi) = \mathcal{L}(\psi)$$

then there exists a conserved quantity, a current, such that:

$$\partial_\mu J^\mu = 0$$

$$J^\mu = \frac{\delta \mathcal{L}}{\delta(\partial_\mu \psi_j)} \delta\psi_j$$

It is relevant to consider symmetries that are local, that is, that depend *explicitely* on space-time. This is called local gauge invariance or locality. It requires the infinitesimal transformation to be written as $\delta\psi(x) = i\epsilon_a(x)T^a\psi(x)$. In this, $[T^a, T^b] = if^{abc}T^c$ defines the *algebra* of the group. The T's are generators of the group transformations, the ϵ's are their infinitesimal amplitudes while the f^{abc} are numbers known as the group structure constants.

The Lagrangian density cannot be made invariant under such a transformation unless the derivative is re-defined as the co-variant derivative:

$$D^\mu = \partial^\mu + i\, g\, T_a A_a^\mu$$

In this, g is some (coupling) constant and A_a^μ is some added piece, some field, to make the invariance scheme work. This added complication really isn't one; it is just a consequence of the imposed constraint of local invariance which *requires* the introduction of a new field, and that *is* most fundamental.

If the chosen group of transformations happens to be the abelian group of local phase transformations $U(1)$, then A^μ turns out to be the photon field: $F^{\mu\nu} = \partial^\mu A^\nu - \partial^\nu A^\mu$. Thus, electric and magnetic (i.e. electromagnetic) interactions of electrons and positrons (*leptons* in general...) are wholly understood in terms of the exchange of such a field quanta and the complete theory is known as quantum electro-dynamics (QED).

In general, invariance under a such a symmetry transformation cannot be made to work unless the mass of the exchanged particle, or gauge boson, is exactly zero. This is because a term like $\frac{1}{2}\, m^2\, A_a^\mu\, A_{a\mu}$ in the Lagrangian is explicitly not gauge invariant.

The gauge group may or may not be abelian (field theories with non-abelian gauge groups are commonly known as Yang-Mills field theories). There's a class of non-abelian finite groups called *special unitary* and

denoted by $SU(n)$ which turns out to be very important. $SU(n)$ is represented by the group of transformations of the n-dimentional complex space by special, that is, unideterminental (determinant= +1) and unitary $n \times n$ matrices. The number of independent real parameters needed to specify an element in the group is called the order "r" and for $SU(n)$, $r = n^2 - 1$. In perhaps a more abstract definition, $SU(n)$ transformations are those which leave the form $\sum_{i=1}^{n} x^i y^{i*}$ invariant. In any case, SU(2) is probably most simply introduced by stating that it is the complex analogue to the group of rotations in real three-dimentional space: $O(3)$. The $SU(2)$ algebra is just $[T_i, T_j] = i\epsilon_{ijk}T_k$ [186] where $\epsilon_{ijk} = \pm 1$ for an even/odd permutation of ijk. Generators of SU(n) have traceless-matrix representations and r of them are needed to specify all transformations of the group. SU(n) algebra has been around for a long while. [187] When imposed on a locally invariant gauge theory, one is lead to the following massless gauge field:

$$F_a^{\mu\nu} = \partial^\mu A_a^\nu - \partial^\nu A_a^\mu - g\, f_{abc} A_b^\mu A_c^\nu$$

The non-abelian group of the gauge theory needs not be just $SU(n)$, it can be more complicated as in $SU(n) \otimes U(1)$ where $\otimes$ stands for a direct product [188] of the groups. It turns out that $SU(2) \otimes U(1)$ is the product required for dealing with all electro-weak interactions of leptons and quarks. (Section 2.4)

12.2.2) **Renormalizability, spontaneous symmetry breakdown & mass generation.**

Whatever the gauge group, unless something is done about the masslessness of the gauge field(s), none of the above formalism would be fully satisfying. Field theories with massive gauge-quanta are needed (weak interactions and nuclear forces have finite range) ‡ and it just won't do to simply throw in a symmetry-spoiling mass term. This is not because of some philosophical bias theorists might have towards symmetric gauge theories but rather because of a very down-to-earth reality: gauge field theories that include *ad hoc* mass terms are not *renormalizable* . [183]. In practical terms, this means that an infinite number of divergent integrals appear when calculating higher order processes and that there is no way to re-define constants in the Lagrangian so as to make them disappear. QED is safe in that respect though, for renormalization can be achieved. However, the weak interaction theory, as conceived by Fermi [189] was not, and therefore fails at high energy.

If the theory could start massless so that it be renormalizable and then, "somehow" develop a massive character, the problem would be solved. Such a process is called *spontaneous symmetry breaking* . The process, perhaps not entirely surprisingly, calls for adding other degrees of freedom to the theory: scalar spinless fields (a multiplet thereof) whose mass remain, even in the end, arbitrary (un-constrained) parameters. A Lagrangian involving such fields is written as:

$$\mathcal{L}(\phi) = \partial_\mu \phi \partial^\mu \phi - V(\phi)$$

where V is some potential term. The symmetry transformation is, as before, $\delta\phi = i\epsilon_a T^a \phi$. The vacuum expectation value of the fields is defined by $\langle\phi\rangle = \lambda$ and it is found by locating the minimum in the potential:

‡ $\Delta E \Delta t \geq \hbar \overset{non\ observation}{\longrightarrow} \Delta E \Delta T < \hbar \longrightarrow mc^2\, r/c < \hbar \longrightarrow r < \hbar/mc$ where m is the mass of the exchanged gauge boson; $r_{strong} \sim 1.5\, F$ and $r_{weak} \sim .002\, F$...

$V_j(\lambda) = 0$ & $V_{ij} \geq 0$ where subscripts stand for the derivatives in the fields. After adding such fields which possess non-zero vacuum expectation values (allowing particles to have imaginary masses) to the original Lagrangian, one then re-defines them through shifts set equal to λ. This then insures that all masses be real. Thus fields become $\phi' = \phi - \lambda$ and there appears a symmetry-breaking mass term: $\frac{1}{2}V_{ij}(\lambda)\phi'_i\phi'_j$ which is also known as the mass-matrix "M".

12.3) QUARK MODEL AND FLAVOUR SYMMETRIES

From the arguments that lead to the Standard Model of electro-weak interactions, (For a quick summary, see Appendix 12.2), it may appear that Special Unitary groups have only had a use in understanding gauge theories; in other words, that Special Unitary symmetry is only useful as a gauge symmetry. That is, however, far from being so. For a long while, even before gauge theories had a respectable name, an $SU(2)_f$ ‡ symmetry of the nuclear forces was known to exist. This is because, in the absense of electromagnetic interactions, the proton and the neutron behave as a single particle: the nucleon (charge-independence [190]). † Thus, nuclear amplitudes are invariant under $SU(2)_f$ transformations: $(uud) \leftrightarrow (udd)$, $p \leftrightarrow n$. This symmetry was called (nuclear) isospin because of a similar, yet seperate, $SU(2)$ symmetry of the electron: its spin.

When, *strange* particles (Λ^0 K^0) were discovered [191], it was just *natural* to try to enlarge the doublet formed by p and n to include a third member: the Λ. In the same way the protons and neutrons were associated with the two $SU(2)_f$ states of the nucleon, the Λ was associated with the quantum number *strangeness* (nuclear-hypercharge) and the group assumed to govern these states was now $SU(3)_f$, of which, $SU(2)_f$ is a subgroup. This became known as the *Eightfold Way*. Fortunately, this symmetry wasn't particularly exact (the particles to which states could be assigned do not have quite the same mass). It was possible to use the observed mass difference between the particles to which state assignments were made as a measure of how *broken* the symmetry actually is. This lead to some mass-predictive power within $SU(3)_f$ multiplets (Gell-Mann Okubo mass relation [38] ¶) and in particular, the the Ω^--particle was found on the basis of such a prediction [192]. In some sense however, the symmetry patterns of the Eightfold Way remained as somewhat of an odd classification scheme until the advent of quarks. As experimental evidence gathered on the existance of internal structure of nucleons, the group-theoretical description of hadron symmetry in terms of more fundamental symmetry building-blocks, namely the quarks [193] [194], became more plausible and the true *flavour* nature of the symmetry exposed. Thus, the u, d and s quarks were assumed to have (broken) $SU(3)_f$ symmetry and direct products of these generate observed hadron quantum numbers. It was natural to think that a heavier quark like charm should enter the picture in a similar way; the group needs only be enlarged to $SU(4)_f$ which still contains $SU(3)_f$ and the latter still contains $SU(2)_f$. However,

---

‡ Actually, the *flavour* nature of this symmetry was not obvious until the advent of quarks. Yet, to avoid confusion with gauge symmetries discussed in other sections, the subscript f is used here to denote "flavour".

† It was found that pp and pn hadronic force has same range and strength, once Coulomb effects were removed.

¶ A simple form of the relation is:

$$M = a + bY$$

and so the masses of hadrons within a multiplet are linearly related to the *hypercharge* and thus it is predicted that there should be equal mass-spacing between the members of a $SU(3)_f$ multiplet...

this symmetry is even more badly broken than the others because of the larger charm-quark mass. In any case, much of the predictive power really lies with the underlying assumption that physical particles should follow representations of $SU(4)_f$. Figure # 4 presents the $SU(4)_f$ weight-space [195] [196] corresponding to two- and three-direct products of flavour-states (u, d, s and c with the corresponding anti-quarks, see Appendix 12.4) . * Instead of considering the complicated n-plet $SU(4)_f$-patterns, perhaps it is more intuitive to just concentrate on a particular subgroup of $SU(4)_f$, the old $SU(3)_f$, and to recognize that, for example, the pseudo-scalar mesons containing the s-quark are arranged in an $SU(3)_f$-octet representation while the pseudo-scalar mesons containing the c-quark are arranged as an $SU(3)_f$-triplet. These subgroups correspond to the shaded areas of the figures. For the sake of completeness, other representations have been included.

In general, flavour symmetries ($SU(2)_f$, $SU(3)_f$, $SU(4)_f$) are known as *dynamical* symmetries as opposed to *gauge* symmetries because, in addition to classifying hadrons in terms of internal quantum numbers (obtained as a result of combining quark-states), they provide dynamical relations between strong interaction amplitudes. Early attempts to build Yang-Mills gauge theories using flavour symmetry have failed [198]. It is now known that the flavour quantum number is related to the (flavour-changing) weak-interactions while color is the attribute of strong interactions; the strong interactions are flavour independent. However, the exact origin of dynamical symmetries which should be related to the origin of the differences between quark masses is still not yet firmly established [199].

* In $SU(3)_f$: with u, d and s, $q\,\overline{q}$ meson-states can be built from quark states using the $3 \otimes \overline{3} = 8 \oplus 1$ direct product. Baryons ($q\,q\,q$) are built from the $(3 \otimes 3) \otimes 3 = (10 \oplus 8) \oplus (8 \oplus 1)$ [197] In $SU(4)_f$, things get slightly more complicated and that is why it is perhaps sufficient to just refer to the weight diagram of Figure # 4 .

12.4) QUARK MODEL QUANTUM NUMBERS [138]

	flavour					
Quantum Number	*d*	*u*	*s*	*c*	*b*	*t*
Baryon number	1/3	1/3	1/3	1/3	1/3	1/3
Spin	1/2	1/2	1/2	1/2	1/2	1/2
Charge	−1/3	+2/3	−1/3	+2/3	−1/3	+2/3
I_3	−1/2	+1/2	0	0	0	0
Strangeness	0	0	−1	0	0	0
Charm	0	0	0	+1	0	0
Beauty	0	0	0	0	−1	0
Truth	0	0	0	0	0	+1

12.5) QCD CORRECTION COEFFICIENTS FOR HEAVY-QUARK DECAY [55]

μ GeV	$C^{L.L.}_{-\,\Lambda_{QCD}=100\ MeV}$	$C^{L.L.}_{+\,\Lambda_{QCD}=100\ MeV}$	$C^{L.L.}_{-\,\Lambda_{QCD}=500\ MeV}$	$C^{L.L.}_{+\,\Lambda_{QCD}=500\ MeV}$
1	1.84	.739	3.12	.566
2	1.58	.794	2.10	.691
5	1.36	.861	1.57	.797
50	1.04	.981	1.06	.972

Note: the number of quark flavours used by the Author of *Ref.* 56 was 6.

μ GeV	$C^{L.L.}_{-\,\Lambda_{QCD}=250\ MeV}$	$C^{L.L.}_{+\,\Lambda_{QCD}=250\ MeV}$	$C^{N.L.L.}_{-\,\Lambda_{QCD}=250\ MeV}$	$C^{N.L.L.}_{+\,\Lambda_{QCD}=250\ MeV}$
1	2.57	.64	2.03	.70
2	1.90	.73	1.69	.77
5	1.49	.82	1.39	.85
50	1.05	.98	1.04	.98

Note: the number of quark flavours used by the Author of *Ref.* 56 was 6 and $\alpha_s^{L.L.} = \alpha_s^{N.L.L.}$.

12.6) RELATIVISTIC RISE IN GASES

Consider a fast charged particle traversing a medium containing N_e atomic electrons per unit volume. It can be shown [123], in a semi-classical approach assuming energy-losses are small compared to that of the incoming particle, that the cross-section per electron (probability per unit energy per electron) for interacting with some outer-shell atomic electron splits into two components:

$$\frac{d\sigma}{dE} = \frac{d\sigma_\perp}{dE} + \frac{d\sigma_\parallel}{dE}$$

The so-called transverse cross-section gathers all the effects due to that part of the electric field of the particle which points perpendicularly to the 3-momentum transfer to the atomic electron. In the limit of zero density, this becomes:

$$\frac{d\sigma_\perp}{dE} \underset{N_e \to 0}{\sim} \left[\ln \gamma^2 - \beta^2\right]$$

which increases linearly with $\ln \gamma$: this is known as the "relativistic rise"... However, it turns out that

$$\frac{d\sigma_\perp}{dE} \underset{\beta \to 1}{\sim} \left[\ln \left(\frac{\omega}{\omega_p'}\right)^2 - 1\right]$$

These two limits show that *saturation* * occurs for velocities of the order of $\gamma = \omega/\omega_p'$ where $\omega_p'^2 = 4\pi N_e e^2/m$ is the *plasma frequency* of the material and ω is a measure of the energy transfer in a single "collision". The largest rise is obtained for materials with low ω_p': gases and large ω: high ionization potentials. Thus noble gases are prime choices to observe these effects.

Note that the second term of the cross-section:

$$\frac{d\sigma_\parallel}{dE} \underset{\beta \ll 1}{\sim} \frac{1}{\beta^2}$$

gathers the contribution of that part of the electric field of the fast particle which points in the direction parallel to the 3-momentum transfer to the atomic electron. In the non-relativistic approach, this is the only contribution to the cross-section. The technique of particle identification due to high ionization losses at low speeds is well known but inadequate for E531 purposes.

The interaction cross-section per electron is an interesting quantity in itself but energy losses occur over a finite thickness of gas; over some finite number of atomic-electrons... The problem of convoluting energy-losses was first solved exactly by Landau [200] using Laplace Transforms. He showed that the probability of

* The saturation effect can be understood qualitatively in the following terms: a *plateau* is reached when the maximum impact parameter of the incident fast charged particle becomes much larger than typical inter-atomic spacings. This starts to happen for large γ because, for the observer sitting on the atomic electron, the electric field of the fast charged particle now appears more and more (*as* $\beta \to 1$) compressed in the direction parallel to its motion while extending further and further away, perpendicularly to it. As the extended electric field reaches over many inter-atomic spacings, the medium *polarises* and its effects are cancelled.

an energy loss Δ at a thickness x is gven by:

$$F(x,\Delta) = \frac{1}{2\pi i}\int_{-i\infty+\sigma}^{+i\infty+\sigma} \exp\left[s\Delta - x\int_0^\infty N\,\frac{d\sigma}{dE}(E)\;(1-\exp(-sE))\;dE\right]\,ds$$

However, because realistic expressions for the cross-section are complicated, his integral solution can only be handled numerically. The main features though, are that this distribution is wide ($\sim$ 100%) and skewed towards large energy losses.

12.7) **HAD. CAL. : AVERAGE SHOWER DEPOSITION (in M.I.) PER PLANE** [149]

	Initial hadron energy (GeV)								
counter #	5 *GeV*	10 *GeV*	20 *GeV*	30 *GeV*	50 *GeV*	100 *GeV*	150 *GeV*	200 *GeV*	250 *GeV*
1 ← EPIC A	11.4	21.1	36.2	51.4	66.0	108.0	138.0	193.0	207.8
2 ← EPIC B	5.1	14.1	32.2	50.6	83.5	157.0	198.0	247.1	283.3
3 ← EPIC C	1.4	6.2	15.3	22.2	41.9	87.7	140.0	183.8	227.6
4 ← PADDLE I	0.1	4.4	9.1	14.0	27.7	59.3	91.8	107.2	132.4
5 ← PADDLE II	0.0	2.0	5.0	9.4	18.9	43.1	73.1	102.1	129.9
6 ← PADDLE III	0.0	1.5	3.0	5.4	11.3	27.1	48.3	57.2	74.2
7	0.0	0.8	1.7	3.8	7.4	19.5	35.9	43.9	60.6
8	0.0	0.4	0.8	2.1	4.4	12.1	23.8	30.6	40.8
9	0.0	0.3	0.5	1.0	3.0	8.4	17.1	20.4	29.7
10	0.0	0.2	0.3	0.7	1.8	5.4	13.0	16.3	23.5
11	0.0	0.1	0.1	0.5	1.4	3.7	7.4	8.2	12.4
12	0.0	0.1	0.1	0.2	0.7	2.2	4.3	5.1	7.4
13	0.0	0.1	0.1	0.1	0.4	1.5	2.7	3.1	4.9
14 ← MU F	0.0	0.1	0.1	0.2	0.5	1.2	2.6	2.0	3.7

Each plane = 10.16 *cm* of steel

12.8) HAD. CAL. : PERCENTAGE SHOWER DEPOSITION PER PLANE [149]

	Initial hadron energy (GeV)								
counter #	5 *GeV*	10 *GeV*	20 *GeV*	30 *GeV*	50 *GeV*	100 *GeV*	150 *GeV*	200 *GeV*	250 *GeV*
1 ← EPIC A	.680	.413	.346	.319	.246	.200	.174	.189	.168
2 ← EPIC B	.224	.276	.306	.310	.306	.288	.249	.242	.229
3 ← EPIC C	.079	.123	.146	.139	.156	.163	.175	.180	.184
4 ← PADDLE I	.017	.083	.087	.088	.105	.112	.116	.105	.107
5 ← PADDLE II	.000	.038	.048	.057	.070	.081	.092	.100	.105
6 ← PADDLE III	.000	.027	.027	.034	.053	.051	.060	.056	.060
7	.000	.016	.016	.023	.028	.037	.045	.043	.049
8	.000	.008	.008	.013	.016	.023	.030	.030	.033
9	.000	.005	.005	.006	.011	.016	.021	.020	.024
10	.000	.004	.003	.004	.007	.010	.016	.016	.019
11	.000	.002	.001	.003	.005	.007	.009	.008	.010
12	.000	.001	.001	.001	.003	.004	.005	.005	.006
13	.000	.001	.001	.001	.002	.003	.004	.003	.004
14 ← MU F	.000	.001	.001	.001	.002	.003	.004	.002	.003

Each plane = 10.16 *cm* of steel

12.9) **CHARM FINDING EFFICIENCIES**

NEUTRAL CHARM FINDING EFFICIENCIES

Combined 1st run scanning groups: $HV_{neutral}$

from [μ m]	to [μ m]	Eff. [%]
0.0	2.0	0.0
2.0	5.0	13.8
5.0	10.0	35.1
10.0	30.0	68.1
30.0	400.0	82.0
400.0	1000.0	73.3
1000.0	60000.0	62.2

Kobe University scanning group: $KH_{neutral}$

from [μ m]	to [μ m]	Eff. [%]
0.0	3.0	0.0
3.0	10.0	50.0
10.0	300.0	67.0
300.0	99999.9	62.0

Nagoya University scanning group: $NV_{neutral}$

from [μ m]	to [μ m]	Eff. [%]
0.0	15.0	0.0
15.0	30.0	71.0
30.0	1000.0	95.0
1000.0	99999.9	92.0

NEUTRAL CHARM FINDING EFFICIENCIES

Osaka University scanning group: $O3_{neutral}$

from [μm]	to [μm]	Eff. [%]
0.0	3.0	0.0
3.0	10.0	63.0
10.0	300.0	84.0
300.0	99999.9	81.0

University of Ottawa scanning group (vertical emulsion): $OV_{neutral}$

from [μm]	to [μm]	Eff. [%]
0.0	15.0	0.0
15.0	30.0	74.0
30.0	1000.0	98.0
1000.0	99999.9	97.0

University of Ottawa scanning group (horizontal emulsion): $OH_{neutral}$

from [μm]	to [μm]	Eff. [%]
0.0	3.0	0.0
3.0	10.0	72.0
10.0	99999.9	96.0

CHARGED CHARM FINDING EFFICIENCIES

Combined 1st run scanning groups: $HV_{charged}$

from [μ m]	to [μ m]	Eff. [%]
0.0	2.0	0.0
2.0	5.0	18.0
5.0	10.0	50.0
10.0	30.0	76.0
30.0	3000.0	95.0
3000.0	6000.0	85.0
6000.0	60000.0	59.0

Kobe University scanning group ($\theta \leq 200$ $mrad$): $KH_{charged}$

from [μ m]	to [μ m]	Eff. [%]
0.0	3.0	0.0
3.0	10.0	74.0
10.0	6000.0	98.0
6000.0	99999.9	60.0

Kobe University scanning group ($\theta > 200$ $mrad$): $2K_{charged}$

from [μ m]	to [μ m]	Eff. [%]
0.0	3.0	0.0
3.0	10.0	74.0
10.0	3000.0	98.0
3000.0	99999.9	60.0

Combined scanning groups (horizontal kinks): $HK_{charged}$

from [μ m]	to [μ m]	Eff. [%]
0.0	5.0	0.0
5.0	10.0	41.0
10.0	15.0	74.0
15.0	20.0	83.0
20.0	6000.0	87.0
6000.0	99999.9	53.0

CHARGED CHARM FINDING EFFICIENCIES

Nagoya University scanning group ($\theta \leq 200\ mrad$): $NV_{charged}$

from [$\mu\ m$]	to [$\mu\ m$]	Eff. [%]
0.0	15.0	0.0
15.0	30.0	75.0
30.0	1000.0	100.0
1000.0	6000.0	99.0
6000.0	99999.9	89.0

Nagoya University scanning group ($\theta > 200\ mrad$): $2N_{charged}$

from [$\mu\ m$]	to [$\mu\ m$]	Eff. [%]
0.0	15.0	0.0
15.0	30.0	75.0
30.0	1000.0	100.0
1000.0	3000.0	99.0
3000.0	99999.9	89.0

Combined scanning groups (vertical kinks): $VK_{charged}$

from [$\mu\ m$]	to [$\mu\ m$]	Eff. [%]
0.0	25.0	0.0
25.0	30.0	41.0
30.0	35.0	55.0
35.0	55.0	66.0
55.0	85.0	77.0
85.0	185.0	86.0
185.0	1000.0	90.0
1000.0	6000.0	91.0
6000.0	99999.9	81.0

Osaka University ($\theta \leq 200\ mrad$): $O3_{charged}$

from [$\mu\ m$]	to [$\mu\ m$]	Eff. [%]
0.0	3.0	0.0
3.0	10.0	74.0
10.0	6000.0	99.0
6000.0	99999.9	78.0

CHARGED CHARM FINDING EFFICIENCIES

Osaka University ($\theta > 200\ mrad$): $2O_{charged}$

from [$\mu\ m$]	to [$\mu\ m$]	Eff. [%]
0.0	3.0	0.0
3.0	10.0	74.0
10.0	3000.0	99.0
3000.0	99999.9	78.0

University of Ottawa (vertical): $OV_{charged}$

from [$\mu\ m$]	to [$\mu\ m$]	Eff. [%]
0.0	15.0	0.0
15.0	30.0	75.0
30.0	6000.0	100.0
6000.0	99999.9	94.0

University of Ottawa (horizontal): $OH_{charged}$

from [$\mu\ m$]	to [$\mu\ m$]	Eff. [%]
0.0	3.0	0.0
3.0	10.0	75.0
10.0	6000.0	100.0
6000.0	99999.9	91.0

12.10) **BREMSSTRAHLUNG: TABLE OF INITIAL ENERGY ERROR**

	Final observed e^{+or-} energy (GeV)						
distance (cm)	0.50	1.00	1.50	2.00	2.50	3.00	4.00
0.50	0.01	0.03	0.05	0.09	0.14	0.21	0.33
1.00	0.12	0.15	0.20	0.36	0.50	0.60	0.90
1.50	0.20	0.50	0.50	0.65	0.75	1.00	1.25
2.00	0.25	0.75	0.70	1.30	1.00	1.50	1.88
3.00	0.50	1.00	1.00	2.00	1.75	2.50	2.63
4.00	0.60	1.25	1.20	2.20	2.40	2.75	3.75
5.00	0.75	1.50	1.40	2.50	2.90	3.75	4.30

Ex: $\sigma_{E^{e^{+or-}}_{initial}} = 0.70\ GeV$ for $d = 2.00\ cm$ and $E^{e^{+or-}}_{final} = 1.50\ GeV$